Spins in quantum dots:
Hyperfine interaction, transport, and coherent control

Inauguraldissertation

zur
Erlangung der Würde eines Doktors der Philosophie
vorgelegt der
Philosophisch-Naturwissenschaftlichen Fakultät
der Universität Basel

von

William Anthony Coish
aus Winnipeg, Kanada

Basel, 2008

Genehmigt von der Philosophisch-Naturwissenschaftlichen Fakultät

auf Antrag von
Prof. Dr. Daniel Loss
Prof. Dr. Boris Altshuler
Prof. Dr. Guido Burkard

Basel, den 27. November, 2006

Prof. Dr. Hans-Peter Hauri
Dekan

Acknowledgements

Working toward a PhD in Basel has been fruitful and exciting primarily because of the many clever and interesting people with whom I have had the pleasure of spending time at work and at play.

First I would like to thank my supervisor, Daniel Loss, for providing inspiration, motivation, countless important ideas, as well as a stimulating research environment throughout the course of my PhD. I also thank the members of my defence committee, Daniel Loss, Boris Altshuler, and Guido Burkard, for their careful reading of my thesis, and their useful questions and comments. This thesis contains work that was completed in direct collaboration with several others, without whom, of course, the work would not have been possible. In addition to Daniel Loss, these collaborators were: Boris Altshuler, Verónica Cerletti, Oliver Gywat, Daniel Klauser, Mathias Gräber, Christian Schönenberger, and Emil Yuzbashyan. In addition to direct collaboration, I have benefited greatly from discussions with others, including, most notably, Guido Burkard, Josh Folk, Vitaly Golovach, Atac Imamoglu, Frank Koppens, and Lieven Vandersypen.

I sincerely thank all co-workers I have had in the physics institute, without whose friendship and support, scientific and otherwise, the PhD process would not have been half as rewarding. In particular, I would like to thank Veniamin Abalmassov, Nasiba Abdurakhmanova, Audrius Alkauskas, Wolfgang Belzig, Massoud Borhani, Bernd Braunecker, Christophe Bruder, Denis Bulaev, Verónica Cerletti, Stefano Chesi, Luca Chirolli, Mahn-Soo Choi, Audrey Cottet, Charles Doiron, Mathias Duckheim, Carlos Egues, Hans-Andreas Engel, Siggi Erlingsson, Jan Fischer, Alex Gaita-Ariño, Hanno Gassmann, Vitaly Golovach, Oliver Gywat, Tero Heikkilä, Sasha Khaetskii, Daniel Klauser, Minchul Lee, Jörg Lehmann, Yong Li, Andriy Lyakhov, Florian Marquardt, Florian Meier, Joël Peguiron, Patrik Recher, Beat Röthlisberger, Daniel Saraga, Pascal Simon, John Schliemann, Christian Schroll, Oleg Shalaev, Dimitrije Stepanenko, Philipp Traber, Björn Trauzettel, Filippo Troiani, Mircea Trif, Mihajlo Vanevic, and Oded Zilberberg for everything they have done to make the work environment in Basel so exceptionally good.

Above all, I thank Agnes Ferenczi for her love, patience, and diligence.

Bill Coish
Basel, Jan. 2008

Contents

Chapter 1

Introduction

In this thesis we investigate several problems that are relevant for the coherent manipulation of electron spins in semiconductor quantum dots. The requirements for quantum computing with electron spins in semiconductor quantum dots are the subject of Sec. 1.1. The primary barrier to coherent manipulation is decoherence due to coupling of the spins with fluctuations in the environment. The primary source of decoherence for electron spins in GaAs quantum dots is now recognized to be the hyperfine coupling between electrons and nuclei in the surrounding lattice, the subject of Sec. 1.2. Two-spin operations (a requirement of quantum computing) require some form of coupling between electron spins. In quantum dots, the strongest and simplest form of spin-spin coupling is the Heisenberg exchange coupling that occurs naturally for two-electron states in double quantum dots with a finite wave function overlap. Sec. 1.3 below presents a basic model used to understand the energy spectrum and eigenstates of double quantum dots, and illustrates the use of double dots for the purpose of two-qubit gating.

1.1 Quantum computing with quantum dots

The qubits of the Loss-DiVincenzo proposal for quantum computing [1] are formed from the two spin states ($|\uparrow\rangle, |\downarrow\rangle$) of a confined electron. The considerations discussed in this proposal are generally applicable to electrons confined to any structure, such as atoms, molecules, etc., although the original proposal focuses on electrons localized in quantum dots. These dots are typically generated from a two-dimensional electron gas (2DEG), in which the electrons are strongly confined in the vertical direction. Lateral confinement is provided by electrostatic top gates, which push the electrons into small localized regions of the 2DEG. Alternative quantum-dot structures include vertical quantum dots, self-assembled dots, and dots formed in nanowires [2] or carbon nanotubes [3,4,5,6,7]. Initialization of the quantum computer could be achieved by allowing all spins to reach their thermodynamic ground state at low temperature T in an applied magnetic field B (i.e., virtually all spins will be aligned if the condition $|g\mu_\mathrm{B}B| \gg k_\mathrm{B}T$ is satisfied, with g-factor g, Bohr magneton μ_B, and Boltzmann's constant k_B). Several alternative initialization schemes have been investigated (see, e.g., Chapter 7 for an adiabatic initialization scheme).

Single-qubit operations can be performed, in principle, by changing the local effective Zeeman interaction at each dot individually. To do this may require large magnetic field gradients [8], g-factor engineering [9], magnetic layers, the inclusion of nearby ferromagnetic dots [1], polarized nuclear spins, or optical schemes. Alternatively, a recent proposal suggests a way to perform single-qubit rotations on three-spin *encoded* qubits through the gate voltage in a few-electron quantum dot without changing the local Zeeman energy [10] (see Chapter 7 for a proposal to do this with single-spin *physical* qubits). In the original proposal [1], two-qubit operations are performed by pulsing the electrostatic barrier between neighbouring spins. When the barrier is high, the spins are decoupled. When the inter-dot barrier is pulsed low, an appreciable overlap develops between the two electron wave functions, resulting in a non-zero Heisenberg exchange coupling J (for an alternative method of tuning the exchange, see Sec. 1.3.3, below). The Hamiltonian describing this time-dependent process is given by

$$H(t) = J(t)\mathbf{S}_L \cdot \mathbf{S}_R. \tag{1.1}$$

This Hamiltonian induces a unitary evolution given by the operator

$$U = \mathcal{T} \exp\left\{-i \int H(t)dt/\hbar\right\}, \tag{1.2}$$

where $\mathcal{T}$ is the time-ordering operator. If the exchange is pulsed on for a time τ_s such that $\int J(t)dt/\hbar = J_0\tau_s/\hbar = \pi$, the states of the two spins, with associated operators $\mathbf{S}_L$ and $\mathbf{S}_R$, will be exchanged. This is the SWAP operation. Pulsing the exchange for the shorter time $\tau_\mathrm{s}/2$ generates the "square-root of SWAP" operation, which can be used in conjunction with single-qubit operations to generate the controlled-NOT (quantum XOR) gate [1]. In addition to the time scale τ_s, which gives the time to perform a two-qubit operation, there is a time scale associated with the rise/fall-time of the exchange $J(t)$. This is the switching time τ_sw. When the relevant two-spin Hamiltonian takes the form of an ideal (isotropic) exchange, as given in (1.1), the total spin is conserved while switching. However, to avoid leakage to higher *orbital* states during gate operation, the exchange coupling must be switched adiabatically. More precisely, $\tau_\mathrm{sw} \gg 1/\omega_0 \approx 10^{-12}\,\mathrm{s}$, where $\hbar\omega_0 \approx 1\,\mathrm{meV}$ is the energy gap to the next orbital state [1, 11, 12, 13]. We stress that this time scale is valid only for the ideal case of a purely isotropic exchange interaction. When the exchange interaction is anisotropic, different spin states may mix and the relevant time scale for adiabatic switching may be significantly longer. For scalability, and application of quantum error correction procedures in *any* quantum computing proposal, it is important to turn off inter-qubit interactions in the idle state. In the Loss-DiVincenzo proposal, this is achieved with exponential accuracy since the overlap of neighbouring electron wave functions is exponentially suppressed with increasing separation. A detailed investigation of decoherence during gating due to a bosonic environment was performed in early work [1]. Since then, there have been many studies of leakage and decoherence in the context of the quantum-dot quantum computing proposal.

The most important source of decoherence for electrons confined to GaAs quantum dots is the contact hyperfine interaction between electron spins and nuclei in the host material. Some consequences of this interaction were recognized and studied theoretically several years ago [14, 15, 16, 17, 18, 19], although conclusive experiments that show clear hyperfine effects for single quantum dots have only appeared very recently [20, 21, 22, 23, 24]. Much of this thesis deals with hyperfine-related effects, so the next section deals with the nature of this interaction in the context of quantum-dot-confined electrons.

1.2 Hyperfine interactions in quantum dots

In this section we derive effective Hamiltonians for the microscopic hyperfine interactions (isotropic and anisotropic). Some details of this derivation can also be found in Ref. [25] and in very early papers [26]. This section is directly relevant to Chapters 2, 3, 4, and 5, all of which deal with hyperfine-induced electron spin dynamics.

We begin from the Dirac Hamiltonian for a relativistic electron

$$\mathcal{H} = \boldsymbol{\alpha} \cdot \boldsymbol{\pi} + \beta mc^2 - |e|V(\mathbf{r}) \tag{1.3}$$

where $V(\mathbf{r})$ is the electric potential at the position of the electron, m is the electron rest mass, $-|e|$ is the electron charge, $\boldsymbol{\pi} = \mathbf{p}c + |e|\mathbf{A}$, and

$$\boldsymbol{\alpha} = \begin{pmatrix} 0 & \boldsymbol{\sigma} \\ \boldsymbol{\sigma} & 0 \end{pmatrix}, \ \beta = \begin{pmatrix} \mathbf{1} & 0 \\ 0 & -\mathbf{1} \end{pmatrix}, \tag{1.4}$$

are a set of 4×4 Dirac matrices ($\boldsymbol{\sigma}$ is the vector of Pauli matrices and $\mathbf{1}$ is the 2×2 identity matrix). The Dirac Hamiltonian acts on a 4-component spinor Ψ, which we write as a vector of two two-component spinors χ_1 and χ_2:

$$\Psi = \begin{pmatrix} \chi_1 \\ \chi_2 \end{pmatrix}. \tag{1.5}$$

The Dirac equation

$$\mathcal{H}\Psi = E\Psi, \tag{1.6}$$

with energy $E = mc^2 + \epsilon$ then results in the pair of coupled linear equations

$$\begin{aligned} \left(\epsilon + |e|V(\mathbf{r})\right)\chi_1 - \boldsymbol{\sigma} \cdot \boldsymbol{\pi}\chi_2 &= 0, & (1.7) \\ -\boldsymbol{\sigma} \cdot \boldsymbol{\pi}\chi_1 + \left(\epsilon + 2mc^2 + |e|V(\mathbf{r})\right)\chi_2 &= 0. & (1.8) \end{aligned}$$

Solving for χ_2 alone gives:

$$H_2\chi_2 = \epsilon\chi_2, \tag{1.9}$$

where H_2 contains three terms that depend explicitly on the electron spin $\boldsymbol{\sigma}$:

$$\begin{aligned} h_{\mathrm{ihf}} &= \frac{e^2\hbar c}{\left(\epsilon + 2mc^2 + |e|V(\mathbf{r})\right)^2}(\mathbf{E} \times \mathbf{A}) \cdot \boldsymbol{\sigma} \ \ \text{(isotropic hyperfine)} & (1.10) \\ h_{\mathrm{ahf}} &= \frac{|e|\hbar c}{\epsilon + 2mc^2 + |e|V(\mathbf{r})}(\boldsymbol{\nabla} \times \mathbf{A}) \cdot \boldsymbol{\sigma} \ \ \text{(anisotropic hyperfine)} & (1.11) \\ h_{\mathrm{so}} &= \frac{\hbar|e|c^2}{\left(\epsilon + 2mc^2 + |e|V(\mathbf{r})\right)^2}(\mathbf{E} \times \mathbf{p}) \cdot \boldsymbol{\sigma} \ \ (\mathrm{spin-orbit}). & (1.12) \end{aligned}$$

In the above, the electric field $\mathbf{E} = -\boldsymbol{\nabla}V(\boldsymbol{r})$ is that due to the electric potential of the nucleus:

$$V(r) = \frac{kZ|e|}{r}, \tag{1.13}$$

where $k = 1/4\pi\epsilon_0 \approx 9.0\times10^9\,\mathrm{Nm^2C^{-2}}$ in SI units and $Z|e|$ is the nuclear charge, so that[1]

$$\mathbf{E} = -\boldsymbol{\nabla}V(r) = \frac{kZ|e|\mathbf{r}}{r^3}, \tag{1.14}$$

and the vector potential is due to the nuclear magnetic moment $\boldsymbol{\mu}$ (again, in SI units):

$$\mathbf{A} = \frac{\mu_0}{4\pi}\frac{\boldsymbol{\mu}\times\mathbf{r}}{r^3}. \tag{1.15}$$

1.2.1 Fermi contact interaction

Using the vector triple-product formula

$$\mathbf{r}\times(\boldsymbol{\mu}\times\mathbf{r}) = \boldsymbol{\mu}(\mathbf{r}\cdot\mathbf{r}) - \mathbf{r}(\boldsymbol{\mu}\cdot\mathbf{r}) \tag{1.16}$$

and the above expressions for $V(r)$, $\mathbf{E}$, and $\mathbf{A}$ gives

$$h_{\mathrm{ihf}} = \frac{\mu_0}{4\pi}\frac{kZ|e|^3\hbar c}{\left(\epsilon + 2mc^2 + kZe^2/r\right)^2}\left(\frac{\boldsymbol{\sigma}\cdot\boldsymbol{\mu} - (\boldsymbol{\sigma}\cdot\hat{\mathbf{r}})\,(\boldsymbol{\mu}\cdot\hat{\mathbf{r}})}{r^4}\right). \tag{1.17}$$

Defining the nuclear length scale d:

$$d = \frac{kZe^2}{2mc^2} \simeq 1.5\times10^{-15}Z\,\mathrm{m} \tag{1.18}$$

and neglecting relativistic corrections to the electron rest energy $\epsilon \ll mc^2$ gives

$$h_{\mathrm{ihf}} = \frac{\mu_0\mu_B}{4\pi}\frac{d}{\left(1+\frac{d}{r}\right)^2}\left(\frac{\boldsymbol{\sigma}\cdot\boldsymbol{\mu} - (\boldsymbol{\sigma}\cdot\hat{\mathbf{r}})\,(\boldsymbol{\mu}\cdot\hat{\mathbf{r}})}{r^4}\right). \tag{1.19}$$

Evaluating the matrix elements of h_{ihf} with respect to the wave functions $\phi_i(\mathbf{r})$ and $\phi_j(\mathbf{r})$ gives

$$\begin{aligned}\langle\phi_i|\,h_{\mathrm{ihf}}\,|\phi_j\rangle &= \frac{\mu_0\mu_B}{4\pi}\int_0^\infty dr\frac{d}{(r+d)^2}f(\mathbf{r}), &(1.20)\\ f(\mathbf{r}) &= \int d\Omega\phi_i^*(\mathbf{r})\left\{\boldsymbol{\sigma}\cdot\boldsymbol{\mu} - (\boldsymbol{\sigma}\cdot\hat{\mathbf{r}})\,(\boldsymbol{\mu}\cdot\hat{\mathbf{r}})\right\}\phi_j(\mathbf{r}). &(1.21)\end{aligned}$$

The radial integral is dominated by the region $r \lesssim d$, so that we can approximate $f(\mathbf{r})$ by its value at the origin:

$$\int_0^\infty dr\frac{d}{(r+d)^2}f(\mathbf{r}) \simeq f(\mathbf{r})|_{r=0}\int_0^\infty \frac{d}{(r+d)^2}dr = f(0). \tag{1.22}$$

The angular integrals give

$$\int d\Omega = 4\pi, \quad \int d\Omega\,(\boldsymbol{\sigma}\cdot\hat{\mathbf{r}})\,(\boldsymbol{\mu}\cdot\hat{\mathbf{r}}) = \frac{4\pi}{3}\boldsymbol{\sigma}\cdot\boldsymbol{\mu}. \tag{1.23}$$

---

[1] There are two sign errors in the derivation of Stoneham [25], one associated with the sign of the isotropic term, Eq. (1.10), and one associated with the electric field due to the nucleus, Eq. (1.14). These two errors cancel to give the correct final result, but we have corrected them here.

We insert $\boldsymbol{\mu} = g_I \mu_N \mathbf{I}$ (where $\mu_N = e\hbar/2m_p = 5.05 \times 10^{-27}\, J/T = 3.15 \times 10^{-8}\, eV/T$ is the nuclear magneton) and recast the contact interaction in a simplified form that has the same matrix elements as Eq. (1.19) within the range of validity of Eq. (1.22):

$$h_{\mathrm{ihf}} = \frac{2\mu_0}{3} g_I \mu_N \mu_B \delta(\mathbf{r}) \boldsymbol{\sigma} \cdot \mathbf{I}. \tag{1.24}$$

In the more general case, where there may be many electrons interacting with many nuclei at positions $\mathbf{r}_k$, we write

$$h_{\mathrm{ihf}} = \frac{4\mu_0}{3} g_I \mu_N \mu_B \sum_k \mathbf{S}(\mathbf{r}_k) \cdot \mathbf{I}_k, \quad \mathbf{S}(\mathbf{r}) = \frac{1}{2} \sum_{s,s'=\{\uparrow,\downarrow\}} \psi_s^\dagger(\mathbf{r}) \boldsymbol{\sigma}_{ss'} \psi_{s'}(\mathbf{r}), \tag{1.25}$$

where the field operators are defined by $\psi_\sigma(\mathbf{r}) = \sum_n \phi_n(\mathbf{r}) c_{n\sigma}$ and $c_{n\sigma}$ annihilates an electron in the state with spin σ and orbital wave function $\phi_n(\mathbf{r})$. The wave functions $\phi_n(\mathbf{r})$ form a complete set:

$$\int d^3r \phi_n^*(\mathbf{r}) \phi_m(\mathbf{r}) = \delta_{nm}, \quad \sum_n \phi_n^*(\mathbf{r}') \phi_n(\mathbf{r}) = \delta(\mathbf{r} - \mathbf{r}'). \tag{1.26}$$

For most of this thesis, we will be concerned with the dynamics of a single electron in the ground orbital state of a quantum dot $\phi_0(\mathbf{r})$, with single-particle orbital level spacing much larger than the typical hyperfine energy scale. In this case, it is appropriate to derive an effective hyperfine spin Hamiltonian projected in the subspace of the orbital ground state:

$$\mathcal{H}_{\mathrm{eff}} = \langle \phi_0 | \, h_{\mathrm{ihf}} \, | \phi_0 \rangle = \frac{4\mu_0}{3} g_I \mu_N \mu_B \sum_k |\phi_0(\mathbf{r}_k)|^2 \, \mathbf{S} \cdot \mathbf{I}_k. \tag{1.27}$$

If we write the wavefunction $\phi_0(\mathbf{r})$ in terms of the $\mathbf{k} = 0$ Bloch amplitude u_0 (which is invariant for all equivalent crystal lattice sites $\mathbf{r}_k$) and a slowly-varying envelope part $F(\mathbf{r})$:

$$\phi_0(\mathbf{r}_i) \approx u_0 F(\mathbf{r}_i), \tag{1.28}$$

and enforce the normalization

$$\int d^3r \, |F(\mathbf{r})|^2 = 1, \tag{1.29}$$

we find the effective Hamiltonian and coupling constants are given by

$$\mathcal{H}_{\mathrm{eff}} = \mathbf{S} \cdot \sum_k A_k \mathbf{I}_k, \quad A_k = A v_0 \, |F(\mathbf{r}_k)|^2 \,, \tag{1.30}$$

where v_0 is the volume of a primitive crystal unit cell and

$$A = \frac{4\mu_0}{3} g_I \mu_N \mu_B \, |u_0|^2 \,. \tag{1.31}$$

We define the effective nuclear magnetic field by

$$\mathbf{B}_N = \frac{A}{g^* \mu_B} \bar{\mathbf{I}}, \tag{1.32}$$

where the quantity $\bar{\mathbf{I}}$, which gives an effective average nuclear spin, is

$$\bar{\mathbf{I}} = v_0 \sum_k |F(\mathbf{r}_k)|^2 \langle \mathbf{I}_k \rangle . \tag{1.33}$$

For GaAs, there are three isotopic species of significant abundance. Paget et al. report values for b_α [27], the effective nuclear field due to isotopic species α. The effective fields b_α are related to the total effective nuclear field by:

$$\mathbf{B}_N = \sum_\alpha b_\alpha \bar{\mathbf{I}}^\alpha , \tag{1.34}$$

where $\bar{\mathbf{I}}^\alpha$ is the effective average over spins for the nucleus of species α. The values reported are [27]

$$\begin{aligned} b_{(^{75}\mathrm{As})} &= -18.4\,\mathrm{kG}, && (1.35)\\ b_{(^{69}\mathrm{Ga})} &= -9.1\,\mathrm{kG}, && (1.36)\\ b_{(^{71}\mathrm{Ga})} &= -7.8\,\mathrm{kG}, && (1.37) \end{aligned}$$

which gives an effective hyperfine coupling constant, using $g^* = -0.44$ for bulk GaAs, and assuming $\bar{\mathbf{I}}^\alpha \simeq \bar{\mathbf{I}}$ (independent of α):

$$A \simeq g^* \mu_B \sum_\alpha b_\alpha = 9.0 \times 10^{-5} eV \tag{1.38}$$

or

$$\frac{A}{\hbar} = 1.4 \times 10^{11} s^{-1}. \tag{1.39}$$

1.2.2 Anisotropic hyperfine interaction

Following the same procedure above for h_{ahf}, the anisotropic contribution, gives

$$h_{\mathrm{ahf}} = \frac{\mu_0}{4\pi} \frac{\mu_B}{\left(1 + \frac{d}{r}\right)} \frac{1}{r^3} \left(3 \left(\boldsymbol{\sigma} \cdot \hat{\mathbf{r}}\right) \left(\boldsymbol{\mu}_N \cdot \hat{\mathbf{r}}\right) - \boldsymbol{\sigma} \cdot \boldsymbol{\mu}_N\right). \tag{1.40}$$

In the limit where the electron and nuclear spin are widely separated, this term reduces to the classical dipole-dipole interaction between the magnetic moments of the electron and nuclear spin. However, this is typically not the case in a quantum dot; the form and magnitude of the effective spin-spin interaction depends strongly on the symmetry of the electron wave function. This dependence can be investigated by projecting onto an electronic orbital wave function $\phi_0(\mathbf{r})$:

$$\langle h_{\mathrm{ahf}} \rangle = \frac{\mu_0 \mu_B}{4\pi} \int dr \frac{1}{(r+d)} \int d\Omega \phi_0^*(\mathbf{r}) \left(3 \left(\vec{\sigma} \cdot \hat{\mathbf{r}}\right) \left(\vec{\mu}_N \cdot \hat{\mathbf{r}}\right) - \vec{\sigma} \cdot \vec{\mu}_N\right) \phi_0(\mathbf{r}). \tag{1.41}$$

For s-states, the angular integral vanishes identically (see Eq. 1.23) and the radial integral is well-behaved at the origin due to the finite size d of the nucleus. For states of higher angular momentum (p,d,f, etc.), the angular integral does not vanish and we can take $d = 0$ since these states vanish at $r = 0$. In this case, after rotating to principal axes (which depend on the nuclear spin site k) h_{ahf} results in an effective spin Hamiltonian with an anisotropic (XYZ-type) exchange between the electron and nucleus:

$$h_{\mathrm{ahf}}^{\mathrm{eff}} = \sum_k b_k^{xx} S^x I_k^x + b_k^{yy} S^y I_k^y + b_k^{zz} S^z I_k^z , \tag{1.42}$$

where

$$b_k^{xx} = \frac{\mu_0}{4\pi} g_I \mu_N g_s \mu_B \left\langle \frac{3(x-x_k)^2 - |\mathbf{r}-\mathbf{r}_k|^2}{|\mathbf{r}-\mathbf{r}_k|^5} \right\rangle, \tag{1.43}$$

$$b_k^{yy} = \frac{\mu_0}{4\pi} g_I \mu_N g_s \mu_B \left\langle \frac{3(y-y_k)^2 - |\mathbf{r}-\mathbf{r}_k|^2}{|\mathbf{r}-\mathbf{r}_k|^5} \right\rangle, \tag{1.44}$$

$$b_k^{zz} = \frac{\mu_0}{4\pi} g_I \mu_N g_s \mu_B \left\langle \frac{3(z-z_k)^2 - |\mathbf{r}-\mathbf{r}_k|^2}{|\mathbf{r}-\mathbf{r}_k|^5} \right\rangle. \tag{1.45}$$

$$\tag{1.46}$$

In the above, $g_s \approx 2$ is the free electron g-factor.

The anisotropic term is small relative to the isotropic (contact) term for electrons in GaAs quantum dots due to the s-type nature of the conduction band [28]. In contrast, the anisotropic interaction may be important for quantum-dot-confined hole spins, since the p-type valence band has the dual effects of reducing the contact term, while enhancing the anisotropic interaction.

1.3 Double quantum dots: stability diagram and transport

In this section we discuss characterization and manipulation techniques that are commonly used to extract microscopic parameters of double quantum dots. This section is directly relevant to Chapters 4, 5, 6, and 7, all of which relate to double quantum dots. In Sec. 1.3.1 we review the charge stability diagram, and illustrate its connection to a commonly used microscopic model Hamiltonian. Sec. 1.3.2 gives a review of sequential tunneling transport through hybridized (molecular) double-dot states. In Sec. 1.3.3 we discuss the use of double quantum dots as two-qubit gates.

1.3.1 The double-dot charge stability diagram

Just as transport through a single quantum dot and Coulomb blockade phenomena give information about the orbital level spacing, charging energy, and spin states of single quantum dots [29], similar studies can be carried out on double quantum dots. Whereas for single dots, transport phenomena are typically understood in terms of one-dimensional plots of conductance versus gate voltage, the primary tool used to understand double quantum dots is the double-dot charge stability diagram. The stability diagram is a two-dimensional plot of current or differential conductance through the double dot or through a neighboring QPC, given as a function of two independent back-gate voltages (one applied locally to each dot). The plot differentiates regions where the double-dot ground state has a charge configuration (N_1, N_2), for various N_1, N_2, where N_1 is the number of charges on the left dot and N_2 is the number of charges on the right. Transport through double quantum dots and the relevant charge stability diagram has been discussed thoroughly in [30]. In the rest of this section, we review some features of the double-dot stability diagram with an emphasis on the connection to a model Hamiltonian that is commonly used in the literature [31, 32, 33, 34].

An isolated double quantum dot is described by the Hamiltonian

$$H_{\mathrm{dd}} = H_{\mathrm{C}} + H_{\mathrm{T}} + H_{\mathrm{S}}, \tag{1.47}$$

where H_{C} gives the single-particle and inter-particle charging energies as well as the orbital energy, H_{T} is the inter-dot tunneling term due to a finite overlap of dot-localized single-particle wavefunctions, which ultimately gives rise to exchange, and H_{S} contains explicitly spin-dependent terms, which may include spin-orbit interaction, dipole-dipole interaction, and the contact hyperfine interaction between the confined electron spins and nuclear spins in the surrounding lattice (see Sec. 1.2 above).

There are several approaches that can be taken to writing the various components of the double-dot Hamiltonian H_{dd}, corresponding to several degrees of microscopic detail. In the simplest form, the Hubbard model, details of the electron wavefunctions are neglected and the Coulomb interaction is given only in terms of on-site and nearest-neighbor coupling. Since this description relies only on very few parameters, it is the most commonly used in the literature on transport phenomena through quantum dots. The shape of the confining potential, quantum-dot localized wavefunctions, and form of the Coulomb interaction may become important in certain circumstances, in which case it is more appropriate to apply either the Heitler-London method (which neglects doubly-occupied dot levels), or the Hund-Mulliken method, which includes the effects of double-occupancy. These methods predict, for instance, a variation of the interdot exchange interaction through zero with increasing out-of-plane magnetic field [14]. Experimentally, it has been confirmed that the exchange coupling can be tuned with an out-of-plane magnetic field in single vertical [35] and single lateral quantum dots [36], which behave effectively as double-dot structures. Here we ignore these effects and focus on the simplest Hubbard model that reproduces much of the double-dot physics that can be seen in transport phenomena.

We model the Coulomb interaction with simple on-site ($U_{1(2)}$ for the left (right) dot) and nearest-neighbor (U') repulsion. The single-particle charging energy is given in terms of a local dot potential $V_{1(2)}$. The charging Hamiltonian is then

$$H_{\mathrm{C}} = \frac{1}{2}\sum_{l} U_l N_l \left(N_l - 1\right) + U' N_1 N_2 - |e| \sum_{l} V_l N_l + \sum_{kl} \epsilon_{lk} n_{lk}, \tag{1.48}$$

where $N_l = \sum_k n_{lk}$ counts the total number of electrons in dot l, with $n_{lk} = \sum_\sigma d^\dagger_{lk\sigma} d_{lk\sigma}$, and here $d_{lk\sigma}$ annihilates an electron on dot l, in orbital k, with spin σ. ϵ_{lk} is the energy of single-particle orbital level k in dot l, which gives rise to the typical orbital level spacing $\epsilon_{lk+1} - \epsilon_{lk} \approx \hbar\omega_0$ (see Fig. 1.1).

Within the capacitive charging model described by the equivalent circuit in the inset of Fig. 1.2(a), the microscopic charging energies are related to capacitances by [34, 30]

$$U_l = \frac{C_1 C_2}{C_1 C_2 - C_{\mathrm{m}}^2} \frac{e^2}{C_l}, \quad U' = \frac{2e^2 C_{\mathrm{m}}}{C_1 C_2 - C_{\mathrm{m}}^2}, \tag{1.49}$$

where $C_1 = C_{\mathrm{s}} + C_{\mathrm{m}} + C_{\mathrm{g1}}$, $C_2 = C_{\mathrm{d}} + C_{\mathrm{m}} + C_{\mathrm{g2}}$, and all capacitances are defined in the inset of Fig. 1.2(a). In experiments, the local quantum dot

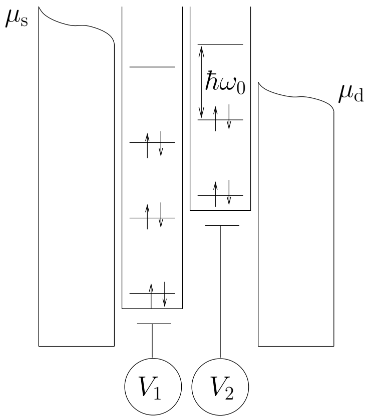

Figure 1.1: Ground-state configuration for a double quantum dot with large orbital and charging energies, and negligible dot-lead and interdot coupling. $\mu_{\rm s(d)}$ is the source (drain) chemical potential, $V_{1(2)}$ is the left (right) local dot potential, which is related to applied gate potentials by a linear transformation (see Eq. (1.50), below), and both dots are assumed to have the same uniform level spacing $\hbar\omega_0$.

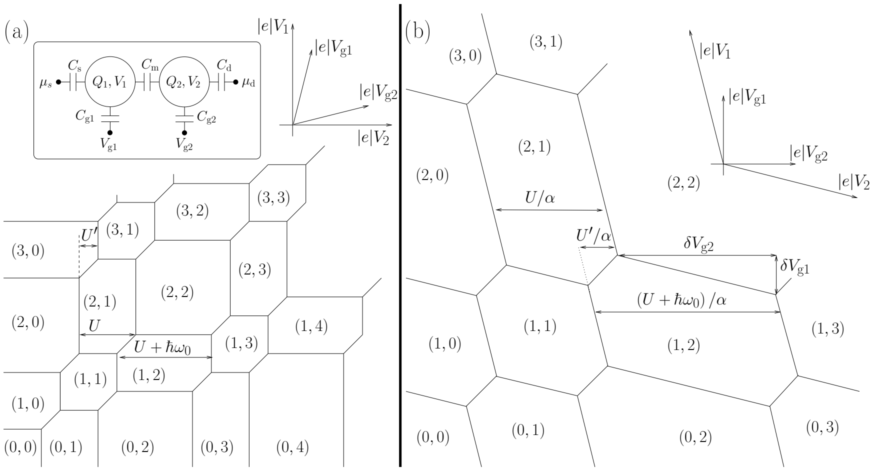

Figure 1.2: Stability diagram plotted in terms of (a) local dot potentials $V_{1,2}$ and (b) applied gate potentials $V_{g1,2}$, with on-site charging energies $U_l = U$, $l = 1, 2$, nearest-neighbor charging energy U', and dot orbital level spacing $\hbar\omega_0$ satisfying $U : \hbar\omega_0 : U' = 3 : 2 : 1$. In addition, for (b) we have assumed the voltage scaling factors are the same for both dots, and are given by $\alpha_1 = \alpha_2 = \alpha = 1/2$. (a) inset: capacitive charging model for a double quantum dot, indicating the source (drain) chemical potential $\mu_{\rm s(d)}$, the charge on the left (right) dot $Q_{1(2)}$, the capacitances to source (drain) $C_{\rm s(d)}$, the mutual capacitance $C_{\rm m}$, and gate capacitances $C_{\rm g1,2}$. (b) Horizontal lines in the $|e|\, V_{1(2)}$ plane become skewed with slope $\delta V_{\rm g1}/\delta V_{\rm g2} = -C_{\rm m}C_{\rm g2}/C_2C_{\rm g1}$ when plotted versus $|e|\, V_{\rm g1(2)}$.

potentials $V_{1,2}$ are controlled indirectly in terms of gate voltages $V_{\mathrm{g}1,2}$, which are capacitively coupled to the dots through gate capacitances $C_{\mathrm{g}1,2}$. For fixed quantum-dot charges $(Q_1, Q_2) = -|e|(N_1, N_2) = \text{const.}$, differences in the dot voltages ΔV_1 and ΔV_2 are related to differences in the gate voltages $\Delta V_{\mathrm{g}1}$ and $\Delta V_{\mathrm{g}2}$ through [34, 30]

$$\begin{pmatrix} C_1 & -C_{\mathrm{m}} \\ -C_{\mathrm{m}} & C_2 \end{pmatrix} \begin{pmatrix} \Delta V_1 \\ \Delta V_2 \end{pmatrix} = \begin{pmatrix} C_{\mathrm{g}1}\Delta V_{\mathrm{g}1} \\ C_{\mathrm{g}2}\Delta V_{\mathrm{g}2} \end{pmatrix}. \tag{1.50}$$

The double-dot stability diagram can then be given equivalently as a two-dimensional plot with energy axes $|e|\,V_1$, $|e|\,V_2$, or with axes $|e|\,V_{\mathrm{g}1}$, $|e|\,V_{\mathrm{g}2}$, which are skewed and stretched with respect to the original axes according to the transformation given in Eq. (1.50). The end effect is that parallel horizontal (vertical) lines in the $|e|\,V_{1(2)}$ plane separated by a distance $dV_{2(1)}$ transform to skewed parallel lines, separated by $dV_{\mathrm{g}2(1)} = dV_{2(1)}/\alpha_{2(1)}$ along the horizontal (vertical) of the new coordinate system, where (see Fig. 1.2):

$$\alpha_l = \frac{C_{\mathrm{g}l}}{C_l}, \quad l = 1, 2. \tag{1.51}$$

Additionally, horizontal lines in the $|e|\,V_{1(2)}$ plane become skewed with a slope $\delta V_{\mathrm{g}1}/\delta V_{\mathrm{g}2} = -C_{\mathrm{m}}C_{\mathrm{g}2}/C_2C_{\mathrm{g}1}$ (see Fig. 1.2(b)), and vertical lines are skewed with slope $\delta V_{\mathrm{g}1}/\delta V_{\mathrm{g}2} = -C_1C_{\mathrm{g}2}/C_{\mathrm{m}}C_{\mathrm{g}1}$.

The Hamiltonian in Eq. (1.48) conserves the number of electrons on each dot: $[H_{\mathrm{C}}, N_l] = 0$, so we label the ground state by the two dot occupation numbers, (N_1, N_2), and indicate where each configuration is the ground state in Fig. 1.2 for equivalent quantum dots that satisfy $\alpha_1 = \alpha_2 = \alpha = 1/2$, $U_1 = U_2 = U$, $\epsilon_{lk+1} - \epsilon_{lk} = \hbar\omega_0$ for all k, l, and $U : \hbar\omega_0 : U' = 3 : 2 : 1$. The charge stability diagram produces a "honeycomb" of hexagons with dimensions that are determined by three typical energy scales: (1) The on-site replusion U, (2) the nearest-neighbor repulsion U', and (3) the typical orbital energy $\hbar\omega_0$. Fig. 1.2 assumes a ground-state electron filling as shown in Fig. 1.1, with constant orbital energy $\hbar\omega_0$. In this case, the orbital energy appears in the dimensions of only every second honeycomb cell of the stability diagram, along the horizontal or vertical direction, since the spin-degenerate orbital states fill with two electrons at a time according to the Pauli principle. This even-odd behavior may not be visible in dots of high symmetry, where the orbital levels are manifold degenerate. Alternatively, the absence of an even-odd effect in low-symmetry single dots has previously been attributed to the absence of spin degeneracy due to many-body effects [37, 38, 30].

Each vertex of a honeycomb cell corresponds to a triple-point, where three double-dot charge states are simultaneously degenerate. For a double dot connected to source and drain leads at low temperature, and in the absence of relaxation or photo-assisted tunneling processes, it is only at these points where resonant sequential transport can occur, through shuttling processes of the form $(0,0) \to (1,0) \to (0,1) \to (0,0)$. This picture changes when a strong inter-dot tunnel coupling H_{T} is considered in addition.

1.3.2 Transport through double quantum dots

Molecule-like states have been observed and studied in detail in two-electron single vertical [35] and lateral quantum dots [36] (the latter behave as an effective

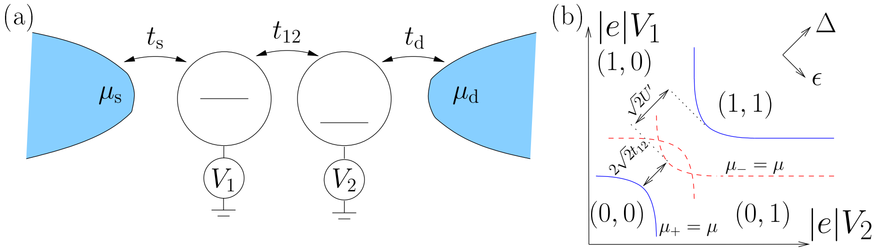

Figure 1.3: (a) A tunnel-coupled double quantum dot, with tunneling amplitude t_{12}. The source and drain leads, at chemical potentials μ_s and μ_d, are connected to the left and right dots through tunnel barriers with tunneling amplitudes t_s and t_d, respectively. The left and right dots are set to local potentials V_1 and V_2. (b) Modification of the stability diagram in the case of a significant tunnel coupling t_{12}. To generate this figure we have chosen the ratio of tunnel coupling to the mutual (nearest-neighbor) charging energy to be $t_{12}/U' \approx 1/5$. At solid lines, transport occurs via the double-dot ground state $|E_+\rangle$ and at dashed lines, additional transport can occur through the first excited state $|E_-\rangle$ (see Eqs. (1.54) and (1.55) below).

double-dot structure, showing good agreement with theory [39]). Evidence of molecular states forming in double quantum dots due to a strong inter-dot tunnel-coupling has also been found in a variety of systems [40, 41, 42, 43, 44, 45, 46, 2, 3, 4, 5]. For example, molecular states have been observed in many-electron gated quantum dots in linear transport [42] (solid lines of Fig. 1.3(b)) and transport through excited states [46] (dashed lines in Fig. 1.3(b)). In addition, molecular states have been observed in vertical-lateral gated double quantum dots [47], gated dots formed in quantum wires [2] and gated carbon-nanotube double dots [3, 4, 5]. A large inter-dot tunnel coupling is essential for generating a large exchange interaction J, and is therefore very important for the implementation of fast two-qubit gates.

In this section, we analyze changes to the double-dot stability diagram that occur due to the inter-dot tunneling term H_T. We focus on the relevant regime for quantum computing, where only a single orbital state is available for occupation on each quantum dot (the lower-left region of Figs. 1.2(a,b)). In the subspace of these lowest dot orbital states, H_T is given by:

$$H_\mathrm{T} = \sum_\sigma t_{12} d^\dagger_{1\sigma} d_{2\sigma} + \mathrm{H.c.}, \tag{1.52}$$

where t_{12} is the tunneling amplitude between the two dots, and $d_{l\sigma}$, $l = 1, 2$, annihilates an electron in the lowest single-particle orbital state localized on quantum dot l with spin σ.

When the double dot is occupied by only $N = 0, 1$ electrons and is coupled weakly to leads, an explicit expression can be found for the current passing through a serially-coupled double dot, as shown in Fig. 1.3(a) [34, 5]. It is straightforward to diagonalize $H_C + H_T$ in the subspace of $N = 1$ electrons on the quantum dot. This gives the (spin-degenerate) eigenenergies and corresponding eigenvectors:

$$E_\pm(\Delta,\epsilon) = -\frac{1}{\sqrt{2}}\left(\Delta \pm \sqrt{\epsilon^2+2t_{12}^2}\right), \tag{1.53}$$

$$|E_\pm\rangle = \cos\left(\frac{\theta_\pm}{2}\right)|1,0\rangle + \sin\left(\frac{\theta_\pm}{2}\right)|0,1\rangle, \tag{1.54}$$

$$\tan\left(\frac{\theta_\pm}{2}\right) = \frac{\epsilon}{\sqrt{2}t_{12}} \pm \sqrt{1+\left(\frac{\epsilon}{\sqrt{2}t_{12}}\right)^2}. \tag{1.55}$$

Here, $E_\pm(\Delta,\epsilon)$ is written in terms of new energy coordinates ϵ, Δ, which are related to the old (voltage) coordinates through a rotation of the axes by 45° (see also Fig. 1.3(b)):

$$\begin{pmatrix}\Delta\\ \epsilon\end{pmatrix} = \frac{1}{\sqrt{2}}\begin{pmatrix}1 & 1\\ -1 & 1\end{pmatrix}\begin{pmatrix}|e|\,V_1\\ |e|\,V_2\end{pmatrix}. \tag{1.56}$$

We then define double-dot chemical potentials:

$$\mu_\pm(\Delta,\epsilon) = E_\pm(\Delta,\epsilon) - E_0, \tag{1.57}$$

where $E_0 = 0$ is the energy of the $(0,0)$ charge configuration. In the presence of a strong tunnel coupling, the eigenstates of the double dot are no longer labeled separately by the quantum numbers N_1, N_2. Instead, the sum $N = N_1+N_2$ is conserved. If we add to H_{dd} the double-dot-lead coupling Hamiltonian $H_{\mathrm{dd}-L} = \sum_{k\sigma} t_{\mathrm{s}} c^\dagger_{\mathrm{s}k\sigma} d_{1\sigma} + t_{\mathrm{d}} c^\dagger_{\mathrm{d}k\sigma} d_{2\sigma} + \mathrm{H.c.}$, where $c^\dagger_{\mathrm{s(d)}k\sigma}$ creates an electron in the source (drain), in orbital k with spin σ, then N can fluctuate between 1 and 0 if the double-dot and lead chemical potentials are equal. We identify double-dot sequential tunneling processes as those that change the total charge on the double dot by one: $N \to N \pm 1$ [39]. One can evaluate golden-rule rates for all sequential-tunneling processes, taking the dot-lead coupling $H_{\mathrm{dd-L}}$ as a perturbation to obtain the stationary current from a standard Pauli master equation (the Pauli master equation is valid for sufficiently high temperature, $k_{\mathrm{B}}T > \Gamma_{\mathrm{s(d)}}$, so that off-diagonal elements can be ignored in the double-dot density matrix). For weak dot-lead coupling, at low temperature $k_{\mathrm{B}}T < \hbar\omega_0$, and at zero bias ($\mu = \mu_s = \mu_d + \Delta\mu$, with $\Delta\mu \to 0$), transport occurs only through the $N = 1$ ground state, with chemical potential μ_+. The differential conductance near the $N = 0, 1$ boundary is then given by

$$\frac{dI}{d\left(\Delta\mu\right)} = |e|\,\Gamma\left(\frac{-2f'(\mu_+)}{1+f(\mu_+)}\right), \quad \Gamma = \frac{\sin^2\left(\theta_+\right)\Gamma_{\mathrm{s}}\Gamma_{\mathrm{d}}}{4\left(\cos^2\left(\frac{\theta_+}{2}\right)\Gamma_{\mathrm{s}} + \sin^2\left(\frac{\theta_+}{2}\right)\Gamma_{\mathrm{d}}\right)}, \tag{1.58}$$

where $f(E) = 1/\left[1+\exp\left(\frac{E-\mu}{k_BT}\right)\right]$ is the Fermi function at chemical potential μ and temperature T, $f'(E) = df(E)/dE$, and $\Gamma_{\mathrm{s(d)}} = \frac{2\pi\nu}{\hbar}\left|t_{\mathrm{s(d)}}\right|^2$ is the tunneling rate to the source (drain) with a lead density of states per spin ν at the Fermi energy. If spin degeneracy is lifted, the quantity in brackets in Eq. (1.58) is replaced by the familiar term $-f'(\mu_+) = 1/\left[4k_BT\cosh^2\left(\frac{\mu_+-\mu}{2k_BT}\right)\right]$ [48]. The differential conductance (Eq. (1.58)) reaches a maximum near the point where the double-dot chemical potential matches the lead chemical potential,

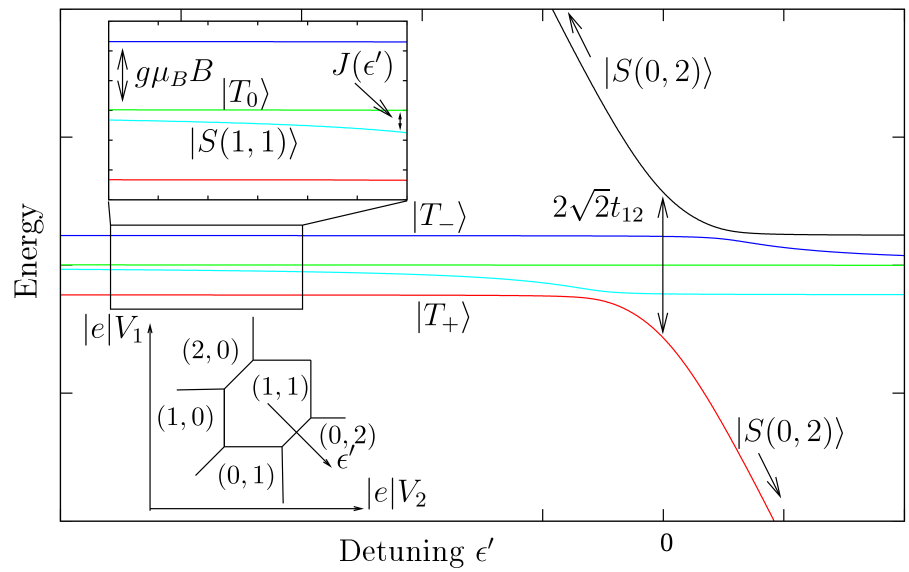

Figure 1.4: Energy-level spectrum for two electrons in a double quantum dot.

$\mu_+(\Delta, \epsilon) = \mu$, which we indicate with a solid line in Fig. 1.3(b). Transport through the excited state can occur where $\mu_-(\Delta, \epsilon) = \mu$, and when the bias $\Delta\mu = \mu_\mathrm{s} - \mu_\mathrm{d}$ or temperature T are sufficiently large to generate a significant population in the excited state $|E_-\rangle$. Dashed lines indicate where $\mu_-(\Delta, \epsilon) = \mu$ in Fig. 1.3(b).

There are several qualitative changes to the double-dot stability diagram that take place in the presence of strong tunnel coupling. First, the number of electrons on each dot is not conserved individually. Instead, the sum $N = N_1 + N_2$ is conserved, which means that there are no longer lines separating, for example, the (1,0) and (0,1) states in Fig. 1.3(b). Second, sequential-tunneling processes allow current to be transported through the double-dot along the length of the "wings" that define the boundaries between N and $N \pm 1$-electron ground states. This is in contrast to the case where t_{12} is weak, in which resonant sequential transport can only occur at triple points, where the shuttling processes of the type $(0,0) \rightarrow (1,0) \rightarrow (0,1) \rightarrow (0,0)$ are allowed by energy conservation.

1.3.3 Double dots for two-qubit gates

The $\sqrt{\text{SWAP}}$ operation described in Sec. 1.1 requires significant control of the exchange coupling J. The value of J can be controlled by raising/lowering the inter-dot barrier, thus changing the tunnel coupling t_{12} [1], or with an out-of-plane magnetic field or weak in-plane electric field [14]. More recently, experiments have controlled J by varying the back-gate voltages on two neighboring quantum dots through a large parameter regime, independently [21]. Here we discuss this last method to control J, which has been analyzed in several recent papers [49, 50, 51, 52].

We consider a double quantum dot in the region of the charge stability diagram indicated in the lower inset of Fig. 1.4. Specifically, we consider the regime of gate voltages where the double dot contains $N = 2$ electrons near the degeneracy point of the $(1,1)$ and $(0,2)$ charge states, and aim to diagonalize the Hamiltonian $H_\mathrm{C} + H_\mathrm{T}$ in the basis of three spin triplets and two relevant singlets:

$$\begin{aligned}
|S(0,2)\rangle &= d^\dagger_{2\downarrow} d^\dagger_{2\uparrow} \left|\mathrm{vac.}\right\rangle, && (1.59)\\
|S(1,1)\rangle &= \frac{1}{\sqrt{2}}\left(d^\dagger_{2\downarrow} d^\dagger_{1\uparrow} - d^\dagger_{2\uparrow} d^\dagger_{1\downarrow}\right)\left|\mathrm{vac.}\right\rangle, && (1.60)\\
|T_0\rangle &= \frac{1}{\sqrt{2}}\left(d^\dagger_{2\downarrow} d^\dagger_{1\uparrow} + d^\dagger_{2\uparrow} d^\dagger_{1\downarrow}\right)\left|\mathrm{vac.}\right\rangle, && (1.61)\\
|T_+\rangle &= d^\dagger_{2\uparrow} d^\dagger_{1\uparrow} \left|\mathrm{vac.}\right\rangle, && (1.62)\\
|T_-\rangle &= d^\dagger_{2\downarrow} d^\dagger_{1\downarrow} \left|\mathrm{vac.}\right\rangle. && (1.63)
\end{aligned}$$

In the absence of additional spin-dependent terms, the triplets are degenerate, with energy $E_\mathrm{Triplet} = E_{(1,1)} = -\sqrt{2}\Delta'$, whereas the two singlet states have energies and associated eigenvectors

$$\begin{aligned}
E^\pm_\mathrm{Singlet} &= E_\mathrm{Triplet} - \frac{1}{\sqrt{2}}\left(\epsilon' \pm \sqrt{(\epsilon')^2 + 4t_{12}^2}\right), && (1.64)\\
\left|E^\pm_\mathrm{Singlet}\right\rangle &= \cos\left(\frac{\theta^S_\pm}{2}\right)|S(1,1)\rangle + \sin\left(\frac{\theta^S_\pm}{2}\right)|S(0,2)\rangle, && (1.65)\\
\tan\left(\frac{\theta^S_\pm}{2}\right) &= \frac{\epsilon'}{2t_{12}} \pm \sqrt{1 + \left(\frac{\epsilon'}{2t_{12}}\right)^2}. && (1.66)
\end{aligned}$$

Here, Δ' and ϵ' are related to the previous coordinates $(\Delta,\, \epsilon)$ through a simple translation of the origin:

$$\begin{pmatrix} \Delta' \\ \epsilon' \end{pmatrix} = \begin{pmatrix} \Delta \\ \epsilon \end{pmatrix} + \frac{1}{\sqrt{2}}\begin{pmatrix} -U' \\ U' - U \end{pmatrix}. \qquad (1.67)$$

This gives rise to the Heisenberg exchange for large negative ϵ' (from Eq. (1.64)):

$$J(\epsilon') = E_\mathrm{Triplet} - E^+_\mathrm{Singlet} \approx \frac{\sqrt{2}t_{12}^2}{|\epsilon'|}, \quad \epsilon' < 0, \quad |\epsilon'| \gg 2t_{12}. \qquad (1.68)$$

By pulsing $\epsilon' = \epsilon'(t)$, the exchange $J(\epsilon'(t))$ can be pulsed on and off again in order to implement the $\sqrt{\mathrm{SWAP}}$ operation, as described in Sec. 1.1 (see the inset of Fig. 1.4). This operation has now been achieved experimentally with a gating time on the order of 180 ps [21], in good agreement with the predictions in [14] for an achievable switching time.

1.4 Outline

This thesis is organized as follows: Chapter 2 provides an exact solution for single-electron-spin dynamics due to the hyperfine interaction for the special case of uniform coupling constants, and analyzes the range of validity of a common semiclassical approximation. Chapter 3 includes a detailed analysis of the non-Markovian (memory-dependent) dynamics for a localized electron spin in the presence of the contact hyperfine interaction with a bath of nuclear spins, including the effects of non-uniform hyperfine coupling constants. Chapter 4 describes the hyperfine-induced dynamics of two-electron spin states in terms of a singlet-triplet correlator. Chapter 5 completes our analysis of two-electron spin state decay with a description of all possible correlation functions, exchange-induced Rabi oscillations, and "spin-state narrowing" of the nuclear spin system, which could extend the lifetime of electron spin states if implemented. Chapter 6 describes an experiment on transport through a carbon-nanotube double quantum dot, from which information about the strong tunnel coupling can be obtained. In Chapter 7 we describe a method that could be used to perform high-fidelity coherent single-spin rotations by pulsing only the exchange interaction in the presence of fixed static magnetic fields.

Each chapter is based on a separate published or submitted work, with the relevant reference given following each chapter title.

Chapter 2

Quantum vs. classical hyperfine-induced spin dynamics

[W. A. Coish, E. A. Yuzbashyan, B. L. Altshuler, and D. Loss, arXiv:cond-mat/0610633, to appear in J. Appl. Phys.]

In this chapter we analyze spin dynamics for electrons confined to semiconductor quantum dots due to the contact hyperfine interaction. We compare mean-field (classical) evolution of an electron spin in the presence of a nuclear field with the exact quantum evolution for the special case of uniform hyperfine coupling constants. We find that (in this special case) the zero-magnetic-field dynamics due to the mean-field approximation and quantum evolution are similar. However, in a finite magnetic field, the quantum and classical solutions agree only up to a certain time scale $t < \tau_c$, after which they differ markedly.

2.1 Introduction

Prospects for future quantum information processing with quantum-dot-confined electron spins [1] have encouraged a series of recent experimental efforts. These efforts have resulted in several very significant achievements, including single-electron confinement in vertical [53] and lateral single [54] and double [55, 56] gated quantum dots, the demonstration of spin-dependent transport in double dots, [57,20,22] and exciting effects arising from the contact hyperfine interaction with nuclear spins in the host material, including coherent undriven oscillations in spin-dependent transport [20], lifting of the spin-blockade [22], enhancement of the nuclear spin decay rate near sequential-tunneling peaks [19, 58], and notably, decay of coherent oscillations between singlet and triplet states as well as the demonstration of two-qubit gates in double quantum dots [21, 23]. Very recently, the hyperfine interaction has also been identified as the source of decay for driven single-spin Rabi oscillations in quantum dots [24].

In spite of rapid progress, there are still many obstacles to quantum computing with quantum dots. In particular, the inevitable loss of qubit coherence due to fluctuations in the environment is acceptable in a quantum computer only if the error rates due to this loss are kept below $10^{-3} - 10^{-4}$ errors per operation [59]. This requirement is particularly difficult to achieve since it means that interactions must be strong while switching so that operations can be performed rapidly, but still very weak in the idle state, to preserve coherence.

For an electron spin confined to a quantum dot, decoherence can proceed through fluctuations in the electromagnetic environment and spin-orbit interaction [60, 61, 62, 63, 64] or through the hyperfine interaction with nuclei in the surrounding host material, which has been shown extensively in theory [14, 65, 15, 17, 66, 16, 18, 67, 68, 69, 70, 71, 72, 73, 74, 75, 76, 51, 77, 78, 50, 79, 80] and experiment [81, 82, 83, 84, 21, 49, 23]. Due to the primarily p-type nature of the valence band in GaAs, hole spins (unlike electron spins) do not couple to the nuclear spin environment via the contact hyperfine interaction, although they can still undergo decay due to spin-orbit coupling. The decay may still occur on an even longer time scale than for electrons [85], which suggests the dot-confined hole spin may be another good candidate for quantum computing. Alternatively, quantum dots fabricated in isotopically purified ^{28}Si [86] or ^{12}C nanotubes [3, 6, 5] would be free of nuclei with spin, and therefore free of hyperfine-induced decoherence.

While the field of quantum-dot spin decoherence has been very active in the last few years, there still remain significant misconceptions regarding the nature of the most relevant (hyperfine) coupling, particularly, the range of validity of semiclassical spin models and traditional decoherence methods involving ensemble averaging have been called into question for a single isolated quantum dot with a potentially controllable environment. We address these issues in Section 2.2.

2.2 Hyperfine interaction: quantum and classical dynamics

Exponential decay of the longitudinal and transverse components of spin is typically measured by the decay time scales T_1 and T_2, respectively [87]. The longitudinal spin relaxation rate $1/T_1$ due to spin-orbit interaction and phonon emission is significantly reduced in quantum dots relative to the bulk in the presence of a weak Zeeman splitting $B = |\mathbf{B}|$ and large orbital level spacing $\hbar\omega_0$ ($1/T_1 \propto B^5/(\hbar\omega_0)^4$) [61,62]. This decay time has been shown to be on the order of $T_1 \sim 1\,\mathrm{ms}$ in gated GaAs quantum dots at $B \approx 8\,\mathrm{T}$, [88] and to reach a value as large as $T_1 = 170\,\mathrm{ms}$ at low magnetic fields ($B = 1.75\,\mathrm{T}$) [89]. Furthermore, since dephasing is absent at leading order for fluctuations that couple through the spin-orbit interaction, the T_2 time due to this mechanism is limited by the T_1 time ($T_2 = 2T_1$) [62] (we note that corrections at higher order in the spin-orbit interaction can lead to pure dephasing, although these corrections are only relevant at very low magnetic fields [90, 91]). Unlike the spin-orbit interaction, the hyperfine interaction *can* lead to pure dephasing of electron spin states at leading order, resulting in a relatively very short decoherence time $\tau_c \approx 1-10\,\mathrm{ns}$ due to non-exponential (Gaussian) decay [15,16]. To perform quantum-dot computations, this and any additional decay must be fully understood and reduced, if possible.

The Hamiltonian for an electron spin **S** in the lowest orbital level of a quantum dot containing nuclear spins is

$$H_{\mathrm{hf}} = \mathbf{S} \cdot (\mathbf{B} + \mathbf{h})\,; \quad \mathbf{h} = \sum_i A_i \mathbf{I}_i, \tag{2.1}$$

where $A_i = Av_0 \left|\psi_0(\mathbf{r}_i)\right|^2$ is the contact hyperfine coupling constant to the nuclear spin at site i, v_0 is the volume of a crystal unit cell containing one nuclear spin, and $A \approx 90\,\mu eV$ is the weighted average hyperfine coupling constant in GaAs, averaged over the coupling constants for the three naturally occurring radioisotopes ^{69}Ga,^{71} Ga, and ^{75}As (weighted by their natural abundances) [27], all with total nuclear spin $I = 3/2$. The nuclear field in H_{hf} is given by the quantum "Overhauser operator" **h**. Although an exact Bethe Ansatz solution exists for H_{hf} [92], using this solution to perform calculations for the full coupled quantum system of $N \approx 10^4 - 10^6$ nuclei and one electron in a quantum dot can be prohibitively difficult [67]. Since the Overhauser operator **h** is a sum of a large number N of spin-I operators, one expects that under certain conditions its quantum fluctuations can be neglected and the operator **h** can be replaced with a classical Overhauser field $\mathbf{h} \to \mathbf{B}_N$ [93,15,16,94,72,95,81,96,82,97,76,98,99,51,21,22,100]. However, this approximation can accurately describe the electron-spin dynamics only at times $t < \tau_c$, where $\tau_c = N^\eta/A$ and $\eta > 0$ [97],[1] after which effects of quantum fluctuations of the Overhauser operator set in. The nuclei in GaAs are indeed quantum objects, which could be verified, in principle, by demonstrating that they can be entangled, as is done in spin-state squeezing experiments that have been performed on atomic ensembles [101]. The replacement $\mathbf{h} \to \mathbf{B}_N$ is therefore not exact and there are several cases in which the electron-spin dynamics at times $t > \tau_c$ differ markedly for quantum and classical nuclear fields. In particular, without performing an ensemble average over initial Overhauser fields, the classical-field picture predicts no decay of the electron spin. This is in direct contradiction to analytical [70,102,50,79] and exact numerical [18,74] studies that show the quantum nature of the nuclei can lead to complete decay of the transverse electron spin, even in the presence of a static environment (fixed initial conditions). Additionally, quantum "flip-flop" processes can lead to dynamics and decay of the electron spin in the quantum problem, even for initial conditions (e.g., a fully-polarized nuclear spin system) that correspond to a fixed-point of the classical equations of motion [15,70,75]. In fact, it can be shown that any decay of the electron spin for pure-state inital conditions will result in quantum entanglement between the electron and nuclear spin systems [18,67]. This entanglement has recently been highlighted as a source of spin-echo envelope decay in the presence of the hyperfine interaction [80]. Finally, even the ensemble-averaged standard classical (mean-field) electron-spin dynamics show large quantitative differences relative to the exact quantum dynamics at times $t > \tau_c$ and in a very weak magnetic field, although an alternative mean-field theory involving the P-representation for the density matrix shows promise [103].

While the classical and quantum dynamics diverge in many cases, the classical-field replacement $\mathbf{h} \to \mathbf{B}_N$ *will* be valid up to some time scale, providing a range

---

[1] This expression, of course, assumes an appropriate scaling of coupling constants $A_i \propto 1/N$, so that the energy of the electron spin scales as N^0 in the thermodynamic limit.

of validity for the classical dynamics. In this chapter, we aim to shed light on this range of validity of the classical solution. As a test of the classical-dynamics picture, we can compare quantum and classical dynamics of an electron spin in the simple case of uniform coupling constants $A_i = \gamma$. When the coupling constants are uniform, an exact solution to the quantum dynamics (see Refs. [17, 104] for the $|\mathbf{B}| = 0$ case) can be evaluated and used to compare with an integration of the equivalent classical equations of motion. For uniform coupling constants, the nuclear Overhauser operator from Eq. (2.1) becomes $\mathbf{h} = \gamma\mathbf{K}$, where $A_i = \gamma = A/N$ and $\mathbf{K} = \sum_i \mathbf{I}_i$ is the collective total spin operator for $N \gg 1$ nuclear spins.

The initial state of the system is taken to be an arbitrary product state of the electron and nuclear system:

$$\begin{aligned} |\psi(0)\rangle &= |\psi_S(0)\rangle \otimes |\psi_K(0)\rangle\,, && (2.2)\\ &= \sum_{m=-K}^{K} \left(\alpha_m^{\uparrow} |\uparrow; K, m\rangle + \alpha_m^{\downarrow} |\downarrow; K, m\rangle\right), && (2.3) \end{aligned}$$

where $|\sigma; K, m\rangle$ is a simultaneous eigenstate of S_z, K_z (we take the direction of the external field $\mathbf{B}$ to define the z-axis), and $\mathbf{K}\cdot\mathbf{K}$ (with eigenvalues $\pm 1/2$ for $\sigma =\uparrow, \downarrow$, m, and $K(K+1)$, respectively). For comparison with the classical spin dynamics, we choose the collective nuclear spin to be initially described by a spin coherent state, given by $|\psi_K(0)\rangle = e^{-iK_y\theta_K} |K, K\rangle = \sum_m d_{mK}^{(K)}(\theta_K) |K, m\rangle$, where $d_{mK}^{(K)}(\theta_K)$ is the Wigner rotation matrix [105] and the electron spin is in an arbitrary initial state $|\psi_S(0)\rangle = \cos(\theta_S/2) |\uparrow\rangle + e^{i\phi_S} \sin(\theta_S/2) |\downarrow\rangle$. The initial conditions are then completely determined by the three angles θ_S, ϕ_S, and θ_K. These initial conditions allow for an arbitrary relative orientation of the spin and magnetic-field vectors, since the azimuthal angle for $\mathbf{K}$ (ϕ_K) can be set to zero with an appropriate shift in ϕ_S: $\phi_K' = 0$, $\phi_S' = \phi_S - \phi_K$. At any later time t, the wave function is given by

$$|\psi(t)\rangle = \sum_{m=-K}^{K} \left(\alpha_m^{\uparrow}(t) |\uparrow; K, m\rangle + \alpha_m^{\downarrow}(t) |\downarrow; K, m\rangle\right). \qquad (2.4)$$

From the time-dependent Schrödinger equation $i\partial_t |\psi(t)\rangle = H_{\mathrm{hf}} |\psi(t)\rangle$ (setting $\hbar = 1$), we find the set of coupled differential equations determining the coefficients $\left\{\alpha_m^{\uparrow}(t), \alpha_m^{\downarrow}(t)\right\}$. For $m = -K, \ldots, K-1$,

$$\begin{aligned} \dot{\alpha}_m^{\uparrow} &= -\frac{i}{2}(B + \gamma m)\alpha_m^{\uparrow} - i\frac{\gamma}{2} C_{Km+1}^{-} \alpha_{m+1}^{\downarrow}, && (2.5)\\ \dot{\alpha}_{m+1}^{\downarrow} &= \frac{i}{2}(B + \gamma(m+1))\alpha_{m+1}^{\downarrow} - i\frac{\gamma}{2} C_{Km}^{+} \alpha_m^{\uparrow}, && (2.6) \end{aligned}$$

where $C_{Km}^{\pm} = \langle Km \pm 1| K_{\pm} |Km\rangle = \sqrt{K(K+1) - m(m \pm 1)}$. These equations are supplemented by two equations for the stationary states $|\uparrow; K, K\rangle$ and $|\downarrow; K, -K\rangle$ with dynamics:

$$\begin{aligned} \alpha_K^{\uparrow}(t) &= \exp\left\{-\frac{i}{2}(B + \gamma K)t\right\} \alpha_K^{\uparrow}(0), && (2.7)\\ \alpha_{-K}^{\downarrow}(t) &= \exp\left\{\frac{i}{2}(B - \gamma K)t\right\} \alpha_{-K}^{\downarrow}(0). && (2.8) \end{aligned}$$

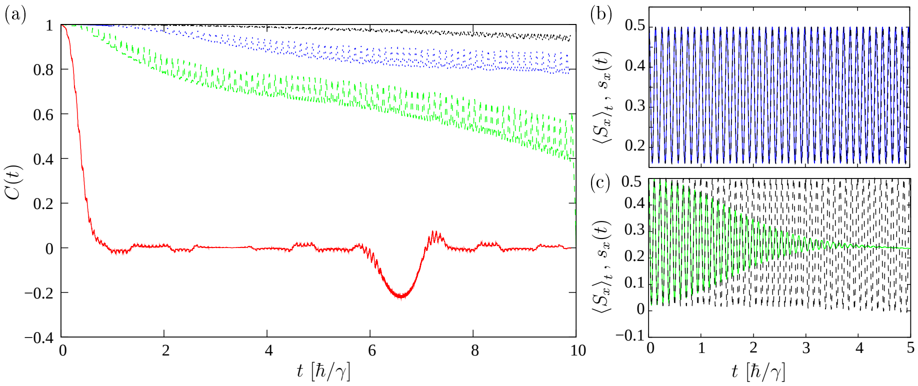

Figure 2.1: (a) Correlation between the mean-field and exact quantum solution $C(t)$ (defined in Eq. (2.15); $C(t) = 1$ indicates perfect agreement between the mean-field and quantum solutions) for evolution of an electron spin in the presence of a total bath spin $K = 50$ and magnetic field $B = 0$ (black dash-dotted line, showing the weakest decay), $B = 5\gamma$ (blue dotted line), $B = 10\gamma$ (green dashed line) and large magnetic field $B = 500\gamma$ (red solid line, showing rapid decay). The inital conditions were $\theta_S = \pi/2$, $\phi_S = 0$, $\theta_K = 0.3\pi$ (see the discussion following Eq. (2.3)). We also show the exact quantum evolution $\langle S_x\rangle_t$ (solid line) and mean-field approximation $s_x(t)$ (dashed line) for (b) $B = 0$ and (c) $B = 10\gamma$.

The solutions to Eqs. (2.5), (2.6) and the expressions in Eqs. (2.7), (2.8) for the coefficients $\{\alpha_m^\uparrow(t), \alpha_m^\downarrow(t) : m = -K \dots K\}$ constitute a complete exact solution for the dynamics of the wave function $|\psi(t)\rangle$ at any later time $t > 0$. We solve Eqs. (2.5) and (2.6) by Laplace transformation to obtain

$$\begin{aligned}\alpha_m^\uparrow(t) = e^{i\frac{\gamma}{4}t}\, &\{\alpha_m^\uparrow(0)\cos(\omega_{Km}t)\\ &-i\left(\alpha_m^\uparrow(0)\left[B+\gamma(m+\frac{1}{2})\right]+\alpha_{m+1}^\downarrow(0)\gamma C_{Km+1}^-\right)\frac{\sin(\omega_{Km}t)}{2\omega_{Km}}\right\},\end{aligned} \tag{2.9}$$

$$\begin{aligned}\alpha_{m+1}^\downarrow(t) = e^{i\frac{\gamma}{4}t}\, &\left\{\alpha_{m+1}^\downarrow(0)\cos(\omega_{Km}t)\right.\\ &\left.+i\left(\alpha_{m+1}^\downarrow(0)\left[B+\gamma(m+\frac{1}{2})\right]-\alpha_m^\uparrow(0)\gamma C_{Km}^+\right)\frac{\sin(\omega_{Km}t)}{2\omega_{Km}}\right\},\end{aligned} \tag{2.10}$$

$$\omega_{Km} = \frac{1}{2}\left[(B+\gamma m)(B+\gamma(m+1))+\gamma^2\left(C_{Km+1}^-C_{Km}^+ + \frac{1}{4}\right)\right]^{1/2}. \tag{2.11}$$

With the coefficients $\{\alpha_m^\uparrow(t), \alpha_m^\downarrow(t) : m = -K, \dots, K\}$ in hand, we can evaluate the expectation values of all spin components exactly: $\langle \mathbf{S}\rangle_t = \langle\psi(t)|\,\mathbf{S}\,|\psi(t)\rangle$, $\langle\mathbf{K}\rangle_t = \langle\psi(t)|\,\mathbf{K}\,|\psi(t)\rangle$.

To evaluate the classical spin dynamics, we perform a mean-field decomposition of the Hamiltonian given in Eq. (2.1) by rewriting the spin operators as $\mathbf{S} = \langle\mathbf{S}\rangle_t + \delta\mathbf{S}$ and $\mathbf{K} = \langle\mathbf{K}\rangle_t + \delta\mathbf{K}$. We then neglect the term that is bilinear in the spin fluctuations ($\propto \delta\mathbf{S}\cdot\delta\mathbf{K}$) and approximate the spin expectation values by their self-consistent mean-field dynamics $\langle\mathbf{S}\rangle_t \approx \mathbf{s}(t)$, $\langle\mathbf{K}\rangle_t \approx \mathbf{k}(t)$, where $\mathbf{s}$ and $\mathbf{k}$ are classical time-dependent vectors of fixed length [97]. Up to a c-number shift, this gives the (time-dependent) mean-field Hamiltonian

$$H_{\mathrm{mf}}(t) = (\mathbf{B} + \gamma\mathbf{k}(t)) \cdot \mathbf{S} + \gamma\mathbf{s}(t) \cdot \mathbf{K}. \tag{2.12}$$

The mean-field dynamics are now given by the Heisenberg equations of motion for the spin operators: $\dot{\mathbf{S}} = i\,[H_{\mathrm{mf}}(t), \mathbf{S}]$, $\dot{\mathbf{K}} = i\,[H_{\mathrm{mf}}(t), \mathbf{K}]$, with the replacements $\langle\mathbf{S}\rangle_t \approx \mathbf{s}(t)$, $\langle\mathbf{K}\rangle_t \approx \mathbf{k}(t)$:

$$\begin{aligned} \dot{\mathbf{s}}(t) &= (\mathbf{B} + \gamma\mathbf{k}(t)) \times \mathbf{s}(t), & (2.13)\\ \dot{\mathbf{k}}(t) &= -\gamma\mathbf{k}(t) \times \mathbf{s}(t). & (2.14) \end{aligned}$$

An exact analytical solution to Eqs. (2.13, 2.14) is known [97]. However, instead of repeating this solution here, we solve Eqs. (2.13, 2.14) by numerical integration for direct comparison with the exact results given above. The mean-field and quantum dynamics are shown in Fig. 2.1 for four values of the Zeeman splitting $B = |\mathbf{B}|$. We compare the two solutions using the correlation function

$$C(t) = \frac{1}{T}\int_t^{t+T} dt' \frac{2\,\langle S_x\rangle_{t'}\, s_x(t')}{\langle S_x\rangle_{t'}^2 + s_x(t')^2}, \tag{2.15}$$

where we average over the time interval $T = 0.1\hbar/\gamma$ to remove rapid oscillations. $C(t) = 1$ if the exact solution and mean-field approximation are identical ($s_x(t) = \langle S_x\rangle_t$) over the time interval $(t, t+T)$. $C(t) < 1$ indicates that the two solutions differ. While the zero-magnetic-field dynamics appear to be well reproduced by the mean-field approximation, at least at short time scales, the high-field solution decays rapidly, which can not appear in the classical dynamics unless averaging is performed over the initial conditions [70]. There is a partial recurrence of the correlator at a time scale given by the inverse level spacing for the quantum problem, $\tau_{\mathrm{p}} = 2\pi\hbar/\gamma$, but the recurrence is only partial since at this time the quantum and classical solutions have already gone out of phase.

It is relatively straightforward to understand the difference in the high-field and low-field behavior shown in Fig. 2.1. At zero magnetic field, the total spin $\mathbf{J}\cdot\mathbf{J}$ ($\mathbf{J} = \mathbf{K} + \mathbf{S}$) commutes with the Hamiltonian, so if the nuclear spin system begins in an eigenstate of $\mathbf{K}\cdot\mathbf{K}$, only a single frequency exists in the quantum dynamics, corresponding to the difference in energies with $J = K \pm 1/2$ [17, 67]. Thus, in this case the quantum dynamics corresponds to simple periodic precession, and mimics the classical dynamics for $K \gg 1$ (see Fig. 2.1(b)). However, the states of fixed J are manifold degenerate. If a term is added to the Hamiltonian which does not commute with $\mathbf{J}\cdot\mathbf{J}$ (in this case, the electron Zeeman term BS^z), many more frequencies are involved in the quantum dynamics, which can lead to decay in the quantum solution, while the classical solution continues to describe simple electron spin precession (see Fig. 2.1(c)). In a large magnetic field ($B \gg \gamma|\mathbf{K}_\perp|$), it is straightforward to evaluate the decay in the quantum mechanical solution [70],[2]

$$\langle S_+\rangle_t \approx \langle S_+\rangle_0 \exp\left\{-\frac{t^2}{2\tau_c^2} + i\left[B + \cos(\theta_K)\gamma K\right] t\right\}, \tag{2.16}$$

$$\tau_c = \frac{1}{\gamma}\sqrt{\frac{2}{K\left[1-\cos^2(\theta_K)\right]}}. \tag{2.17}$$

The x-component of spin is then given by the real part $\langle S_x\rangle_t = \mathrm{Re}\left[\langle S_+\rangle_t\right]$. We consider the hyperfine problem with $I = 1/2$. When the initial nuclear-spin coherent state is generated by rotating the spins from a fully-polarized state such that K is maximal (as in Ref. [70]), we then have $K = N/2$. In addition, $\gamma = A/N$ and for nuclear spin polarization $p = \cos(\theta_K) \ll 1$ this gives the decay time

$$\tau_c = 2\frac{\sqrt{N}}{A}. \tag{2.18}$$

Since the classical dynamics at times $t < \tau_c$ describe simple precession for fixed initial conditions, any decay in the quantum solution signifies a disagreement between the quantum and classical problems. Thus, the mean-field solution will give an accurate description of the full quantum dynamics only for times $t < \tau_c$, with τ_c given by Eq. (2.18).

The crossover from precession to decay of the quantum solution with the addition of a magnetic field suggests that the uniform coupling-constants picture should only be used with caution, since the Hamiltonian in Eq. (2.1) also does not commute with $\mathbf{J}\cdot\mathbf{J}$ when the coupling constants vary from one nuclear-spin site to the next (as is true in a quantum dot). Indeed, in the presence of randomly-varying coupling constants, the straightforward mean-field electron-spin dynamics at times $t > \tau_c$ are quantitatively very different from the exact quantum dynamics at weak magnetic fields $B \to 0$ [103].

2.3 Conclusions

We have presented an exact solution for the problem of an electron spin interacting with a large bath of spins with uniform Heisenberg coupling. This exact solution has been compared to the corresponding mean-field (classical spin) model. We have seen that the mean-field and quantum solutions show striking agreement at times shorter than the transverse-spin correlation time τ_c, which diverges at zero magnetic field. This divergence, however, may only be due to the assumption of uniform coupling constants, which is unphysical for a quantum dot with strong confinement.

In this work we have focused on a comparison of dynamics for fixed initial conditions of the quantum and classical problem. Some of the quantum behavior, including Gaussian decay, can be recovered with an average over classical solutions [15, 16]. An intriguing question therefore remains: How much of the quantum dynamics can be obtained by averaging over classical solutions with different initial conditions?

---

[2] The decay formula (Eq. (2.16)) is obtained from Eq. (19) of Ref. [70] by restoring the formula to dimensionful units and applying the replacements $p \to \cos(\theta_K)$, $A/N \to \gamma$, $N/2 \to K$.

Chapter 3

Single-spin dynamics

[W. A. Coish and D. Loss, Phys. Rev. B **70**, 195340 (2004)]

In this Chapter we perform a systematic calculation for the non-Markovian dynamics of a localized electron spin interacting with an environment of nuclear spins via the Fermi contact hyperfine interaction. This work applies to an electron in the *s*-type orbital ground state of a quantum dot or bound to a donor impurity, and is valid for arbitrary polarization p of the nuclear spin system, and arbitrary nuclear spin I in high magnetic fields. In the limit of $p = 1$ and $I = \frac{1}{2}$, the Born approximation of our perturbative theory recovers the exact electron spin dynamics. We have found the form of the generalized master equation (GME) for the longitudinal and transverse components of the electron spin to all orders in the electron spin–nuclear spin flip-flop terms. Our perturbative expansion is regular, unlike standard time-dependent perturbation theory, and can be carried-out to higher orders. We show this explicitly with a fourth-order calculation of the longitudinal spin dynamics. In zero magnetic field, the fraction of the electron spin that decays is bounded by the smallness parameter $\delta = 1/p^2 N$, where N is the number of nuclear spins within the extent of the electron wave function. However, the form of the decay can only be determined in a high magnetic field, much larger than the maximum Overhauser field. In general the electron spin shows rich dynamics, described by a sum of contributions with non-exponential decay, exponential decay, and undamped oscillations. There is an abrupt crossover in the electron spin asymptotics at a critical dimensionality and shape of the electron envelope wave function. We propose a scheme that could be used to measure the non-Markovian dynamics using a standard spin-echo technique, even when the fraction that undergoes non-Markovian dynamics is small.

3.1 Introduction

Prospects for the development of new spintronic devices [106] and the controlled manipulation of electron or nuclear spins for quantum information processing [107] have sparked substantial research efforts in recent years. One of the major obstacles to achieving these goals is decoherence due to the influence of an uncontrollable environment. For quantum computing tasks, the strict requirements for error correction [108] put strong limits on the degree of decoherence allowed in such devices. From this point of view, single-electron semiconductor quantum dots represent good candidates for spin-based information processing since they show particularly long longitudinal relaxation times, $T_1 = 1\,\mathrm{ms}$ [88]. In GaAs quantum wells, the transverse dephasing time T_2^* for an ensemble of electron spins, which typically provides a lower bound for the intrinsic decoherence time T_2 of an isolated spin, has been measured to be in excess of $100\,\mathrm{ns}$ [109].

Possible sources of decoherence for a single electron spin confined to a quantum dot are spin-orbit coupling and the contact hyperfine interaction with the surrounding nuclear spins [14]. The relaxation rate due to spin-orbit coupling $\frac{1}{T_1}$ is suppressed for localized electrons at low temperatures [60, 61] and recent work has shown that T_2, due to spin-orbit coupling, can be as long as T_1 under realistic conditions [110]. However, since spin-carrying isotopes are common in the semiconductor industry, the contact hyperfine interaction (in contrast to the spin-orbit interaction) is likely an unavoidable source of decoherence, which does not vanish with decreasing temperature or carefully chosen quantum dot geometry [67].

In the last few years, a great deal of effort has been focused on a theoretical description of interesting effects arising from the contact hyperfine interaction for a localized electron [14,15,17,18,19,111,112,113,114,65,66,68,69,94,16,115]. The predicted effects include a dramatic variation of T_1 with gate voltage in a quantum dot near the Coulomb blockade peaks or valleys [19], all-optical polarization of the nuclear spins [113], use of the nuclear spin system as a quantum memory [111,112], and several potential spin relaxation and decoherence mechanisms [15, 65, 66, 114, 68]. This theoretical work is spurred-on by intriguing experiments that show localized electrical detection of spin resonance phenomena [116], nuclear spin polarization near quantum point contacts [117], gate-controlled transfer of polarization between electrons and nuclei [118], nuclear spin polarization and manipulation due to optical pumping in GaAs quantum wells [119], and voltage-controlled nuclear spin polarization in a field-effect transistor [120]. In addition, recent experiments have shown hyperfine induced oscillations in transport current through a double quantum dot [20], and long T_2 times for electrons trapped at shallow donor impurities in isotopically purified ^{28}Si:P [121]. Our system of interest in this chapter is an electron confined to a single GaAs quantum dot, but this work applies quite generally to other systems, such as electrons trapped at shallow donor impurities in Si:P [67].

In this chapter, we investigate electron spin dynamics at times shorter than the nuclear dipole-dipole correlation time τ_{dd} ($\tau_{\mathrm{dd}} \approx 10^{-4}\,\mathrm{s}$ in GaAs is given directly by the inverse width of the nuclear magnetic resonance (NMR) line [27]). At these time scales, the relevant Hamiltonian for a description of the electron and nuclear spin dynamics is that for the Fermi contact hyperfine interaction (see Eq. (3.1), below). Dynamics under the action of this Hamiltonian may be of fundamental interest, since in zero magnetic field, Eq. (3.1) corresponds to the well-known integrable Gaudin magnet, which is soluble via Bethe ansatz [92,67]. Though the Hamiltonian appears simple, a detailed microscopic description for the dynamics of a spin coupled to a spin environment remains an open question [122,123]. A degree of success has been achieved some time ago in bulk systems through the development of phenomenological models [124]. These models invoke certain approximations, namely, assumptions of Markovian dynamics and ensemble averaging. Care should therefore be taken in applying the same models to the problem of single-spin decoherence for an electron spin strongly coupled to a nuclear spin environment, where they may not apply [15, 17].

For nuclear spin $I = \frac{1}{2}$, an exact solution for the electron spin dynamics has been found in the special case of a *fully* polarized initial state of the nuclear spin system [15,17]. This solution shows that the electron spin only decays by a fraction $\propto \frac{1}{N}$ of its initial value, where N is the number of nuclear spins within the extent of the electron wave function. The decaying fraction was shown to have a non-exponential tail for long times, which suggests non-Markovian (history dependent) behavior. For an initial nuclear spin configuration that is not fully polarized, no exact solution is available and standard time-dependent perturbation theory fails [15]. Subsequent exact diagonalization studies on small spin systems [18] have shown that the electron spin dynamics are highly dependent on the type of initial nuclear spin configuration, and the dynamics of a randomly correlated initial nuclear spin configuration are reproduced by an ensemble average over direct-product initial states. The unusual (non-exponential) form of decay, and the fraction of the electron spin that undergoes decay may be of interest in quantum error correction (QEC) since QEC schemes typically assume exponential decay to zero.

In this chapter we formulate a systematic perturbative theory of electron spin dynamics under the action of the Fermi contact hyperfine interaction. This theory is valid for *arbitrary* nuclear spin polarization and *arbitrary* nuclear spin I in high magnetic fields. For nuclear spin $I = \frac{1}{2}$ and a fully polarized nuclear spin system, we recover the exact solution for the electron spin dynamics within the Born approximation of our perturbative theory. Our approach follows a method recently applied to the spin-boson model [125]. This method does not suffer from unbounded secular terms that occur in standard perturbation theory [15] and does not involve Markovian approximations.

This chapter is organized as follows. In Section 3.2 we review the model Hamiltonian and address the question of realistic initial conditions. In Section 3.3 we derive the form of the exact generalized master equation (GME) for the electron spin dynamics. In Section 3.4 we consider the leading-order electron spin dynamics in high magnetic fields. In Section 3.5 we proceed to calculate the complete non-Markovian dynamics within the Born approximation. We describe a procedure that could be used to measure the non-Markovian dynamics in Section 3.6. In Section 3.7 we show that our method can be extended to higher orders without the problems of standard perturbation theory by explicitly calculating the corrections to the longitudinal spin self-energy at fourth order in the nuclear spin-electron spin flip-flop terms. We conclude in Section 3.8 with a summary of the results. Technical details are deferred to Appendices A–E.

3.2 Model

We consider a localized electron spin interacting with N_{tot} nuclear spins via the Fermi contact hyperfine interaction. The Hamiltonian for this system is

$$\mathcal{H} = bS_z + \epsilon_{nz} I_z + \mathbf{h} \cdot \mathbf{S}, \tag{3.1}$$

where $\mathbf{S} = (S_x, S_y, S_z)$ is the electron spin operator. $b = g^*\mu_B B_z$ ($\epsilon_{nz} = g_I \mu_N B_z$) is the electron (nuclear) Zeeman splitting in a magnetic field B_z, with effective g-factor g^* (g_I) for the electron (nuclei) and Bohr (nuclear) magneton μ_B (μ_N). Further, $\mathbf{h} = (h_x, h_y, h_z) = \sum_{k=0}^{N_{\mathrm{tot}}-1} A_k \mathbf{I}_k$ gives the (quantum) field generated by an environment of nuclear spins. $\mathbf{I}_k = (I_k^x, I_k^y, I_k^z)$ is the nuclear spin operator at lattice site k and A_k is the associated hyperfine coupling constant. $I_z = \sum_k I_k^z$ is the total z-component of nuclear spin.

The nuclear Zeeman term can be formally eliminated from the Hamiltonian $\mathcal{H}$ (Eq. (3.1)) by transforming to a rotating reference frame. The z-component of total angular momentum is $J_z = S_z + I_z$. Adding and subtracting $\epsilon_{nz} J_z$ gives $\mathcal{H} = \mathcal{H}' + \epsilon_{nz} J_z$. The Hamiltonian in the rotating frame, $\mathcal{H}'$, is then

$$\mathcal{H}' = \mathcal{H}'_0 + \mathcal{H}'_V, \tag{3.2}$$

$$\mathcal{H}'_0 = b' S_z + h_z S_z, \tag{3.3}$$

$$\mathcal{H}'_V = \frac{1}{2}\left(h_+ S_- + h_- S_+\right), \tag{3.4}$$

where $b' = b - \epsilon_{nz}$ and we have introduced $h_\pm = h_x \pm i h_y$. The usual Heisenberg-picture operators in the rotating frame are $S'_X(t) = e^{i\mathcal{H}'t} S_X e^{-i\mathcal{H}'t}$, $X = z, +$, $S_\pm = S_x \pm i S_y$. Noting that $[J_z, \mathcal{H}] = 0$, we find they are related to the operators $S_X(t) = e^{i\mathcal{H}t} S_X e^{-i\mathcal{H}t}$ in the rest frame by

$$S'_z(t) = S_z(t) \tag{3.5}$$

$$S'_+(t) = e^{-i\epsilon_{nz}t} S_+(t). \tag{3.6}$$

In the following, $\langle S'_z \rangle_t$ and $\langle S'_+ \rangle_t$ will be evaluated in the rotating frame, but we omit primes on all expectation values.

The hyperfine coupling constants A_k are given by [67]

$$A_k = A v_0 |\psi(\mathbf{r}_k)|^2. \tag{3.7}$$

Here, v_0 is the volume of a crystal unit cell containing one nuclear spin, $\psi(\mathbf{r})$ is the electron envelope wave function, and A is the strength of the hyperfine coupling. In GaAs, all naturally occurring isotopes carry spin $I = \frac{3}{2}$. In bulk GaAs, A has been estimated [27] to be $A = 90\,\mu eV$ $\left(\frac{A}{|g^*|\mu_B} = 3.5\,\mathrm{T}\right)$. This estimate is based on an average over the hyperfine coupling constants for the three nuclear isotopes ^{69}Ga, ^{71}Ga, and ^{75}As, weighted by their relative abundances. Natural silicon contains 4.7% ^{29}Si, which carries $I = \frac{1}{2}$, and 95% ^{28}Si, with $I = 0$. An electron bound to a phosphorus donor impurity in natural Si:P interacts with $N \approx 10^2$ surrounding ^{29}Si nuclear spins, in which case the hyperfine coupling constant is on the order of $A \approx 0.1\,\mu eV$ [67]. We consider a localized electron in its orbital ground state, described by an isotropic envelope wave function of the form

$$\psi(r_k) = \psi(0) \exp\left[-\frac{1}{2}\left(\frac{r_k}{l_0}\right)^m\right]. \tag{3.8}$$

When $m = 2$, $\psi(r)$ is a Gaussian with Bohr radius l_0, and for $m = 1$, $\psi(r)$ corresponds to a hydrogen-like s-state with Bohr radius $a_0 = 2l_0$. N_{tot} nuclear spins are in the system, but the effective number N of spins interacting appreciably with the electron is smaller (see Fig. 3.1). N is defined as the number of nuclear spins within radius l_0 of the origin and the integer index k gives the

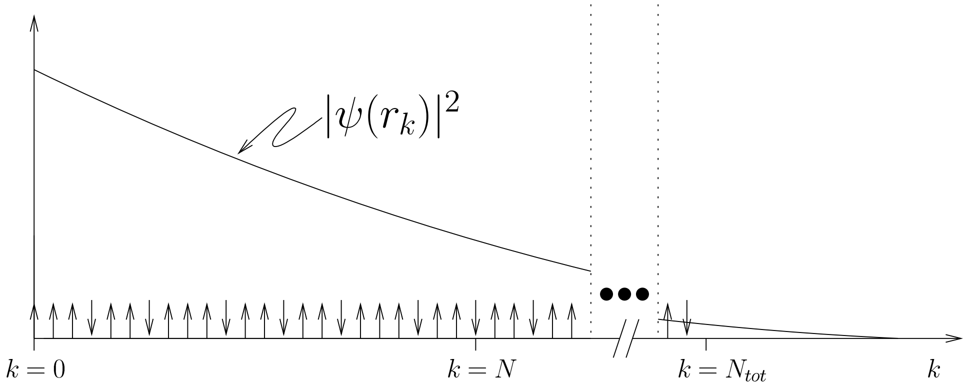

Figure 3.1: Schematic of the square modulus of the electron envelope wave function $|\psi(r)|^2$ and nuclear spins (arrows). k is the nuclear site index, N is the number of nuclear spins within radius $r = l_0$, and N_{tot} is the total number of nuclear spins in the system.

number of spins within radius r_k. In d dimensions, $\left(\frac{r_k}{l_0}\right)^d = \frac{k}{N}$. It is convenient to work in energy units such that $\frac{A_0}{2} = 1$, where A_0 is the coupling constant at the origin ($r_0 = 0$). In these units A_k takes the simple form

$$A_k = 2\exp\left[-\left(\frac{k}{N}\right)^{\frac{m}{d}}\right]. \tag{3.9}$$

3.2.1 Initial conditions

3.2.1.1 Sudden approximation

The electron spin and nuclear system are decoupled for times $t < 0$, and prepared independently in states described by the density operators $\rho_S(0)$ and $\rho_I(0)$, respectively. At $t = 0$, the electron and nuclear spin system are coupled "instantaneously", i.e., the electron spin and nuclear system are brought into contact over a switching time scale τ_{sw},[1] which is sufficiently small–see Eq. (3.11), below. The state of the entire system, described by the total density operator $\rho(t)$ is then continuous at $t = 0$, and is given by

$$\rho(0^-) = \rho(0^+) = \rho_S(0) \otimes \rho_I(0). \tag{3.10}$$

The evolution of the density operator $\rho(t)$ for $t \geq 0$ is governed by the Hamiltonian $\mathcal{H}'$ for an electron spin coupled to an environment of nuclear spins. Since the largest energy scale in this problem is given by $|b' + A|$, in general the condition

$$\tau_{\text{sw}} \ll \frac{2\pi\hbar}{|b' + A|} \tag{3.11}$$

---

[1] τ_{sw} is, e.g., the time taken to inject an electron into a quantum dot.

should be satisfied for the sudden approximation (Eq. (3.10)) to be valid. In bulk GaAs, $\frac{2\pi\hbar}{A} \simeq 50\,\mathrm{ps}$ and for an electron bound to a phosphorus donor in natural silicon, $\frac{2\pi\hbar}{A} \simeq 10\,\mathrm{ns}$.

3.2.1.2 Dependence on the nuclear state: zeroth order dynamics

Evolution of the electron spin for different initial nuclear configurations has been addressed previously [17,18]. In Ref. [18] it was found, through numerical study, that the dynamics of the electron spin were highly dependent on the initial state of the nuclear system. The goal of this section is to shed more light on the role of the initial nuclear configuration by evaluating the much simpler zeroth order dynamics, i.e., the electron spin evolution is evaluated under $\mathcal{H}' = \mathcal{H}'_0$ alone, neglecting the flip-flop terms $\mathcal{H}'_V$.

Since $[\mathcal{H}'_0, S_z] = 0$, $\langle S_z\rangle_t$ is constant. However, $[\mathcal{H}'_0, S_\pm] \neq 0$, so the transverse components, $\langle S_+\rangle_t = \langle S_x\rangle_t + i\,\langle S_y\rangle_t$, will have a nontrivial time dependence. We evaluate the expectation value $\langle S_+\rangle_t = \mathrm{Tr}\left\{e^{-i\mathcal{H}'_0 t} S_+ e^{i\mathcal{H}'_0 t}\rho(0)\right\}$ (setting $\hbar = 1$), with the initial state given in Eq. (3.10). After performing a partial trace over the electron spin Hilbert space, we obtain an expression in terms of the initial nuclear spin state:

$$\langle S_+\rangle_t = \langle S_+\rangle_0 \,\mathrm{Tr}_I \left\{e^{i(b'+h_z)t}\rho_I(0)\right\}, \tag{3.12}$$

where Tr_I is a partial trace over the nuclear spin space alone. For simplicity, here we consider $I = \frac{1}{2}$, and the coupling constants are taken to be uniform. After enforcing the normalization $\sum_k A_k = 2N$ in units where $\frac{A_0}{2} = \frac{A}{2N} = 1$, the hyperfine coupling constants are

$$A_k = \left\{ \begin{array}{ll} 2, & k = 0, 1 \cdots N-1 \\ 0, & k \geq N \end{array} \right. . \tag{3.13}$$

The zeroth-order electron spin dynamics can now be evaluated exactly for three types of initial nuclear spin configuration:

$$\begin{aligned} \rho_I^{(1)}(0) &= |\psi_I(0)\rangle\,\langle\psi_I(0)| && (3.14)\\ \rho_I^{(2)}(0) &= \sum_{N_\uparrow=0}^{N} P(N_\uparrow; N, f_\uparrow)\,|N_\uparrow\rangle\,\langle N_\uparrow| && (3.15)\\ \rho_I^{(3)}(0) &= |n\rangle\,\langle n|\,. && (3.16) \end{aligned}$$

$\rho_I^{(1)}$ is a pure state, where $|\psi_I(0)\rangle = \prod_{k=0}^{N}\left(\sqrt{f_\uparrow}\,|\uparrow_k\rangle + e^{i\phi_k}\sqrt{1-f_\uparrow}\,|\downarrow_k\rangle\right)$ is chosen to render the z-component of nuclear spin translationally invariant: $\langle\psi_I(0)|\, I_k^z\, |\psi_I(0)\rangle = \frac{1}{2}(2f_\uparrow - 1) = \frac{p}{2}$, and $p = 2f_\uparrow - 1$ is the polarization of the nuclear spin system. ϕ_k is an arbitrary site-dependent phase factor. $P(x; n, f) = \left(\begin{array}{c} n \\ x \end{array}\right) f^x(1-f)^{n-x}$ is a binomial distribution, and $|N_\uparrow\rangle$ is a product state of the form $|\uparrow\uparrow\downarrow\cdots\rangle$ with $N_\uparrow$ spins up and $N - N_\uparrow$ spins down. $\rho_I^{(2)}(0)$ then corresponds to a mixed state; this is an ensemble of product states where the N spins in each product state are selected from a bath of polarization $p = 2f_\uparrow - 1$. $\rho_I^{(3)}$, like $\rho_I^{(1)}$, is a pure state, but for this state $|n\rangle$ is chosen to be an eigenstate of h_z with eigenvalue pN (corresponding to a nuclear system with polarization p): $h_z\,|n\rangle = pN\,|n\rangle$. We insert the initial nuclear spin states $\rho_I^{(i)}(0)$ into (3.12) to obtain the associated time evolution $\langle S_+\rangle_t^{(i)}$:

$$\langle S_+\rangle_t^{(1,2)} = \langle S_+\rangle_0 \sum_{N_\uparrow=0}^{N} P(N_\uparrow; N, f_\uparrow) e^{i(b'+M(N_\uparrow))t}, \tag{3.17}$$

$$\langle S_+\rangle_t^{(3)} = \langle S_+\rangle_0\, \mathrm{e}^{i(b'+pN)t}. \tag{3.18}$$

$M(N_\uparrow) = 2N_\uparrow - N$ is the nuclear magnetization on a dot with $N_\uparrow$ nuclear spins up.

The similarity in dynamics between randomly correlated (entangled) pure states and mixed states has been demonstrated for evolution under the full Hamiltonian ($\mathcal{H}' = \mathcal{H}'_0 + \mathcal{H}'_V$) via exact diagonalizations of small ($N_{\mathrm{tot}} \lesssim 19$) spin systems [18]. Here, the zeroth-order electron spin dynamics are identical for the pure state $\rho_I^{(1)}(0)$ and the mixed state $\rho_I^{(2)}(0)$ even when the initial pure state $|\psi_I(0)\rangle$ is a direct product. Direct application of the central limit theorem gives a Gaussian decay for large N:

$$\langle S_+\rangle_t^{(1,2)} \approx \langle S_+\rangle_0\, e^{-\frac{t^2}{2t_c^2}+i(b'+pN)t}, \quad t_\mathrm{c} = \frac{1}{\sqrt{N(1-p^2)}}. \tag{3.19}$$

Returning to dimension-full units (c.f. Table 3.1 below), the time scale for this decay is given by $\tau_\mathrm{c} = \frac{2N\hbar}{A} t_\mathrm{c} \approx 5\,\mathrm{ns}$ for a GaAs quantum dot with $p^2 \ll 1$ containing $N = 10^5$ nuclei and $\tau_c \approx 100\,\mathrm{ns}$ for an electron trapped at a shallow donor impurity in Si : P, with $N = 10^2$. For an ensemble of nuclear spin states, Gaussian decay with the time scale τ_c has been found previously [15, 17, 16]. Gaussian decay for a Hamiltonian with an Ising coupling of electron and nuclear spins has been demonstrated [123] for a more general class of *pure* initial states and for coupling constants A_k that may vary from site-to-site.

For the initial states $\rho_I^{(1,2)}(0)$, precise control over the nuclear spin polarization between measurements or a spin-echo technique would be needed to reduce or eliminate the rapid decay described by (3.19). However, the quantum superposition of h_z eigenstates can be removed, in principle, from the pure state $\rho_I^{(1)}(0)$ by performing a strong (von Neumann) measurement on the nuclear Overhauser field pN.[2] After the nuclear system is prepared in an h_z-eigenstate, to zeroth order the electron spin dynamics will be given by $\langle S_+\rangle_t^{(3)}$, i.e., a simple precession about the z-axis with no decay.

When higher-order corrections are taken into account, and the coupling constants A_k are allowed to vary from site-to-site, even an initial h_z-eigenstate can lead to decay of the electron spin. This has been shown [15, 17] in an exact solution for the specific case of a fully-polarized system of nuclear spins-$\frac{1}{2}$ and by exact diagonalization on small systems [18]. The goal of the present work

---

[2] It may be possible to measure the Overhauser field directly by locating the position of the electron spin resonance (ESR) line, where the magnetic field compensates the nuclear Overhauser field. We have confirmed by exact diagonalizations on small ($N_{\mathrm{tot}} = 15$) spin systems that the resonance is indeed centered at a magnetic field corresponding to the negative nuclear Overhauser field, even for a nuclear spin system with $p < 1$. Alternatively, a state where all nuclear spins are aligned along the magnetic field can be generated by allowing the nuclear spins to relax in the presence of the nuclear spin-lattice interaction.

is to perform an analytical calculation with a larger range of validity (a large system of nuclear spins with arbitrary polarization and arbitrary nuclear spin I in a sufficiently strong magnetic field) that recovers previous exact results in the relevant limiting cases. In the rest of this chapter, the effect of higher- (beyond zeroth-) order corrections will be considered for a nuclear spin system prepared in an arbitrary h_z eigenstate: $\rho_I(0) = \rho_I^{(3)}(0)$, as given in Eq. (3.16). Specifically, the initial state of the nuclear system $|n\rangle$ can be written as an arbitrary linear combination of g_n degenerate product states:

$$|n\rangle = \sum_{j=1}^{g_n} \alpha_j |n_j\rangle, \quad |n_j\rangle = \bigotimes_{i=0}^{N_{\mathrm{tot}}-1} \left| I, m_i^j \right\rangle \tag{3.20}$$

where $|I, m_i\rangle$ is an eigenstate of the operator I_i^z with eigenvalue m_i and $h_z |n_j\rangle = [h_z]_{nn} |n_j\rangle$ for all j, where we write the matrix elements of any operator $\mathcal{O}$ as $\langle i| \mathcal{O} |j\rangle = [\mathcal{O}]_{ij}$.

3.3 Generalized master equation

To evaluate the dynamics of the reduced (electron spin) density operator, we introduce a projection superoperator P, defined by its action on an arbitrary operator $\mathcal{O}$: $P\mathcal{O} = \rho_I(0)\mathrm{Tr}_I\mathcal{O}$. P is chosen to preserve all electron spin expectation values: $\langle S_\beta \rangle_t = \mathrm{Tr} S_\beta \rho(t) = \mathrm{Tr} S_\beta P \rho(t)$, $\beta = x, y, z$, and satisfies $P^2 = P$. For factorized initial conditions (Eq. (3.10)), $P\rho(0) = \rho(0)$, which is a sufficient condition to rewrite the von Neumann equation $\dot{\rho}(t) = -i\left[\mathcal{H}', \rho(t)\right]$ in the form of the exact Nakajima-Zwanzig generalized master equation (GME) [126]:

$$\begin{aligned} P\dot{\rho}(t) &= -iPLP\rho(t) - i\int_0^t dt' \Sigma(t-t')\rho(t'), && (3.21) \\ \Sigma(t) &= -iPLQe^{-iLQt}QLP, && (3.22) \end{aligned}$$

where $\Sigma(t)$ is the self-energy superoperator and $Q = \mathbf{1} - P$ is the complement of P ($\mathbf{1}$ is the identity superoperator). $L = L_0 + L_V$ is the full Liouvillian, where L_α ($\alpha = V, 0$) is defined by $L_\alpha \mathcal{O} = [\mathcal{H}'_\alpha, \mathcal{O}]$. When the initial nuclear state is of the form $\rho_I(0) = |n\rangle\langle n|$, where $|n\rangle$ is an arbitrary eigenstate of h_z, as in Eq. (3.20), P obeys the useful identities

$$\begin{aligned} PL_V P &= 0, && (3.23) \\ PL_0 P &= L_0 P. && (3.24) \end{aligned}$$

We apply Eqs. (3.23) and (3.24), and perform a trace on (3.21) over the nuclear spins to obtain

$$\begin{aligned} \dot{\rho}_S(t) &= -iL_0^n \rho_S(t) - i\int_0^t dt' \Sigma_S(t-t')\rho_S(t'), && (3.25) \\ \Sigma_S(t) &= -i\mathrm{Tr}_I L e^{-iQLt} L_V \rho_I(0), && (3.26) \end{aligned}$$

where $L_0^n \mathcal{O} = [S_z \omega_n, \mathcal{O}]$ and $\omega_n = b' + [h_z]_{nn}$. $\Sigma_S(t)$ is the reduced self-energy superoperator. $\rho_S(t) = \mathrm{Tr}_I \rho(t) = \frac{1}{2}\sigma_0 + \langle S_x \rangle_t \sigma_x + \langle S_y \rangle_t \sigma_y + \langle S_z \rangle_t \sigma_z$ is the reduced electron spin density operator, where σ_β, $\beta = x, y, z$, are the usual Pauli matrices and σ_0 is the 2×2 identity.

We iterate the Schwinger-Dyson identity [126]

$$e^{-iQ(L_0+L_V)t} = e^{-iQL_0t} - i\int_0^t dt' e^{-iQL_0(t-t')}QL_V e^{-iQLt'} \tag{3.27}$$

on (3.26) to generate a systematic expansion of the reduced self-energy in terms of the perturbation Liouvillian L_V:

$$\Sigma_S(t) = \Sigma_S^{(2)}(t) + \Sigma_S^{(4)}(t) + \cdots, \tag{3.28}$$

where the superscript indicates the number of occurrences of L_V. Quite remarkably, to all orders in L_V, the equations for the longitudinal $\left(\langle S_z\rangle_t\right)$ and transverse $\left(\langle S_+\rangle_t = \langle S_x\rangle_t + i\langle S_y\rangle_t\right)$ electron spin components are decoupled and take the form:

$$\begin{aligned} \langle \dot{S_z}\rangle_t &= N_z(t) - i\int_0^t dt'\Sigma_{zz}(t-t')\langle S_z\rangle_{t'} & (3.29)\\ \langle \dot{S_+}\rangle_t &= i\omega_n\langle S_+\rangle_t - i\int_0^t dt'\Sigma_{++}(t-t')\langle S_+\rangle_{t'}. & (3.30)\end{aligned}$$

Details of the expansion (Eq. (3.28)) are given in Appendix A. It is most convenient to evaluate the inhomogeneous term $N_z(t)$ and the memory kernels $\Sigma_{zz}(t)$, $\Sigma_{++}(t)$ in terms of their Laplace transforms: $f(s) = \int_0^\infty dt e^{-st}f(t)$,$\mathrm{Re}[s] > 0$. $N_z(s)$ and $\Sigma_{zz}(s)$ are given in terms of matrix elements of the reduced self-energy by

$$\begin{aligned} N_z(s) &= -\frac{i}{2s}\left(\Sigma_{\uparrow\uparrow}(s) + \Sigma_{\uparrow\downarrow}(s)\right), & (3.31)\\ \Sigma_{zz}(s) &= \Sigma_{\uparrow\uparrow}(s) - \Sigma_{\uparrow\downarrow}(s). & (3.32)\end{aligned}$$

Explicit expressions for the matrix elements $\Sigma_{++}(s)$, $\Sigma_{\uparrow\uparrow}(s)$, and $\Sigma_{\uparrow\downarrow}(s)$ are given in Appendix A. We find that the self-energy at $(2k)^{\mathrm{th}}$ order is suppressed by the factor Δ^k, where

$$\Delta = \frac{N}{\omega_n}. \tag{3.33}$$

The parameter Δ and some other commonly used symbols are given in dimensionless and dimension-full units in Table 3.1 below. For high magnetic fields $|b'| \gg N$ $\left(|B_z| \gg \left|\frac{A}{g^*\mu_B}\right|\right)$, we have $|\Delta| \simeq \left|\frac{N}{b'}\right| \ll 1$, and the expansion is well-controlled. The non-perturbative regime is given by $|\Delta| \geq 1$, and the perturbative regime by $|\Delta| < 1$. Thus, a perturbative expansion is possible when the electron Zeeman energy produced by the magnetic and/or Overhauser field (provided by N nuclear spins) is larger than the single maximum hyperfine coupling constant A. In the rest of this section we apply the Born approximation $\Sigma_S \simeq \Sigma_S^{(2)}$ to the reduced self-energy, and perform the continuum limit for a large uniformly polarized nuclear spin system. Later, we also consider higher orders.

3.3.1 Born approximation

In the Born approximation, the memory kernels $\Sigma_{zz}(t)$, $\Sigma_{++}(t)$ and inhomogeneous term $N_z(t)$ in (3.29) and (3.30) are replaced by the forms obtained from the lowest-order self-energy, i.e., $N_z(t) \rightarrow N_z^{(2)}(t)$, $\Sigma_{zz}(t) \rightarrow \Sigma_{zz}^{(2)}(t)$, $\Sigma_{++}(t) \rightarrow \Sigma_{++}^{(2)}(t)$. In Laplace space, $\Sigma_{\uparrow\uparrow}^{(2)}(s)$, $\Sigma_{\uparrow\downarrow}^{(2)}(s)$, and $\Sigma_{++}^{(2)}(s)$ are given for an arbitrary initial h_z eigenstate $|n\rangle$ (see Eq. (3.20)) in Appendix A, Eqs. (A.20), (A.21), and (A.22). Inserting an initial state $|n\rangle$ for a large nuclear spin system with uniform polarization gives (see Appendix B):

$$\begin{aligned}
\Sigma_{\uparrow\uparrow}^{(2)}(s) &= -iNc_+\left[I_+(s-i\omega_n)+I_-(s+i\omega_n)\right], && (3.34)\\
\Sigma_{\uparrow\downarrow}^{(2)}(s) &= iNc_-\left[I_-(s-i\omega_n)+I_+(s+i\omega_n)\right], && (3.35)\\
\Sigma_{++}^{(2)}(s) &= -iN\left[c_-I_+(s)+c_+I_-(s)\right], && (3.36)\\
I_\pm(s) &= \frac{1}{4N}\sum_k \frac{A_k^2}{s\mp i\frac{A_k}{2}}. && (3.37)
\end{aligned}$$

In the above, the coefficients

$$c_\pm = I(I+1) - \langle\langle m(m\pm 1)\rangle\rangle \tag{3.38}$$

have been introduced, where $\langle\langle F(m)\rangle\rangle = \sum_{m=-I}^{I} P_I(m)F(m)$ for an arbitrary function $F(m)$. $P_I(m)$ is the probability of finding a nuclear spin I with z-projection m. The polarization p of the initial nuclear state is defined through the relation $\langle\langle m\rangle\rangle = pI$. Without loss of generality, in the rest of this chapter $p > 0$, but b' may take on positive or negative values. Assuming a uniform polarization in the nuclear spin system, we can evaluate the nuclear Overhauser field in terms of the initial polarization:

$$[h_z]_{nn} = \sum_i A_i\,\langle\langle m\rangle\rangle = pIA, \tag{3.39}$$

where we have used $\sum_i A_i = A$.

The continuum limit is performed by taking $N_{\mathrm{tot}} \rightarrow \infty$, while $N \gg 1$ is kept constant. For times $t \ll \sqrt{N}$, this allows the replacement of sums by integrals $\sum_k \rightarrow \int_0^\infty dk$, with small corrections (see Appendix C). We insert the coupling constants A_k from Eq. (3.9) into Eq. (3.37), perform the continuum limit and make the change of variables $x = \frac{A_k}{2}$ to obtain

$$I_\pm(s) = \frac{d}{m}\int_0^1 dx \frac{x\,|\ln x|^\nu}{s\mp ix}, \quad \nu = \frac{d}{m} - 1. \tag{3.40}$$

We use the relation $I_\pm(t=0) = \lim_{s\rightarrow\infty} sI_\pm(s)$ to obtain the initial amplitude

$$I_0 \equiv I_\pm(t=0) = \frac{d}{m}\left(\frac{1}{2}\right)^{\frac{d}{m}}\Gamma\left(\frac{d}{m}\right) \tag{3.41}$$

for an arbitrary ratio $\frac{d}{m}$. For parabolic confinement in two dimensions, $m = d = 2$. The integral in (3.40) can then be performed easily, which yields

$$I_\pm(s) = s\left[\log(s\mp i) - \log(s)\right] \pm i \quad (m = d = 2). \tag{3.42}$$

In dimensionless units $\frac{A_0}{2} = 1$, we find $A = \sum_k A_k \rightarrow \int dk A_k$, with the coupling constants A_k given in Eq. (3.9):

$$A = A_0 N\frac{d}{m}\Gamma\left(\frac{d}{m}\right) = 2N\frac{d}{m}\Gamma\left(\frac{d}{m}\right). \tag{3.43}$$

3.4 High field solution

In the next section, we will obtain a complete solution to the GME within the Born approximation. This complete solution will exhibit non-perturbative features (which can not be obtained from standard perturbation theory), in the weakly perturbative regime for the self-energy, which we define by $|\Delta| \lesssim 1$. Here, we find the leading behavior in the strongly perturbative (high magnetic field) limit, defined by $|\Delta| \ll 1$, or equivalently, $|b'| \gg N$. We do this in two ways. First, we apply standard perturbation theory, where we encounter known difficulties [15] (secular terms that grow unbounded in time). Second, we extract the leading-order spin dynamics from the non-Markovian remainder term in a Born-Markov approximation performed directly on the GME. We find that the secular terms are absent from the GME solution. We then give a brief description of the dependence of the spin decay on the form and dimensionality of the electron envelope wave function.

3.4.1 Perturbation theory

Applying standard time-dependent perturbation theory (see Appendix D) to lowest (second) order in $\mathcal{H}'_V$, performing the continuum limit, and expanding the result to leading order in $\frac{1}{\omega_n}$, we find

$$\begin{aligned} \langle S_+\rangle_t &= \sigma_+^{\mathrm{osc}}(t) + \sigma_+^{\mathrm{dec}}(t) + \sigma_+^{\mathrm{sec}}(t), && (3.44)\\ \langle S_z\rangle_t &= \overline{\langle S_z\rangle_\infty} + \sigma_z^{\mathrm{dec}}(t), && (3.45) \end{aligned}$$

where

$$\begin{aligned} \sigma_+^{\mathrm{osc}}(t) &= \left[1 - \delta I_0\left(c_+ + c_-\right)\right]\langle S_+\rangle_0\, e^{i\omega_n t}, && (3.46)\\ \sigma_+^{\mathrm{dec}}(t) &= \delta\left[C_+^+ I_-(t) + C_-^+ I_+(t)\right], && (3.47)\\ \sigma_+^{\mathrm{sec}}(t) &= i\Delta I_0\left(c_+ + c_-\right)\langle S_+\rangle_0\, t, && (3.48) \end{aligned}$$

and

$$\begin{aligned} \overline{\langle S_z\rangle_\infty} &= \left[1 - 2\delta I_0\left(c_+ + c_-\right)\right]\langle S_z\rangle_0 + 2pI\delta I_0, && (3.49)\\ \sigma_z^{\mathrm{dec}}(t) &= 2\delta\,\mathrm{Re}\left[e^{-i\omega_n t}\left(C_+^z I_-(t) + C_-^z I_+(t)\right)\right]. && (3.50) \end{aligned}$$

We have introduced the smallness parameter $\delta = \frac{N}{\omega_n^2}$ and the coefficients

$$C_\pm^X = \left\{ \begin{array}{c} c_\pm\left(\langle S_z\rangle_0 \pm \frac{1}{2}\right),\ X = z \\ c_\pm \langle S_+\rangle_0,\ X = +. \end{array} \right. \qquad (3.51)$$

$\langle S_z\rangle_t$ is the sum of a constant contribution $\overline{\langle S_z\rangle_\infty}$ and a contribution that decays to zero $\sigma_z^{\mathrm{dec}}(t)$ with initial amplitude $O(\delta)$. The transverse spin $\langle S_+\rangle_t$ is the sum of an oscillating component $\sigma_+^{\mathrm{osc}}(t)$, a decaying component $\sigma_+^{\mathrm{dec}}(t)$ with initial amplitude $O(\delta)$, and a secular term $\sigma_+^{\mathrm{sec}}(t)$, which grows unbounded (linearly) in time. At fourth order in $\mathcal{H}'_V$, $\langle S_z\rangle_t$ also contains a secular term. These difficulties, which have been reported previously [15, 17], suggest the need for a more refined approach. In the next subsection these problems will be resolved by working directly with the GME (in Born approximation) to find the correct leading-order spin dynamics for high magnetic fields.

3.4.2 Non-Markovian corrections

Markovian dynamics are commonly assumed in spin systems [124, 68], often leading to purely exponential relaxation and decoherence times T_1, and T_2, respectively. For this reason, it is important to understand the nature of corrections to the standard Born-Markov approximation, and, as will be demonstrated in Section 3.6 on measurement, there are situations where the non-Markovian dynamics are dominant and observable.

To apply the Born-Markov approximation to $\langle S_+\rangle_t$, we change variables $\left\langle S''_+\right\rangle_t = e^{-i(\omega_n+\widetilde{\omega})t}\langle S_+\rangle_t$ in (3.30) and substitute $\Sigma_{++}(t) \to \Sigma^{(2)}_{++}(t)$, which gives:

$$\left\langle \dot{S''_+}\right\rangle_t = -i\widetilde{\omega}\left\langle S''_+\right\rangle_t - i\int_0^t dt' e^{-i\omega(t-t')}\Sigma^{(2)}_{++}(t-t')\left\langle S''_+\right\rangle_{t'}, \tag{3.52}$$

where $\omega = \omega_n + \widetilde{\omega}$. We define the function $\psi(t) = \int_t^\infty dt' e^{-i\omega t'}\Sigma^{(2)}_{++}(t')$, so that $\psi(0) = \Sigma^{(2)}_{++}(s = i\omega)$. We find [126]

$$\left\langle \dot{S''_+}\right\rangle_t = -i\left(\psi(0)+\widetilde{\omega}\right)\left\langle S''_+\right\rangle_t + i\frac{d}{dt}\int_0^t dt'\psi(t-t')\left\langle S''_+\right\rangle_{t'}. \tag{3.53}$$

The frequency shift $\widetilde{\omega}$ is chosen to satisfy $\widetilde{\omega}{=}-\mathrm{Re}\left[\psi(0)\right]{=}-\mathrm{Re}\left[\Sigma^{(2)}_{++}\left(s = i\left(\omega_n+\widetilde{\omega}\right)\right)\right]$ to remove the oscillating part from $\langle S''\rangle_t$. When $|\omega| > 1$, and after performing the continuum limit, we find a *vanishing* decay rate $\Gamma = -\mathrm{Im}\left[\Sigma^{(2)}_{++}\left(s = i\omega\right)\right] = 0$, which shows that there is no decay in the Markovian solution for $|\omega| > 1$. After integrating the resulting equation, we have

$$\left\langle S''_+\right\rangle_t = \left\langle S''_+\right\rangle_0 + R_+(t). \tag{3.54}$$

The Markovian solution is given by $\left\langle S''_+\right\rangle_t = \left\langle S''_+\right\rangle_0$, and the remainder term $R_+(t) = i\int_0^t dt'\psi(t-t')\left\langle S''_+\right\rangle_{t'}$ gives the exact correction to the Markovian dynamics (within the Born approximation). We rewrite the remainder term as

$$R_+(t) = i\int_0^t dt'\psi(t-t')\left(\left\langle S''_+\right\rangle_0 + R_+(t')\right). \tag{3.55}$$

Within the Born approximation, $R_+(t)$ is associated with a smallness $O(\delta = \frac{N}{\omega_n^2})$ (since $\psi(t) \sim \Sigma^{(2)}_{++}(t)$), so the above expression can be iterated to evaluate the leading-order contribution to $R_+(t)$ in an asymptotic expansion for large ω_n. This gives

$$R_+(t) \sim -\delta I_0(c_+ + c_-)\langle S_+\rangle_0 + e^{-i\omega_n t}\sigma_+^{\mathrm{dec}}(t), \tag{3.56}$$

with $\sigma_+^{\mathrm{dec}}(t)$ given in Eq. (3.47).

Due to the inhomogeneous term $N_z(t)$ in (3.29), the $\langle S_z\rangle_t$ equation does not have a simple convolution form, so it is not clear if a Markov approximation for $\langle S_z\rangle_t$ is well-defined. However, applying the same procedure that was used on $\langle S_+\rangle_t$ to determine the deviation of $\langle S_z\rangle_t$ from its initial value gives the remainder $R_z(t)$, to leading order in $\frac{1}{\omega_n}$,

$$R_z(t) \sim -2\delta I_0\left(c_+ + c_-\right)\langle S_z\rangle_0 + 2pI\delta I_0 + \sigma_z^{\mathrm{dec}}(t). \tag{3.57}$$

Symbol	$A_0/2 = 1$, $\hbar = 1$	$A_0 = A/N$	$B_z = 0$
b'	$b - \epsilon_{nz}$	$g^* \mu_B B_z - g_I \mu_N B_z$	0
ω_n	$b' + 2pIN$	$b' + pIA$	pIA
Δ	N/ω_n	$A/2\omega_n$	$1/2pI$
δ	N/ω_n^2	$A^2/4N\omega_n^2$	$1/(2pI)^2 N$
c_+	$1 - f_\uparrow$	–	–
c_-	$f_\uparrow$	–	–
Ω_0	$\sqrt{\frac{N}{2}(c_+ + c_-)}$	$\frac{A}{\hbar\sqrt{8N}}$	$\frac{A}{\hbar\sqrt{8N}}$
$t_{\mathrm{hf}}/\tau_{\mathrm{hf}}$	1	$2N\hbar/A$	$2N\hbar/A$
$t_{\mathrm{c}}/\tau_{\mathrm{c}}$	$\frac{1}{\sqrt{N(1-p^2)}}$	$\frac{2\hbar}{A}\sqrt{\frac{N}{1-p^2}}$	$\frac{2\hbar}{A}\sqrt{\frac{N}{1-p^2}}$

Table 3.1: Some symbols used in the text. The second column gives the value in dimensionless units, the third column gives the value in dimension-full units assuming $A_0 = \frac{A}{N}$, and the fourth column gives the value of each symbol in zero magnetic field. The values shown are: the effective applied field b', the total effective field (applied field and Overhauser field) seen by the electron ω_n, the smallness parameter Δ, which determines the perturbative regime for electron spin dynamics, the smallness parameter δ, which bounds the deviation of the electron spin from a Markovian solution, the coefficients c_+ and c_-, in terms of the fraction of nuclear spins $I = \frac{1}{2}$ up in the initial state $f_\uparrow$, the electron spin precession frequency Ω_0 when the resonance condition $\omega_n = 0$ is satisfied, the time scale t_{hf} for the decay of the electron spin in the presence of an initial h_z eigenstate of the nuclear system, and the time scale t_{c} for the decay of the electron spin in the presence of an ensemble of initial nuclear spin states or a superposition of h_z eigenstates at zeroth order in the nuclear spin–electron spin flip-flop terms.

Here, $\sigma_z^{\mathrm{dec}}(t)$ is identical to the result from standard perturbation theory, given by Eq. (3.50).

Corrections to the Markov approximation can indeed be bounded for all times to a negligible value by making the parameter δ sufficiently small. However, the dynamics with amplitude $O(\delta)$ are completely neglected within a Markov approximation.

If we use $\langle S_z \rangle_t = \langle S_z \rangle_0 + R_z(t)$ and Eq. (3.54), and return to the rest frame for $\langle S_+ \rangle_t$, Eqs. (3.56) and (3.57) recover the high-field results from standard perturbation theory, given in Eqs. (3.44) and (3.45), with one crucial difference. The result from standard perturbation theory contains a secular term, which is absent in the current case. Thus, by performing an expansion of the self-energy instead of the spin operators directly, the contributions that led to an unphysical divergence in $\langle S_+ \rangle_t$ have been successfully resummed.

3.4.3 Dependence on the wave function

The purpose of this subsection is to evaluate the dependence of the non-Markovian dynamics on the form of the electron envelope wave function $\psi(r)$. The high-field dynamics, described by Eqs. (3.56) and (3.57), depend only on the integrals

	GaAs	Si:P
A	$90\,\mu eV$	$0.1\,\mu eV$
N	10^5	10^2
B_z	$7\,\mathrm{T}$	$0.1\,\mathrm{T}$
p	0	0
Δ	0.25	0.25
δ	10^{-6}	10^{-3}
Ω_0	$10^8\mathrm{s}^{-1}$	$10^7\mathrm{s}^{-1}$
τ_{hf}	$1\,\mu\mathrm{s}$	$1\,\mu\mathrm{s}$
τ_{c}	$5\,\mathrm{ns}$	$100\,\mathrm{ns}$

Table 3.2: Sample numerical values for the symbols listed in Table 3.1 for a GaAs quantum dot or an electron trapped at a donor impurity in natural Si:P.

$I_{\pm}(t)$. From Eq. (3.40) we find

$$I_{\pm}(t) = \frac{d}{m}\int_0^1 dx\,|\ln x|^{\nu}\,xe^{\pm ixt}, \quad \nu = \frac{d}{m} - 1. \tag{3.58}$$

The time scale τ_{hf} for the initial decay of $I_{\pm}(t)$ is given by the inverse bandwidth (range of integration) of the above integral. In dimension-full units, $\tau_{\mathrm{hf}} = \frac{2\hbar}{A_0}$. The long-time asymptotic behavior of $I_{\pm}(t)$ depends sensitively on the dimensionality d and the form of the envelope wave function through the ratio $\frac{d}{m}$. When $\frac{d}{m} < 2$, the major long time contribution to (3.58) comes from the upper limit $x \approx 1$ corresponding to nuclear spins near the origin, and the asymptotic form of $I_{\pm}(t)$ shows slow oscillations with period $\frac{4\pi\hbar}{A_0}$:

$$I_{\pm}(t \gg 1) \propto \left(\frac{1}{t}\right)^{\frac{d}{m}} e^{\pm it}, \quad \frac{d}{m} < 2. \tag{3.59}$$

When $\frac{d}{m} \geq 2$, the major contribution comes from the lower limit $x \approx 0$, i.e., nuclear spins far from the center, where the wave function is small. The resulting decay has a slowly-varying (non-oscillatory) envelope:

$$I_{\pm}(t \gg 1) \propto \frac{\ln^{\nu} t}{t^2}, \quad \nu = \frac{d}{m} - 1 \geq 1. \tag{3.60}$$

Both of the above cases can be realized in physical systems. For an electron with an s-type hydrogenic wave function bound, e.g., to a phosphorus donor impurity in Si, $m = 1$ and $d = 3$, which corresponds to the case in Eq. (3.60). For an electron trapped in a parabolic quantum dot, the envelope wave function is a Gaussian ($m = 2$) and for $d \leq 3$, the asymptotics of $I_{\pm}(t)$ are described by Eq. (3.59). These two cases are illustrated in Fig. 3.2, where $\mathrm{Re}\,[I_+(t)/I_0]$ is shown for $d = m = 2$ and $d = 3$, $m = 1$.

3.5 Non-Markovian dynamics

In this section we describe a *complete* calculation for the non-Markovian electron spin dynamics within the Born approximation. In the limit of a fully polarized

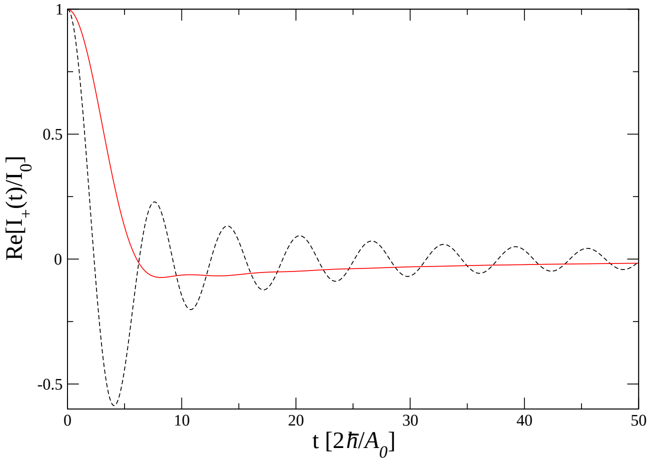

Figure 3.2: $\mathrm{Re}\,[I_+(t)/I_0]$ determined numerically from Eq. (3.58). For $d = 3$, $m = 1$ (solid line), this corresponds to a hydrogen-like s-type envelope wave function, and for $d = m = 2$ (dashed line), corresponding to a two-dimensional Gaussian envelope wave function. For the hydrogen-like wave function, nuclear spins far from the origin, with small coupling constants, are responsible for the slow (non-oscillatory) asymptotic behavior. In contrast, for the Gaussian envelope wave function nuclear spins near the center, with larger coupling constants, give rise to oscillations in the asymptotic behavior of $I_+(t)/I_0$.

initial state, our Born approximation applied to $\langle S_+\rangle_t$ recovers the exact solution of Ref. [15]. All results of this section are, however, valid for *arbitrary* polarization in high magnetic fields when the condition $|\Delta| \ll 1$ is satisfied. In addition, we find that the remainder term is bounded by the small parameter δ, $|R_X(t)| \leq O(\delta)$, and the stationary limit (long-time average) of the spin can be determined with the much weaker condition $\delta \ll 1$. In zero magnetic field, and for nuclear spin $I = \frac{1}{2}$, the relevant smallness parameter is $\delta = \frac{1}{p^2 N}$ (see Table 3.1).

We evaluate the Laplace transforms of (3.29), (3.30):

$$S_X(s) = \int_0^\infty dt e^{-st} \langle S_X\rangle_t\,, \quad \mathrm{Re}[s] > 0,\ X = z, +, \tag{3.61}$$

to convert the integro-differential equations into a pair of linear algebraic equations which can be solved to obtain

$$S_z(s) = \frac{\langle S_z\rangle_0 + N_z(s)}{s + i\Sigma_{zz}(s)}, \tag{3.62}$$

$$S_+(s) = \frac{\langle S_+\rangle_0}{s - i\omega_n + i\Sigma_{++}(s)}. \tag{3.63}$$

When the functions $N_z(s)$, $\Sigma_{zz}(s)$, $\Sigma_{++}(s)$ are known, the Laplace transforms in (3.62) and (3.63) can be inverted by evaluating the Bromwich contour integral:

$$\langle S_X\rangle_t = \frac{1}{2\pi i}\int_{\gamma - i\infty}^{\gamma + i\infty} ds\, \mathrm{e}^{st} S_X(s), \tag{3.64}$$

where all non-analyticities of $S_X(s)$ lie to the left of the line of integration. To simplify the calculation, here we specialize to the case of an electron confined to a two-dimensional parabolic quantum dot ($d = m = 2$), where the coupling constant integrals can be performed easily to obtain the explicit form for $I_\pm(s)$, given in Eq. (3.42).

Within the Born approximation, $S_z(s)$ has six branch points, located at $i\omega_n$, $i(\omega_n \pm 1)$, $-i\omega_n$, $-i(\omega_n \pm 1)$. We choose the principal branch for all logarithms, defined by $\log(z) = \ln|z| + i\arg(z)$, where $-\pi < \arg(z) \leq \pi$, in which case there are five poles in general. Three of these poles are located on the imaginary axis and two have finite negative real part. $S_+(s)$ has three branch points (at $s = 0, \pm i$), and three poles in general. One pole has finite negative real part and two are located on the imaginary axis.

Applying the residue theorem to the integral around the closed contour C shown in Fig. 3.3, $\frac{1}{2\pi i}\oint_C ds e^{st} S_X(s)$, gives

$$\langle S_X\rangle_t + \beta^X(t) = \sum_i P_i^X(t), \quad X = z, +, \tag{3.65}$$

where the pole contribution $P_i^X(t) = \mathrm{Res}\left[e^{st}S_X(s),\, s = s_i\right]$ is the residue from the pole at s_i, and the branch cut contributions are

$$\beta^z(t) = \sum_{\alpha=0,+,-} \frac{1}{\pi}\mathrm{Im}\left[e^{-i\omega_n t}K_\alpha^z(t)\right], \tag{3.66}$$

$$\beta^+(t) = \frac{1}{2\pi i}\sum_{\alpha=0,+,-} K_\alpha^+(t), \tag{3.67}$$

with branch cut integrals given by

$$K_\alpha^z(t) = \int_{C_\alpha} ds e^{st} S_z(s - i\omega_n), \tag{3.68}$$

$$K_\alpha^+(t) = \int_{C_\alpha} ds e^{st} S_+(s). \tag{3.69}$$

The contour C_α runs from $\gamma_\alpha - \infty + i\eta$, around γ_α, and back to $\gamma_\alpha - \infty - i\eta$, where $\eta \to 0^+$. The branch points are given by $\gamma_\alpha = \alpha i$, $\alpha = 0, +, -$, as illustrated in Fig. 3.3. In (3.66) we have used the fact that the branch cut integrals for $S_z(s)$ come in complex conjugate pairs, since $S_z(s^*) = [S_z(s)]^*$. This relationship follows directly from the definition for the Laplace transform of the real quantity $\langle S_z\rangle_t$.

Combining Eqs. (3.32), (3.34), (3.35), and (3.42) to obtain $\Sigma_{zz}^{(2)}(s - i\omega_n)$, and expanding in $\frac{1}{\omega_n}$ gives

$$\Sigma_{zz}^{(2)}(s - i\omega_n) = \Sigma_{++}^{(2)}(s) + \frac{\Delta}{4}(c_+ + c_-) + O(\delta), \tag{3.70}$$

where we recall $\Delta = \frac{N}{\omega_n}$ and $\delta = \frac{N}{\omega_n^2}$. The term $\frac{\Delta}{4}(c_+ + c_-)$ gives rise to a small shift in the effective magnetic field experienced by $\langle S_z\rangle_t$. To simplify the presentation, this shift is neglected, but it could easily be included by introducing

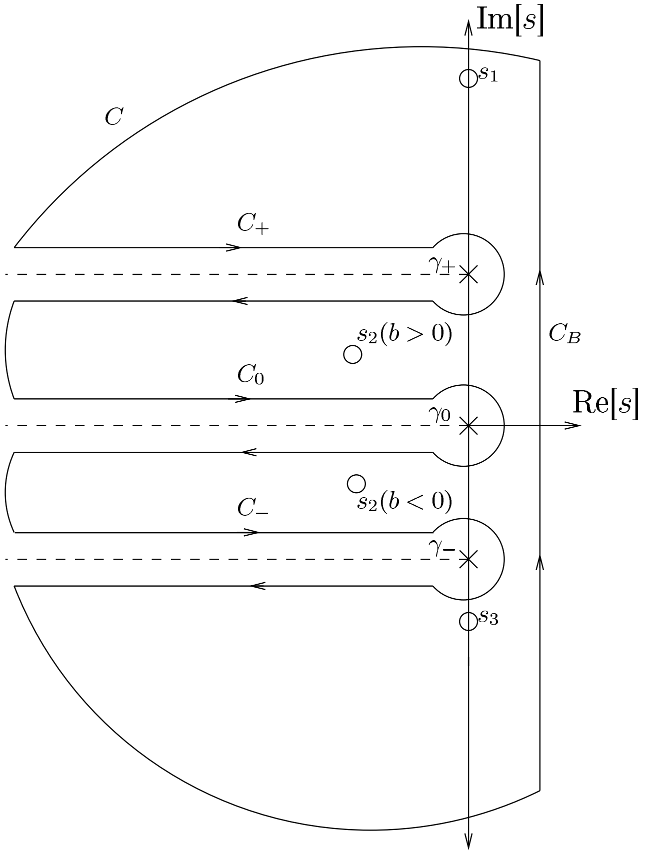

Figure 3.3: The closed contour C used for evaluation of the inverse Laplace transforms of $S_X(s)$, $X = z, +$. All non-analyticities of $1/D(s)$ are shown above, where $D(s)$ is given in Eq. (3.73). Branch cuts are indicated by dashed lines, branch points by crosses, and open circles mark pole positions. The contour C_α surrounds the branch cut extending from branch point $\gamma_\alpha = \alpha i$, $\alpha = 0, +, -$. When the arc that closes the contour in the negative-real half-plane is extended to infinity, C_B becomes the Bromwich contour. The pole at s_2 has finite real part and is present for $b \neq 0$. The poles at s_1 and s_3 are always located on the imaginary axis.

a slight difference in the denominators of $S_z(s)$ and $S_+(s)$. This gives

$$\begin{aligned} S_z(s - i\omega_n) &\simeq \frac{\langle S_z \rangle_0 + N_z^{(2)}(s - i\omega_n)}{D(s)}, && (3.71) \\ S_+(s) &= \frac{\langle S_+ \rangle_0}{D(s)}. && (3.72) \end{aligned}$$

The denominator $D(s) = s - i\omega_n + i\Sigma_{++}^{(2)}(s)$ and numerator $N_z^{(2)}(s - i\omega_n)$ are given explicitly by

$$D(s) = s - ib' + Ns\left[c_- \log(s - i) + c_+ \log(s + i) - (c_+ + c_-) \log(s)\right], \quad (3.73)$$

$$\begin{aligned} N_z^{(2)}(s - i\omega_n) = &-\frac{\Delta}{2}(c_+ + c_-) \\ &- i\Delta\frac{s}{2}\left[c_+ \log(s + i) - c_- \log(s - i) + (c_- - c_+) \log(s)\right] + O\left(\delta\right). \quad (3.74) \end{aligned}$$

The branch cuts and poles of $S_z(s - i\omega_n)$ and $S_+(s)$, as given in Eqs. (3.71) and (3.72), are shown in Fig. 3.3. We note that different analytic features will produce different types of dynamic behavior after the inversion integral has been evaluated. The branch cut contributions $\beta^X(t)$ have long-time tails that are non-exponential. Poles with finite negative real part will give rise to exponential decay. Poles on the imaginary axis away from the origin will lead to undamped oscillations, and a pole at the origin will give a constant residue, independent of time. The rest of this section is divided accordingly, describing each type of contribution to the total time evolution of $\langle S_X \rangle_t$.

3.5.1 Non-exponential decay

The contribution to $K_\alpha^X(t)$ circling each branch point γ_α is zero, so the branch cut integrals can be rewritten as

$$K_\alpha^X(t) = e^{\gamma_\alpha t} \int_0^\infty dx e^{-xt} \xi_X(x, \gamma_\alpha) \quad (3.75)$$

where

$$\xi_X(x, \gamma_\alpha) = \lim_{\eta \to 0^+} \left[S_X(s_\alpha^X(x) + i\eta) - S_X(s_\alpha^X(x) - i\eta)\right], \quad (3.76)$$

with

$$s_\alpha^X(x) = -x + \gamma_\alpha + \left\{ \begin{array}{c} -i\omega_n,\ X = z \\ 0,\ X = + \end{array} \right. . \quad (3.77)$$

The form of $K_\alpha^X(t)$ in Eq. (3.75) suggests a direct procedure for evaluating the long-time asymptotics of the branch cut contributions. For long times, the integrand of (3.75) is cut off exponentially at $x \sim \frac{1}{t} \to 0$. To find the asymptotic behavior, we find the leading x-dependence of $\xi_X(x, \gamma_\alpha)$ for $x \to 0^+$. We substitute this into (3.75), and find the first term in an asymptotic expansion of the remaining integral. The leading-order long-time asymptotics obtained in this way for all branch cut integrals $K_\alpha^X(t)$ are given explicitly in Appendix E. When $b' = 0$, the denominator $D(s) \to 0$ when $s \to 0$, and the dominant asymptotic behavior comes from $K_0^X(t\to\infty)\propto\frac{1}{\ln t}$. For $b'\neq 0$, $D(s)$ remains finite at the $s=0$ branch point and the dominant long-time contributions come from $K_\pm^X(t\to\infty)\propto\frac{1}{t\ln^2 t}$. In zero magnetic field, the leading-order term in the asymptotic expansion is dominant for times $t\gg 1$, but in a finite magnetic field, the leading term only dominates for times $t\gg e^{|b'|/N}$. In summary,

$$\begin{aligned}\beta^X(t\gg 1) &\propto \frac{1}{\ln t}, \qquad b'=0, && (3.78)\\ \beta^X(t\gg e^{|b'|/N}) &\propto \frac{1}{t\ln^2 t}, \qquad b'\neq 0. && (3.79)\end{aligned}$$

This is in agreement with the exact result [17] for a fully-polarized system of nuclear spins $I=\frac{1}{2}$ in a two-dimensional quantum dot. This inverse logarithmic time dependence cannot be obtained from the high-field solutions of Section 3.4. The method used here to evaluate the asymptotics of the Born approximation therefore represents a nontrivial extension of the exact solution to a nuclear spin system of reduced polarization, but with $|\Delta|<1$ (see Table 3.1).

The branch cut integrals can be evaluated for shorter times in a way that is asymptotically exact in a high magnetic field. To do this, we expand the integrand of Eq. (3.75) to leading nontrivial order in $\frac{1}{\omega_n}$, taking care to account for any singular contributions. For asymptotically large positive magnetic fields, we find (see Appendix E):

$$\sum_\alpha K_\alpha^X(t)\sim -i2\pi\delta\left(C_-^X I_+(t)+C_+^X I_-(t)\right)-\frac{C_-^X}{Nc_-^2}e^{-z_0 t} \qquad (3.80)$$

with coefficients $C_\pm^X$ given in (3.51) and in the above,

$$\begin{aligned}z_0 &= x_0-i\epsilon(x_0), && (3.81)\\ x_0 &= \frac{\omega_n}{2\pi Nc_-}, && (3.82)\\ \epsilon(x) &= \frac{x}{2\pi c_- N}+\frac{c_++c_-}{4\pi c_- x}. && (3.83)\end{aligned}$$

In high magnetic fields, we will show that the exponential contribution to Eq. (3.80) *cancels* with the contribution from the pole at s_2, $P_2^X(t)$. We stress that this result is only true in the high-field limit $\frac{|b'|}{N}\gg 1$, where the asymptotics are valid.

3.5.2 Exponential decay

When $b'=0$, there are no poles with finite real part. For $b'\neq 0$, a pole (at s_2 in Fig. 3.3) emerges from the branch point at $s=0$. The pole contribution $P_2^X(t)$ decays exponentially with rate $\Gamma_2=-\mathrm{Re}[s_2]$, and has an envelope that oscillates at a frequency determined by $\omega_2=\mathrm{Im}[s_2]$:

$$\begin{aligned}P_2^z(t) &= e^{-\Gamma_2 t}e^{-i(\omega_n-\omega_2)t}P_2^z(0) && (3.84)\\ P_2^+(t) &= e^{-\Gamma_2 t}e^{i\omega_2 t}P_2^+(0). && (3.85)\end{aligned}$$

Setting $s_2=-\Gamma_2+i\omega_2$, we find the decay rate Γ_2, frequency renormalization ω_2, and amplitudes of these pole contributions from asymptotic solutions to the

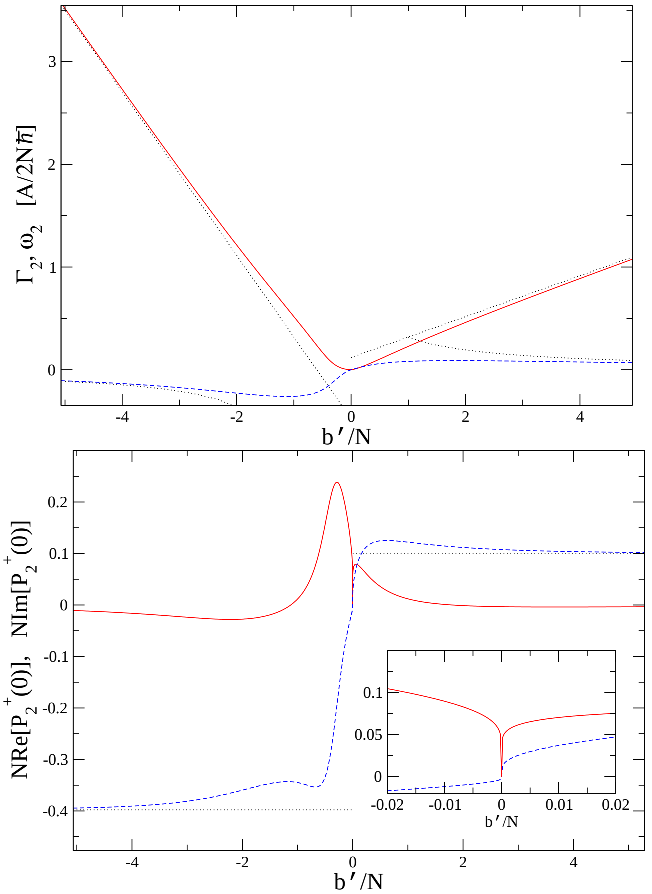

Figure 3.4: Top: numerically determined rate Γ_2 (solid line) and frequency renormalization ω_2 (dashed line) as a function of magnetic field b'/N. Bottom: $N\mathrm{Re}\left[P_2^+(0)\right]$ (solid line) and $N\mathrm{Im}\left[P_2^+(0)\right]$ (dashed line) as a function of magnetic field for the initial state $\langle S_+\rangle_0 = \langle S_x\rangle_0 = \frac{1}{2}$. The dotted lines give the asymptotics for high magnetic fields from Eqs. (3.86), (3.87), and (3.88). The parameters used were $p = 0.6$, $N = 10^5$, $I = \frac{1}{2}$.

pair of equations $\mathrm{Re}[D(s_2)] = \mathrm{Im}[D(s_2)] = 0$ and $P_2^X(0) = \mathrm{Res}[\mathrm{S_X(s)}, s = s_2]$ for high and low magnetic fields b'. Γ_2, ω_2, and $P_2^X(0)$ have the asymptotic field dependences (for high magnetic fields $b' \gg N$):

$$\Gamma_2 \sim \pm\frac{\omega_n}{2\pi N c_\mp}, \quad \omega_n \gtrless 0, \tag{3.86}$$

$$\omega_2 \sim \pm\frac{\Gamma_2}{2\pi c_\mp N} \pm \frac{c_+ + c_-}{4\pi c_\mp \Gamma_2}, \quad \omega_n \gtrless 0, \tag{3.87}$$

$$P_2^X(0) \sim \frac{C_\mp^X / c_\mp}{1 \mp i2\pi N c_\mp}, \quad \omega_n \gtrless 0. \tag{3.88}$$

Although it does not correspond to the perturbative regime, it is interesting to consider the behavior of the exponentially decaying pole contribution $P_2^X(t)$ in the limit $b' \to 0$, since the Hamiltonian $\mathcal{H}$ in Eq. (3.1) is known to be integrable for $B_z = 0$ ($b' = 0$) [67]. For vanishing positive magnetic fields ($b' \to 0^+$), with logarithmic corrections in $\frac{b'}{Eb_0}$, where $b_0 = N(c_+ + c_-)$ and $E = \exp\left\{1 + O\left(\frac{1}{N}\right)\right\}$:

$$\Gamma_2 \sim \frac{\zeta b'/b_0}{\ln^2\left(\frac{b'}{Eb_0}\right)}, \tag{3.89}$$

$$\omega_2 \sim -\frac{b'/b_0}{\ln\left(\frac{b'}{Eb_0}\right)}, \tag{3.90}$$

$$P_2^+(0) \sim -\frac{\langle S_+\rangle_0}{N(c_+ + c_-)\ln\left(\frac{b'}{b_0}\right)}, \tag{3.91}$$

$$P_2^z(0) \sim -\frac{\langle S_z\rangle_0 - (c_+ + c_-)/2pI}{N(c_+ + c_-)\ln\left(\frac{b'}{b_0}\right)}, \tag{3.92}$$

where $\zeta = \frac{\pi c_-}{c_+ + c_-}$. The exponentially decaying contribution vanishes only when $b' = 0$, and does so in an interval that is logarithmically narrow. We have determined the rate, frequency renormalization, and amplitude of the pole contribution $P_2^+(t)$ numerically. The results are given in Fig. 3.4 along with the above asymptotics for high magnetic fields, $|b'| \gg N$.

3.5.3 Undamped oscillations

The point s_1 in Fig. 3.3 corresponds to $s = 0$ for $S_z(s)$, so undamped oscillations in $\langle S_z\rangle_t$ arise only from the pole at s_3:

$$P_3^z(t) = e^{-i(\omega_n - \omega_3)t} P_3^z(0). \tag{3.93}$$

Both poles on the imaginary axis give undamped oscillations in $\langle S_+\rangle$:

$$P_1^+(t) + P_3^+(t) = e^{i\omega_1 t} P_1^+(0) + e^{i\omega_3 t} P_3^+(0). \tag{3.94}$$

For high magnetic fields, $|b'/N| \gg 1$,

$$\omega_{1/3} \sim b' + 2pIN = \omega_n, \quad b' \gtrless 0, \tag{3.95}$$

$$\omega_{3/1} \sim \mp 1 \mp f_\pm \exp\left(-\frac{|b'|}{c_\pm N}\right), \quad b' \gtrless 0, \tag{3.96}$$

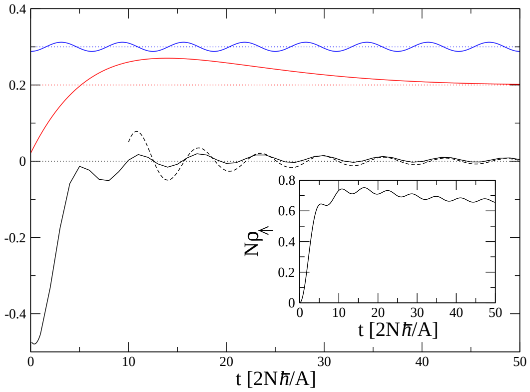

Figure 3.5: Contributions to the inverse Laplace transform of $\langle S_z \rangle_t$. We show the envelopes of the rapidly oscillating functions $2N\mathrm{Re}\left[P_3^z(t)\right] + 0.3$, $2N\mathrm{Re}\left[P_2^z(t)\right] + 0.2$, and $-N\beta^z(t)$, determined numerically. The long-time asymptotics of $\beta^z(t)$ from Appendix E are also shown (dashed line). The sum of all contributions is used to obtain the population of the spin-up state: $\rho_\uparrow(t) = \frac{1}{2} + \langle S_z \rangle_t$ (inset). The electron spin begins down: $\langle S_z \rangle_0 = -\frac{1}{2}$. Other parameters were $I = \frac{1}{2}$, $N = 10^5$, $b' = \frac{N}{2}$ (this value of b' gives, e.g., $B_z \simeq 1\mathrm{T}$ in GaAs), and $p = 0.6$. The time t is given in units of $\frac{2\hbar}{A_0} = \frac{2N\hbar}{A}$ for $d = m = 2$ in Eq. (3.43) ($\frac{2N\hbar}{A} \simeq 1\mu\mathrm{s}$ in GaAs). These values correspond to the weakly perturbative regime, with $\Delta = \frac{10}{11} < 1$. Note that $\rho_\uparrow(t) \lesssim \frac{1}{N}$ for all times.

where $f_\pm = \left(\frac{1}{2}\right)^{\left(\frac{c_\mp}{c_\pm}\right)}\left(1 + O\left(\frac{1}{N}\right)\right)$. The frequency in Eq. (3.95) corresponds to a simple precession of the electron spin in the sum of the magnetic and Overhauser fields. The second frequency, Eq. (3.96), describes the back-action of the electron spin, in response to the slow precession of the nuclear spins in the effective field of the electron.

For large b', the pole corresponding to simple precession is dominant, while the other has a residue that vanishes exponentially:

$$P_{1/3}^+(0) \sim \frac{\langle S_+ \rangle_0}{1 + \frac{1}{2}(c_+ + c_-)\delta}, \quad b' \gtrless 0, \tag{3.97}$$

$$P_{3/1}^+(0) \sim \frac{\langle S_+ \rangle_0}{N c_\pm} f_\pm \exp\left(-\frac{|b'|}{c_\pm N}\right), \quad b' \gtrless 0, \tag{3.98}$$

$$P_3^z(0) \sim \frac{b'}{2c_+ N} f_+ \exp\left(-\frac{|b'|}{c_+ N}\right), \quad b' > 0. \tag{3.99}$$

When the magnetic field b' compensates the nuclear Overhauser field $[h_z]_{nn}$ ($\omega_n \approx 0$, the usual ESR resonance condition in the rotating frame), the poles at points s_1 and s_3 have equal weight, and are the dominant contribution to the electron spin dynamics. Since the resonance condition corresponds to the strongly non-perturbative regime, $|\Delta| \gg 1$, we delay a detailed discussion of the resonance until Section 3.7.

3.5.4 Stationary limit

The contribution to $\langle S_z\rangle_t$ from the pole at $s = 0$ gives the long-time average value $\overline{\langle S_z\rangle}_\infty$, which we define as the stationary limit:

$$\overline{\langle S_z\rangle}_\infty = \lim_{T\to\infty} \frac{1}{T}\int_0^T \langle S_z\rangle_t \, dt = \lim_{s\to 0} sS_z(s). \tag{3.100}$$

Within the Born approximation, we find

$$\overline{\langle S_z\rangle}_\infty = \frac{\langle S_z\rangle_0 + pI\delta + O\left(\frac{N}{\omega_n^4}\right)}{1 + (c_+ + c_-)\delta + O\left(\frac{N}{\omega_n^4}\right)}. \tag{3.101}$$

The result in Eq. (3.101) follows from Eqs. (3.62), (3.31), (3.32), (3.34), (3.35), and (3.37) by expanding the numerator and denominator in $\frac{1}{\omega_n}$, using the coupling constants $A_k = 2e^{-k/N}$ and performing the continuum limit. $\overline{\langle S_z\rangle}_\infty$ gives the stationary level populations for spin-up and spin-down: $\bar\rho_{\uparrow/\downarrow} = \frac{1}{2} \pm \overline{\langle S_z\rangle}_\infty$, which would be fixed by the initial conditions in the absence of the hyperfine interaction. This difference in $\bar\rho_{\uparrow/\downarrow}$ from the initial values can be regarded as leakage due to the nuclear spin environment. We note that the stationary value depends on the initial value $\langle S_z\rangle_0$, from which it deviates only by a small amount of order δ. This means, in particular, that the system is non-ergodic. We will find that corrections to $\overline{\langle S_z\rangle}_\infty$ at fourth order in the flip-flop terms will be of order δ^2, so that the stationary limit can be determined even outside of the perturbative regime $|\Delta| < 1$, in zero magnetic field, where $\delta = \frac{1}{p^2N}$ for $I = \frac{1}{2}$, provided $p \gg \frac{1}{\sqrt{N}}$.

3.5.5 Summary

The results of this section for low magnetic fields are summarized in Fig. 3.5, which corresponds to the weakly perturbative case, $|\Delta| \lesssim 1$, and displays all of the dynamical features outlined here.

In very high magnetic fields ($b' \gg N$), corresponding to the strongly perturbative case, we combine Eqs. (3.80), (3.95), (3.97), and (3.101) to obtain the asymptotic forms to leading order in $\frac{1}{\omega_n}$:

$$\langle S_+\rangle_t \sim \sigma_+^{\mathrm{osc}}(t) + \sigma_+^{\mathrm{dec}}(t), \tag{3.102}$$

$$\langle S_z\rangle_t \sim \overline{\langle S_z\rangle}_\infty + \sigma_z^{\mathrm{dec}}(t), \tag{3.103}$$

where the functions $\sigma_+^{\mathrm{osc}}(t)$, $\sigma_+^{\mathrm{dec}}(t)$, $\overline{\langle S_z\rangle}_\infty$, $\sigma_z^{\mathrm{dec}}(t)$, given in Eqs. (3.46), (3.47), (3.49), and (3.50) are evaluated for $d = m = 2$. We stress that $\sigma_X^{\mathrm{dec}}(t) \propto \delta \ll 1$ is a small fraction of the total spin. The exponentially decaying contribution from $P_2^X(t)$ is *canceled* by the exponential part of the high-field branch cut, given in Eq. (3.80). This result is in agreement with the high-field asymptotic forms found earlier in Section 3.4. Numerical results for the level populations $\rho_{\uparrow/\downarrow}(t) = \frac{1}{2} \pm \langle S_z\rangle_t$ are given in Fig. 3.6 along with the above asymptotic forms. The secular term that appeared at lowest order in the standard perturbation expansion of $\langle S_+\rangle_t$ is again absent from the result obtained here via the GME. At fourth order, t-linear terms also appear in the standard perturbation expansion

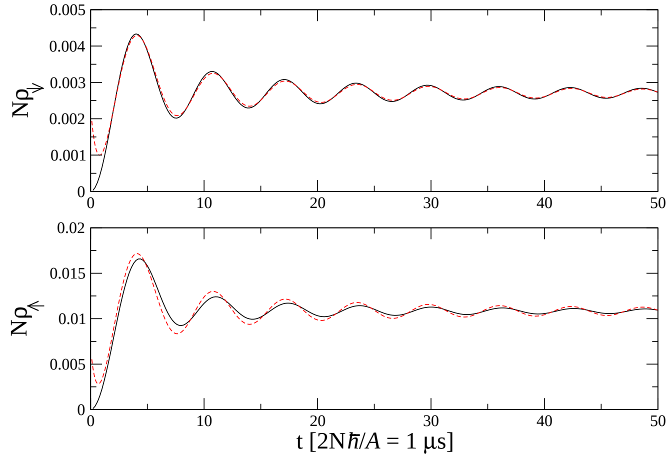

Figure 3.6: Envelope of the time-dependent spin level populations in high magnetic fields. We give results from numerical inversion of the Laplace transform (solid line) and the asymptotic branch cut integral for high magnetic fields combined with numerical results for the pole positions and residues (dashed line). Top: spin-down level population when the electron begins in the up state, along the nuclear spin polarization direction ($\langle S_z \rangle_0 = \frac{1}{2}$). Bottom: spin-up population for an electron that begins pointing in the opposite direction ($\langle S_z \rangle_0 = -\frac{1}{2}$). The parameters used were $N = 10^5$, $p = 0.6$, $I = \frac{1}{2}$ and $b' = 8N$, corresponding to a field of $B_z = 14\,\mathrm{T}$ in GaAs.

for the longitudinal spin $\langle S_z \rangle_t$ [15, 17]. Due to the numerator term $N_z(s)$ in the expression for $S_z(s)$ (Eq. (3.62)), it is not clear if all divergences have been resummed for $\langle S_z \rangle_t$ in the perturbative expansion of the self-energy. This question is addressed in Sec. 3.7 with an explicit calculation of the fourth-order spin dynamics.

In the next section we propose a method that could be used to probe the non-Markovian electron spin dynamics experimentally.

3.6 Measurement

In high magnetic fields ($b' \gg N$), the decaying fraction of the electron spin is very small $\left(O\left(\delta \approx \frac{N}{b'^2}\right)\right)$. Nevertheless, the large separation between the hyperfine interaction decay time ($\tau_{\mathrm{hf}} = \frac{2\hbar}{A_0} \approx 1\mu\mathrm{s}$) and the dipolar correlation time ($\tau_{\mathrm{dd}} \approx 100\,\mu\mathrm{s}$ in GaAs) of the nuclear spins should allow one to obtain valuable information about the electron spin decay from a conventional spin echo technique applied to an ensemble of electron spins.

In principle, the non-Markovian electron spin dynamics should be visible in the electron spin echo envelope obtained by applying the conventional Hahn echo sequence [87]: $\frac{\pi}{2} - \tau - \pi_x - \tau -$ECHO to a large ensemble of electron spins. This can be done by conventional means for an electron trapped at donor impurities in a solid [121], or from a measurement of transport current through a quantum dot [127, 128]. The effect of this echo sequence can be summarized as follows. The electron spins are initially aligned along the external magnetic field B_z. At time $t = 0$ the spins are tipped into the $x-y$ plane with an initial $\frac{\pi}{2}$-pulse. Each spin precesses in its own local effective magnetic field ω_n. The phase factor $e^{i\omega_n t}$ winds in the "forward" direction for a time τ. The sign of ω_n (direction of the local magnetic field) is then effectively reversed with a π-pulse along the x-axis: $\omega_n \rightarrow -\omega_n$. The phase factor $e^{-i\omega_n t}$ unwinds in the following time interval τ, and the electron spin magnetization refocuses to give an echo when the phase factor $e^{-i\omega_n 2\tau} = 1$ simultaneously for all spins in the ensemble. As is usually assumed, we take the pulse times and measurement time during the echo to be negligible [87]. The spin echo envelope gives the ensemble magnetization (the electron spin expectation value) at the time of the echo as a function of the free evolution time 2τ before the echo. We note that the decaying fraction of $\langle S_z \rangle_t$, $\sigma_z^{\mathrm{dec}}(t)$, also precesses with the phase factor $e^{i\omega_n t}$ (see Eq. (3.50)), so the same pulse sequence can also be applied to measure the decay of the longitudinal spin, omitting the initial $\frac{\pi}{2}$-pulse. The Hahn echo envelope should show a small initial decay by $O(\delta)$ in a time scale τ_{hf} due to the contact hyperfine interaction, followed by a slow decay due to spectral diffusion [68, 69, 129] with a time scale $\tau_{\mathrm{dd}} \approx 10^{-4}\,\mathrm{s}$. We note that a rapid initial decay of the Hahn echo envelope has been measured for natural $\mathrm{Si:P}$, but is absent in isotopically enriched $^{28}\mathrm{Si:P}$, in which no nuclei carry spin [130].

The fraction of the spin that decays in the time τ_{hf} is small, of order δ, in the perturbative regime. It may be difficult to detect this small fraction using the conventional Hahn echo. This problem can be reduced by taking advantage of the quantum Zeno effect, using the Carr-Purcell-Meiboom-Gill (CPMG) echo sequence $\frac{\pi}{2} - (\tau - \pi_x - \tau - \mathrm{ECHO} - \tau - \pi_{-x} - \tau - \mathrm{ECHO})_{\mathrm{repeat}}$. During each free evolution time between echoes, the electron decays by an amount of order δ. At each echo, a measurement of the electron spin magnetization is performed. For a large ensemble of electron spins, this measurement determines the state ρ_S of the electron spin ensemble, forcing the total system into a direct product of electron and nuclear states, as in Eq. (3.10). Repetition of such measurement cycles will then reveal the spin decay due to the hyperfine interaction (by order δ after each measurement) until the magnetization envelope reaches its stationary value. If the electron spin decays during the free evolution time due to spectral diffusion with a Gaussian envelope, then we require the condition $\left(\frac{2\tau}{\tau_{dd}}\right)^2 \ll \delta \ll 1$ for the effect of spectral diffusion to be negligible compared to the effect of the hyperfine interaction.[3] The non-Markovian remainder term gives the total change in electron spin that has occurred during the free evolution time 2τ: $R_X(2\tau)|_{e^{\pm i\omega_n 2\tau}=1} = \langle S_X \rangle_{2\tau} - \langle S_X \rangle_0 |_{e^{\pm i\omega_n 2\tau}=1} = M_X(2\tau) - M_X(0)$, where $M_X(t)$ is the CPMG magnetization envelope. In high magnetic fields, and when there are many echoes before the magnetization envelope decays, the CPMG

---

[3] Abe *et al.* [129] have recently measured a pure Gaussian decay of the Hahn spin echo envelope with time scale given by the dipolar correlation time $\tau_{\mathrm{dd}} \approx 10^{-4}\,\mathrm{s}$ for electrons trapped at phosphorus donors in isotopically enriched $^{29}\mathrm{Si:P}$, where all silicon nuclei carry spin $I = \frac{1}{2}$. In contrast to the CPMG echo sequence, only a single measurement (a single echo) is made following each preparation in the Hahn technique. We assume the echo envelope is the product of a Gaussian with time scale τ_{dd} and a part $f(2\tau) = 1 - O(\delta)$, $2\tau \gtrsim \tau_{\mathrm{hf}}$, that gives the decay due to the contact hyperfine interaction: $\exp\left[-\frac{1}{2}\left(\frac{2\tau}{\tau_{dd}}\right)^2\right] f(2\tau) \approx 1 - \frac{1}{2}\left(\frac{2\tau}{\tau_{dd}}\right)^2 - O(\delta)$, for times $\tau_{\mathrm{hf}} \lesssim 2\tau \ll \tau_{\mathrm{dd}}$. When $\left(\frac{2\tau}{\tau_{dd}}\right)^2 \ll \delta$, the dominant contribution comes from $f(2\tau)$ at each echo of the CPMG sequence.

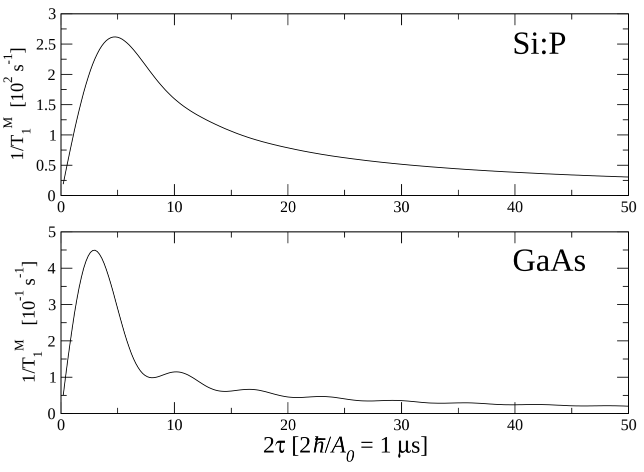

Figure 3.7: Longitudinal decay rate $\frac{1}{T_1^M}$ of the CPMG echo envelope as a function of the free evolution time 2τ between π-pulses for an electron trapped at a phosphorus donor impurity in Si:P (top) and in a two-dimensional GaAs quantum dot (bottom). The free evolution time is given in units of $\frac{2\hbar}{A_0} \approx \frac{2N\hbar}{A}$ (the equality is exact for $d = m = 2$ in Eq. (3.43)). In a GaAs quantum dot containing $N = 10^5$ nuclei or for an electron trapped at a shallow donor impurity in Si:P with $N = 100$ nuclear spins within one Bohr radius, $\frac{2N\hbar}{A} \approx 1\,\mu$s. We have used $I = \frac{1}{2}$, $p = 0.6$, and magnetic field values from Table 3.2 to determine the frequency units on the vertical axis.

magnetization envelopes $M_X(t)$ will therefore obey the differential equations

$$\frac{d}{dt}M_X(t) = \left.\frac{R_X(2\tau)}{2\tau}\right|_{\langle S_X\rangle_0 = M_X(t),\, e^{\pm i\omega_n 2\tau}=1}, \quad X = +, z, \tag{3.104}$$

where the high-field expressions for $R_X(t)$, given in Eqs. (3.56) and (3.57), should be used. Thus, the decay rate of the CPMG echo envelope M_X, as a function of the free evolution time 2τ, is a *direct probe* of the non-Markovian remainder term $R_X(t)$.

Since the magnetization envelopes $M_X(t)$ are found as the result of an ensemble measurement, it is necessary to perform an average over different nuclear initial states $|n\rangle$ that may enter into the solutions to Eq. (3.104). The local field-dependent phase factors have been removed by the echo sequence, so the only effect of the ensemble average is to average over $\delta = \frac{N}{\omega_n^2}$ and $c_\pm$, which appear in the overall amplitude of $\frac{d}{dt}M_X(t)$. The relative fluctuations in these quantities are always suppressed by the factor $\frac{1}{\sqrt{N}}$ for a large nuclear spin system.

In the high-field limit, we find the longitudinal and transverse magnetization envelopes $M_z(t)$ and $M_+(t)$ decay exponentially with time constants T_1^M and $T_2^M = 2T_1^M$, respectively. $M_+(t)$ decays to zero, and $M_z(t)$ decays to the limiting value

$$M_z(\infty) = \frac{1}{2}\frac{c_- - c_+}{c_- + c_+} = \frac{pI}{c_- + c_+}.$$

For nuclear spin $I = \frac{1}{2}$, $M_z(\infty) = \frac{p}{2}$, i.e., the electron magnetization acquires the polarization of the nuclear spin bath. However, since $c_\pm \propto I^2$, $M_z(\infty) \to 0$

in the large-spin limit. Thus, a *larger* fraction of the electron spin decays in the limit of large nuclear spin. We give plots of the longitudinal spin decay rate for $M_z(t)$, $\frac{1}{T_1^M}$, as a function of the free evolution time 2τ for two types of envelope wave function in Fig. 3.7. These plots have been determined by integrating Eq. (3.104) using the high-field expression for $R_z(t)$ given in Eq. (3.57). No ensemble averaging has been performed to generate these plots. When $2\tau \ll \tau_{\mathrm{hf}}$, the envelope decay rate increases as a function of 2τ as more of the electron spin is allowed to decay before each measurement. The rates reach a maximum at some time $2\tau \approx \tau_{\mathrm{hf}}$, and for $2\tau \gg \tau_{\mathrm{hf}}$, the electron spin saturates at its stationary value and the envelope decay rates $\propto \frac{1}{2\tau}$ are determined only by the free evolution time. Note that there are slow oscillations in the CPMG decay rate for an electron in a GaAs quantum dot, with a Gaussian wave function, but none for an electron trapped at a donor impurity in Si:P.

3.7 Beyond Born

The goal of this section is to address the range of validity of the results obtained in Sec. 3.5. First, we show that the Born approximation for $\langle S_+\rangle_t$ recovers the exact solution for $I = \frac{1}{2}$, $p = 1$. We then discuss the behavior of the Born approximation near the ESR resonance, where $\omega_n \approx 0$. Finally, we consider the expression for $\langle S_z\rangle_t$, obtained by including all fourth-order corrections to the reduced self-energy, and show that our expression is well-behaved in the continuum limit.

3.7.1 Recovery of the exact solution

When $I = \frac{1}{2}$ and $p = 1$, we have $c_- = 1$ and $c_+ = 0$, which gives $\Sigma_{++}^{(2)}(s) = -\frac{i}{4}\sum_k \frac{A_k^2}{s - i\frac{A_k}{2}}$ from Eq. (A.22). We insert this into (3.63) and use $\omega_n = b' + \frac{1}{2}\sum_k A_k = b' + \frac{A}{2}$ to obtain

$$S_+(s) = \frac{\langle S_+\rangle_0}{s - i\left(b' + \frac{A}{2}\right) + \frac{1}{4}\sum_k \frac{A_k^2}{s - iA_k/2}}. \tag{3.105}$$

The Schrödinger equation for a state of the form $|\psi(t)\rangle = \alpha_{\Uparrow}(t)\,|\Uparrow\uparrow\uparrow\cdots\rangle + \alpha_{\Downarrow}(t)\,|\Downarrow\uparrow\uparrow\cdots\rangle + \sum_k \beta_k(t)\,|\Uparrow\uparrow\cdots\downarrow_k\uparrow\cdots\rangle$, where the large arrow gives the state of the electron spin and the thin arrows give the states of the nuclear spins, has been written and solved (for a fully polarized nuclear spin initial state, $\beta_k(t=0) = 0\,\forall\, k$) in Laplace space to find the long-time asymptotic electron spin dynamics previously. In Ref. [17] the symbol $\alpha(t)$ was used in place of $\alpha_{\Downarrow}(t)$. The fully-polarized state $|\Uparrow\uparrow\uparrow\cdots\rangle$ is an eigenstate of the full Hamiltonian $\mathcal{H}'$, so $\alpha_{\Uparrow}(t) = e^{-\frac{i}{2}\left(b' + \frac{A}{2}\right)t}\alpha_{\Uparrow}(0)$, which allows us to write $S_+(s) = \alpha_{\Uparrow}^*(t = 0)\alpha_{\Downarrow}\left(s - \frac{i}{2}\left(b' + \frac{A}{2}\right)\right)$. We solve the time-dependent Schrödinger equation for $|\psi(t)\rangle$ in Laplace space, giving

$$\alpha_{\Downarrow}(s') = \frac{\alpha_{\Downarrow}(t = 0^+)}{s - i\left(b' + \frac{A}{2}\right) + \frac{1}{4}\sum_k \frac{A_k^2}{s - iA_k/2}}, \tag{3.106}$$

where $s' = s - \frac{i}{2}\left(b' + \frac{A}{2}\right)$. Thus, in the limit of full polarization of the nuclear system, the Born approximation applied to $\langle S_+\rangle_t$ becomes exact. For a

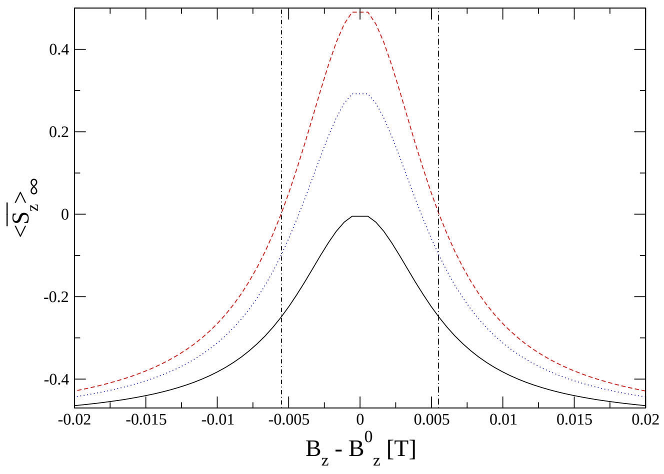

Figure 3.8: $\overline{\langle S_z\rangle}_\infty$ evaluated within Born approximation near the resonance, from Eq. (3.101) where $B_z^0 = -\frac{pA}{2g^*\mu_B}$. We have used the value of A for GaAs, $g^* = -0.44$, $N = 10^5$, and $I = \frac{1}{2}$. $\langle S_z\rangle_0 = -\frac{1}{2}$ for all three curves and results are given for $p = 0$ (solid line), $p = \frac{6}{10}$ (dotted line), and $p = 1$ (dashed line). The vertical dash-dotted lines indicate the magnetic fields where the relevant smallness parameter is unity: $|\delta| = 1$.

fully polarized nuclear spin system $\langle S_z\rangle_t$ is given by the relationship $\langle S_z\rangle_t = \frac{1}{2}\left(1 - 2\left|\alpha_\Downarrow(t)\right|\right) = \frac{1}{2}\left(1 - 2\left|\frac{\langle S_+\rangle_t}{\alpha^*_\Uparrow(t=0)}\right|^2\right)$. Unfortunately, this result is not recovered directly from the Born approximation for $\langle S_z\rangle_t$, as we will show in the next subsection.

3.7.2 Resonance

On resonance, $\omega_n = 0$, i.e., the external field b' compensates the Overhauser field $[h_z]_{nn}$. The resonance is well outside of the perturbative regime, defined by $|\Delta| = \left|\frac{N}{\omega_n}\right| < 1$, but we proceed in the hope that the Born approximation applied to the self-energy captures some of the correct behavior in the non-perturbative limit. On resonance, the major contributions to $\langle S_z\rangle_t$ come from three poles, at $s = 0$, $s = s_3$, and $s = s_3^*$:

$$\langle S_z\rangle_t \approx \overline{\langle S_z\rangle}_\infty + 2\mathrm{Re}\left[P_3^z(t)\right]. \tag{3.107}$$

Before applying the continuum limit, the stationary limit for $\langle S_z\rangle_t$ is

$$\overline{\langle S_z\rangle}_\infty = \frac{\langle S_z\rangle_0 + \frac{1}{4}\left(c_- - c_+\right)N_{\mathrm{tot}}}{1 + \frac{c_+ + c_-}{2}N_{\ \mathrm{tot}}}. \tag{3.108}$$

After applying the continuum limit, $N_{\mathrm{tot}} \to \infty$, we obtain

$$\overline{\langle S_z\rangle}_\infty = \frac{1}{2}\frac{c_- - c_+}{c_- + c_+} = \frac{pI}{c_- + c_+}. \tag{3.109}$$

For $I = \frac{1}{2}$, $\overline{\langle S_z \rangle_\infty} = \frac{p}{2}$, which appears to be an intuitive result. However, evaluating the remaining pole contributions at the resonance, we find, for a two-dimensional quantum dot,

$$2\mathrm{Re}\left[P_3(t)\right] = \left[\langle S_z \rangle_0 - \frac{2pI}{c_- + c_+}\right] \cos\left(\Omega_0 t\right) + O\left(\frac{1}{N}\right), \tag{3.110}$$

where

$$\Omega_0 = \sqrt{\frac{N}{2}\left(c_+ + c_-\right)}. \tag{3.111}$$

The results in (3.109) and (3.110) do not reproduce the exact solution in the limit $p = 1$, $I = \frac{1}{2}$, and do not recover the correct $t = 0$ value of $\langle S_z \rangle_t$. The Born approximation for $\langle S_z \rangle_t$, as it has been defined here, breaks down in the strongly non-perturbative limit, although the transverse components are better behaved.

On resonance, the poles at s_1 and s_3 are equidistant from the origin, and the major contributions to $\langle S_+ \rangle_t$ come from these two poles: $\langle S_+ \rangle_t \approx P_1(t) + P_3(t)$. Evaluating the residues at these poles,

$$\langle S_+ \rangle_t = \langle S_+ \rangle_0 \left(1 - O\left(\frac{1}{N}\right)\right) \cos\left(\Omega_0 t\right), \tag{3.112}$$

which suggests that a fraction $O\left(\frac{1}{N}\right)$ of the spin undergoes decay, and the rest precesses at a frequency Ω_0. When $I = \frac{1}{2}$, and in proper energy units we have $\Omega_0 = \frac{A}{\sqrt{8N}}$ from Eq. (3.111). While it does not violate positivity, as in the case of $\langle S_z \rangle_t$, this expression should not be taken seriously in general, since this result has been obtained well outside of the perturbative regime. The above does, however, recover the exact solution in the limit $p = 1$. We show the stationary limit of $\langle S_z \rangle_t$ in Fig. 3.8, using typical values for an electron confined to a GaAs quantum dot.

3.7.3 Fourth-order corrections

The fourth order expansion of the self-energy for $\langle S_z \rangle_t$ is given in Appendix A. The discrete expression for the numerator term $N_z^{(4)}(s)$ contains second order poles (secular terms). The fourth-order expression for $S_z(s)$ inherits these second order poles (see Eq. (3.62)). When the Laplace transform is inverted, this will result in pole contributions that grow linearly in time. However, when the continuum limit is performed, which is strictly valid for times shorter than $t \approx \sqrt{N}$ (see Appendix C), all poles in $N_z^{(4)}(s)$ are replaced by branch cuts. The integrals around the branch cuts can then be performed to obtain a solution for $\langle S_z \rangle_t$, valid for times $t \lesssim \sqrt{N}$.

All relevant non-analytic features (branch points and poles) of $S_z(s)$ occur in two regions of the complex plane: about the origin $s \approx 0$, and at high frequencies, around $s \approx \pm i\omega_n$. Inserting an initial nuclear state $|n\rangle$ for a large uniform system (see Appendix B), expanding the fourth-order self-energy to leading order in $\frac{1}{\omega_n}$ about the points $s = 0$ and $s = -i\omega_n$, performing the continuum limit, and evaluating the integrals over coupling constants, we obtain (where the overbar and "conj." indicate complex conjugate for s real):

$$N_z^{(4)}(s-i\omega_n) \simeq -\frac{\Delta^2}{2}\left\{c_+c_-\left[L_1(s)+L_2(s)-L_3(s)-\text{conj.}\right] \right. \\ \left. +c_+^2 L_1(s) - c_-^2 \bar{L}_1(s)\right\} \tag{3.113}$$

$$\Sigma_{zz}^{(4)}(s-i\omega_n) \simeq -N\Delta\left\{c_+c_-\left[L_1(s)+L_2(s)-L_3(s)+\text{conj.}\right] \right. \\ \left. +c_+^2 L_1(s) + c_-^2 \bar{L}_1(s)\right\} \tag{3.114}$$

$$N_z^{(4)}(s) \simeq \frac{\delta^2}{2}\left(c_+^2 - c_-^2\right)\left(\frac{3}{4} + s^2 L_4(s)\right) \tag{3.115}$$

$$\Sigma_{zz}^{(4)}(s) \simeq is\delta^2\left[3\left(pI\right)^2 + \left(c_+^2 + c_-^2 + 14c_+c_-\right)s^2 L_4(s)\right] \tag{3.116}$$

with coupling constant integrals $L_i(s)$ given by

$$L_1(s) = \frac{i}{2(s+i)} - \frac{1}{2}\left[\log(s+i) - \log(s)\right], \tag{3.117}$$

$$L_3(s) = \left[s\log(s+i) - s\log(s) - i\right]^2, \tag{3.118}$$

$$\tag{3.119}$$

$$L_4(s) = \frac{1}{6} - \frac{1}{6s}\left[s^3+3s+2i\right]\left[\log(s+i)-\log(s)\right] \\ - \frac{1}{6s}\left[s^3+3s-2i\right]\left[\log(s-i)-\log(s)\right], \tag{3.120}$$

and

$$L_2(s) = \log(s+i) - \log(s) - i\left[(s+i)\log(s+i) - (s+2i)\log(s+2i)\right. \\ \left. +s\log(s) - (s-i)\log(s-i)\right] + is\int_s^{s+i} du \frac{\log(2u-s-i) - \log(2u-s)}{u}. \tag{3.121}$$

Noting that $\lim_{s\to 0} s^2 L_4(s) = 0$, we find the corrections to the stationary limit for $\left\langle S_z\right\rangle_t$. At fourth order in the flip-flop terms, this gives

$$\overline{\left\langle S_z\right\rangle_\infty} = \frac{\left\langle S_z\right\rangle_0 + pI\delta + \frac{3}{8}\left(c_+^2 - c_-^2\right)\delta^2 + O\left(\frac{N}{\omega_n^4}\right)}{1 + (c_+ + c_-)\delta - 3(pI)^2\delta^2 + O\left(\frac{N}{\omega_n^4}\right)}. \tag{3.122}$$

The fourth-order corrections to the self-energy at high frequency ($s \approx -i\omega_n$) are suppressed relative to the Born approximation by an additional factor of the smallness parameter Δ, as expected from the analysis given in Appendix A. However, the low-frequency ($s \approx 0$) part of the fourth-order self-energy is suppressed by the much smaller parameter δ. This allows us to determine the stationary limit of $\left\langle S_z\right\rangle_t$ with confidence even when the magnetic field is small

	$\Sigma_S \simeq \Sigma_S^{(2)}$	$\Sigma_S \simeq \Sigma_S^{(2)}$	$\Sigma_S \simeq \Sigma_S^{(2)}$
	$b' = 0,$ $\frac{d}{m} = 1,$ $t \gg 1$	$b' \neq 0,$ $\frac{d}{m} = 1,$ $\Gamma_2^{-1} \gtrsim t \gg 1$	$b' \neq 0,$ $\frac{d}{m} = 1,$ $t \gg e^{\left\|b'\right\|/N} \gg \Gamma_2^{-1}$
$R_X(t) \propto$	$1/\ln t$	$e^{i\omega_2 t}e^{-\Gamma_2 t}$	$1/t\ln^2 t$

	$\Sigma_S \simeq \Sigma_S^{(2)} + \Sigma_S^{(4)}$	$\Sigma_S \simeq \Sigma_S^{(2)}$	$\Sigma_S \simeq \Sigma_S^{(2)}$
	$p \neq 1,$ $\frac{d}{m} = 1,$ $t \gg e^{\left\|b'\right\|/N}$, $b' \gg 2pIN$	$\|\Delta\| \ll 1,$ $\frac{d}{m} < 2,$ $t \gg 1$	$\|\Delta\| \ll 1,$ $\frac{d}{m} \geq 2,$ $t \gg 1$
$R_X(t) \propto$	$1/t\ln^3 t$, $X = z$	$(1/t)^{\frac{d}{m}} e^{\pm it}$	$\ln^\nu t/t^2, \quad \nu = \frac{d}{m} - 1$

Table 3.3: Results for the decaying fraction of the spin ($|R_X(t)| < O(\delta)\,\forall\, t$) in various parameter regimes. Results are given for both remainder terms $R_X(t)$, $X = z, +$, within the Born approximation for the self-energy $\Sigma_S \simeq \Sigma_S^{(2)}$ and for $R_z(t)$ at fourth order in the nuclear spin–electron spin flip-flop terms $\Sigma_S \simeq \Sigma_S^{(2)} + \Sigma_S^{(4)}$ when $p \neq 1$. The first three columns are exact in the limit of full polarization ($p = 1$) of the nuclear spin system, but still may describe the correct electron spin dynamics in the weakly perturbative regime, $|\Delta| \lesssim 1$. The last two columns give the correct electron spin dynamics in the strongly perturbative regime, $|\Delta| \ll 1$.

or zero, provided the polarization is sufficiently large. When $b' = 0$ and $I = \frac{1}{2}$, we have $\delta = \frac{1}{p^2 N}$, so the stationary limit can be determined whenever $p \gg \frac{1}{\sqrt{N}}$.

It is relatively straightforward to find the time-dependence as $t \to \infty$ for the S_z branch cut integrals at fourth order. Neglecting contributions from the branch cuts near $s \simeq 0$, which are suppressed by the factor δ^2, and when $p < 1$ so that the coefficient $c_+ \neq 0$ (c.f. Eq. (3.38)), we find the major contributions at long times come from the branch points at $s = \pm i$, where $L_2(s) \propto \log^2(s+i)$. For any magnetic field, we find:

$$R_z\left(t \to \infty\right) \propto \frac{1}{t\ln^3 t}. \tag{3.123}$$

For $b' \gg 2pIN$, this time-dependence will be dominant when $t \gg \exp\left(\frac{|b'|}{N}\right)$. Thus, we find that the fourth-order result has a faster long-time decay than the Born approximation, and that the associated asymptotics are valid at the same times as the Born approximation asymptotics (see Eq. (3.79)). Thus, higher-order corrections may change the character of the long-time decay in the weakly perturbative regime, where they are not negligible. In contrast, in the strongly perturbative regime $|\Delta| \ll 1$, the fourth- and higher-order terms are negligible, so the Born approximation dominates for all times $t < \exp\left(|b'|/N\right)$.

3.8 Conclusions

We have given a complete analytical description for the dynamics of an electron spin interacting with a nuclear spin environment via the Fermi contact hyperfine interaction. In a large magnetic field, our calculation applies to a nuclear spin system of arbitrary polarization p and arbitrary spin I, prepared in an eigenstate of the total z-component of the (quantum) nuclear Overhauser field. In the limit of full polarization $p = 1$ and nuclear spin $I = \frac{1}{2}$, the Born approximation applied to the self-energy recovers the exact dynamics for $\langle S_+ \rangle_t$ and $\langle S_z \rangle_t$, with all non-perturbative effects. We have shown explicitly that the dynamical behavior we calculate in Born approximation is purely non-Markovian, and can be obtained in the limit of high magnetic fields directly from the remainder term to a Born-Markov approximation. By performing our expansion on the self-energy superoperator, we have resummed secular divergences that are present in standard perturbation theory at lowest (second) order for the transverse components $\langle S_+ \rangle_t$ and at fourth and higher order for the longitudinal spin $\langle S_z \rangle_t$. For low magnetic fields $b' \lesssim N$, but still within the perturbative regime ($|\Delta| < 1$), the Born approximation for the electron spin shows rich dynamics including non-exponential (inverse logarithm) decay, exponential decay, and undamped oscillations. For high magnetic fields $b' \gg N$, and for $\frac{d}{m} < 2$, the electron spin shows a power-law decay ($\sim \left(\frac{1}{t}\right)^{\frac{d}{m}}$ in d-dimensions for an isotropic envelope wave function of the form $\psi(r) \propto \exp\left[-\frac{1}{2}\left(\frac{r}{l_0}\right)^m\right]$) to its stationary value with a time scale $\tau_{\mathrm{hf}} \approx \frac{2N\hbar}{A}$, in agreement with the exact solution for a fully-polarized nuclear spin system [15, 17]. Above a critical ratio, $\frac{d}{m} \geq 2$, the spin decay asymptotics undergo an abrupt change, signaled by a disappearance of slow oscillations in the decay envelope. We have summarized these results in Table 3.3. We have also suggested a method that could be used to probe the non-Markovian electron spin dynamics directly, using a standard spin-echo technique. We emphasize that the electron spin only decays by some small fraction of its initial value, of order δ (see Tables 3.1, 3.2), and the decay is generically non-exponential at long times (see Table 3.3). The results of this work may therefore be of central importance to the development of future quantum error correction schemes, which typically assume an exponential decay to zero. The fact that the stationary value of the spin depends on the initial value implies that this system is non-ergodic. Based on this observation, we postulate a general principle, that non-ergodic quantum systems can preserve phase-coherence to a higher degree than systems with ergodic behavior. It would be interesting to explore this connection further.

Chapter 4

Two-spin dynamics: Singlet-triplet correlations

[W. A. Coish and D. Loss Phys. Rev. B **72**, 125337 (2005)]

In this chapter we evaluate hyperfine-induced electron spin dynamics for two electrons confined to a double quantum dot. Our quantum solution accounts for decay of a singlet-triplet correlator even in the presence of a fully static nuclear spin system, with no ensemble averaging over initial conditions. In contrast to an earlier semiclassical calculation, which neglects the exchange interaction, we find that the singlet-triplet correlator shows a long-time saturation value that differs from 1/2, even in the presence of a strong magnetic field. Furthermore, we find that the form of the long-time decay undergoes a transition from a rapid Gaussian to a slow power law ($\sim 1/t^{3/2}$) when the exchange interaction becomes nonzero and the singlet-triplet correlator acquires a phase shift given by a universal (parameter independent) value of $3\pi/4$ at long times. The oscillation frequency and time-dependent phase shift of the singlet-triplet correlator can be used to perform a precision measurement of the exchange interaction and Overhauser field fluctuations in an experimentally accessible system. We also address the effect of orbital dephasing on singlet-triplet decoherence, and find that there is an optimal operating point where orbital dephasing becomes negligible.

4.1 Introduction

Decoherence due to the coupling of a qubit to its environment is widely regarded as the major obstacle to quantum computing and quantum information processing in solid-state systems. Electron spins confined in semiconductor quantum dots [1] couple to their environments primarily through the spin-orbit interaction and hyperfine interaction with nuclear spins in the surrounding lattice [14, 28]. To reach the next step in coherent electron spin state manipulation, the strongest decoherence effects in this system must be understood and reduced, if possible.

The effects of spin-orbit interaction are reduced in confined quantum dots at low temperatures [60]. Indeed, recent experiments give longitudinal relaxation times T_1 for quantum-dot-confined electrons that reach $T_1 \approx 20\,\mathrm{ms}$ [131] in self-assembled dots and $T_1 \approx 0.85\,\mathrm{ms}$ in gated dots [88], in agreement with theory [62]. These times suggest that the spin-orbit interaction is a relatively weak source of decoherence in these structures since theory predicts that the transverse spin decay time T_2 due to spin-orbit interaction alone (neglecting other sources of decoherence) would be given by $T_2 = 2T_1$ [62]. Other strategies for reducing the effects of spin-orbit interaction may include using hole (instead of electron) spin, where a recent study has found that $T_2 = 2T_1$ also applies, and the hole spin relaxation time can be made even longer than that for the electron spin [132].

Unlike the spin-orbit interaction, the hyperfine interaction of a single electron spin with a random nuclear spin environment can lead to pure dephasing, giving a transverse spin decay time on the order of $5\,\mathrm{ns}$ [15, 16, 70], six orders of magnitude shorter than the measured longitudinal decay times T_1. To minimize errors during qubit gating operations in these proposed devices, this decay must be fully understood. The hyperfine interaction in a single quantum dot is described by a Hamiltonian $H = \mathbf{h} \cdot \mathbf{S}$, where $\mathbf{S}$ is the electron spin operator and $\mathbf{h}$ is a collective quantum nuclear spin operator, which we will refer to as the "Overhauser operator". A common assumption in the literature is to replace the Overhauser operator by a classical effective magnetic field $\mathbf{h} \to \mathbf{B}_N$ [93, 16, 15, 66, 72, 81, 96, 82, 76, 21, 22, 133, 97]. Since a classical magnetic field only induces precession (not decoherence), the classical-field picture necessitates an ensemble of nuclear spin configurations to induce decay of the electron spin expectation value [15, 16]. For experiments performed on a large bulk sample of electron spins, or experiments performed over timescales that are longer than the typical timescale for variation of $\mathbf{B}_N$, the source of the ensemble averaging is clear. However, one conclusion of this model is that single-electron-spin experiments performed over a timescale shorter than the nuclear spin correlation time should show no decay. This conclusion is contradicted by numerical [18, 74] and analytical [123, 70] results, which show that the quantum nature of the Overhauser operator can lead to rapid decay of a single electron spin, even for a fully static nuclear spin system. This rapid decay is, however, reversible with a standard Hahn spin-echo sequence in an applied magnetic field and the timescale of the decay can be increased by squeezing the nuclear spin state [70].

Another potential solution to the hyperfine decoherence problem is to polarize the nuclear spins. Polarizing the nuclear spin system in zero applied magnetic field reduces the longitudinal spin-flip probability by the factor $1/p^2N$, where p is the nuclear spin polarization and N is the number of nuclear spins within the quantum dot [14, 70]. The effect on the transverse components of electron spin is different. Unless the nuclear spin state is squeezed or a spin-echo sequence is performed, the transverse components of electron spin will decay to zero in a time $t_c \approx 5\,\mathrm{ns}$ in a typical GaAs quantum dot. Polarizing the nuclear spin system increases t_c by reducing the phase-space available for fluctuations in the Overhauser operator, resulting in $t_c \approx 5\,\mathrm{ns}/\sqrt{1-p^2}$ [70]. Recent experiments show that the nuclear spin system can be polarized by as much as 60% [81]. However, to achieve an order-of-magnitude increase in t_c, the polarization degree would have to be on the order of 99% [28], for which more ambitious polarization schemes have been proposed [113].

If electron spins in quantum dots are to be used as quantum information processors, the two-electron states of double quantum dots must also be coherent during rapid two-qubit switching times.[1] Measurements of singlet-triplet relaxation times t_{ST} in vertical double dots ($t_{ST} \approx 200\,\mu\mathrm{s}$) [35], gated lateral double dots ($t_{ST} \approx 70\,\mu\mathrm{s}$) [83], and single dots ($t_{ST} \approx 2.58\,\mathrm{ms}$) [134] suggest that these states may be very long-lived. Recent experiments have now probed the decoherence time of such states, which is believed to be limited by the hyperfine interaction with surrounding nuclear spins [21]. The dramatic effect of the hyperfine interaction on two-electron states in a double quantum dot has previously been illustrated in experiments that show slow time-dependent current oscillations in transport current through a double dot in the spin blockade regime [20].

It may be possible to circumvent some of the complications associated with single-spin decoherence by considering an encoded qubit, composed of the two-dimensional subspace of states with total z-projection of spin equal to zero for two electrons in a double quantum dot [76]. One potential advantage of such a setup is that it may be possible to reduce the strength of hyperfine coupling to the encoded state space for a symmetric double-dot (see Appendix F). A potential disadvantage of this scheme is that coupling to the orbital (charge) degree of freedom can then lead to additional decoherence, but we find that orbital dephasing can be made negligible under appropriate conditions (see Section 4.4). To achieve control of the singlet-triplet subspace, however, the decoherence process for the two-electron system should be understood in detail.

In this chapter we give a fully quantum mechanical solution for the spin dynamics of a two-electron system coupled to a nuclear-spin environment via the hyperfine interaction in a double quantum dot. Although we focus our attention here on quantum dots, decoherence due to a spin bath is also an important problem for, e.g., proposals to use molecular magnets for quantum information processing [28,135,136,137]. In fact, the problem of a pair of electrons interacting with a bath of nuclear spins via the contact hyperfine interaction has been addressed long ago to describe spin-dependent reaction rates in radicals [93,138]. A semiclassical theory has been developed [93], in which electron spins in radicals experience a randomly oriented effective classical magnetic field due to the contact hyperfine interaction between electron and nuclear spins. In this semiclassical theory, random hopping events of the electrons were envisioned to induce a randomly fluctuating local magnetic field at the site of the electron spin, resulting in decay of a singlet-triplet correlator. Here, we solve a different problem. Ensemble averaging over nuclear spin configurations is natural for a large sample of $\sim 10^{23}$ radicals. In contrast, we consider the coherent dynamics of two-electron spin states within a single double quantum dot. More importantly, the Heisenberg exchange interaction, which was found to be negligible in Ref. [93], can be any value (large or small) in our system of interest. We find that a nonzero exchange interaction can lead to a drastic change in the form and timescale of decoherence. Moreover, this chapter is of direct relevance to very recent experiments [83, 21, 22] related to such double-dot systems.

The rest of this chapter is organized as follows. In Section 4.2 we solve the problem for electron spin dynamics in the subspace of total spin z-component

---

[1] For exchange gates with spin-1/2 qubits [1], the relevant requirement is that the qubit switching time t_S should be much smaller than the singlet-triplet decoherence time. [14]

$S^z = 0$ with an exact solution for the projected effective Hamiltonian. In Section 4.3 we show that a perturbative solution is possible for electron spin dynamics in the subspace of singlet and $S^z = +1$ triplet states. Section 4.4 contains a discussion of the contributions to singlet-triplet decoherence from orbital dephasing. In Section 4.5 we review our most important results. Technical details are given in Appendices F to H.

4.2 Dynamics in the $S^z = 0$ subspace

We consider two electrons confined to a double quantum dot, of the type considered, for example, in Refs. [83, 21, 22]. Each electron spin experiences a Zeeman splitting $\epsilon_z = g\mu_B B$ due to an applied magnetic field $\mathbf{B} = (0, 0, B)$, $B > 0$, defining the spin quantization axis z, which can be along or perpendicular to the quantum dot axis. In addition, each electron interacts with an independent quantum nuclear field $\mathbf{h}_l$, $l = 1, 2$, due to the contact hyperfine interaction with surrounding nuclear spins. The nuclear field experienced by an electron in orbital state l is $\mathbf{h}_l = \sum_k A_k^l \mathbf{I}_k$, where $\mathbf{I}_k$ is the nuclear spin operator for a nucleus of total spin I at lattice site k, and the hyperfine coupling constants are given by $A_k^l = vA \left|\psi_0^l(\mathbf{r}_k)\right|^2$, with v the volume of a unit cell containing one nuclear spin, A characterizes the hyperfine coupling strength, and $\psi_0^l(\mathbf{r}_k)$ is the single-particle envelope wavefunction for orbital state l, evaluated at site k. This problem simplifies considerably in a moderately large magnetic field ($B \gg \max\{\langle\delta\mathbf{h}\rangle_{\mathrm{rms}}/\mathrm{g}\mu_{\mathrm{B}}, \langle\mathbf{h}\rangle_{\mathrm{rms}}/\mathrm{g}\mu_{\mathrm{B}}\}$, where $\langle\mathcal{O}\rangle_{\mathrm{rms}} = \langle\psi_I|\,\mathcal{O}^2\,|\psi_I\rangle^{1/2}$ is the root-mean-square expectation value of the operator $\mathcal{O}$ with respect to the nuclear spin state $|\psi_I\rangle$, $\delta\mathbf{h} = \frac{1}{2}(\mathbf{h}_1 - \mathbf{h}_2)$, and $\mathbf{h} = \frac{1}{2}(\mathbf{h}_1 + \mathbf{h}_2)$). In a typical unpolarized GaAs quantum dot, this condition is $B \gg IA/\sqrt{N}g\mu_B \approx 10\,\mathrm{mT}$ (see Appendix F). For this estimate, we have used $IA/g\mu_{\mathrm{B}} \approx 5\,\mathrm{T}$, based on a sum over all three nuclear spin isotopes (all three hyperfine coupling constants) present in GaAs [27] and $N \approx 10^5$ nuclei within each quantum dot. In this section, we also require $B \gg J/g\mu_B$, where J is the Heisenberg exchange coupling between the two electron spins. For definiteness we take $J > 0$, but all results are valid for either sign of J, with J replaced by its absolute value. In the above limits, the electron Zeeman energy dominates all other energy scales and the relevant spin Hamiltonian becomes block-diagonal, with blocks labeled by the total spin projection along the magnetic field S^z (see Appendix G). In the subspace of $S^z = 0$ we write the projected two-electron spin Hamiltonian in the subspace of singlet and $S^z = 0$ triplet states ($|S\rangle, |T_0\rangle$) to zeroth order in the inverse Zeeman splitting $1/\epsilon_z$ as $H_0 = \frac{J}{2}\mathbf{S}\cdot\mathbf{S} + \delta h^z \delta S^z$, where $\mathbf{S} = \mathbf{S}_1 + \mathbf{S}_2$ is the total spin operator in the double dot and $\delta\mathbf{S} = \mathbf{S}_1 - \mathbf{S}_2$ is the spin difference operator. In terms of the vector of Pauli matrices $\boldsymbol{\tau} = (\tau^x, \tau^y, \tau^z)$: $|S\rangle \to |\tau^z = -1\rangle$, $|T_0\rangle \to |\tau^z = +1\rangle$ H_0 can be rewritten as:

$$H_0 = \frac{J}{2}(1 + \tau^z) + \delta h^z \tau^x. \tag{4.1}$$

Diagonalizing this two-dimensional Hamiltonian gives eigenvalues and eigenvectors

$$E_n^{\pm} = \frac{J}{2} \pm \frac{1}{2}\sqrt{J^2 + 4\left(\delta h_n^z\right)^2}, \tag{4.2}$$

$$\left|E_n^{\pm}\right\rangle = \frac{\delta h_n^z \left|S\right\rangle + E_n^{\pm}\left|T_0\right\rangle}{\sqrt{\left(E_n^{\pm}\right)^2 + \left(\delta h_n^z\right)^2}} \otimes \left|n\right\rangle, \tag{4.3}$$

where $|n\rangle$ is an eigenstate of the operator δh^z with eigenvalue δh_n^z. Since the eigenstates $|E_n^{\pm}\rangle$ are simultaneous eigenstates of the operator δh^z, we note that there will be no dynamics induced in the nuclear system under the Hamiltonian H_0. In other words, the nuclear system remains static under the influence of H_0 alone, and there is consequently no back action on the electron spin due to nuclear dynamics.

We fix the electron system in the singlet state $|S\rangle$ at time $t = 0$:

$$|\psi(t=0)\rangle = |S\rangle \otimes |\psi_I\rangle\,; \quad |\psi_I\rangle = \sum_n a_n \left|n\right\rangle, \tag{4.4}$$

where a_n is an arbitrary set of (normalized) coefficients ($\sum_n |a_n|^2 = 1$). The initial nuclear spin state $|\psi_I\rangle$ is, in general, not an eigenstate $|n\rangle$. The probability to find the electron spins in the state $|T_0\rangle$ at $t > 0$ is then given by the correlation function (setting $\hbar = 1$):

$$C_{T_0}(t) = \sum_n \rho_I(n) \left|\langle n| \otimes \langle T_0|\, e^{-iH_0 t}\, |S\rangle \otimes |n\rangle\right|^2, \tag{4.5}$$

where $\rho_I(n) = |a_n|^2$ gives the diagonal matrix elements of the nuclear-spin density operator, which describes a pure (not mixed) state of the nuclear system: $\rho_I = |\psi_I\rangle\langle\psi_I| = \sum_n \rho_I(n)\,|n\rangle\langle n| + \sum_{n\neq n'} a_n^* a_{n'}\,|n'\rangle\langle n|$. $C_{T_0}(t)$ is the sum of a time-independent piece $\overline{C_n}$ and an interference term $C_{T_0}^{\mathrm{int}}(t)$:

$$C_{T_0}(t) = \overline{C_n} + C_{T_0}^{\mathrm{int}}(t), \tag{4.6}$$

$$C_n = \frac{2\left(\delta h_n^z\right)^2}{J^2 + 4\left(\delta h_n^z\right)^2}, \tag{4.7}$$

$$C_{T_0}^{\mathrm{int}}(t) = -\overline{C_n \cos\left(\left[E_n^+ - E_n^-\right] t\right)}. \tag{4.8}$$

Here, the overbar is defined by $\overline{f(n)} = \sum_n \rho_I(n) f(n)$. Note that C_n depends only on the exchange and Overhauser field inhomogeneity δh_n^z through the ratio $\delta h_n^z / J$.

For a large number of nuclear spins $N \gg 1$ in a superposition of δh^z-eigenstates $|n\rangle$, we assume that $\rho_I(n)$ describes a continuous Gaussian distribution of δh_n^z values, with mean $\overline{\delta h_n^z} = 0$ (for the case $\overline{\delta h_n^z} \neq 0$, see Section 4.2.1) and variance $\sigma_0^2 = \overline{\left(\delta h_n^z - \overline{\delta h_n^z}\right)^2} = \overline{\left(\delta h_n^z\right)^2}$ (i.e. $\sigma_0 = \langle \delta h^z \rangle_{\mathrm{rms}}$). The approach to a Gaussian distribution in the limit of large N for a sufficiently randomized nuclear system is guaranteed by the central limit theorem [70]. The assumption of a continuous distribution of δh_n^z precludes any possibility of recurrence in the correlator we calculate.[2] A lower-bound for the Poincaré

---

[2] We recall that a superposition $f(t)$ of oscillating functions with different periods leads to quasiperiodic behavior, i.e., after the so-called Poincaré recurrence time t_p, the function $f(t)$ will return back arbitrarily close to its initial value (see, e.g., Ref. [126]).

recurrence time in this system is given by the inverse mean level spacing for the fully-polarized problem [15]: $t_\mathrm{p} \gtrsim N^2/A$. In a GaAs double quantum dot containing $N \simeq 10^5$ nuclear spins, this estimate gives $t_\mathrm{rec} \gtrsim 0.1\,\mathrm{s}$. Moreover, by performing the continuum limit, we restrict ourselves to the free-induction signal (without spin-echo). In fact, we remark that *all* decay in the correlator given by (4.8) can be recovered with a suitable π-pulse, defined by the unitary operation $U_\pi \left|E_n^\pm\right\rangle = \left|E_n^\mp\right\rangle$. This statement follows directly from the sequence

$$e^{-iJt}\left|E_n^\pm\right\rangle = U_\pi e^{-iH_0 t} U_\pi e^{-iH_0 t}\left|E_n^\pm\right\rangle. \tag{4.9}$$

Thus, under the above sequence of echoes and free induction, all eigenstates are recovered up to a common phase factor. Only higher-order corrections to the effective Hamiltonian H_0 may induce completely irreversible decay. This irreversible decay could be due, for example, to the variation in hyperfine coupling constants, leading to decay on a timescale $t \sim N/A$, as in the case of a single electron spin in Refs. [15,70]. Another source of decay is orbital dephasing (see Section 4.4).

We perform the continuum limit for the average of an arbitrary function $f(n)$ according to the prescription

$$\begin{aligned} \sum_n \rho_I(n) f(n) \quad &\rightarrow \quad \int dx P_{\sigma;\overline{x}}(x) f(n(x)), && (4.10)\\ P_{\sigma;\overline{x}}(x) \quad &= \quad \frac{1}{\sqrt{2\pi}\sigma}\exp\left(-\frac{(x-\overline{x})^2}{2\sigma^2}\right), && (4.11)\end{aligned}$$

with $\overline{x}=0$, $\sigma^2 = \overline{x^2}$, and here we take $x = \delta h_n^z$, $\sigma = \sigma_0$. Using

$$C_n = C(\delta h_n^z) = C(x) = \frac{2x^2}{J^2+4x^2}, \tag{4.12}$$

we evaluate $C_{T_0}^\mathrm{int}(t) = \mathrm{Re}\left[\tilde{C}_{T_0}^\mathrm{int}(t)\right]$, where the complex interference term is given by the integral

$$\tilde{C}_{T_0}^\mathrm{int}(t) \quad = \quad -\int_{-\infty}^{\infty} dx C(x) P_{\sigma_0;0}(x) e^{it\sqrt{J^2+4x^2}}. \tag{4.13}$$

In general, the interference term given by Eq. (4.13) will decay to zero after the singlet-triplet decoherence time. We note that the interference term decays *even* for a *purely static* nuclear spin configuration with no ensemble averaging performed over initial conditions, as is the case for an isolated electron spin [18,123,70]. The total z-component of the nuclear spins will be essentially static in any experiment performed over a timescale less than the nuclear spin diffusion time (the diffusion time is several seconds for nuclei surrounding donors in GaAs [139]). We stress that the relevant timescale in the present case is the spin diffusion time, and not the dipolar correlation time, since nonsecular corrections to the dipole-dipole interaction are strongly suppressed by the nuclear Zeeman energy in an applied magnetic field of a few Gauss [87] (as assumed here). Without preparation of the initial nuclear state or implementation of a spin-echo technique, this decoherence process therefore cannot be eliminated with fast measurement, and in general cannot be modeled by a classical nuclear field

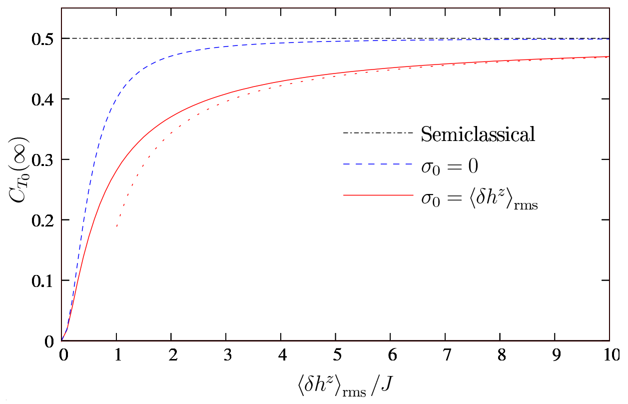

Figure 4.1: Saturation value of the triplet occupation probability $C_{T_0}(\infty) = \overline{C_n}$ vs. $\langle\delta h^z\rangle_{\mathrm{rms}}/J$ when the nuclear spin system has been squeezed into an eigenstate of δh^z (dashed line) and when the state of the nuclear spin system describes a Gaussian distribution of eigenvalues δh_n^z, with mean $\overline{\delta h_n^z} = 0$ and variance $\sigma_0^2 = \overline{(\delta h_n^z)^2}$ (solid line). We also show the analytical asymptotics for $\sigma_0 \gg J$, given by Eq. (4.15) (dotted line) and the semiclassical value ($C_{T_0}(\infty) = 1/2$) (dash-dotted line).

moving due to slow internal dynamics; a classical nuclear field that does not move cannot induce decay.

At times longer than the singlet-triplet decoherence time the interference term vanishes, leaving $C_{T_0}(\infty) = \overline{C_n}$, which depends only on the ratio $\delta h_n^z/J$, and could therefore be used to trace-out the slow adiabatic dynamics $\delta h_n^z(t)$ of the nuclear spins, or to measure the exchange coupling J when the size of the hyperfine field fluctuations is known. We evaluate $C_{T_0}(\infty)$ from

$$C_{T_0}(\infty) = \overline{C_n} = \int_{-\infty}^{\infty} dx C(x) P_{\sigma_0;0}(x). \tag{4.14}$$

In two limiting cases, we find the saturation value is given by (see Appendix H)

$$C_{T_0}(\infty) \sim \begin{cases} \frac{1}{2} - \sqrt{\frac{\pi}{2}}\frac{J}{4\sigma_0}, & \sigma_0 \gg J, \\ 2\left(\frac{\sigma_0}{J}\right)^2, & \sigma_0 \ll J. \end{cases} \tag{4.15}$$

We recover the semiclassical high-magnetic-field limit [93] ($C_{T_0}(\infty) = 1/2$) *only* when the exchange J is much smaller than σ_0. Furthermore, due to the average over δh_n^z eigenstates, the approach to the semiclassical value of $\frac{1}{2}$ is a slowly-varying (linear) function of the ratio J/σ_0, in spite of the fact that $C_n \propto (J/\delta h_n^z)^2$ as $J \to 0$. In Figure 4.1 we plot the correlator saturation value $C_{T_0}(\infty)$ as a function of the ratio $\langle\delta h^z\rangle_{\mathrm{rms}}/J$ for a nuclear spin system described by a fixed eigenstate of δh^z (i.e. $\rho_I = |n\rangle\langle n|$), and for a nuclear spin system that describes a Gaussian distribution of δh^z eigenstates with variance $\sigma_0^2 = \overline{(\delta h_n^z)^2} = \langle\delta h^z\rangle_{\mathrm{rms}}^2$. We also show the asymptotic expression for $\sigma_0 \gg J$, as given in Eq. (4.15).

Now we turn to the interference term $C_{T_0}^{\mathrm{int}}(t)$ given by Eq. (4.13), which can be evaluated explicitly in several interesting limits. First, in the limiting case of

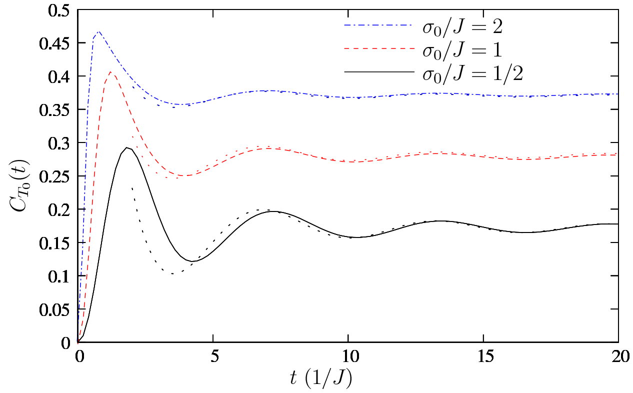

Figure 4.2: Decay of the correlator $C_{T_0}(t)$ evaluated by numerical integration of Eq. (4.13) for three ratios of σ_0/J: $\sigma_0/J = 2$ (dashed-dotted line), $\sigma_0/J = 1$ (dashed line), and $\sigma_0/J = 1/2$ (solid line). The analytical long-time asymptotic expressions from Eq. (4.17) are shown as dotted lines.

vanishing exchange ($J = 0$), we have $C(x) = \frac{1}{2}$ from (4.12). Direct integration of Eq. (4.13) then gives

$$C_{T_0}^{\text{int}}(t) = -\frac{1}{2}\exp\left(-\frac{t^2}{2t_0^2}\right), \quad t_0 = \frac{1}{2\sigma_0}, \quad J = 0. \tag{4.16}$$

For zero exchange interaction, the correlator decays purely as a Gaussian, with decoherence time $t_0 = \frac{1}{2\sigma_0} \approx \frac{\sqrt{N}}{IA}$ for a typical asymmetric double quantum dot (see Appendix F). However, for arbitrary nonzero exchange interaction $J \neq 0$, we find the asymptotic form of the correlator at long times is given by (see Appendix H):

$$C_{T_0}^{\text{int}}(t) \sim -\frac{\cos\left(Jt + \frac{3\pi}{4}\right)}{4\sigma_0\sqrt{J}t^{3/2}}, \quad t \gg \max\left(\frac{1}{J}, \frac{1}{2\sigma_0}, \frac{J}{4\sigma_0^2}\right). \tag{4.17}$$

Thus, for arbitrarily small exchange interaction J, the asymptotic decay law of the correlator is modified from the Gaussian behavior of Eq. (4.16) to a (much slower) power law ($\sim 1/t^{3/2}$). We also note that the long-time correlator has a universal phase shift of $\frac{3\pi}{4}$, which is independent of any microscopic parameters. Our calculation therefore provides an example of interesting non-Markovian decay in an experimentally accessible system. Furthermore, the slow-down of the asymptotic decay suggests that the exchange interaction can be used to modify the *form* of decay, in addition to the decoherence time, through a narrowing of the distribution of eigenstates (see the discussion following Eq. (4.19) below). We have evaluated the full correlator $C_{T_0}(t)$ by numerical integration of Eq. (4.13) and plotted the results in Figure 4.2 along with the analytical asymptotic forms from (4.17).

We now investigate the relevant singlet-triplet correlator $C_{T_0}(t)$ in the limit of large exchange J. In this case, we have $x \lesssim \sigma_0 \ll J$ for the typical x contributing to the integral in Eq. (4.13). Thus, we can expand the prefactor

$C(x)$ and frequency term in the integrand:

$$C(x) \approx 2\frac{x^2}{J^2}, \tag{4.18}$$

$$\sqrt{J^2+4x^2} \approx J + 2\frac{x^2}{J}. \tag{4.19}$$

From Eq. (4.19) it is evident that the range of frequencies that contribute to the correlator is suppressed by σ_0/J (increasing the exchange narrows the distribution of eigenenergies that can contribute to decay). This narrowing of the linewidth will increase the decoherence time. Moreover, the leading-order x^2-dependence in (4.19) collaborates with the Gaussian distribution of δh^z eigenstates to induce a power-law decay. With the approximations in Eqs. (4.18) and (4.19), we find an expression for the correlator that is valid for all times in the limit of large exchange J by direct evaluation of the integral in Eq. (4.13):

$$C_{T_0}^{\mathrm{int}}(t) = -2\left(\frac{\sigma_0}{J}\right)^2 \frac{\cos\left(Jt + \frac{3}{2}\arctan\left(\frac{t}{t_0'}\right)\right)}{\left(1+\left(\frac{t}{t_0'}\right)^2\right)^{3/4}}, \tag{4.20}$$

$$t_0' = \frac{J}{4\sigma_0^2},\ J \gg \sigma_0. \tag{4.21}$$

There is a new timescale ($t_0' = J/4\sigma_0^2$) that appears for large J due to dynamical narrowing; increasing the exchange J results in rapid precession of the pseudospin $\boldsymbol{\tau}$ about the z-axis, which makes transverse fluctuations along τ^x due to δh^z progressively unimportant. Explicitly, we have $t_0' \approx JN/4A^2 \gg \sqrt{N}/A$ for $J \gg \sigma_0 \approx A/\sqrt{N}$.

Eq. (4.20) provides a potentially useful means of extracting the relevant microscopic parameters from an experiment. J and σ_0 can be determined independent of each other exclusively from a measurement of the oscillation frequency and phase shift of $C_{T_0}^{\mathrm{int}}(t)$. In particular, any loss of oscillation amplitude (visibility) due to systematic error in the experiment can be ignored for the purposes of finding σ_0 and J. The loss in visibility can then be quantified by comparison with the amplitude expected from Eq. (4.20). We illustrate the two types of decay that occur for large and small J in Figure 4.3.

4.2.1 Inhomogeneous polarization, $\overline{\delta h_n^z} \neq 0$

It is possible that a nonequilibrium inhomogeneous average polarization could be generated in the nuclear spin system, in which case $\overline{\delta h_n^z} \neq 0$. Pumping of nuclear spin polarization occurs naturally, for example, at donor impurities in GaAs during electron spin resonance (ESR), resulting in a shift of the ESR resonance condition [140]. It is therefore important to investigate the effects of a nonzero average Overhauser field inhomogeneity on the decay law and timescale of the singlet-triplet correlator. In this subsection we generalize our previous results for the case $\overline{\delta h_n^z} \neq 0$.

We set the mean Overhauser field inhomogeneity to $\overline{\delta h_n^z} = x_0$, in which case the complex singlet-triplet interference term is given by

$$\tilde{C}_{T_0}^{\mathrm{int}}(t) = -\int_{-\infty}^{\infty} dx C(x) P_{\sigma_0;x_0}(x) e^{it\sqrt{J^2+4x^2}}. \tag{4.22}$$

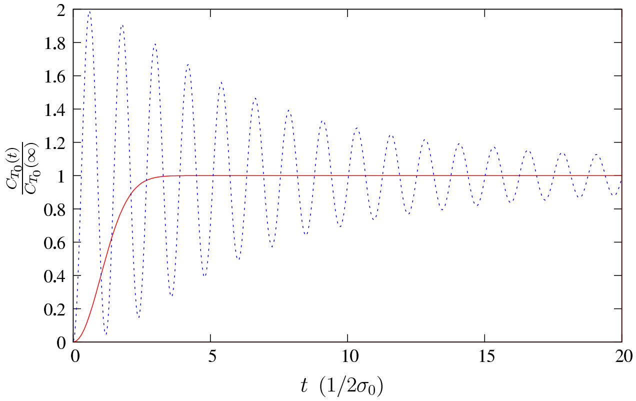

Figure 4.3: The correlator $C_{T_0}(t)/C_{T_0}(\infty)$ shows a rapid Gaussian decay when $J = 0$ (solid line, from Eq. (4.16)), but has a much slower power-law decay $\sim 1/t^{3/2}$ for large exchange $J = 10\sigma_0 \gg \sigma_0$ (dotted line, from Eq. (4.20)).

When the mean value of the Overhauser field inhomogeneity x_0 is much larger than the fluctuations σ_0 ($x_0 \gg \sigma_0$), we approximate $C(x) \approx C(x_0)$ and expand the frequency term $\sqrt{J^2 + 4x^2} = \omega_0 + \frac{4x_0}{\omega_0}(x - x_0) + \frac{2J^2}{\omega_0^3}(x - x_0)^2 + \cdots$, where $\omega_0 = \sqrt{J^2 + 4x_0^2}$. We retain only linear order in $x - x_0$ for the frequency term, which is strictly valid for times $t \ll (J^2 + 4x_0^2)^{3/2}/2J^2\sigma_0^2$. This time estimate is found by replacing $(x - x_0)^2 \approx \sigma_0^2$ in the quadratic term and demanding that the quadratic term multiplied by time be much less than one. In this limit, the correlator and range of validity are then

$$C^{\mathrm{int}}_{T_0}(t) = -\frac{2x_0^2}{\omega_0^2} e^{-\frac{1}{2}\left(\frac{t}{t_0''}\right)^2} \cos\left(\omega_0 t\right), \tag{4.23}$$

$$t_0'' = \frac{\omega_0}{4x_0\sigma_0}, \quad \omega_0 = \sqrt{J^2 + 4x_0^2}, \tag{4.24}$$

$$x_0 \gg \sigma_0, \quad t \ll \frac{\left(J^2 + 4x_0^2\right)^{3/2}}{2J^2\sigma_0^2}. \tag{4.25}$$

This expression is valid for any value of the exchange J, up to the timescale indicated.

In contrast with the previous result for $x_0 = 0$, from Eq. (4.23) we find that the long-time saturation value of the correlator deviates from the semiclassical result ($C_{T_0}(\infty) = -C^{\mathrm{int}}_{T_0}(0) = 1/2$) by an amount that is quadratic in the exchange J for $J \ll x_0$:

$$C_{T_0}(\infty) = C^{\mathrm{int}}_{T_0}(0) \sim \left\{ \begin{array}{c} \frac{1}{2} - \frac{1}{8}\left(\frac{J}{x_0}\right)^2, \ J \ll x_0, \\ 2\left(\frac{x_0}{J}\right)^2, \ J \gg x_0. \end{array} \right\}, \quad x_0 \gg \sigma_0. \tag{4.26}$$

In the limit of large exchange, $J \gg \max\left(\sigma_0, x_0\right)$, we can once again apply the approximations given in Eqs. (4.18) and (4.19). Using these approximations in Eq. (4.22) and integrating then gives

$$\tilde{C}^{\mathrm{int}}_{T_0}(t) = -2\left(\frac{\sigma_0}{J}\right)^2 \xi^3(t)\left(1+\left(\frac{x_0}{\sigma_0}\right)^2 \xi^2(t)\right) \times \exp\left\{iJt - \frac{x_0^2}{2\sigma_0^2}\left(1-\xi^2(t)\right)\right\}, \quad (4.27)$$

where

$$\xi(t) = \left(1 - i\frac{t}{t_0'}\right)^{-1/2}, \; t_0' = \frac{J}{4\sigma_0^2}, \quad J \gg \max(x_0,\sigma_0), \; t \ll \frac{J^3}{2\max\left(x_0^4,\sigma_0^4\right)}. \quad (4.28)$$

We have found the limit on the time range of validity in Eq. (4.27) using the same estimate that was used for Eqs. (4.23 – 4.25). At short times, $t \ll t_0' = J/4\sigma_0^2$, we expand $\xi^2(t) \approx 1 + i\frac{t}{t_0'} - \left(\frac{t}{t_0'}\right)^2$ and find that this function decays initially as a Gaussian with timescale $t_0'' \approx J/4x_0\sigma_0$:

$$C^{\mathrm{int}}_{T_0}(t) \sim -2\frac{\sigma_0^2+x_0^2}{J^2}e^{-\frac{1}{2}\left(\frac{t}{t_0''}\right)^2}\cos\left(\omega_0' t\right), \quad (4.29)$$

$$t_0'' \approx \frac{J}{4x_0\sigma_0}, \quad \omega_0' = J + \frac{2x_0^2}{J}, \quad (4.30)$$

$$t \ll t_0' = \frac{J}{4\sigma_0^2}, \quad J \gg \max(x_0,\sigma_0). \quad (4.31)$$

This agrees with the result in Eq. (4.23) when $J \gg x_0 \gg \sigma_0$.

For sufficiently large exchange J, the expression given by Eq. (4.27) is valid for times longer than the previous expression, given by Eq. (4.23). We perform an asymptotic expansion of Eq. (4.27) for long times using $\xi(t \gg t_0') \sim e^{i\pi/4}\sqrt{t_0'/t}$. This gives

$$C^{\mathrm{int}}_{T_0}(t) \sim -\frac{e^{-x_0^2/2\sigma_0^2}\cos(Jt+\frac{3\pi}{4})}{4\sigma_0\sqrt{J}t^{3/2}}, \quad (4.32)$$

$$t \gg t_0' = \frac{J}{4\sigma_0^2}, \quad J \gg \max(x_0,\sigma_0). \quad (4.33)$$

As in the case of $x_0 = 0$, the long-time asymptotics of Eq. (4.27) once again give a power law $\sim 1/t^{3/2}$, although the amplitude of the long-time decay is exponentially suppressed in the ratio x_0^2/σ_0^2. When $x_0 = 0$, Eq. (4.32) recovers the previous result, given in Eq. (4.17).

4.2.2 Reducing decoherence

The results of this section suggest a general strategy for increasing the amplitude of coherent oscillations between the singlet $|S\rangle$ and triplet $|T_0\rangle$ states, and for weakening the form of decay. To avoid a rapid Gaussian decay with a timescale $t_0'' = J/4x_0\sigma_0$, the mean Overhauser field inhomogeneity should be made smaller than the fluctuations ($\overline{\delta h_n^z} = x_0 \lesssim \sigma_0$) and the exchange J should be made larger than x_0 and σ_0 ($J \gg \max(x_0,\sigma_0)$). Explicitly, the ideal condition for slow and weak (power-law) decay can be written as

$$J \gg \sigma_0 \gtrsim x_0. \quad (4.34)$$

The condition in Eq. (4.34) can be achieved equally well by increasing the exchange coupling J for fixed hyperfine fluctuations σ_0 or by reducing the fluctuations σ_0 through state squeezing or by making the double-dot confining potential more symmetric (see Appendix F).

4.3 Dynamics in the subspace of $|S\rangle$ and $|T_+\rangle$

We now consider the case when the Zeeman energy of the $S^z = 1$ triplet state approximately compensates the exchange ($|\Delta| \ll J$, where $\Delta = \epsilon_z + J$). In addition, we assume the exchange is much larger than the nuclear field energy scales $J \gg \max\{\langle \delta\mathbf{h}\rangle_{\mathrm{rms}}, \langle \mathbf{h}\rangle_{\mathrm{rms}}\}$. Under these conditions, we consider the dynamics in a subspace formed by the singlet $|S\rangle \to |\tau^z = -1\rangle$ and the $S^z = 1$ triplet state $|T_+\rangle \to |\tau^z = +1\rangle$, governed by the Hamiltonian (to zeroth order in $1/J$, see Appendix G):

$$H_+ = \frac{1}{2}(\Delta + h^z)(1 + \tau^z) - \frac{1}{\sqrt{2}}\left(\delta h^- \tau^+ + \mathrm{H.c.}\right). \tag{4.35}$$

Here, $\delta h^\pm = \delta h^x \pm i\delta h^y$ and $\tau^\pm = \frac{1}{2}(\tau^x \pm i\tau^y)$. The $|T_+\rangle$ probability at time $t > 0$ is

$$C_{T_+}(t) = \sum_{n,n'} \rho_I(n) \left| \langle n'| \otimes \langle T_+| e^{-iH_+ t} |S\rangle \otimes |n\rangle \right|^2. \tag{4.36}$$

This case is essentially different from the previous one, since the eigenstates of H_+ are no longer simply product states of electron and nuclear spin, implying a back-action of the electron on the nuclear system. Nevertheless, when $\langle h^z + \Delta\rangle_{\mathrm{rms}} \gg \langle \delta\mathbf{h}^\pm\rangle_{\mathrm{rms}}$, we can evaluate the correlator in standard time-dependent perturbation theory to leading order in the term

$$V = -\frac{1}{\sqrt{2}}\left(\tau^+ \delta h^- + \tau^- \delta h^+\right). \tag{4.37}$$

Neglecting corrections of order $h_n^z/\Delta \ll 1$, this gives

$$C_{T_+}^{(2)}(t) \approx \overline{\frac{\alpha_n^2}{\Delta^2}\left(1 - \cos\left(\left[[h^z]_n + \Delta\right] t\right)\right)}, \tag{4.38}$$

where $\alpha_n = \sum_{n'} |\langle n'| \delta h^- |n\rangle|^2$, and $|n\rangle$ is now an eigenstate of the operator h^z with eigenvalue $[h^z]_n$. To estimate the size of α_n, we assume identical completely decoupled dots and nuclear polarization $p \ll 1$, which gives $\alpha_n^2 \approx \frac{1}{2} I(I+1) \sum_k A_k^2$, where A_k is the hyperfine coupling constant to the nuclear spin at lattice site k (with total nuclear spin I) and the sum $\sum_k$ runs over all lattice sites in one of the dots. We estimate the typical size of α_n with the replacements $A_k \to \frac{A}{N}$, $\sum_k \to N$, which gives $\alpha_n \approx \alpha/\sqrt{2} = \sqrt{\frac{I(I+1)}{2N}}A$, where N characterizes the number of nuclear spins within the dot envelope wavefunction. If we assume the nuclear spin state is described by a continuous Gaussian distribution of h^z eigenstates with mean $\overline{h_n^z} = 0$ and variance σ_+^2, we find

$$C_{T_+}^{(2)}(t) \approx \frac{1}{2}\left(\frac{\alpha}{\Delta}\right)^2 \left(1 - e^{-t^2/2t_+^2} \cos(\Delta t)\right), \quad t_+ = \frac{1}{2\sigma_+}. \tag{4.39}$$

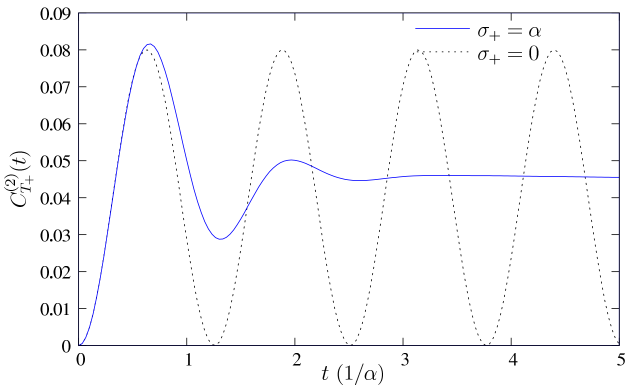

Figure 4.4: Decay of the correlator $C_{T_+}(t)$ in two cases. A typical unprepared initial state, where the nuclear spin system is in a superposition of h^z eigenstates, results in a Gaussian decay (solid line, from Eq. (4.39)). If the nuclear spin state is squeezed into an h^z eigenstate, there is no decay, only coherent oscillations (dotted line, from Eq. (4.38)). For this plot we have used $\Delta = 5\alpha$.

Thus, if we ignore any possibility for recurrence, the distribution of h^z eigenstates will lead to Gaussian decay of the two-electron spin state, as is the case for a single electron [18, 70]. However, as in the case of a single electron, this decay can be reduced or eliminated altogether by narrowing the distribution of h^z eigenstates $|n\rangle$ through measurement (squeezing the nuclear spin state) [70]. We show these two cases (with and without squeezing of the nuclear state) in Figure 4.4.

4.4 Singlet-triplet decoherence due to orbital dephasing

To this point we have neglected dephasing of the singlet $|S\rangle$ and triplet $|T_j\rangle$ $(j = 0, +)$ states due to coupling in the orbital sector. The effective Hamiltonian description ignores the different character of the orbital states for singlet and triplet, and so it is tempting to assume that orbital dephasing is unimportant where the effective Hamiltonian is valid. However, the singlet and triplet do have different orbital states which can, in general, couple differently to the environment through the charge degree of freedom, and therefore acquire different phases. Examples of such environmental influences are charge fluctuators or measurement devices, such as quantum point contacts used for charge readout [141, 88]. Here we briefly step away from the effective Hamiltonians derived in Appendix G to give a physical picture of the effects of orbital dephasing in terms of the true double-dot wavefunctions. We then return to the effective Hamiltonian picture in order to give a more general estimate of the effects of orbital dephasing on singlet-triplet decoherence for a two-electron double dot.

We consider a double quantum dot containing a fixed (quantized) number of electrons N. Within the far-field approximation, the double-dot charge distribution couples to the environment first through a monopole, and then a dipole term. Since the charge on the double dot is quantized, the monopole term gives an equal contribution for both the singlet and triplet wavefunctions. The leading interaction that can distinguish singlet from triplet is the electric dipole term:

$$V_{\mathrm{orb}}(t) \approx -\mathbf{p}_N \cdot \mathbf{E}(t). \tag{4.40}$$

Here, $\mathbf{p}_N$ is the electric dipole moment operator for the charge distribution in a double dot containing N electrons and $\mathbf{E}(t)$ is a fluctuating electric field due to the surrounding environment, which we model by a Gaussian random process. For a double quantum dot with well-localized single-particle eigenstates we denote the charge states by $|(n,m)\rangle$, indicating that the double-dot has n electrons in dot 1 and m electrons in dot 2, where $n+m=N$. If the double dot contains only a single electron ($N=1$), the environment can distinguish the two localized states through the difference in the dipole moment operator, which has the size $|\Delta\mathbf{p}_1| = |\langle(1,0)|\,\mathbf{p}_1\,|(1,0)\rangle - \langle(0,1)|\,\mathbf{p}_1\,|(0,1)\rangle| \approx 2\,|e|\,a$, where e is the electron charge and $2a$ is the inter-dot spacing. When $N=2$, for highly-localized states, only the states with double-occupancy ($|(0,2)\rangle$ and $|(2,0)\rangle$) contribute to the dipole moment. If the typical hyperfine energy scale is much smaller than the detuning from resonance δ of the $|(1,1)\rangle$ and $|(0,2)\rangle$ states ($\max\left(\langle\delta\mathbf{h}\rangle_{\mathrm{rms}}, \langle\mathbf{h}\rangle_{\mathrm{rms}}\right) \ll \delta$), only the $|(1,1)\rangle$ singlet state (not the triplets) will mix with the doubly-occupied states, so the singlet and triplet states will be energetically distinguishable through $|\Delta\mathbf{p}_2| = |\langle S|\,\mathbf{p}_2\,|S\rangle| \approx 2\,|e|\,a\left|P_{(0,2)} - P_{(2,0)}\right| \lesssim 2\,|e|\,aD$, where $P_{(0,2)}$ $\left(P_{(2,0)}\right)$ is the probability to find the singlet $|S\rangle$ in the $|(0,2)\rangle$ ($|(2,0)\rangle$) state and $D = P_{(0,2)} + P_{(2,0)}$ is the double occupancy. In this discussion, we assume that the exchange is much larger than the hyperfine energy scales, $J \gg \max\left(\langle\mathbf{h}\rangle_{\mathrm{rms}}, \langle\delta\mathbf{h}\rangle_{\mathrm{rms}}\right)$, so that the singlet and triplet states are good approximates for the true two-electron eigenstates.

For weak coupling to the environment, and assuming the environment correlation time is much less than the orbital dephasing time $t_\phi^{(N)}$, we can apply standard techniques to determine the dephasing time for a two-level system described by the Bloch equations [142]. We find that the fluctuations in $\mathbf{E}(t)$ lead to exponential dephasing with the rate $1/t_\phi^{(N)} = \frac{1}{4}\left|\Delta\mathbf{p}_N\right|^2 \int_{-\infty}^{\infty} dt E(t)E(0)$, where the scalar $E(t)$ is the component of $\mathbf{E}(t)$ along $\Delta\mathbf{p}_N$ and we assume $\lim_{t\to\infty}\frac{1}{t}\int_0^t dt' E(t') = 0$. Assuming equivalent environments for the single-particle and two-particle cases, the ratio of the single-particle to two-particle dephasing times is then

$$\frac{t_\phi^{(1)}}{t_\phi^{(2)}} = \left|\frac{\Delta\mathbf{p}_2}{\Delta\mathbf{p}_1}\right|^2 \lesssim D^2. \tag{4.41}$$

The single-electron orbital dephasing rate has been measured to be $t_\phi^{(1)} \approx 1\,\mathrm{ns}$ [143] and $t_\phi^{(1)} \approx 400\,\mathrm{ps}$ [56] in different gated double quantum dots. If the hyperfine interaction (which becomes important on the timescale $t \gtrsim 5\,\mathrm{ns}$) is to provide the major source of decoherence in these two-electron structures, we therefore require $t_\phi^{(2)} \gg t_\phi^{(1)}$. This condition can be achieved by ensuring a small double occupancy $D \ll 1$ of the singlet state. When the inter-dot tunnel coupling t_{12} is much less than the detuning from resonance δ ($t_{12} \ll \delta \ll U+U'$, with on-site and nearest-neighbor charging energies U and U', respectively – see

Appendix G) we find the double-occupancy of $|S\rangle$ in perturbation theory is

$$D \approx 2\left(\frac{t_{12}}{\delta}\right)^2 \ll 1. \tag{4.42}$$

Even in this regime, orbital dephasing may become the limiting timescale for singlet-triplet decoherence after the removal of hyperfine-induced decoherence by spin echo. A detailed analysis of the double-occupancy and its relation to the concurrence (an entanglement measure) for a symmetric double dot can be found in Refs. [110, 39].

With this physical picture in mind, we can generalize the above results to the case when the electrons experience fluctuations due to any time-dependent classical fields. In particular, if the separation in single-particle energy eigenstates for $N = 1$ is $\epsilon + \delta\epsilon(t)$, where $\delta\epsilon(t)$ fluctuates randomly with amplitude $\delta\epsilon$, and similarly, if for $N = 2$ the singlet and triplet levels are separated by an exchange $J + \delta J(t)$, where $\delta J(t)$ has amplitude δJ, we find

$$\frac{t_\phi^{(1)}}{t_\phi^{(2)}} = \left|\frac{\delta J}{\delta\epsilon}\right|^2. \tag{4.43}$$

From this expression we conclude that the optimal operating point of the double dot is where the slope of J vs. ϵ vanishes, i.e., $\delta J/\delta\epsilon = 0$. At this optimal point, $t_\phi^{(2)} \to \infty$, within the approximations we have made. Eq. (4.43) is valid for weak coupling to the environment (i.e. $\delta J \ll J$ and $\delta\epsilon \ll \epsilon$), and when the environment correlation time is small compared to the dephasing times. If, for example, we take $J \approx 2t_{12}^2/\delta$ for $U + U' \gg \delta \gg t_{12}$ from Eq. (G.11) and if $\delta\epsilon$ corresponds to fluctuations in the single-particle charging energy difference ($\epsilon \sim (V_{g1} - V_{g2}) \sim \delta$ from Eq. (G.9)), we find $t_\phi^{(1)}/t_\phi^{(2)} \approx 4t_{12}^4/\delta^4$, in agreement with Eqs. (4.41) and (4.42). In particular, the hyperfine-dominated singlet-triplet decoherence becomes visible when $t_\phi^{(2)} \gg t_0'$, $t_0'' \gg t_0$, t_+. This regime is achievable by choosing $\delta \gg t_{12}$, but still $J \approx 2t_{12}^2/\delta \gg \sigma_0$, since $t_\phi^{(2)}$ is a much stronger function of δ than t_0', t_0''. That is, the two-particle dephasing time scales like $t_\phi^{(2)} \sim \delta^4$, but the typical hyperfine-induced decay times scale like $t_0', t_0'' \sim J \sim 1/\delta$. On the other hand, when $t_{12} \approx \delta$, we have $|\delta J/\delta\epsilon| \sim O(1)$, which gives $t_\phi^{(2)} \sim t_\phi^{(1)}$, and thus a very short singlet-triplet decoherence time ($\approx 1\,\mathrm{ns}$), which is dominated by orbital dephasing.

4.5 Conclusions

We have shown that a fully quantum mechanical solution is possible for the dynamics of a two-electron system interacting with an environment of nuclear spins under an applied magnetic field. Our solution shows that the singlet-triplet correlators $C_{T_0}(t)$ and $C_{T_+}(t)$ will decay due to the quantum distribution of the nuclear spin system, even for a nuclear system that is static. We have found that the asymptotic behavior of $C_{T_0}(t)$ undergoes a transition from Gaussian to power-law ($\sim 1/t^{3/2}$) when the Heisenberg exchange coupling J becomes nonzero, and acquires a universal phase shift of $3\pi/4$. The oscillation frequency and phase shift as a function of time can be used to determine the exchange and Overhauser field fluctuations. We have also investigated the effects of an inhomogeneous polarization on $C_{T_0}(t)$, and have suggested a general strategy for reducing decoherence in this system. Finally, we have discussed orbital dephasing and its effect on singlet-triplet decoherence.

Chapter 5

Two-spin dynamics: Spin state narrowing

[D. Klauser, W. A. Coish, and D. Loss, Phys. Rev. B **73**, 205302 (2005)]

In this chapter we study spin dynamics for two electrons confined to a double quantum dot under the influence of an oscillating exchange interaction. This leads to driven Rabi oscillations between the $|\uparrow\downarrow\rangle$–state and the $|\downarrow\uparrow\rangle$–state of the two–electron system. The width of the Rabi resonance is proportional to the amplitude of the oscillating exchange. A measurement of the Rabi resonance allows one to narrow the distribution of nuclear spin states and thereby to prolong the spin decoherence time. Further, we study decoherence of the two-electron states due to the hyperfine interaction and give requirements on the parameters of the system in order to initialize in the $|\uparrow\downarrow\rangle$–state and to perform a $\sqrt{\mathrm{SWAP}}$ operation with unit fidelity.

5.1 Introduction

One of the important proposals for quantum information processing in solid–state systems is the spin–qubit proposal for quantum computing with electron spins in quantum dots [1]. Much effort has been put into the realization of this proposal leading to exciting theoretical [144] and experimental achievements [28, 57, 20, 83, 47, 22, 21]. Still many challenges remain such as decoherence and the implementation of single-qubit gates.

A major obstacle to quantum computation with the quantum-dot spin qubit is decoherence due to the coupling of the qubit to its environment. The hyperfine interaction between the electron spin and the nuclear spins present in all III-V semiconductors [67] leads to the strongest decoherence effect [14, 65, 66, 15, 16, 17, 70, 50, 21]. Experiments [81, 82, 22, 21] have yielded values for the free-induction spin dephasing time T_2^* that are consistent with $T_2^* \sim \sqrt{N}/A \sim 10\mathrm{ns}$ [15, 16, 17] for $N = 10^6$ and $A = 90\mu\mathrm{eV}$ in GaAs, where N is the number of nuclei within one quantum-dot Bohr radius and A characterizes the hyperfine coupling strength [27]. This is to be contrasted to potential spin-echo envelope decay, which may be much larger [69, 74, 77]. With a two-qubit switching time of $\tau_s \sim 50$ps [14] this only allows $\sim 10^2$ gate operations within T_2^*, which falls short (by a factor of 10 to 10^2) of current requirements for efficient quantum error correction [59].

There are several ways to overcome the problem of hyperfine-induced decoherence, of which measurement and thus projection of the nuclear spin state seems to be the most promising one [70]. Other methods include polarization [14, 17, 113, 70] of the nuclear spins and spin echo techniques [70, 74, 21]. However, in order to extend the decay time by an order of magnitude through polarization of the nuclear spins, a polarization of above 99% is required [70], but the best result so far reached is only ∼60% in quantum dots [81, 28]. With spin-echo techniques, gate operations still must be performed within the single-spin free-induction decay time, which requires faster gate operations. A projective measurement of the nuclear spin state leads to an extension of the free-induction decay time for the spin. This extension is only limited by the ability to do a strong measurement since the longitudinal nuclear spin in a quantum dot is expected to survive up to the spin diffusion time, which is on the order of seconds for nuclear spins surrounding donors in GaAs [139].

The implementation of quantum computation schemes requires coherent control of the qubits. Rabi oscillations between the two qubit states are an important signature of coherence and thus observation of controlled Rabi oscillations is an important intermediate step in the experimental implementation of quantum information processors. Despite recent experimental achievements [28, 21], there has still been no experimental observation of driven Rabi oscillations for a system of two quantum–dot spin qubits. What has been observed is electron spin resonance via g-tensor modulation in a bulk semiconductor [145].

In the quantum-dot spin qubit proposal, two-qubit gates are realized through tuning of the exchange coupling J between the two spins [1, 14]. The splitting between singlet and triplet states of the two-electron system is given by the exchange coupling J and in devices such as those in Refs. [21] and [22], J can be controlled through gate voltages. Petta *et al.* [21] have recently managed to implement the $\sqrt{\text{SWAP}}$-gate in their setup. However, in order to implement single-qubit gates, control over local magnetic fields or g-factors is required [14].

As we will show in Section 5.2, an oscillating exchange $J(t)$ induces Rabi oscillations between the states $|\uparrow\downarrow\rangle$ and $|\downarrow\uparrow\rangle$ of two electron spins (one electron in each dot). The amplitude of these oscillations is resonant on the splitting between $|\uparrow\downarrow\rangle$ and $|\downarrow\uparrow\rangle$ and the width of this resonance is proportional to the amplitude j of the oscillating component of $J(t) = J_0 + j\cos(\omega t)$, where ω is the driving frequency. Since the splitting depends on the state of the nuclear system, a measurement of the resonance is also a measurement of the state of the nuclear spins and thus provides a way to narrow the quantum distribution of the nuclear spin states. This narrowing of the spin state is one possible solution to suppress hyperfine-induced decoherence in quantum-dot spin qubits [70]. It has been proposed to measure the nuclear spin polarization using a phase estimation method [146]. In the ideal case, phase estimation yields one bit of information about the nuclear-spin system for each perfectly measured electron. Optical methods have also been proposed [147]. The all-electrical method we present here can be applied with current technology.

The rest of this chapter is organized as follows. In Section 5.2 we show that an oscillating exchange leads to driven Rabi oscillations and calculate the resonance linewidth. In Section 5.3 we propose a method to narrow the distribution of the nuclear spin states. in Section 5.4 we consider decoherence induced through the hyperfine interaction for a static exchange coupling J. We use these results in Section 5.5 to analyze under which conditions we reach unit fidelity for the initialization to the state $|\uparrow\downarrow\rangle$ and a $\sqrt{\mathrm{SWAP}}$ operation [1]. Section 5.6 contains a summary of our results.

5.2 Oscillating Exchange and ESR

In this section we show that under suitable conditions an oscillating exchange interaction may be used to induce Rabi oscillations in a system of two electrons confined to a double quantum dot like those in Refs. [83, 21, 22, 47].

We denote by $\mathbf{h}_i = (h_i^x, h_i^y, h_i^z)$, $i = 1, 2$, the collective quantum nuclear spin operator, the "Overhauser operator", in dot one and two, respectively, and write $\delta h^z = \frac{1}{2}(h_1^z - h_2^z)$. The collective quantum nuclear spin operator $\mathbf{h}_i$ is defined as $\mathbf{h}_i = \sum_k A_k^i \mathbf{I}_k$, where $\mathbf{I}_k$ is the nuclear spin operator for a nucleus of total spin I at lattice site k, and the hyperfine coupling constants are given by $A_k^i = vA|\psi_0^i(\mathbf{r}_k)|^2$, where v is the volume of a unit cell containing one nuclear spin, A characterizes the hyperfine coupling strength, and $\psi_0^i(\mathbf{r}_k)$ is the single-particle envelope wavefunction of the electron evaluated at site k. Further, $\langle\mathcal{O}\rangle_{\mathrm{rms}} = \langle\psi_I|\,\mathcal{O}^2\,|\psi_I\rangle^{1/2}$ is the root–mean–square expectation value of the operator $\mathcal{O}$ with respect to the nuclear spin state $|\psi_I\rangle$. We assume that the Zeeman splitting $\epsilon_z = g\mu_B B$ induced by a uniform applied magnetic field $\mathbf{B} = (0, 0, B)$, $B > 0$, is much larger than $\langle\delta\mathbf{h}\rangle_{\mathrm{rms}}$ and $\langle\mathbf{h}_i\rangle_{\mathrm{rms}}$. Under these conditions the relevant spin Hamiltonian becomes block diagonal with blocks labeled by the total electron spin projection along the magnetic field S^z. In the subspace of $S^z = 0$ the Hamiltonian can be written as ($\hbar = 1$) [50]

$$H_0 = \frac{J}{2}\left(1 + \tau^z\right) + \delta h^z \tau^x + \delta b^z \tau^x. \tag{5.1}$$

Here, J is the Heisenberg exchange coupling between electron spins on the two dots and δb^z the inhomogeneity of an externally applied classical static magnetic field which we add in addition to the treatment in Ref. [50]. Further, $\boldsymbol{\tau} = (\tau^x, \tau^y, \tau^z)$ is the vector of Pauli matrices in the basis of $S^z = 0$ singlet $|S\rangle$ and triplet $|T_0\rangle$ ($|S\rangle \to |\tau^z = -1\rangle$, $|T_0\rangle \to |\tau^z = +1\rangle$). It has been proposed to use two pseudo-spin states such as $|S\rangle$ and $|T_0\rangle$ as a logical qubit [148].

We assume a time–dependent exchange of the form

$$J = J(t) = J_0 + j\cos(\omega t). \tag{5.2}$$

The operator δh^z commutes with the Hamiltonian at all times. Thus, if the nuclear–spin system is in an eigenstate $|n\rangle$ of δh^z with $\delta h^z|n\rangle = \delta h_n^z|n\rangle$, we have $H|\psi\rangle = H_n|\psi_e\rangle \otimes |n\rangle$, where in H_n the operator δh^z has been replaced by δh_n^z and $|\psi_e\rangle$ is the electron spin part of the wave function. In order to bring H_n to a form that is very similar to the standard ESR (electron spin resonance) Hamiltonian [87] ($H_{ESR} = -\frac{1}{2}\epsilon_z\sigma_z - \frac{1}{2}\Delta_x\cos(\omega t)\sigma_x$) we perform a unitary transformation $U_1 = \exp(-i\frac{\pi}{4}\tau^y)$ which is just a rotation about the y-axis in a Bloch–sphere picture. Also introducing $\Omega_n = 2(\delta h_n^z + \delta b^z)$, the above Hamiltonian becomes

$$\tilde{H}_n = U_1 H_n U_1^\dagger = \frac{J_0}{2}\tau^x + \frac{j}{2}\cos(\omega t)\tau^x - \frac{1}{2}\Omega_n\tau^z. \tag{5.3}$$

The Pauli matrices are now given in the new basis of $|\downarrow\uparrow\rangle = |\tau^z = 1\rangle = |+\rangle$ and $|\uparrow\downarrow\rangle = |\tau^z = -1\rangle = |-\rangle$. For $J_0 = 0$ this is just the standard ESR Hamiltonian. We have evaluated pseudo-spin dynamics under this Hamiltonian in a rotating wave approximation close to resonance for $j \ll \Omega_n$. When we treat the J_0-term as a perturbation and calculate the transition probability between unperturbed eigenstates of the Hamiltonian we find that it is proportional to J_0^2/Ω_n^2 and we may thus neglect this term close to resonance and if $J_0 \ll \Omega_n$. Hence, we are left with the standard ESR Hamiltonian which leads to Rabi oscillations. Initializing the two-electron system in the state $|\downarrow\uparrow\rangle = |+\rangle$ (which can be done as proposed in Section 5.5) we obtain for the expectation value of $\tau^z(t)$:

$$\begin{aligned} \langle\tau^z(t)\rangle_n &= \langle n| \otimes \langle +| \, \tau^z(t) \, |+\rangle \otimes |n\rangle \\ &= \frac{(\Omega_n - \omega)^2 + (j/2)^2 \cos(\omega' t)}{(\Omega_n - \omega)^2 + (j/2)^2}, \end{aligned} \tag{5.4}$$

$$\omega' = 2\sqrt{(\Omega_n - \omega)^2 + (j/2)^2}, \tag{5.5}$$

$$j \ll \Omega_n, \;\; J_0 \ll \Omega_n, \;\; |\Omega_n - \omega| \ll \Omega_n. \tag{5.6}$$

For $\omega = \Omega_n$ the system undergoes coherent Rabi oscillations between the states $|+\rangle$ and $|-\rangle$ with a frequency of j. Averaged over time, the expectation value of τ^z is

$$\langle\langle\tau^z\rangle_n\rangle = \lim_{T\to\infty} \frac{1}{T} \int_0^T \langle\tau^z(t)\rangle_n dt = \frac{(\Omega_n - \omega)^2}{(\Omega_n - \omega)^2 + (j/2)^2}. \tag{5.7}$$

In order to measure the time–averaged value $\langle\langle\tau^z\rangle_n\rangle$ the measurement time must be much larger than the period of Rabi oscillations ($\sim 1/j$ on resonance). $1 - \langle\langle\tau^z\rangle_n\rangle$ has a Lorentzian lineshape with a full width at half maximum (FWHM) of j. Most importantly, the resonance frequency depends on the nuclear–spin eigenstate through $\Omega_n = 2(\delta h_n^z + \delta b^z)$ and thus a measurement of the resonance will determine δh_n^z.

5.2.1 Superposition of nuclear-spin eigenstates

Before a measurement on the nuclear-spin system is performed, there is no reason for the nuclear-spin system to be in an eigenstate of δh^z, but it is most likely in some generic superposition of these eigenstates. Thus, we now investigate how the resonance changes if we consider the nuclear-spin system to be in a superposition of eigenstates of the collective nuclear spin operator δh^z.

At $t = 0$ we fix the electron system in the state $|\downarrow\uparrow\rangle = |+\rangle$ while the nuclear-spin system is in an arbitrary state: $\rho(0) = \rho_e(0) \otimes \rho_I(0)$ with

$$\rho_e(0) = |+\rangle\langle+|, \tag{5.8}$$

$$\rho_I(0) = \sum_i p_i \left|\psi_I^i\right\rangle\left\langle\psi_I^i\right|; \;\; \left|\psi_I^i\right\rangle = \sum_n a_n^i |n\rangle, \tag{5.9}$$

where the a_n^i satisfy the normalization condition $\sum_n |a_n^i|^2 = 1$ and $\sum_i p_i = 1$. Here, $\rho_I(n) = \sum_i p_i |a_n^i|^2$ are the diagonal elements of the nuclear–spin density operator. The Hamiltonian H_0 commutes with δh^z and thus we find

$$\overline{\langle\tau^z(t)\rangle} = \sum_n \rho_I(n) \langle\tau^z(t)\rangle_n, \tag{5.10}$$

which defines the overbar.

We assume that for a large number of nuclear spins $N \gg 1$ which are in a superposition of δh^z-eigenstates $|n\rangle$, $\rho_I(n)$ describes a continuous Gaussian distribution of δh^z_n values, with mean $\overline{\delta h^z}$ and variance $\sigma^2 = \overline{\left(\delta h^z - \overline{\delta h^z}\right)^2}$. In the limit of large N the approach to a Gaussian distribution for a sufficiently randomized nuclear system is guaranteed by the central limit theorem [70]. We perform the continuum limit according to

$$\begin{aligned} \sum_n \rho_I(n) f(n) &\rightarrow \int dx \rho_{I;\overline{x},\sigma}(x) f(x), && (5.11)\\ \rho_{I;\overline{x},\sigma}(x) &= \frac{1}{\sqrt{2\pi}\sigma} \exp\left(-\frac{(x-\overline{x})^2}{2\sigma^2}\right), && (5.12) \end{aligned}$$

where $x = \delta h^z_n$, $\overline{x} = \overline{\delta h^z}$ and $\sigma^2 = \overline{x^2} - \overline{x}^2$. The only effect of δb^z is to shift the mean value of the Overhauser field inhomogeneity to $x_0 = \overline{x} + \delta b^z$, whereas the width is left unchanged: $\sigma_0 = \sigma$. According to this description we obtain

$$\begin{aligned} \overline{\langle \tau^z(t) \rangle} &= \int_{-\infty}^{\infty} dx \rho_{I;x_0,\sigma_0}(x) \left(f(x) + g(x,t)\right), && (5.13)\\ f(x) &= \frac{(2x-\omega)^2}{(2x-\omega)^2 + (j/2)^2}, && (5.14)\\ g(x,t) &= \frac{(j/2)^2 \cos\left(2\sqrt{(2x-\omega)^2 + (j/2)^2}t\right)}{(2x-\omega)^2 + (j/2)^2}. && (5.15) \end{aligned}$$

The second term (Eq.(5.15)) vanishes when it is averaged over time and we find

$$1 - \left\langle \overline{\langle \tau^z \rangle} \right\rangle = \frac{1}{2\sigma_0\sqrt{2\pi}} \int_{-\infty}^{\infty} dx \exp\left(-\frac{(x-2x_0)^2}{8\sigma_0^2}\right) \frac{(j/2)^2}{(x-\omega)^2 + (j/2)^2}. \quad (5.16)$$

This integral (a convolution of a Lorentzian and Gaussian) is the well-known Voigt function, [149] and the resulting lineshape is the so-called "Voigt profile". The Voigt function may be expressed as ($\tilde{\omega} = j + 4ix_0 - 2i\omega$)

$$\left\langle \overline{\langle \tau^z \rangle} \right\rangle = 1 - \frac{j}{4\sigma_0}\sqrt{\frac{\pi}{2}} \mathrm{Re}\left[\exp\left(\frac{\tilde{\omega}^2}{32\sigma_0^2}\right) \mathrm{erfc}\left(\frac{\tilde{\omega}}{4\sqrt{2}\sigma_0}\right)\right], \quad (5.17)$$

where erfc(z) is the complementary error function. In the regime where $\sigma_0 \ll j$ we may approximate the Lorentzian in the convolution (Eq.(5.16))by its value at $x = 2x_0$ and obtain

$$\left\langle \overline{\langle \tau^z \rangle} \right\rangle \approx \frac{(2x_0-\omega)^2}{(2x_0-\omega)^2 + (j/2)^2}; \quad \sigma_0 \ll j. \quad (5.18)$$

In this case the resulting resonance has the same FWHM as the Lorentzian, viz. j. On the other hand, if $\sigma_0 \gg j$, we may approximate the Gaussian with its value at $x = \omega$ and thus obtain

$$\left\langle \overline{\langle \tau^z \rangle} \right\rangle \approx 1 - \frac{j}{4\sigma_0}\sqrt{\frac{\pi}{2}} \exp\left(-\frac{(2x_0-\omega)^2}{8\sigma_0^2}\right); \quad \sigma_0 \gg j. \quad (5.19)$$

In this regime the width is twice the width σ_0 of the Gaussian distribution of the nuclear spin states. In order to make a statement about the width of the Voigt profile in general we look at the peak–to–peak separation Δ_V of the first derivative of the Voigt profile. For a Gaussian with a standard deviation of $2\sigma_0$ we find $\Delta_G = 4\sigma_0$ for the peak–to–peak separation of the derivative and for a Lorentzian with FWHM of j we have $\Delta_L = j/\sqrt{3}$. A Padé approximant for Δ_V in terms of Δ_L and Δ_G yields [150]

$$\Delta_V = \frac{\Delta_G^2 + a_1\Delta_G\Delta_L + a_2\Delta_L^2}{\Delta_G + a_2\Delta_L} \tag{5.20}$$

where $a_1 = 0.9085$, $a_2 = 0.4621$. This approximation is accurate to better than $0.01\Delta_V$ for all values of Δ_L, Δ_G [150]. A similar formula may also be given for the half width at half maximum (HWHM) of the Voigt profile [151].

5.3 State narrowing

The general idea behind state narrowing is that the evolution of the two–electron system is dependent on the nuclear spin state and thus knowing the evolution of the two–electron system determines the nuclear spin state. Thus, in this section we describe how the Gaussian superposition $\rho_{I;\sigma_0,x_0}(x)$ of collective nuclear spin eigenstates $|n\rangle$ can be narrowed through a sequence of measurements performed on a double quantum dot on a time scale much less than the timescale of variation of δh^z and for $j \lesssim \sigma_0$. We first give a general description of how a complete measurement of the lineshape of the Rabi resonance narrows the Gaussian superposition. Such a complete measurement of the lineshape consists of many single measurements of the operator τ^z. In Section 5.3.1 we present a detailed analysis of such a complete measurement and in Section 5.3.2 we discuss different measurement schemes.

The operator δh^z was defined in Section 5.2 and it describes the difference in the z-components of total nuclear field in each of the two dots. The total nuclear field is the result of $N \sim 10^6$ single nuclear spins and thus the eigenvalues of δh^z will be highly degenerate. In the limit of large N the spectrum of δh^z is quasi-continuous and the probability density of eigenvalues of δh^z is given by a Gaussian distribution, as described in Section 5.2.1. For such a Gaussian superposition of nuclear spin eigenstates, the lineshape of the Rabi resonance is given by a Voigt profile, as described in Section 5.2.1. This Voigt profile can be seen as a superposition of Lorentzian lineshapes, where each Lorentzian results from a nuclear spin eigenvalue δh_n^z and is centered around $\Omega_n = 2(\delta h_n^z + \delta b^z)$. In the Voigt profile, these Lorentzian lineshapes are weighted according to the amplitude of the corresponding eigenvalue δh_n^z in the Gaussian-distributed superposition. Through a perfect complete measurement of the Rabi-resonance lineshape, the superposition of Lorentzian lineshapes collapses and we are left with one single Lorentzian (see Figure 5.1). This Lorentzian corresponds to one single eigenvalue of δh^z and thus the Gaussian distribution has been narrowed to zero width; the nuclear–spin system is in a state with fixed eigenvalue δh_n^z.

In principle, we would need to do infinitely many single measurements in order to completely measure the lineshape of the Rabi resonance with perfect accuracy, since each point on this resonance curve is a (time-averaged) expectation value of the quantum mechanical operator τ^z. Still, we may perform a

1

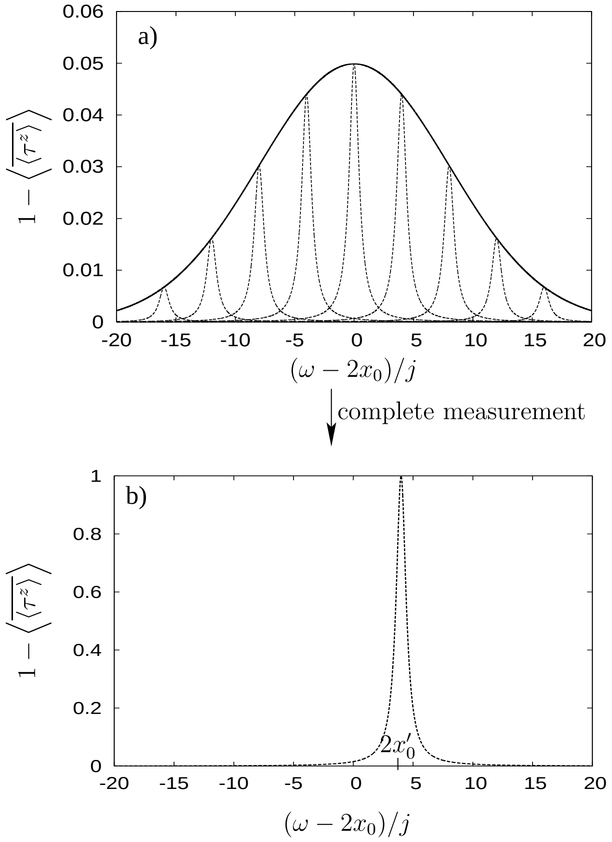

Figure 5.1: a) This figure illustrates the projection obtained through an ideal complete measurement of the Rabi–resonance lineshape. All the different Lorentzian resonances corresponding to different nuclear spin eigenstates add up to a Gaussian lineshape. b) Through a perfect complete measurement of the lineshape of the Rabi resonance, which involves many single measurements of τ^z, the superposition collapses and we are left with one single Lorentzian centered around $2x_0' = \Omega_n$, which in general is different from $2x_0$.

finite number M of single measurements (see Section 5.3.1) for each of a set of driving frequencies ω and thus obtain the series of expectation values for different ω up to some error. This error depends on M. There will then in general be more than one Lorentzian which can be fit (within error) to these expectation values and thus we would not narrow to zero width. We would still have a distribution of nuclear spin eigenstates, but one with smaller width than before the measurements.

For such a narrowing through measurement to be successful, the amplitude j of the oscillating exchange $J(t)$ which determines the width of the Lorentzian lineshapes should be smaller than the width σ_0 of the Gaussian distribution. Otherwise, the Rabi resonance would be dominated by the Lorentzian (see Eq.(5.18)) and the method would not result in narrowing of the nuclear–spin distribution. The general requirements on the system parameters to narrow the distribution of nuclear spin eigenvalues are

$$j, J_0, \sigma_0 \ll x_0; \quad j \lesssim \sigma_0. \tag{5.21}$$

We note that, unlike in standard ESR, power absorption is not measured here, but instead the expectation value of the pseudo-spin τ^z, for instance via a quantum point contact (QPC) nearby one quantum dot (for a detailed description of the measurement process via such a QPC we refer the interested reader to Ref. [141]). To determine the expectation value of the pseudo-spin τ^z many single measurements of the pseudo-spin are necessary and we thus proceed to give a detailed description of the state narrowing by considering the effect of these single measurements on the nuclear spin state.

5.3.1 Description of state narrowing by consecutive pseudo–spin measurements

In this subsection we describe in detail how a single measurement of the pseudo-spin τ^z of the two–electron system affects the nuclear–spin system. Further, we give a general formula for the diagonal elements of the nuclear–spin–system density operator in the continuum limit after M measurements. The sequence of M measurements is referred to as a "complete measurement".

At $t = 0$ the two–electron system is initialized to the state $|+\rangle = |\downarrow\uparrow\rangle$ and we assume that the electron and the nuclear system are initially factorized. Thus, the total system at $t = 0$ is described generally by the following density operator

$$\rho(0) = \rho_e(0) \otimes \rho_I(0) = |+\rangle \langle+| \otimes \sum_i p_i \left|\psi_I^i\right\rangle \left\langle\psi_I^i\right|, \tag{5.22}$$

with nuclear–spin state $\left|\psi_I^i\right\rangle = \sum_n a_n^i |n\rangle$. The diagonal elements of the nuclear–spin density operator at $t = 0$ are given by $\rho_I(n) = \rho_I(n, 0) = \sum_i p_i |a_n^i|^2$ and in the continuum limit we obtain the probability density $\rho_{I;\overline{x},\sigma}(x)$ for the eigenvalues $\delta h_n^z = x$ as given in Eq.(5.12). At time t_m a measurement of the two-electron system (at driving frequency ω, where ω is defined in Eq.(5.2)) is performed with two possible outcomes $|+\rangle$ and $|-\rangle$. The diagonal elements of the nuclear-spin density operator after the measurement are given by (see Appendix J)

$$\rho_I^{(1,\pm)}(n, t_m) = \frac{\rho_I(n, 0)}{P^{\pm}(t_m)} \frac{1}{2} \left(1 \pm \langle \tau^z(t_m) \rangle_n\right), \tag{5.23}$$

where $\langle \tau^z(t)\rangle_n$ is given by Eq.(5.4) and the probabilities $P^{\pm}(t_m)$ to measure $|\pm\rangle$ are

$$P^{\pm}(t_m) = \sum_i \sum_n \frac{1}{2}\left(1 \pm \langle \tau^z(t_m)\rangle_n\right) p_i |a_n^i|^2. \tag{5.24}$$

In the case where a measurement is performed with a low time resolution[1] Δt, i.e., if $\Delta t \gg 1/j$, the density operator after the measurement is the time average over the time interval Δt and the cosine term in $\langle \tau^z(t_m)\rangle_n$ averages out (note that in the case of a measurement with low time resolution, t_m is arbitrary, as long as Δt is chosen to be large enough). For the rest of this subsection we thus assume[2] that measurements are performed with low time resolution $\Delta t \gg 1/j$. Further, we perform the continuum limit and obtain for the probability density of eigenvalues, i.e., the diagonal part of the density operator in the continuum limit (with $x = \delta h_n^z + \delta b^z$ and $\rho_I(x) \equiv \rho_{I;x_0,\sigma_0}(x)$, see Eq.(5.12)):

$$\begin{aligned} \rho_I^{(1,+,\omega)}(x) &= \rho_I(x)(1 - L_\omega(x))\frac{1}{P_\omega^+}, & (5.25)\\ \rho_I^{(1,-,\omega)}(x) &= \rho_I(x)L_\omega(x)\frac{1}{P_\omega^-}, & (5.26)\end{aligned}$$

where the probabilities for measuring $|+\rangle$ or $|-\rangle$ are given by

$$\begin{aligned} P_\omega^+ &= \int_{-\infty}^{\infty} dx \rho_I(x)(1 - L_\omega(x)), & (5.27)\\ P_\omega^- &= \int_{-\infty}^{\infty} dx \rho_I(x) L_\omega(x), & (5.28)\end{aligned}$$

with

$$L_\omega(x) = \frac{1}{2}\frac{(j/4)^2}{(x - \frac{\omega}{2})^2 + (j/4)^2}. \tag{5.29}$$

After the first measurement, the two–electron system is reinitialized to the state $|+\rangle$ if necessary and a second measurement is performed. Since the initial density matrix factors out in the above results, it is clear how to generalize Eqs.(5.25) and (5.26) to the case where M consecutive measurements (without randomization of the nuclear-spin system in between measurements) are performed: every time $|+\rangle$ is measured, the diagonal elements $\rho_I(x)$ of the nuclear density matrix is multiplied by $1 - L_\omega(x)$ and every time $|-\rangle$ is measured, $\rho_I(x)$ is multiplied by $L_\omega(x)$. Thus, we obtain the diagonal elements $\rho_I^{(M,\alpha^-,\omega)}(x)$ of the nuclear density matrix after M measurements, of which α^- times the measurement outcome was $|-\rangle$ (and $(M - \alpha^-)$-times $|+\rangle$):

$$\rho_I^{(M,\alpha^-,\omega)}(x) = \frac{\rho_I(x)}{Q_\omega(M,\alpha^-)} W_\omega(M,\alpha^-;x). \tag{5.30}$$

---

[1] By "low time resolution", we mean that the measurement is performed at an unknown time t_m (giving rise to state $\rho(t_m)$) in the interval $\Delta t = t_b - t_a$, with a uniform probability density $1/\Delta t$. The state after the measurement is then $\frac{1}{\Delta t}\int_{t_a}^{t_b} dt_m \rho(t_m)$.

[2] This assumption is not necessary for our narrowing scheme. However, it does allow for the derivation of the analytical formulas in this section, which give insight into the mechanism of narrowing. In the case of perfect time resolution, one would have an additional factor of $(1 - \cos(\omega' t_m))$ in Eq. (5.29) (ω' is given in Eq.(5.5)) and would also have to take into account the time t_m at which each measurement was performed.

Here, $W_\omega(M,\alpha^-;x)$ and the normalization factor $Q_\omega(M,\alpha^-)$ are given by

$$\begin{aligned} W_\omega(M,\alpha^-;x) &= L_\omega(x)^{\alpha^-}(1-L_\omega(x))^{M-\alpha^-}, & (5.31)\\ Q_\omega(M,\alpha^-) &= \int_{-\infty}^{\infty} dx\rho_I(x)W_\omega(M,\alpha^-;x). & (5.32)\end{aligned}$$

The normalization factor $Q_\omega(M,\alpha^-)$ is related to $P_\omega^\pm$ through $P_\omega^- = Q_\omega(1,1)$, $P_\omega^+ = Q_\omega(1,0)$. In the case where measurements are performed at m_f different frequencies, Eq.(5.30) generalizes to

$$\rho_I^{(\{M_i\},\{\alpha_i^-\},\{\omega_i\})}(x) = \rho_I(x)\prod_{i=1}^{m_f}\frac{W_{\omega_i}(M_i,\alpha_i^-;x)}{Q_{\omega_i}(M_i,\alpha_i^-)}. \tag{5.33}$$

The probability density $\rho_I^{(\{M_i\},\{\alpha_i^-\},\{\omega_i\})}(x)$ after M measurements performed at m_f different driving frequencies depends on the frequencies $\{\omega_i\} = \{\omega_1,\ldots,\omega_{m_f}\}$, the number of measurements at each frequency $\{M_i\} = \{M_1,\ldots,M_{m_f}\}$, and the number of times $|-\rangle$ was measured at each frequency $\{\alpha_i^-\} = \{\alpha_1^-,\ldots,\alpha_{m_f}^-\}$. Eq.(5.33) gives the distribution of nuclear spin eigenvalues for any sequence of M measurements, i.e., without randomization of the nuclear–spin system in between measurements.

5.3.2 Measurement schemes

In this subsection we describe different measurement schemes. One main characteristic of the schemes is whether we have unconditional evolution of the nuclear-spin density matrix between measurements (one waits for the nuclear-spin system to rerandomize between subsequent measurements), or whether we have conditional evolution, i.e., the nuclear-spin system is assumed to be static between measurements.

5.3.2.1 Unconditional scheme

The simplest scheme is to measure only once at one single driving frequency ω. If the outcome is $|-\rangle$, the nuclear–spin distribution after the measurement is given by Eq.(5.26); the FWHM ($2\sigma_0\sqrt{2\ln 2}\approx 2\sigma_0$) of the initial distribution will have been narrowed by a factor $\approx j/4\sigma_0$ (the nuclear–spin distribution will approximately be a Lorentzian with FWHM of $j/2$). For $j \ll \sigma_0$ and $\omega = 2x_0$, the probability P_ω^- to measure $|-\rangle$ in the first measurement is $P_{\omega=2x_0}^- \approx j/6\sigma_0$ (the exact formula is given in Eq.(5.28)). If the measurement outcome is $|-\rangle$, we stop measuring. Otherwise, we wait for the system to rerandomize (in contrast to the conditional schemes) and perform another measurement. This is repeated until $|-\rangle$ is measured for the first time. On average one needs to perform $M' \approx 6\sigma_0/j$ measurements in order to narrow by a factor of $\approx j/4\sigma_0$ (we write M' because this number of measurements should not be confused with the number of measurements M used above in the case of measurements performed without rerandomization in between). If the driving frequency ω is far from the center x_0 of the initial Gaussian distribution, the number of required measurements increases by a factor of $\exp((x_0-\omega/2)^2/2\sigma_0^2)$. This always leads to a narrowed distribution which is centered around $\omega/2$. Thus, with this scheme it is possible to choose the center of the nuclear–spin distribution after the measurement.

This unconditional measurement scheme is the one which should be easiest to implement in an experiment since one only needs to measure once at one single frequency. However, if measurements at several different frequencies can be performed, a systematic narrowing of the distribution can be implemented as we show next.

5.3.2.2 Adaptive conditional scheme

The probability of measuring $|-\rangle$ in a measurement is determined by the overlap of the Lorentzian $L_\omega(x)$ and the probability density of eigenvalues $\rho_I^{(M,\alpha^-,\omega)}(x)$ (for the first measurement this probability is P_ω^-, which is given in Eq.(5.28)). Then, if we have the outcome $|-\rangle$ for a measurement at driving frequency ω, $\rho_I^{(M,\alpha^-,\omega)}(x)$ as a function of x becomes peaked around $\omega/2$ (since $L_\omega(x)$ is centered around $x = \omega/2$), the overlap of the Lorentzian $L_\omega(x)$ and $\rho_I^{(M,\alpha^-,\omega)}(x)$ increases and therefore the probability to measure $|-\rangle$ in a subsequent measurement also grows. If, on the other hand, we have outcome $|+\rangle$, the term $1-L_\omega(x)$ causes a dip in $\rho_I^{(M,\alpha^-,\omega)}(x)$ at $x = \omega/2$, the overlap of the Lorentzian $L_\omega(x)$ and $\rho_I^{(M,\alpha^-,\omega)}(x)$ decreases and thus the probability to measure $|-\rangle$ in a subsequent measurement with the same driving frequency ω also decreases. Since it is the measurement outcome $|-\rangle$ that primarily leads to narrowing, the measurement scheme should maximize the probability to measure $|-\rangle$. This can be achieved by changing the driving frequency ω always in such a way that before each measurement $L_\omega(x)$ and the nuclear–spin distribution $\rho_I^{(M,\alpha^-,\omega)}(x)$ have their maximum at the same x, i.e., set $\omega/2 = x_{\max}$, where $x_{\max}$ is the x for which $\rho_I^{(M,\alpha^-,\omega)}(x)$ has a maximum. Thanks to the adaptive driving frequency ω, the probability P_ω^- to measure $|-\rangle$ is $\approx j/6\sigma_0$ in each measurement until $|-\rangle$ is measured for the first time. Without adapting, i.e., when measuring always at the same driving frequency ω, P_ω^- decreases, as explained above (as long as we do not measure $|-\rangle$). After measuring $|-\rangle$ for the first time, the probability P_ω^- to measure $|-\rangle$ increases. Every time the measurement outcome is $|-\rangle$, the distribution $\rho_I^{(M,\alpha^-,\omega)}(x)$ is multiplied by $L_\omega(x)$ and becomes narrower (since $L_\omega(x)^{\alpha^-}$ has a FWHM of $(j/2)\sqrt{2^{1/\alpha^-}-1}$). However, the measurement outcome $|+\rangle$, for which $\rho_I^{(M,\alpha^-,\omega)}(x)$ is multiplied by $1 - L_\omega(x)$, is still more likely and leads to a small widening of the distribution. Our simulations of this measurement scheme do, however, show that after $|-\rangle$ has been measured several times, the nuclear spin distribution is narrowed by more than a factor $j/4\sigma_0$.

This adaptive scheme was first proposed in an optical setup by Stepanenko et al. in Ref. [147]. This scheme requires that $x_{\max}$ can be calculated (or read from a table) between subsequent measurements and that the driving frequency ω can be tuned with a precision that is better than the width of the nuclear–spin distribution before each measurement. For this adaptive scheme (and other conditional schemes) to work, it is important that the nuclear–spin system does *not* randomize during the course of the complete measurement, i.e., the complete measurement must be carried out within a time that is shorter than the time scale for nuclear spin dynamics. We thus assume that the nuclear–spin system (viz. δh^z) has no internal dynamics between the single measurements of $\tau^z(t)$, but only changes due to the measurements performed on the two–electron

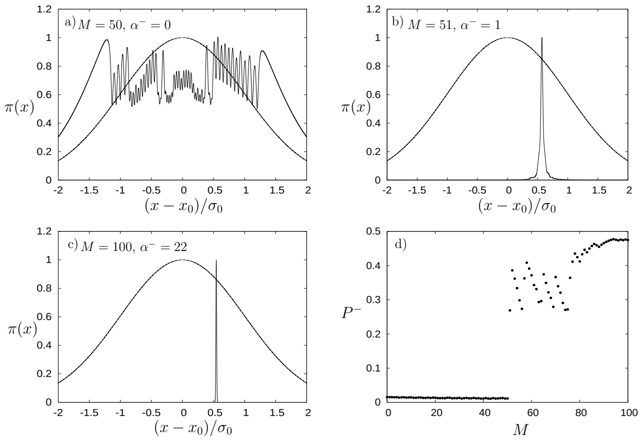

Figure 5.2: In this figure we show a typical sequence of the rescaled probability density of eigenvalues $\pi(x) = \rho_I^{(\{M_i\},\{\alpha_i^-\},\{\omega_i\})}(x)/\max\left(\rho_I^{(\{M_i\},\{\alpha_i^-\},\{\omega_i\})}(x)\right)$ for the adaptive conditional scheme. Here, $\rho_I^{(\{M_i\},\{\alpha_i^-\},\{\omega_i\})}(x)$ is given in Eq.(5.33). We have $x = \delta h_n^z + \delta b^z$, $j/\sigma_0 = 1/10$ and in a)–c) the initial Gaussian distribution (with FWHM $2\sigma_0\sqrt{2\ln 2} \approx 2\sigma_0$) is plotted for reference. a) Up to $M = 50$ measurements the outcome is never $|-\rangle$ and thus each measurement "burns a hole" into the distribution where it previously had its maximum. b) In the 51^{st} measurement the outcome is $|-\rangle$ which leads to a narrowed distribution of nuclear spin eigenvalues (peak centered at ≈ 0.5) with a FWHM that is reduced by a factor $\approx j/4\sigma_0$. c) Adapting the driving frequency ω to this peak, i.e., setting $\omega/2 = x_{\max}$ in subsequent measurements, leads to further narrowing every time $|-\rangle$ is measured. In this example the final FWHM is $\approx \sigma_0/100$, i.e., the distribution has been narrowed by a factor $\approx j/10\sigma_0$. d) The probability P^- to measure $|-\rangle$ jumps up after the 51^{st} measurement and after $|-\rangle$ is measured several more times, this probability saturates close to 1/2.

system, i.e., due to single measurements of $\tau^z(t)$. We expect δh^z to vary on the time scale of nuclear spin diffusion out of the dot, which is on the order of seconds for nuclear spins surrounding donor impurities in GaAs. [139] However, there may be other sources of nuclear spin dynamics (see also Appendix I).

In Figure 5.2 we show a typical[3] sequence of nuclear spin distributions for the adaptive scheme with total number of measurements $M = 100$ and $j/\sigma_0 = 1/10$. We see (Figure 5.2 (a)) that up to $M = 50$ the measurement outcome is never $|-\rangle$ and thus each measurement "burns a hole" into the distribution where it previously had its maximum. In the 51^{st} measurement (Figure 5.2(b)) the outcome is $|-\rangle$, which narrows the distribution by a factor of $\approx j/4\sigma_0$. Adapting the driving frequency ω to this peak, i.e., setting $\omega/2 = x_{\max}$ in subsequent measurements, leads to further narrowing, i.e., to a total narrowing by more than a factor $j/4\sigma_0$ (Figure 5.2(c)). In this example we have $\alpha^- = 22$ after $M = 100$ measurements and the final FWHM is $\approx \sigma_0/100$, i.e., the distribution has been narrowed by a factor $\approx j/10\sigma_0$. In Figure 5.2(d) the probability P^-

---

[3] We have performed more than 60 runs of the simulation, varying M and j/σ_0

to measure $|-\rangle$ before each measurement is shown. After the first time $|-\rangle$ is measured, P^- jumps up and after several more times $|-\rangle$ was measured, it saturates close to 1/2. P^- is a good signature of the distribution's width. As the width of the distribution goes to zero, P^- approaches 1/2. This adaptive conditional scheme is more intricate than the unconditional scheme, but allows one to narrow by more than a factor $j/4\sigma_0$.

5.3.2.3 Other conditional schemes

Other possible measurement schemes involve measurements at several frequencies, as in the adaptive scheme. One may either choose a fixed number of frequencies within one or two σ_0 and measure several times at each frequency (without randomization between the measurements) or sweep the frequency, i.e., measure only once at each frequency but vary the frequency only in small steps. Based on numerical simulations of these schemes, we find that the typical number of measurements to narrow by a factor of j/σ_0 is greater than in the adaptive or the unconditional (single–frequency) schemes.

5.3.2.4 Time-domain measurement scheme

We note that when a complete measurement of one of the correlators discussed in Section 5.4 is performed with perfect resolution in time and perfect accuracy, this would also determine the state of the nuclear spin system and thus narrow the distribution of nuclear spin states. This is because the frequency of the oscillating correlators is given by $\sqrt{J^2 + 4(\delta h_n^z)^2}$ and thus measuring the frequency of the correlator determines the eigenvalue δh_n^z of the nuclear–spin system. However, it may be possible to perform a weak measurement of the decay of the correlators and thus also to see the prolongation of the decay after applying a narrowing scheme. To understand in detail the effect of measurements in the time domain, further study is required. Narrowing through measurement of the correlators is a time-domain measurement. In contrast, the narrowing schemes we have proposed above are frequency-domain measurements. If the frequency resolution is better than the time resolution, our method would most likely be more suitable.

5.4 Correlation Functions in the $S^z = 0$ Subspace

In this section we investigate the Hamiltonian H_0 of Eq. (5.1) with static exchange coupling J. Using this Hamiltonian we wish to calculate correlation functions for several observables in the subspace of zero total spin in the z–direction. In our previous work [50] we calculated the time evolution of a particular correlator involving the states $|S\rangle$ and $|T_0\rangle$. However, there are four additional independent correlators involving the x and y components of pseudo–spin which require a separate calculation. Quite surprisingly, it will turn out that these correlators have different decay behavior in time. The correlators we calculate here show the decoherence properties of the pseudo–spin states under the influence of the hyperfine interaction. There may be additional sources of decoherence which we do not consider here, such as orbital dephasing, corrections to the effective Hamiltonian, [50] the coupling of the QPC to the dot spins, [64] etc. The results of this section will help to give requirements on the parameters of the system in order to initialize in the state $|\uparrow\downarrow\rangle$ and to assess the fidelity of a $\sqrt{\mathrm{SWAP}}$ operation with static J (see Section 5.5).

Diagonalizing H_0 gives the following eigenvalues and eigenvectors

$$\begin{aligned} E_n^{\pm} &= \frac{J}{2} \pm \frac{1}{2}\sqrt{J^2+\Omega_n^2}, && (5.34)\\ \left|E_n^{\pm}\right\rangle &= \frac{(\Omega_n/2)\,|S\rangle + E_n^{\pm}\,|T_0\rangle}{\sqrt{\left(E_n^{\pm}\right)^2+(\Omega_n/2)^2}} \otimes |n\rangle\,, && (5.35)\end{aligned}$$

where again $|n\rangle$ is an eigenstate of the operator δh^z with $\delta h^z\,|n\rangle = \delta h_n^z\,|n\rangle$. At $t=0$ we fix the electron system in an arbitrary superposition of $|T_0\rangle$ and $|S\rangle$

$$|\psi_e(t=0)\rangle\rangle = |A\rangle\,;\ \ |A\rangle = \cos\frac{\theta_A}{2}\,|S\rangle + e^{i\varphi_A}\sin\frac{\theta_A}{2}\,|T_0\rangle\,. \qquad (5.36)$$

The nuclear-spin system is again in a general state (see Section 5.2.1). As will be shown in Sec. 5.5, it is possible, in principle, to initialize to an arbitrary state in the subspace spanned by $|T_0\rangle$ and $|S\rangle$. The probability to find the electron spins in a state $|B\rangle$ at $t>0$ is given by the correlation function:

$$C_{BA}(t) = \sum_n \rho_I(n)\left|\langle n|\otimes\langle B|\,e^{-iH_0t}\,|A\rangle\otimes|n\rangle\right|^2, \qquad (5.37)$$

where $\rho_I(n) = \sum_i p_i|a_n^i|^2$. The correlation function has the following symmetry: $C_{BA}(t) = C_{AB}(-t)$, and if $|B\rangle$ and $|D\rangle$ are orthogonal states we have $C_{BA}(t) = 1 - C_{DA}(t)$. Further, we may decompose $C_{BA}(t)$ into the sum of a time-independent term $\overline{C_{BA}^n}$ and an interference term $C_{BA}^{\mathrm{int}}(t)$:

$$C_{BA}(t) = \overline{C_{BA}^n} + C_{BA}^{\mathrm{int}}(t), \qquad (5.38)$$

where the overbar is defined in Eq. (5.10).

We have further $C_{BA}^n = C_{BA}(\delta h_n^z) = C_{BA}(x)$. Performing the continuum limit as described in Eq. (5.11) we obtain for the correlation function

$$\begin{aligned} C_{BA}(t) &= \int_{-\infty}^{\infty} dx\rho_{I;\sigma_0,x_0}(x)\left(C_{BA}(x) + C_{BA}^{\mathrm{int}}(x,t)\right) && (5.39)\\ &= C_{BA}^{\infty} + C_{BA}^{\mathrm{int}}(t). && (5.40)\end{aligned}$$

Here, C_{BA}^{∞} is the assymptotic value of the correlator $C_{BA}(t)$ for $t\to\infty$.

We have calculated correlation functions for the following states: $|S\rangle \to |\tau^z=-1\rangle\,,\ |T_0\rangle \to |\tau^z=+1\rangle\,,\ |X\rangle \to |\tau^x=+1\rangle = \frac{1}{\sqrt{2}}\left(|T_0\rangle + |S\rangle\right),\ |Y\rangle \to |\tau^y=+1\rangle = \frac{1}{\sqrt{2}}\left(|T_0\rangle + i\,|S\rangle\right)$. The frequency in the interference term is always given by $s(x) = \sqrt{J^2+4x^2}$. In Table 5.1 we list the integrands according to the notation in Eq. (5.39). From the Heisenberg equation of motion we find $\frac{d\tau^x}{dt} = -J\tau^y$, which leads to relations for the correlators. In the notation used in Table 5.1 we obtain $\frac{dC_{XX}}{dt} = -J\left(C_{YX} - \frac{1}{2}\right)$, which is satisfied by the results shown in Table 5.1. Similar relations can be derived for the other correlators

$C_{BA}(t)$	$C_{BA}(x)$	$C_{BA}^{\text{int}}(x,t)$
$C_{T_0S}(t)$	$\frac{2x^2}{s(x)^2}$	$-\frac{2x^2}{s(x)^2}\cos(s(x)t)$
$C_{T_0X}(t)$	$\frac{1}{2}+\frac{Jx}{s(x)^2}$	$-\frac{Jx}{s(x)^2}\cos(s(x)t)$
$C_{T_0Y}(t)$	$\frac{1}{2}$	$\frac{x}{s(x)}\sin(s(x)t)$
$C_{YX}(t)$	$\frac{1}{2}$	$\frac{J}{2s(x)}\sin(s(x)t)$
$C_{YY}(t)$	$\frac{1}{2}$	$\frac{1}{2}\cos(s(x)t)$
$C_{XX}(t)$	$\frac{1}{2}+\frac{2x^2}{s(x)^2}$	$\frac{J^2}{2s(x)^2}\cos(s(x)t)$

Table 5.1: Functions $C_{BA}(x)$ and $C_{BA}^{\text{int}}(x,t)$ according to the notation of Eq. (5.39) for different correlators (with $s(x) = \sqrt{J^2+4x^2}$). $C_{XX}(t)$ is a linear combination of other correlators.

and used to check the results in Table 5.1. We see that $C_{XX}(t)$ is a linear combination of other correlators: $C_{XX}(t) = C_{YY}(t) + C_{T_0S}(t)$. For C_{T_0X} and C_{T_0Y} the interference term is an odd function in x. Thus, the time dependence vanishes for $x_0 = 0$ and we have $C_{T_0X} = C_{T_0Y} = 1/2$ for all t. In general, the integral in Eq. (5.39) is difficult to solve exactly. Thus, we concentrate on several interesting limits. We illustrate this for the case of $C_{YX}(t)$ and give results for the other correlators. We have

$$\begin{aligned} C_{YX}(t) &= \frac{1}{2} + \text{Im}\left[\tilde{C}_{YX}^{\text{int}}\right], && (5.41)\\ \tilde{C}_{YX}^{\text{int}} &= \int_{-\infty}^{\infty} \rho_{I;\sigma_0,x_0}(x)\frac{J}{2s(x)}e^{is(x)t}. && (5.42)\end{aligned}$$

In the regime of $|x_0| \gg \sigma_0$ the main contribution to the integral comes from a narrow region around x_0 and we may approximate $\frac{J}{2s(x)} \approx \frac{J}{2\omega_0}$ where $\omega_0 = s(x_0)$ and in the frequency term $s(x) \approx \omega_0 + \frac{4x_0}{\omega_0}(x-x_0) + \dots$. For this to be a good approximation, we require $\frac{2J^2}{w_0^3}(x-x_0)^2 t \ll 1$. We use $(x-x_0)^2 \approx \sigma_0^2$ and thus obtain for the correlator and the range of validity in this limit

$$\begin{aligned} C_{YX}^{\text{int}}(t) &= \frac{J}{2\omega_0}e^{-\frac{1}{2}\left(\frac{t}{t_0''}\right)^2}\sin(\omega_0 t), && (5.43)\\ & t_0'' = \frac{\omega_0}{4|x_0|\sigma_0},\ \ \omega_0 = \sqrt{J^2+4x_0^2}, && (5.44)\\ & |x_0| \gg \sigma_0,\ \ t \ll \frac{(J^2+4x_0^2)^{3/2}}{2J^2\sigma_0^2}. && (5.45)\end{aligned}$$

The results for the other correlators are (with the same range of validity)

$$C^{\rm int}_{T_0S}(t) = -\frac{2x_0^2}{\omega_0^2}e^{-\frac{1}{2}\left(\frac{t}{t_0''}\right)^2}\cos(\omega_0 t), \tag{5.46}$$

$$C^{\rm int}_{T_0X}(t) = -\frac{Jx_0}{\omega_0^2}e^{-\frac{1}{2}\left(\frac{t}{t_0''}\right)^2}\cos(\omega_0 t), \tag{5.47}$$

$$C^{\rm int}_{T_0Y}(t) = \frac{x_0}{\omega_0}e^{-\frac{1}{2}\left(\frac{t}{t_0''}\right)^2}\sin(\omega_0 t), \tag{5.48}$$

$$C^{\rm int}_{YY}(t) = \frac{1}{2}e^{-\frac{1}{2}\left(\frac{t}{t_0''}\right)^2}\cos(\omega_0 t). \tag{5.49}$$

In this limit we obtain a Gaussian decay for all correlators on a time scale $t_0'' = \frac{\omega_0}{4|x_0|\sigma_0}$ which grows with the absolute value of the exchange coupling $|J|$ and with $1/\sigma_0$. The long–time saturation value is 1/2 for C_{YX}. For some of the other correlators we find non–trivial parameter–dependent saturation values. In the limit of $|x_0| \gg \sigma_0$ we obtain these correlators by the same approximation as for the interference term, i.e. we set $C_{BA}(x) = C_{BA}(x_0)$ and obtain

$$C^{\infty}_{T_0S} = \frac{2x_0^2}{J^2+4x_0^2}; \quad |x_0| \gg \sigma_0, \tag{5.50}$$

$$C^{\infty}_{T_0X} = \frac{1}{2} + \frac{Jx_0}{J^2+4x_0^2}; \quad |x_0| \gg \sigma_0, \tag{5.51}$$

$$C^{\infty}_{T_0Y} = C^{\infty}_{YX} = C^{\infty}_{YY} = \frac{1}{2}. \tag{5.52}$$

For large J the saturation value is quadratic in x_0/J for C_{T_0S} and linear for C_{T_0X}. The saturation value for C_{T_0S} goes to zero for $|J| \gg |x_0|$ and for C_{T_0X} approaches 1/2. $C^{\infty}_{T_0X}$ reaches extrema equal to $\frac{1}{2} + \frac{1}{4}\mathrm{sign}(Jx_0)$ for $|J| = 2|x_0|$.

Next we consider Eq. (5.39) for $|J| \gg \max(|x_0|, \sigma_0)$ and find

$$s(x) = \sqrt{J^2+4x^2} \approx |J| + \frac{2x^2}{|J|}, \tag{5.53}$$

$$\frac{J}{2s(x)} = \frac{J}{2\sqrt{J^2+4x^2}} \approx \mathrm{sign}(J)\left(\frac{1}{2} - \frac{x^2}{J^2}\right). \tag{5.54}$$

For Eq. (5.53) we have the additional requirement that $t \ll \frac{|J|^3}{2\max(x_0^4,\sigma_0^4)}$. Under these approximations we find the following result:

$$\begin{aligned}\tilde{C}^{\rm int}_{YX}(t) = \mathrm{sign}(J)&\left(\frac{1}{2}\xi(t) - \frac{\sigma_0^2}{J^2}\xi^3(t) - \frac{x_0^2}{J^2}\xi^5(t)\right)\\ &\times \exp\left(i|J|t - \frac{x_0^2}{2\sigma_0^2}\left(1-\xi^2(t)\right)\right),\\ \xi(t) &= \left(1 - i\frac{t}{t_0'}\right)^{-1/2}, \quad t_0' = \frac{|J|}{4\sigma_0^2},\\ &|J| \gg \max(|x_0|, \sigma_0), \quad t \ll \frac{|J|^3}{2\max(x_0^4,\sigma_0^4)}.\end{aligned} \tag{5.55}$$

At short times we expand $\xi^2(t) \sim 1 + i\frac{t}{t_0'} - \left(\frac{t}{t_0'}\right)^2$. Keeping only lowest order in t/t_0' in the prefactor and second order in the frequency term we obtain

$$C^{\rm int}_{YX}(t) = \mathrm{sign}(J)\frac{1}{2}e^{-\frac{1}{2}\left(\frac{t}{t_0''}\right)^2}\sin\left(\omega_0' t\right), \tag{5.56}$$

$$t_0'' \approx \frac{|J|}{4|x_0|\sigma_0}, \quad \omega_0' = |J| + \frac{2(x_0^2+\sigma_0^2)}{|J|}, \tag{5.57}$$

$$t \ll t_0' = \frac{|J|}{4\sigma_0^2}, \quad |J| \gg \max(|x_0|, \sigma_0). \tag{5.58}$$

The $|x_0| \gg \sigma_0$ limit of this result agrees with the $|J| \gg |x_0|$ limit of Eq. (5.43). Again, we have a Gaussian decay on the same time scale t_0'' as in Eq. (5.43) ($\omega_0 = \sqrt{J^2 + 4x_0^2} \sim |J|$ for $|J| \gg |x_0|$). One interesting feature of this correlator is the fact that there is a change of phase by π when the sign of the exchange coupling J changes. This feature offers the possibility of measuring J even for small values of J through a measurement of this correlator. We also list the other correlators in this regime:

$$C^{\rm int}_{T_0S}(t) = -\frac{2(x_0^2+\sigma_0^2)}{J^2}e^{-\frac{1}{2}\left(\frac{t}{t_0''}\right)^2}\cos(\omega_0' t), \tag{5.59}$$

$$C^{\rm int}_{T_0X}(t) = -\frac{x_0}{J}e^{-\frac{1}{2}\left(\frac{t}{t_0''}\right)^2}\cos(\omega_0' t), \tag{5.60}$$

$$C^{\rm int}_{T_0Y}(t) = \frac{x_0}{|J|}e^{-\frac{1}{2}\left(\frac{t}{t_0''}\right)^2}\sin(\omega_0' t), \tag{5.61}$$

$$C^{\rm int}_{YY}(t) = \frac{1}{2}e^{-\frac{1}{2}\left(\frac{t}{t_0''}\right)^2}\cos(\omega_0' t). \tag{5.62}$$

Finally, we are also interested in the behavior for large t. Thus, we expand Eq. (5.55) for large times $\xi(t \gg t_0') \sim e^{i\pi/4}\sqrt{t_0'/t}$ and obtain

$$C^{\rm int}_{YX}(t) \sim \mathrm{sign}(J)e^{-\frac{x_0^2}{2\sigma_0^2}}\frac{\sqrt{|J|}\sin(|J|t+\frac{\pi}{4})}{4\sigma_0 t^{\frac{1}{2}}}, \tag{5.63}$$

$$t \gg t_0' = \frac{|J|}{4\sigma_0^2}, |J| \gg \max(|x_0|, \sigma_0). \tag{5.64}$$

For the other correlators we find

$$C^{\rm int}_{T_0S}(t) \sim -e^{-\frac{x_0^2}{2\sigma_0^2}}\frac{\cos(|J|t+\frac{3\pi}{4})}{4\sigma_0\sqrt{|J|}\,t^{\frac{3}{2}}}, \tag{5.65}$$

$$C^{\rm int}_{T_0X}(t) \sim -\mathrm{sign}(J)e^{-\frac{x_0^2}{2\sigma_0^2}}\frac{x_0\sqrt{|J|}\cos(|J|t+\frac{3\pi}{4})}{8\sigma_0^3 t^{\frac{3}{2}}}, \tag{5.66}$$

$$C^{\rm int}_{T_0Y}(t) \sim e^{-\frac{x_0^2}{2\sigma_0^2}}\frac{x_0\sqrt{|J|}\sin(|J|t+\frac{3\pi}{4})}{8\sigma_0^3 t^{\frac{3}{2}}}, \tag{5.67}$$

$$C^{\rm int}_{YY}(t) \sim e^{-\frac{x_0^2}{2\sigma_0^2}}\frac{\sqrt{|J|}\cos(|J|t+\frac{\pi}{4})}{4\sigma_0 t^{\frac{1}{2}}}. \tag{5.68}$$

$$\tag{5.69}$$

Thus, the transverse components of the pseudo-spin have a slower decay ($\sim t^{-1/2}$) than the longitudinal component ($\sim t^{-3/2}$). This results from the fact that the Hamiltonian only has fluctuations along only one direction.

5.5 Analysis of $\sqrt{\mathrm{SWAP}}$

In this section we analyze the $\sqrt{\mathrm{SWAP}}$ gate using the correlation functions derived in the previous section, i.e., we analyze the $\sqrt{\mathrm{SWAP}}$ gate taking into account the hyperfine–induced decoherence. The $\sqrt{\mathrm{SWAP}}$ gate and single–qubit operations can be used to perform the quantum XOR gate (CNOT) which, in combination with single–qubit operations, is sufficient for universal quantum computation [1, 152]. In Ref. [21] implementation of $\sqrt{\mathrm{SWAP}}$ has been demonstrated. However, in these experiments there was a contrast reduction of $\sim 40\%$. Here we show that taking into account hyperfine induced decoherence, still near–unit fidelity can be obtained for this operation.

The Hamiltonian of Eq. (5.1) induces unitary time evolution on the states of the system: $|\psi(t)\rangle = U(t)\,|\psi(0)\rangle$ with $U(t) = T\exp(-i\int_0^t H(t')dt')$. We assume that J and x_0 can be switched adiabatically [13] on a time scale that is much shorter than the time required for the gate operation and thus the time evolution operator at time τ_s has the form

$$U_s = \exp\left(-i\tau_s H\right). \tag{5.70}$$

In a Bloch–sphere picture this operator induces a rotation about an axis in the plane spanned by eigenstates of τ^x and τ^z, $|X\rangle = |{\uparrow\downarrow}\rangle$ and $|S\rangle = (|{\uparrow\downarrow}\rangle - |{\downarrow\uparrow}\rangle)/\sqrt{2}$ [148]. The axis of rotation is determined by the parameters J and x_0. Through such an operation any state may be rotated into any other state on the Bloch sphere. Thus, it is possible to rotate from $|S\rangle$ to any initial state in the subspace of $S^z = 0$ by a single operation. This is important since initialization to the singlet is feasible by preparing a ground–state singlet with both electrons on the same dot and then changing the bias [21]. We now investigate initialization to the state $|X\rangle$ taking into account hyperfine–induced decoherence. The scheme we propose here is different from the one used in Ref. [21], where adiabatic passage from the singlet to the $|{\uparrow\downarrow}\rangle$–state is used. Our scheme requires control of x_0. We assume the system to be in the singlet state $|S\rangle$ at $t = 0$ and then switch J and x_0 such that $J = -2x_0$ and $|x_0| \gg \sigma_0$. In a Bloch–sphere picture, this corresponds to a rotation about an axis that halves the angle between $|S\rangle$ and $|X\rangle$. Since $C_{XS}(t) = C_{SX}(-t) = 1 - C_{T_0X}(-t)$ we have, for the above choice of parameters, according to Eqs. (5.47) and (5.51):

$$\begin{aligned} C_{XS}(t) &= \frac{1}{2} + \frac{1}{4}\left(1 - \cos(\sqrt{2}|J|t)e^{-\frac{1}{2}\left(\frac{t}{t_0''}\right)^2}\right), && (5.71)\\ & J = -2x_0,\ \ |x_0| \gg \sigma_0, && (5.72)\\ & t_0'' = \frac{1}{\sqrt{2}\sigma_0},\ \ t \ll \frac{(J^2 + 4x_0^2)^{3/2}}{2J^2x_0^2}. && (5.73)\end{aligned}$$

This correlator reaches its maximum for $\sqrt{2}|J|t = \pi$, i.e., at $\tau_s = \frac{\pi}{\sqrt{2}|J|}$. The time scale for the Gaussian decay is $t'' = \frac{1}{\sqrt{2}\sigma_0}$. To approach unit fidelity we therefore require $|J| \gg \sigma_0$, which is the case in the range of validity of the above correlator since $|x_0| \gg \sigma_0$ and J and x_0 are of the same order. At $t = \tau_s$ we switch J to zero and since $|X\rangle \otimes |n\rangle$ is an eigenstate of the remaining Hamiltonian, the system remains in this product state, untouched by decoherence induced via the nuclear spins. This scheme thus provides a way to initialize the double quantum dot system to the state $|X\rangle = \frac{1}{\sqrt{2}}(|T_0\rangle + |S\rangle) = |\uparrow\downarrow\rangle$, where arrows denote the z-component of the electron spin in each dot. In the same way, it is also possible to initialize in the state $|-X\rangle = |\tau^x = -1\rangle = \frac{1}{\sqrt{2}}(|T_0\rangle - |S\rangle) = |\downarrow\uparrow\rangle$ by switching to $J = 2x_0$.

It was already proposed in Ref. [1] to implement the $\sqrt{\mathrm{SWAP}}$ gate by pulsing the exchange interaction J between the two dots. Here we give a detailed analysis of the $\sqrt{\mathrm{SWAP}}$ gate taking into account hyperfine–induced decoherence.

The SWAP operation acts on the basis of the two–electron system as: $|\downarrow\downarrow\rangle \to |\downarrow\downarrow\rangle, |\downarrow\uparrow\rangle \to |\uparrow\downarrow\rangle, |\uparrow\downarrow\rangle \to |\downarrow\uparrow\rangle, |\uparrow\uparrow\rangle \to |\uparrow\uparrow\rangle$. The SWAP is an operation that acts only on the subspace of $S^z = 0$ and leaves the states $|\uparrow\uparrow\rangle$ and $|\downarrow\downarrow\rangle$ unchanged. In the system we consider this is naturally implemented through the large Zeeman splitting that separates $|\uparrow\uparrow\rangle$ and $|\downarrow\downarrow\rangle$ from the singlet and the $S^z = 0$ triplet. In order to analyze the SWAP in the $S^z = 0$ subspace we consider the regime of $|J| \gg \max(x_0, \sigma_0)$. The correlator $C_{-X,X}(t)$ gives the probability of being in the state $|-X\rangle = |\downarrow\uparrow\rangle$ for a system initialized in $|X\rangle = |\uparrow\downarrow\rangle$. Due to the symmetry relations for the correlation functions we have $C_{-X,X}(t) = 1 - C_{XX}(t) = 1 - C_{YY}(t) - C_{T_0S}(t)$ and thus find (using Eqs. (5.59) and (5.62) and neglecting terms of order $(\sigma_0^2 + x_0^2)/J^2$),

$$\begin{aligned} C_{-X,X}(t) &= 1 - C_{XX}(t) \approx \frac{1}{2} - \frac{1}{2} e^{-\frac{1}{2}\left(\frac{t}{t_0''}\right)^2} \cos(|J|t), \\ t_0'' &= \frac{|J|}{4\sigma_0|x_0|}, \;\; |J| \gg \max(|x_0|, \sigma_0), \;\; t \ll t_0' = \frac{|J|}{4\sigma_0^2}. \end{aligned} \tag{5.74}$$

We obtain the maximum value for this correlator when $\tau_s = \frac{\pi}{|J|}$. The Gaussian has a decay time of $t_0'' = \frac{|J|}{4\sigma_0|x_0|}$, so for $x_0 \to 0$ the Gaussian decay is negligible and we obtain unit fidelity for this SWAP operation $|\uparrow\downarrow\rangle \to |\downarrow\uparrow\rangle$ up to a global phase factor (which is not visible in the correlator).

From the SWAP operation it is only a small step towards the $\sqrt{\mathrm{SWAP}}$ which we obtain when we let the system evolve with the same parameter values but for only half the time. Starting in the state $|X\rangle$ we obtain $|Y\rangle$ after applying a $\sqrt{\mathrm{SWAP}}$. For large $|J|$ we find for the correlator C_{YX} in the limit $x_0 \to 0$

$$C_{YX}(t) = \frac{1}{2} + \mathrm{sign}(J) \frac{1}{2} e^{-\frac{1}{2}\left(\frac{t}{t_0''}\right)^2} \sin(|J|t), \tag{5.75}$$

$$t_0'' = \frac{|J|}{4\sigma_0|x_0|}, \; |J| \gg \max(|x_0|, \sigma_0), \; t \ll t_0' = \frac{|J|}{4\sigma_0^2}. \tag{5.76}$$

Here again the time scale of the Gaussian decay is $\frac{|J|}{4\sigma_0|x_0|}$ and approaches infinity for $x_0 \to 0$. The time during which we have to operate with these values of the parameters J and x_0 is now $\tau_s = \frac{\pi}{2|J|}$. Our calculations show that for the time during which J is pulsed high there is a regime in which unit fidelity may be approached. The reduced visibility in the experiment [21] may be due to several reasons such as reduced visibility in the readout of $|\downarrow\uparrow\rangle$ or the initialization of $|\uparrow\downarrow\rangle$.

5.6 Conclusion

We have developed a method that uses the measurement of a Rabi resonance in the quantum–dot spin qubit to narrow the distribution of the nuclear spin states. This method relies on Rabi oscillations induced via an oscillation of the singlet–triplet splitting J in the subspace $S^z = 0$ of two electrons in a double quantum dot forming a two–qubit system. Further, we have calculated several correlators in the $S^z = 0$ subspace for static J and found that the transverse components of pseudo–spin have a slower decay than the longitudinal one. We have also discussed the implementation and fidelity of the $\sqrt{\text{SWAP}}$–gate in this system and the initialization to the $|\uparrow\downarrow\rangle$, $|\downarrow\uparrow\rangle$ states.

Chapter 6

Molecular states in cabon-nanotube double quantum dots

[M. R. Gräber, W. A. Coish, C. Hoffmann, M. Weiss, J. Furer, S. Oberholzer, D. Loss, and C. Schönenberger Phys. Rev. B **74**, 075427 (2006)]

In this chapter we report electrical transport measurements through a semiconducting single-walled carbon nanotube (SWNT) with three additional top-gates. At low temperatures the system acts as a double quantum dot with large interdot tunnel coupling allowing for the observation of tunnel-coupled molecular states extending over the whole double-dot system. We precisely extract the tunnel coupling and identify the molecular states by the sequential-tunneling line shape of the resonances in differential conductance.

6.1 Introduction

The interference of quantum states is one of the most striking features of nature enabling the formation of molecular bonds. This bond formation can be studied in coupled quantum dots (artificial molecules) in regimes that are not accessible in true molecules [153, 42, 154, 21, 55]. Additionally, these engineered artificial molecules have been proposed as logic elements for future applications in spin-based quantum computing [14]. Whereas most electrical transport experiments on coupled quantum dots so far have investigated GaAs-based semiconductor quantum dots (see [30] and references therein), only recently such structures have been realized in carbon nanotubes and semiconducting nanowires [3, 2]. These materials are attractive not just for the relative ease in production, but also for the fact that superconducting and ferromagnetic contacts have been demonstrated [155, 156, 157], opening up a road for various kinds of novel quantum devices [158]. In addition, large spin dephasing times are expected for carbon-based quantum dots, since the nuclear spin of the dominant isotope ^{12}C is zero, yielding a strongly reduced hyperfine interaction.

In this chapter, we report electrical transport measurements through a semiconducting single-walled carbon nanotube (SWNT) with source and drain electrodes and three additional top-gates. In specific gate-voltage ranges the system acts as a double quantum dot with *large* inter-dot tunnel coupling t, allowing for the observation of a quantum-mechanical superposition of $|n, m+1\rangle$ and $|n+1, m\rangle$ states where n and m denote the number of charges on the left and right dot, respectively. Using an effective single-particle picture, we precisely determine the tunnel coupling and identify molecular-like states with wave functions extending over the whole nanotube double dot.

6.2 Experiment

Single-walled carbon nanotubes were grown by means of chemical vapor deposition (for details see Ref. [159]) on a highly-doped Si substrate covered by an insulating layer of 400 nm SiO_2. Single nanotubes were selected using a scanning electron microscope. Three 200 nm wide local gates equally spaced by 400 nm were then defined by means of standard electron beam lithography and e-gun evaporation of SiO_2, Ti and Pd. Finally, Pd source and drain contacts were fabricated. Figure 6.1(a) shows a schematic of the device, the materials used, and corresponding film thicknesses. A scanning electron micrograph of a device is shown in Figure 6.1(b).

Room temperature characterization identifies the semiconducting nature and an intrinsic p-doping state of the nanotube. Figure 6.1(c) shows the linear conductance through the device as a function of the three top-gate voltages. At a top-gate voltage of roughly 0.4 V conductance is suppressed indicating that the chemical potential is shifted into the semiconducting gap of the tube. Five identically-prepared devices were tested at room temperature and showed the same behavior.

Low-temperature measurements were performed in a ^{3}He cryostat with a base temperature of 290 mK. Differential conductance dI/dV_{sd} was measured using standard lock-in techniques with an excitation voltage of typically 7.5 μV at a frequency of 327.7 Hz and an I/V converter with a gain of 10^7 V/A. The inset of Figure 6.1(c) shows a colorscale plot of the linear conductance versus voltages applied at gates 1 and 2 for a constant center gate voltage $V_C = -1$ V at 2.2 K. Again, applying positive voltages of the order 1 V to any of the top-gates locally shifts the chemical potential into the energy gap of the intrinsically p-doped SWNT and thus suppresses electrical transport. Additionally, sweeping gate 1 and gate 2 leads to pronounced oscillations of the conductance due to single-electron charging and finite-size effects of the nanotube, which are accessible at low temperatures. For the measurements presented in the following, the center and back-gate were kept at constant voltages $V_C = -0.1\,\mathrm{V}$, $V_{BG} = 0\,\mathrm{V}$, respectively, and no magnetic field was applied.

A magnified colorscale plot of the differential conductance dI/dV_{sd} in a reduced gate-voltage range is shown in Figure 6.2(a). The visible high-conductance ridges define a charge-stability map that is shaped like a honeycomb. This honeycomb pattern is characteristic of a double quantum dot. Within each cell, the number of holes (n,m) on the two dots is constant. Energizing gate 1 (2) to more negative voltages successively fills holes into dot 1 (2), whereas a more positive voltage pushes holes out of the dot. Two identical devices were measured at low

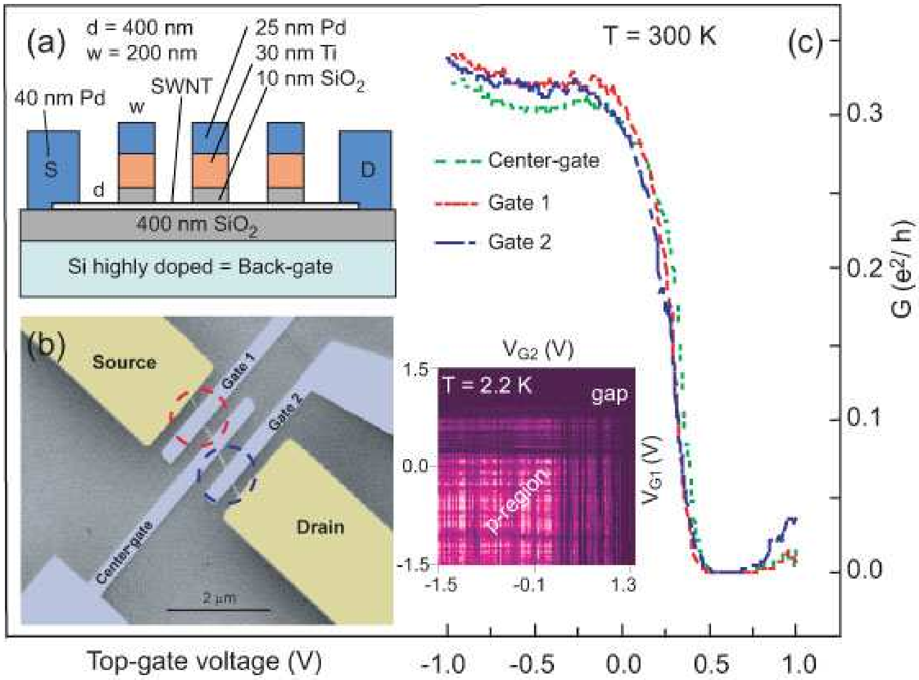

Figure 6.1: (a) Schematic of the fabricated device, with three top-gates as labelled in (b). (b) Scanning electron micrograph of a sample fabricated identically to the one measured. The distance from source to drain is 2.2 μm. Dashed circles denote the regions affected by gates 1 and 2. (c) Conductance G through the device at $T = 300\,\mathrm{K}$ versus top-gate voltage. All gates not swept are connected to ground. Note: Differences between the individual gate scans at 0 V arise from slightly hysteretic gate responses. Inset: Colorscale plot of G versus gate 1 and gate 2 for fixed $V_C = -1\,\mathrm{V}$ at 2.2 K. Bright corresponds to 0.4 e^2/h, dark to 0 $\mathrm{e}^2/$ h.

temperatures and both exhibited a similar honeycomb pattern

Of particular importance for sequential tunneling through the double dot are the so-called triple points, the two blue points in Figure 6.2(a), for example. At these points, three charge states are simultaneously degenerate (e.g. (n, m), $(n + 1, m)$, and $(n, m + 1)$), enabling the shuttling of a single electron from source to drain through the two dots. The conductivity in the vicinity of a triple point strongly depends on the relative magnitude of the electrostatic and tunnel coupling. For purely electrostatic coupling, the triple points are sharply defined, while they become blurred, leading to curved edges, if quantum-mechanical tunneling is turned on.

We will first analyze the honeycomb pattern, assuming purely electrostatic interaction as illustrated in Figure 6.2(d). Hence, we disregard the tunnel coupling between the dots for the moment. In the quantitative determination of the dot and gate capacitances, we follow the work of van der Wiel *et al* [30]. From the dimensions of a single cell $\Delta V_{G1,2} =\mid e \mid /C_{G1,2}$ as illustrated in Figure 6.2(b), one obtains the gate capacitances $C_{G1} = 23\,\mathrm{aF}$ and $C_{G2} = 21\,\mathrm{aF}$. Applying a finite source-drain bias voltage V_{sd} results in a broadening of the triple points at the honeycomb edges into triangular-shaped regions, see Figure 6.2(c). In our device the triangles are less clearly defined due to finite temperature and the strong tunnel coupling between the dots which we will discuss in the following paragraphs. Using the relation $C_{G1,2}/C_{1,2} = |V_{sd}|/\delta V_{G1,2}$, the capacitances $C_1 = C_S + C_{G1} + C_m$ and $C_2 = C_D + C_{G2} + C_m$ follow to be 84 aF and 145 aF, respectively, from which we obtain $U_{C_{1,2}} = e^2/C_{1,2} \approx 1.9\,\mathrm{meV}$ and 1.1 meV for the on-site charging energies of the dots, in agreement with the dimensions of the Coulomb blockade diamonds at finite bias (not shown). The mutual capacitance C_m between the two dots can now be estimated from the triple-point spacing $\Delta V^m_{G1,2}$ in Figure 6.2(b) using $\Delta V^m_{G1,2} = |e|C_m/C_{G1,2}C_{2,1}$. We obtain $C_m \approx 15\,\mathrm{aF}$.

We emphasize that disregarding tunneling between the dots is a very strong assumption. The purely electrostatic model, which we have used up to now, overestimates C_m and can only yield an upper bound. That tunneling is appreciable in this double-dot system is evidenced by the honeycomb borders in Figure 6.2(a), which are bright over an extended range. In addition, the high-conductance ridges are *curved* in the vicinity of the triple points, as expected for strongly tunnel-coupled dots. Analyzing this curvature allows us to precisely extract the tunnel coupling amplitude t (see Figure 6.3). To do so, a convenient description is developed first.

We adopt a model Hamiltonian of the form $H = H_C + H_T + H_L$, describing the system depicted in Figure 6.2(e). Here, H_C describes the orbital and Coulomb energies of the double-dot system, $H_T = t\,(|n+1, m\rangle \langle n, m+1| + \mathrm{h.c.})$ the tunnel-coupling between the two dots, and H_L the coupling of each dot to the leads. In H_C, we include on-site (U) and nearest-neighbor (U') charging energies. States with a fixed number of charges on each dot are eigenstates of H_C: $H_C\,|n, m\rangle = E_{nm}\,|n, m\rangle$, where $E_{nm} = E^{orb}_{nm} + \frac{U}{2}\,[n(n-1) + m(m-1)] + U'nm + E_1 n + E_2 m$. E^{orb}_{nm} is the total orbital energy of the $|n, m\rangle$ charge configuration, and $E_{1(2)}$ is the single-particle energy of the left (right) dot, supplied by the gate voltages $V_{G1,2}$. In a simple picture of sequential tunneling[1] through

---

[1] We define a sequential-tunneling process for the double dot as a process that changes the total charge on the double-dot by one, as in Ref. [39].

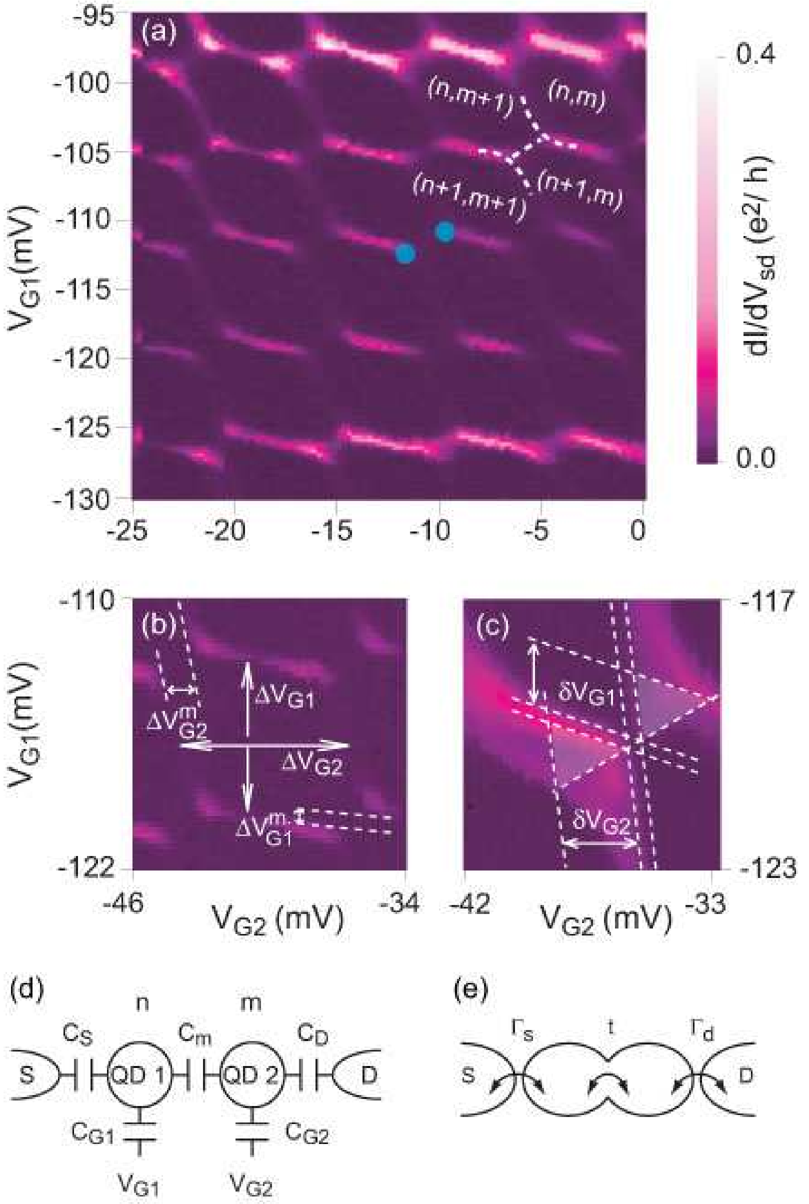

Figure 6.2: (a) Colorscale plot of the conductance versus voltage applied on gate 1 (V_{G1}) and gate 2 (V_{G2}) at a temperature of $T = 290\,\text{mK}$ and $V_{sd} = -128\,\mu\text{V}$. The resulting honeycomb pattern represents the charge stability diagram of coupled double quantum dots. Two triple points are marked by blue dots for clarity. Dashed lines are guides to the eye. (b) Close-up of a single honeycomb cell. (c) Vicinity of the triple points at a source-drain bias voltage of $391\,\mu\text{V}$. (d) and (e) Capacitive and molecular model of a double quantum dot, respectively.

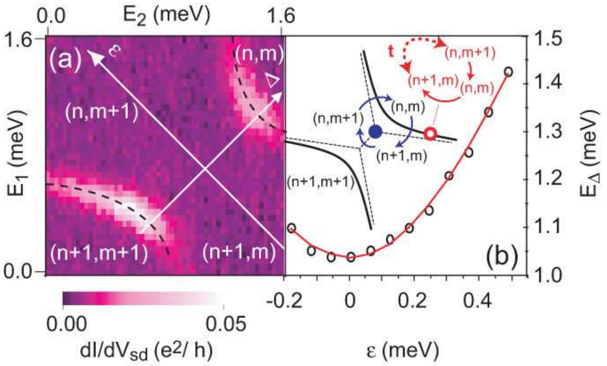

Figure 6.3: (a) Colorscale plot of the differential conductance ($V_{sd} = 20\,\mu$V, $T = 290\,$mK) in the vicinity of two triple points. Dashed lines are guides to the eye. (b) Spacing E_Δ (see Eq. (6.2)) of the two high conductance wings with respect to the Δ-direction versus detuning ϵ. Inset: Schematics of sequential tunnel processes allowed at the triple points (blue dot) and at the honeycomb edges (red circle) via molecular states.

H_C-eigenstates (neglecting H_T to leading order), one would expect nonzero conductance only at the triple points. It is only at these points that energy-conserving processes of the kind $|n,m\rangle \rightarrow |n+1,m\rangle \rightarrow |n,m+1\rangle \rightarrow |n,m\rangle$ can lead to charge transport through the double dot (blue sequence in the inset of Figure 6.3(b)).

However, if we allow for superposed double-dot states of the form $|E\rangle = \alpha\,|n+1,m\rangle + \beta\,|n,m+1\rangle$, sequential transport is possible along the honeycomb edges as well (red sequence in the inset of Figure 6.3(b)). Such superposed states are eigenstates of the full double-dot Hamiltonian $H_C + H_T$. For spinless holes[2] and assuming that only a single eigenstate $|E\rangle$ participates in transport, the stationary sequential-tunneling current is then given by

$$I = |e|\,\Gamma[f_s(\mu_{2dot}) - f_d(\mu_{2dot})]. \tag{6.1}$$

Here, $f_l(\mu_{2dot}) = 1/\left(\exp\left[(\mu_{2dot} - \mu_l)/kT\right] + 1\right)$ is a Fermi function at temperature T, μ_l ($l = s(d)$) the chemical potential of the source (drain) lead, and $\Gamma = |\alpha\beta|^2\Gamma_s\Gamma_d/(\alpha^2\Gamma_s + \beta^2\Gamma_d)$, with $\Gamma_{s(d)}$ the dot-lead tunneling rate to the source (drain). The chemical potential of the double dot μ_{2dot} depends on whether sequential tunneling occurs at $|n,m\rangle \leftrightarrow |E\rangle$ (right branch in the inset of Figure 6.3(b)), or at $|n+1,m+1\rangle \leftrightarrow |E\rangle$ (left branch): $\mu_{2dot} = E - E_{nm}$ for the former and $E_{n+1,m+1} - E$ for the latter.

With the help of Eq. (6.1), the data allow for a precise quantitative analysis of the tunnel coupling t between the dots. Figure 6.3(a) shows a colorscale plot (linear scale) of the differential conductance at $V_{sd} = 20\,\mu\text{V} \approx kT$ in the vicinity of a triple point region. As expected in the presence of tunnel-coupled eigenstates, transport is possible not only at the triple points, but also on the wings extending from the triple points. The two gate voltages V_{G1} and V_{G2} are converted into energies E_1 and E_2 by multiplying them with the conversion factors $\alpha_1 = 0.42e$

---

[2] Note that in a spinless description we exclude the possibility of e.g. spin-blockade, which, in our experiment, has not been observed.

and $\alpha_2 = 0.29e$, which we obtain from the splitting of a differential conductance resonance at finite bias voltage, as will be discussed in the context of Figure 6.4. We then change variables to $\epsilon = (E_1 - E_2)/\sqrt{2}$ and $\Delta = (E_1 + E_2)/\sqrt{2}$. In terms of these new variables, the double-dot molecular eigenenergies are (up to a constant offset) $E^{\pm}(\Delta, \epsilon) = E_{mn}(\Delta, \epsilon) + \left(\Delta \mp \sqrt{\epsilon^2 + 2t^2}\right)/\sqrt{2}$. When the bias and temperature are smaller than the double-dot level spacing (i.e., $V_{sd}, kT < E^- - E^+$), transport occurs only through the ground-state $|E^+\rangle$. For small bias, we set $\mu_1 = \mu_2 = \mu$, then transport is due to energy-conserving transitions between the state $|E^+\rangle$ and either $|n, m\rangle$ (when $E^+ - E_{nm} = \mu$) or $|n+1, m+1\rangle$ (when $E_{n+1,m+1} - E^+ = \mu$). These conditions are fulfilled at the two high-conductance wings. The separation of the wings in the Δ-direction (E_Δ) is given by:

$$E_\Delta = \sqrt{2}U' + \sqrt{4\epsilon^2 + 8t^2}. \tag{6.2}$$

In Figure 6.3(b) the spacing of the two wings E_Δ is plotted versus the detuning ϵ and fit to Eq. (6.2). Satisfactory fits to the data yield a tunnel coupling of $t = 310 \ldots 360\,\mu\text{eV}$ and $U' < 100\,\mu eV$. The parameters of the fit shown are $t = 358\,\mu\text{eV}$ and $U' = 16\,\mu eV$. The relative magnitudes are compared as $2t \approx 0.7\,\text{meV} \gg U' < 0.1\,\text{meV}$. The fact that the tunnel coupling dominates by almost an order of magnitude over the electrostatic coupling between the dots reflects the one-dimensional geometry of a nanotube; electrostatic interactions are reduced due to the large separation of the "center of mass" of the charges (while still allowing a significant overlap of the wavefunctions). Similar molecular states have been analyzed in semiconductor vertical-lateral double dots, yielding a smaller tunnel coupling $t \approx 80\mu\text{eV}$ and larger $\text{U}' \approx 175\mu\text{eV}$ [47]. Using $U' < 100\,\mu\text{eV}$ and $U' = \frac{2e^2 C_m}{C_1 C_2 - C_m^2}$ [34], one obtains a mutual capacitance of $C_m \lesssim 4\,\text{aF}$, consistent with the previous estimate $C_m \leq 15\,\text{aF}$ from the purely electrostatic model.

Because $t \gg kT$ at $T = 0.3\,\text{K}$, charge transport in the vicinity of the triple points takes place through a single molecular orbital (the bonding orbital of the two dots). This can be distinguished from two-stage hopping if dI/dV_{sd} is further analyzed as a function of bias voltage. More specifically, we demonstrate next that the finite-bias differential conductance through the double dot is accurately described by the sequential tunneling through a single molecular state according to Eq. (6.1).

Figure 6.4 shows a map of the differential conductance in the vicinity of the two triple points (same region as Figure 6.3) for three different source-drain voltages. On the right side, traces of the differential conductance with respect to gate 1 are extracted for fixed voltage applied to gate 2 (dashed line), well separated from the triple points. In Figure 6.4(a) the conductance trace has a single peak. In the finite-bias cases (b) and (c) the single peak splits into two peaks. Because of the linear dependence of the peak splitting on bias (inset of Figure 6.4(a) for gate 1), the second peak is not due to an additional level entering the bias window. To understand this feature, we note that the differential conductance is measured by modulating the source voltage μ_1, keeping the drain voltage μ_2 and all other gate voltages fixed. Assuming the double-dot charge is fixed, capacitive coupling of the source to the double dot induces a simultaneous modulation of μ_{2dot}, albeit with an amplitude reduced by the factor $r = \partial\mu_{2dot}/\partial\mu_1 = C_S/C_\Sigma$, where $C_\Sigma \approx C_S + C_D + C_{G1} + C_{G2}$. From Eq. (6.1)

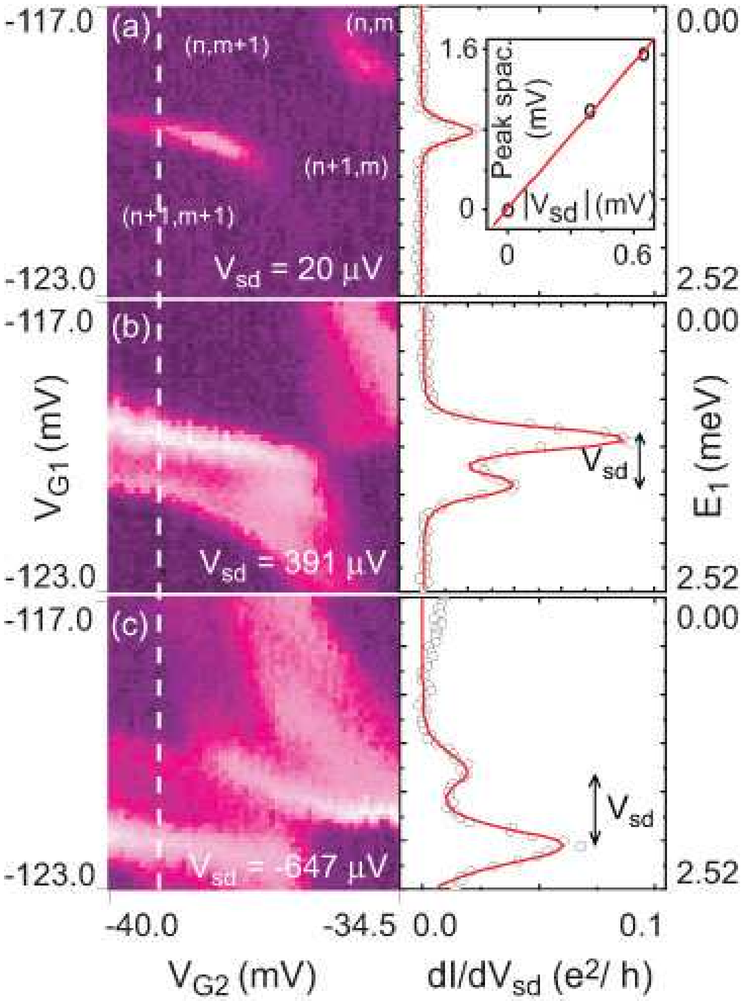

Figure 6.4: Colorscale plot of the differential conductance in the vicinity of the same triple point as in Figure 3 for three different bias voltage: (a) $V_{sd} = 20\,\mu$V, (b) $V_{sd} = 391\,\mu$V and (c) $V_{sd} = -647\,\mu$V. Dark corresponds to 0 e^2/h and bright to 0.1 e^2/h. On the right side, open circles denote traces of the differential conductance taken at the position of the dashed line. Solid lines represent fits to the line shape given by Eq. (6.3). Left-hand vertical scale: Voltage applied to gate 1. Right-hand vertical scale: Voltage applied to gate 1 converted into energy.

the differential conductance for our setup is then given by

$$\frac{dI}{d\mu_1} = -\,|e|\Gamma[(1-r)\,f_s'(\mu_{2dot}) + r f_d'(\mu_{2dot})]\,, \tag{6.3}$$

where $f_l'(x) = \frac{d}{dx} f_l(x)$. Sequential tunneling through a single molecular level therefore predicts a double-peaked structure with *peaks separated by the bias voltage*, as observed in Figure 4. The spacing of the two peaks can thus be used to convert top-gate voltages into energy and one obtains the conversion factors given above. For our device, we have $C_S \approx 65\,\mathrm{aF}$, $C_\Sigma \approx 230\,\mathrm{aF}$, which yields $r \approx 0.3$. According to this model the relative height of the two differential conductance peaks should be roughly $\frac{r}{1-r} \approx 0.5$. This value is consistent with the data shown in Figure 4 (with ratios of 0.42 in (b) and 0.28 in (c)). Additionally, we find that the asymmetry of the peaks switches from positive (b) to negative (c) bias, as is expected from Eq. (6.3).

The data in Figure 4(a) have been fit to Eq. (6.3) yielding a peak width of $49\,\mu\mathrm{eV}$. Note that in this case $V_{sd} \approx kT$ and the peak thus does not split. Subtracting the bias of $20\,\mu\mathrm{eV}$ one obtains an effective temperature of the electrons of $29\,\mu\mathrm{eV} \approx 335\,\mathrm{mK}$. Fitting Figure 4(b) and 4(c) to Eq. (6.3), one obtains a larger peak width corresponding to temperatures of 785 mK and 1180 mK, respectively, which we attribute to Joule heating at finite bias.

The excellent agreement of the sequential-tunneling fits demonstrates that transport occurs through a single level. In this regime of a strongly tunnel-coupled double dot, transport cannot be captured by dot-to-dot hopping, but takes root in the formation of coherent molecular states.

Chapter 7

Exchange-controlled single-spin rotations in quantum dots

[W. A. Coish and D. Loss, arXiv:cond-mat/0610443]

In this chapter e show that arbitrary coherent rotations can be performed with high fidelity on the spin of a single electron confined to a quantum dot using exchange. These rotations can be performed using electrostatic gating operations, without the need for spin-orbit interaction or ac electromagnetic fields. We expect that implementations of this proposal would achieve gate error rates on the order of $\eta \lesssim 10^{-3}$, within reach of error-correction schemes.

7.1 Introduction

The elementary building-blocks for universal quantum computing are a two-qubit entangling operation, such as the CNOT-gate or $\sqrt{\text{SWAP}}$-gate and arbitrary single-qubit rotations. For qubits based on single electron spins confined to quantum dots [1], recent experiments have proven that the two-qubit $\sqrt{\text{SWAP}}$-gate [21] and single-spin coherent rotations [24] can be achieved in practice. If these operations are to be used in a viable quantum information processor, they must be performed with a sufficiently small gate error per operation $\eta \ll 1$. The threshold values of η required for effective quantum error correction depend somewhat on error models and the particular error-correction scheme, but current estimates range from as low as $\eta < 10^{-3} - 10^{-4}$ [59] to $\eta < 10^{-2}$ [160]. In order to achieve these low error rates in the presence of fluctuations in a solid-state environment, new schemes must be developed which allow gating operations to be performed quickly and accurately within the relevant decoherence times.

Previous proposals [127] and recent implementations [24] for single-spin rotation in quantum dots have relied on ac magnetic fields to perform electron-spin resonance (ESR). In ESR, high power requirements for the ac field limit single-

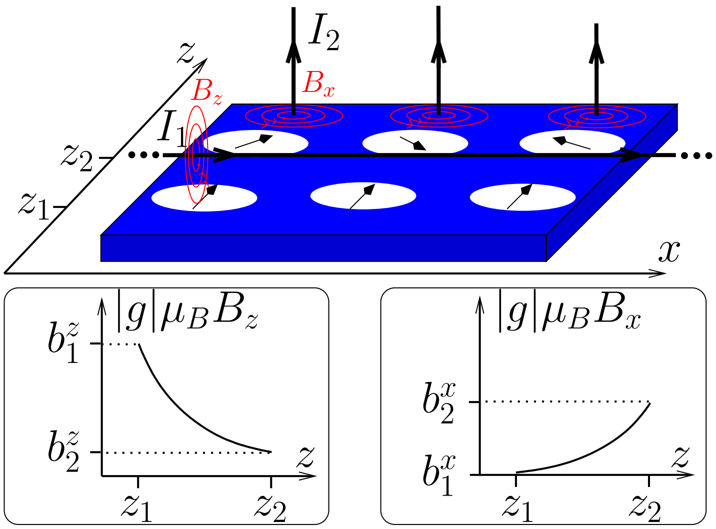

Figure 7.1: Possible setup to implement the scheme proposed here. Ancillary electron spins at z_1 are maintained in a polarized state with a large Zeeman field b_1^z along z. Qubit spins at z_2 are free to precess in a weaker effective Zeeman field lying in the x-z plane: $\mathbf{\Delta} = (b_2^x, 0, b_2^z - J/2)$. Here, J is the exchange coupling between the qubit and ancillary spins and $\mathbf{b}_2$ is the qubit Zeeman field in the absence of exchange. When $b_1^z \gg b_2^z \gg b_2^x$, z-rotations are performed if $J \approx 0$ and x-rotations are achieved when $J \approx 2b_2^z$. An inhomogeneous effective Zeeman field could be generated using strip lines carrying currents I_1 and I_2 as shown, using nanomagnets, by manufacturing dots with different g-factors, or by selectively polarizing nuclei in one dot relative to the other.

spin Rabi frequencies to values that are much smaller than the operation rates typically associated with two-qubit operations mediated by exchange [21]. To circumvent problems associated with high power and to achieve fast coherent single-qubit rotations, there have been several proposals to use electric-field (rather than magnetic field) control of electron spin states. These proposals aim to perform rotations on multiple-spin encoded qubits [161, 162], require strong spin-orbit interaction [163, 164, 165, 166], or coupling to excited orbital states [167]. Qubits encoded in two states having different orbital wave functions, such as two-spin singlet-triplet qubits [148] or hybridized orbital states [167] are susceptible to dephasing through fluctuations in the electric environment, even in the idle state [50, 168, 52]. Proposals that make use of the spin-orbit interaction [163,164,165,166] are restricted to systems where the spin-orbit coupling is sufficiently strong, which may exclude promising architectures such as quantum dots made from Si:SiGe [86] and carbon nanotubes [3,5], where spin-orbit coupling is very weak.

Fortunately, recent groundbreaking experiments have shown that fast subnanosecond control of the exchange interaction can be achieved in quantum dots, and can be coupled with viable readout schemes [21]. Here we suggest to perform single-qubit rotations in a way that would marry the benefits of fast electrical control of the exchange interaction [21] with the benefits of naturally long-lived single-electron spin qubits [1]. Our proposal would operate in the absence of spin-orbit coupling and would act on single electron spins without ac electromagnetic fields. The trade-offs in this proposal are that we require a large gradient in the electron Zeeman splitting and each qubit electron spin must be paired with a polarized ancillary spin (see Fig. 7.1). We have analyzed our proposal in the presence of the primary sources of error, including hyperfine interaction, spin-orbit interaction, and orbital dephasing during gating.

7.2 Hamiltonian

We begin from a standard tunneling model for the two lowest orbital levels of a double quantum dot, including tunnel coupling t_{12}, on-site repulsion U, nearest-neighbor repulsion U', local electrostatic potentials $V_{1(2)}$ and a local Zeeman field $\mathbf{b}_{1(2)}$ on dot 1(2) (see Refs. [30, 169] and references therein):

$$\begin{aligned}\mathcal{H} = -\sum_{l\sigma} V_l n_{l\sigma} + U \sum_l n_{l\uparrow} n_{l\downarrow} + U' \prod_l (n_{l\uparrow} + n_{l\downarrow}) \\ + t_{12} \sum_\sigma \left(d_{1\sigma}^\dagger d_{2\sigma} + d_{2\sigma}^\dagger d_{1\sigma} \right) - \sum_l \mathbf{S}_l \cdot \mathbf{b}_l. \end{aligned} \tag{7.1}$$

Here, $d_{l\sigma}$ annihilates an electron in dot $l = 1, 2$ with spin σ, $n_{l\sigma} = d_{l\sigma}^\dagger d_{l\sigma}$ is the usual number operator, and $\mathbf{S}_l$ is the spin density on dot l. We consider a regime in which the dot potentials $V_{1,2}$ are tuned to a charge ground state that lies between $(1,1)$ and $(0,2)$ (where (N_1, N_2) denotes a state with $N_{1(2)}$ electrons on dot 1(2), see Figs. 7.2(a,b)). Additionally, we require a large Zeeman field along z in dot 1 ($|b_1^z| \gg |b_1^{x,y}|$) so that the spin on dot 1 is frozen into its spin-up ground state. Finally, we also choose $|\epsilon \pm \delta b^z| \gg |t_{12}|$, $|\delta b^z| \gtrsim |t_{12}|$, with $\delta b^z = (b_1^z - b_2^z)/2$ and $\epsilon = V_2 - V_1 - U + U'$, which favors the $(1,1)$ charge state. For simplicity, we furthermore choose $b_2^y = 0$. Eq. (7.1) then reduces to the following low-energy effective Hamiltonian for the spin on dot 2:

$$\mathcal{H}_{\text{eff}} = -\frac{1}{2} \mathbf{\Delta} \cdot \boldsymbol{\sigma}; \; \mathbf{\Delta} = (b_2^x, 0, b_2^z - J(\epsilon)/2). \tag{7.2}$$

When $|\epsilon| \gg |\delta b^z|$, Eq. (7.1) gives $J(\epsilon) \approx -2t_{12}^2/\epsilon$. Thus, for a fixed Zeeman field $\mathbf{b}_2$, the direction and magnitude of the effective field $\mathbf{\Delta}$ can be tuned with gate voltages via its dependence on ϵ (see Fig. 7.2(c)). This can be done in the absence of spin-orbit coupling and without the application of ac electric or magnetic fields, which can give rise to "heating" in the electron system. However, rapid pulsing of $J(\epsilon)$ could also be used to drive an electron spin on- and off-resonance in the presence of a transverse ac magnetic field. We note that Eq. (7.2) follows directly from a much more general class of Hamiltonians of the form $H = -\sum_l \mathbf{b}_l \cdot \mathbf{S}_l + J(\epsilon) \mathbf{S}_1 \cdot \mathbf{S}_2$ in the limit where $|\mathbf{b}_1| \gg |\mathbf{b}_2|, J$, and so our proposal is not limited to the simplified Hamiltonian given in Eq. (7.1). Eq. (7.1) neglects the Coulomb exchange energy and excited orbital states. The Coulomb exchange energy contributes a small fraction to the exchange coupling compared to the tunneling contribution when the out-of-plane magnetic field is zero [14] and contributions to $J(\epsilon)$ due to excited orbital states [52] are a small correction when $|\epsilon| < J_{(0,2)}$, where $J_{(0,2)}$ is the single-dot exchange coupling on dot 2. The model therefore makes quantitatively accurate predictions for $J(\epsilon)$ in this limit. Outside of this range of validity, the functional form $J(\epsilon)$ could be obtained empirically from experiment, as has been done in Ref. [23]. We now proceed to apply the model in Eq. (1) to describe a complete set of single-qubit gates and potential sources of gating errors.

7.3 Qubit gates

Arbitrary single-qubit rotations can be achieved with the appropriate composition of the Hadamard gate (H), $\pi/8$ gate (T), and phase gate ($S = T^2$) [170]:

$$H = \frac{1}{\sqrt{2}}\begin{pmatrix} 1 & 1 \\ 1 & -1 \end{pmatrix}, \quad T = \begin{pmatrix} 1 & 0 \\ 0 & e^{i\pi/4} \end{pmatrix}. \tag{7.3}$$

T and S are not independent, but both enter naturally in fault-tolerant constructions [170]. Up to a global phase, the gates T and S correspond to rotations about z by an angle $\phi = \pi/8$ and $\phi = \pi/4$, respectively. These gates can therefore be performed with high fidelity by allowing the electron spin to precess coherently for a switching time $t_\mathrm{s} = \phi/\Delta_z$ at the operating point ϵ_A in Figure 7.2(a), where $\Delta_z \gg \Delta_x$. The H gate can be implemented by pulsing ϵ (see Fig. 7.2(c)) from ϵ_A, where $\Delta_z \approx b_2^z$ to $\epsilon_B = -t_{12}^2/b_2^z$, where $\Delta_z \approx 0$. The pulse is achieved with a characteristic rise time τ, then returns to $\epsilon = \epsilon_A$ after spending the pulse time t_p at $\epsilon = \epsilon_B$. The entire switching process (with total switching time $t_\mathrm{s} = t_\mathrm{p} + 4\tau$) is described by a time evolution opearator $\mathcal{U} = \mathcal{T} e^{i\int_0^{t_\mathrm{s}} dt \boldsymbol{\Delta}(t)\cdot\boldsymbol{\sigma}/2}$, which, for $b_2^x \ll b_2^z$ is approximately

$$\mathcal{U} \approx \mathcal{U}(\phi_x, \phi_z) = R_{\hat{z}}\left(-\frac{\phi_z}{2}\right) R_{\hat{x}}\left(-\phi_x\right) R_{\hat{z}}\left(-\frac{\phi_z}{2}\right), \tag{7.4}$$

where $\phi_x = \Delta_x t_\mathrm{p}/\hbar$ and $\phi_z = \int_0^{t_\mathrm{s}} dt \Delta_z(t)/\hbar$. Here, $R_{\hat{n}}(\phi)$ is a rotation about the $\hat{n}$-axis by angle ϕ. When $\phi_x = \pi/2$ and $\phi_z = \pi$, Eq. (7.4) gives an H gate, up to a global phase: $\mathcal{U}(\pi/2, \pi) = iH$.

7.4 Errors

We quantify gate errors with the error rate $\eta = 1 - \mathcal{F}$, where $\mathcal{F}$ is the average gate fidelity, defined by

$$\mathcal{F} = \frac{1}{4\pi}\int d\Omega \overline{\mathrm{Tr}\left(U\rho_\mathrm{in}(\theta,\phi)U^\dagger \tilde{U}\rho_\mathrm{in}(\theta,\phi)\tilde{U}^\dagger\right)}. \tag{7.5}$$

Here, $\rho_\mathrm{in}(\theta,\phi) = |\theta,\phi\rangle\langle\theta,\phi|$, where $|\theta,\phi\rangle = \cos(\theta/2)|\uparrow\rangle + e^{i\phi}\sin(\theta/2)|\downarrow\rangle$ indicates an inital spin-1/2 coherent state in the qubit basis, $U = H, T$, or S is the ideal intended single-qubit gate operation, and $\tilde{U} = \mathcal{T}\exp\left[-i\int_0^{t_\mathrm{s}} dt \mathcal{H}(t)\right]$ is the true time evolution of the system under the time-dependent Hamiltonian $\mathcal{H}(t)$. The overbar indicates an isotropic gaussian average over fluctuations in the classical Zeeman field $\mathbf{b}_2$, which we take to model the effects of hyperfine-induced decoherence. This procedure (an average over classical fields) is an appropriate model only when the fields have an average magnitude larger than the hyperfine

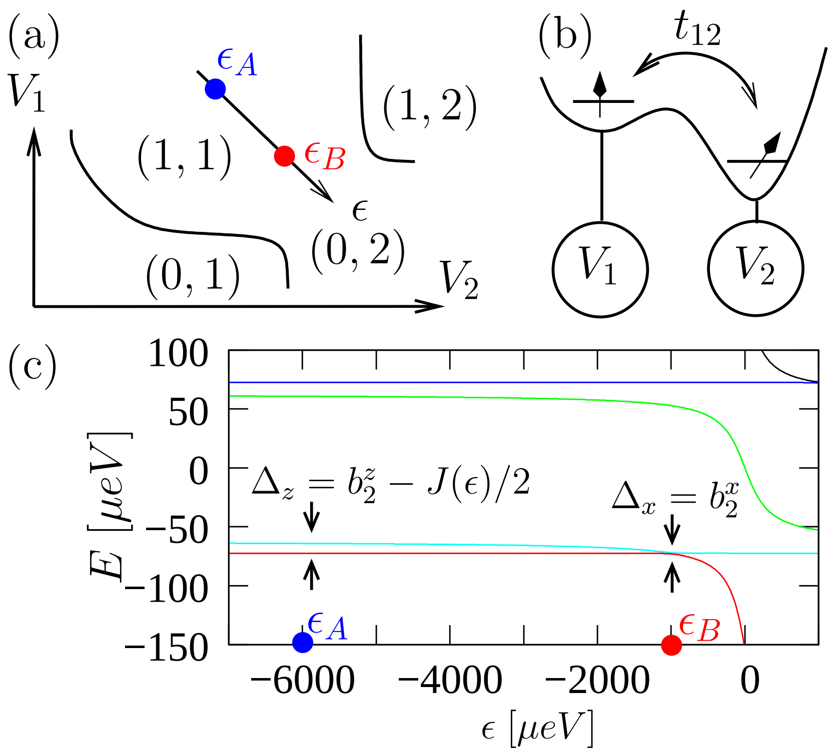

Figure 7.2: (a) Charge stability diagram indicating the ground-state charge configuration (N_1, N_2) for local dot potentials V_1, V_2, where $N_{1(2)}$ gives the number of electrons in dot 1 (2). In the $(1,1)$ configuration, the exchange interaction $J(\epsilon)$ can be tuned by shifting the double-dot potential difference $\epsilon \sim V_2 - V_1$. (b) When the electron spin in dot 1 is polarized, the qubit electron acquires a Zeeman shift given by $t_{12}^2/\epsilon = -J(\epsilon)/2$ due to virtual hopping processes that are allowed for spin-down, but forbidden for spin-up due to the Pauli principle. (c) Energy spectrum of the Hamiltonian given in Eq. (7.1) for a strong inhomogeneous magnetic field. At $\epsilon = \epsilon_A$ the effective Zeeman field points along the z-direction for $b_2^z \gg b_2^x$ and has the size $\Delta_z = b_2^z - J(\epsilon_A)/2$. ϵ_B is chosen to satisfy $J(\epsilon_B) = 2b_2^z$, in which case the remaining magnetic field component is oriented along x with size $\Delta_x = b_2^x$.

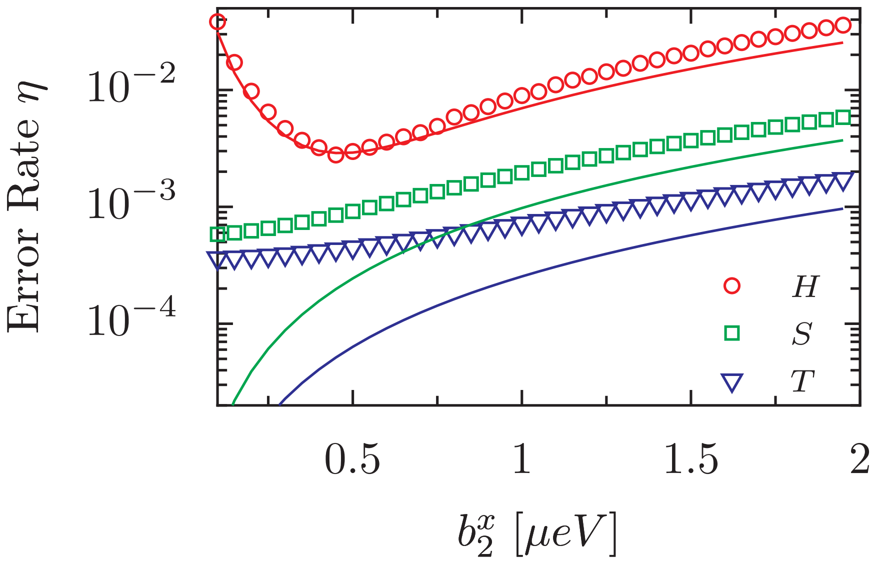

Figure 7.3: Error rates for the operations described in Figure 7.2. For these plots we have chosen the parameters $t_{12} = 100\,\mu eV$, $b_1^z = 135\,\mu eV$ (corresponding to the effective Zeeman splitting for a fully-polarized nuclear spin system in GaAs), $b_2^z = 10\,\mu eV$, $b_2^x = 1\,\mu eV$, and $\epsilon_A = -6\,\text{meV}$. For the Hadamard gate, these values result in $\epsilon_B = -t_{12}^2/b_2^z = -1000\,\mu eV$, a pulse time $t_\text{p} = \pi\hbar/2b_2^x = 1\,\text{ns}$, and a rise/fall time $\tau \approx \pi\hbar/4b_2^z = 50\,\text{ps}$. Symbols give the results of numerical integration of the time-dependent Schrödinger equation for the Hadamard gate (H, circles), phase gate (S, squares), and $\pi/8$ gate (T, triangles) where we include the effect of finite hyperfine fluctuations by averaging the result over 100 Zeeman fields, sampled from an isotropic gaussian distribution of width $\sigma_N = 0.03\,\mu eV$ (error bars due to a finite sample of Zeeman fields are smaller than the symbol size). Solid lines give the estimates for gating error from Equation (7.9).

fluctuations: $\left|\overline{\mathbf{b}_2}\right|^2 \gg \sigma_N^2 = \overline{\mathbf{b}_2 \cdot \mathbf{b}_2}$ [50]. For a gated GaAs quantum dot, σ_N due to hyperfine fluctuations has been measured to be $\sigma_N = 0.03\,\mu eV$ [22].

Based on the above protocol for gating operations, and assuming that hyperfine fluctuations limit the decoherence time of the qubit spins, we find a suitable parameter regime for high-fidelity single-qubit operations is given by the following hierarchy:

$$\sigma_N \ll b_2^x \ll b_2^z \ll t_{12} \lesssim b_1^z \ll |\epsilon_B| < |\epsilon_A|. \tag{7.6}$$

A set of values for these parameters that satisfies the above inequalities is given in the caption of Fig. 7.3. We now proceed to evaluate the error in H,T, and S gates due to the most dominant mechanisms.

The error rate for z-rotations is dominated by the misalignment of the average field $\mathbf{b}_2$ with the z-axis. For a rotation by angle $-\phi$ (to leading order in

b_2^x/b_2^z), this error rate is

$$\eta^z(\phi) \approx \frac{2}{3}\left(\frac{b_2^x}{b_2^z}\right)^2 \sin^2\left(\frac{\phi}{2}\right). \tag{7.7}$$

When $\Delta_z = 0$, the error rate for x-rotations is dominated by hyperfine fluctuations. We find this error rate, for an x-rotation by angle $-\phi$ (to leading order in σ_N/b_2^x) is

$$\eta^x(\phi) \approx \left(\frac{\phi^2}{18} + \frac{4}{9}\sin^2\left(\frac{\phi}{2}\right)\right)\left(\frac{\sigma_N}{b_2^x}\right)^2. \tag{7.8}$$

We estimate the error in T and S gates using η^z with $\phi = \pi/8$ and $\phi = \pi/4$, respectively. To estimate the error in the Hadamard gate, we use Eq. (7.4) in combination with Eqs. (7.7) and (7.8), assuming the errors incurred by each rotation are independent. These estimates give

$$\eta \approx \begin{cases} \eta^z\left(\frac{\pi}{8}\right), & (U = T), \\ \eta^z\left(\frac{\pi}{4}\right), & (U = S), \\ \eta^x\left(\frac{\pi}{2}\right) + 2\eta^z\left(\frac{\pi}{2}\right), & (U = H). \end{cases} \tag{7.9}$$

From Eq. (7.9), we find that the error rate for the H gate provides an upper bound for all error rates, and this rate reaches a minimum at an optimal value of b_2^x. The optimal value of b_2^x and η at this point are:

$$b_2^{x,\mathrm{opt}} = \sqrt{C|b_2^z|\sigma_N}, \quad \eta(b_2^{x,\mathrm{opt}}) = \frac{4}{3}C\frac{\sigma_N}{|b_2^z|}, \tag{7.10}$$

where C is a numerical prefactor $C = \sqrt{1/3 + \pi^2/48} \simeq 0.73$. Using the measured value $\sigma_N = 0.03\,\mu eV$ and $b_2^z = 10\,\mu eV$, we find an optimized error rate of $\eta \sim 10^{-3}$. Here we have included the two most dominant error mechanisms. There are many other potential sources of error, which we discuss in the following paragraph. All numerical estimates are based on the parameter values given in Fig 7.3.

We estimate error due to leakage to the (0,2) singlet state or hyperfine-induced spin flips of the ancillary spin to be $\sim$ max $\left[(\sigma_N/b_1^z)^2, (t_{12}/\epsilon_A)^2\right] \sim 10^{-4}$. If switching is done too slowly during the Hadamard gate, the qubit states will follow the adiabatic eigenbasis, introducing an additional source of error. We estimate this error to be $1 - P \approx \alpha$, where $P = e^{-\alpha}$ is the Landau-Zeener tunneling probability, given by [171]

$$\alpha = \frac{\pi}{\hbar}\frac{|b_2^x|^2}{|dJ(t)/dt|} \approx \frac{\pi |b_2^x|^2 \epsilon_B^2 \tau}{2\hbar t_{12}^2 \Delta\epsilon} \sim 10^{-4}. \tag{7.11}$$

Here, we have used $dJ(t)/dt \approx -2\dot{\epsilon}t_{12}^2/\epsilon_B^2$, with $\dot{\epsilon} \approx \Delta\epsilon/\tau$, where $\Delta\epsilon = |\epsilon_A - \epsilon_B|$. In the opposite limit, $\alpha \gg 1$, the qubit spin could be initialized to $|\uparrow\rangle$ with high probability (as has been done for singlet intialization [21]) by allowing the system to relax in the (0,2) singlet ground state at large positive ϵ and then slowly sweeping ϵ to large negative values. In systems with finite spin-orbit coupling, errors in our scheme could, in principle, arise from spin-orbit mediated decoherence mechanisms. For these mechanisms, the transverse-spin decay time T_2 is limited by the energy relaxation time T_1 (i.e., $T_2 = 2T_1$ [62]), so it is sufficient to analyze this error in terms of T_1, which has been measured to be $T_1 \gtrsim 1\,\mathrm{ms}$ at magnetic fields of $1 - 10\,\mathrm{T}$ [88]. This value gives an error estimate on the order of $t_\mathrm{s}/T_1 \lesssim 10^{-6}$ for a switching time $t_\mathrm{s} \simeq 1\,\mathrm{ns}$. Finally, rapid voltage-controlled gating in this proposal is made possible only because the electron spin states are associated with different orbital wave functions during pulsing, which also makes these states susceptible to orbital dephasing. The associated dephasing time is, however, strongly suppressed in the limit where the double occupancy is small: $D \approx (t_{12}/\epsilon)^2 \ll 1$. In particular, the dephasing time for the two-electron system is $\tau_\phi^{(2)} \approx D^{-2}\tau_\phi^{(1)}$ [50], where $\tau_\phi^{(1)} \approx 1\,\mathrm{ns}$ [143] is the single-electron dephasing time in a double quantum dot. This gives an error estimate of $t_\mathrm{s}/\tau_\phi^{(2)} \sim 10^{-4}$, using $t_\mathrm{s} \approx 1\,\mathrm{ns}$ and $D \sim 10^{-2}$ at the operating point $\epsilon = \epsilon_B$. It should be possible to further suppress the error rate due to orbital dephasing by choosing the operating point ϵ_B to coincide with a "sweet spot", where $dJ(\epsilon_B)/d\epsilon = 0$ [50, 168, 52].

7.5 Numerical analysis

To confirm the validity of the approximations made here and to verify the smallness of error mechanisms associated with leakage and finite pulse times, we have numerically integrated the time-dependent Schrödinger equation for the Hamiltonian given in Eq. (7.1) in the basis of the (0,2) singlet state and four (1,1) states (including spin). We have used the pulse scheme described in Fig. 7.2 and evaluated the gate error rates for T, S, and H from the fidelity in Eq. (7.5). For the Hadamard gate, we used the symmetric pulse shape

$$\epsilon(t) = \left\{ \begin{array}{c} \epsilon_0 + \frac{\Delta\epsilon}{2}\tanh\left(\frac{2[t-2\tau]}{\tau}\right), 0 < t < \frac{t_s}{2} \\ \epsilon_0 + \frac{\Delta\epsilon}{2}\tanh\left(\frac{2[t_s-2\tau-t]}{\tau}\right), \frac{t_s}{2} < t < t_s \end{array} \right., \tag{7.12}$$

where $\epsilon_0 = (\epsilon_A + \epsilon_B)/2$ and $\Delta\epsilon = \epsilon_B - \epsilon_A$. The pulse time t_p and rise/fall time $\tau = (t_s - t_p)/4$ were fixed using

$$t_p = \frac{\pi\hbar}{2b_2^x}; \quad \pi\hbar = \int_0^{t_s} \Delta_z(t)dt, \tag{7.13}$$

where the solution to the above integral equation was found numerically. The results of our numerics are shown in Fig. 7.3. We find good agreement between the predicted error rates for S and T gates in the limit of large b_2^x (the saturation values for η at low b_2^x are consistent with our estimates of $\sim 10^{-4}$ for error due to leakage). Additionally, we find reasonable agreement with our estimate for the H-gate error rate, confirming that we have identified the dominant error mechanisms, which gives us confidence that an error rate on the order of $\sim 10^{-3}$ should be achievable with this proposal.

Appendix A

Self-energy expansion

To expand the self-energy superoperator Σ_S in powers of L_V, we have found it convenient to work in terms of a superoperator matrix representation. Here we give a brief description of its use and apply it to generate the reduced self-energy at second order in L_V for all spin components, and the fourth order for the longitudinal spin.

Any operator $\mathcal{O}$ that acts on both the electron spin and nuclear spin Hilbert spaces can be written in terms of the 2×2 identity, σ_0, and the Pauli matrices σ_i, $i = (x, y, z)$:

$$\mathcal{O} = \sum_{i=(0,x,y,z)} c_i \sigma_i \tag{A.1}$$

where the coefficients c_i are operators that act only on the nuclear spin space. Equivalently, $\mathcal{O}$ can be written in terms of the operators $\rho_{\uparrow/\downarrow} = \frac{1}{2}(\sigma_0 \pm \sigma_z)$, $S_\pm = \frac{1}{2}(\sigma_x \pm i\sigma_y)$, i.e.:

$$\mathcal{O} = k_\uparrow \rho_\uparrow + k_\downarrow \rho_\downarrow + k_+ S_- + k_- S_+ \tag{A.2}$$

with operators k_j that act on the nuclear spin space. We have labeled the coefficients k_j in this way so that when $\mathcal{O} = \rho_S$ is the electron spin density operator, $k_\pm = \langle S_\pm \rangle$. A superoperator $\mathcal{S}$ acting on $\mathcal{O}$ maps it to the operator $\mathcal{O}'$ with new coefficients:

$$\mathcal{S}\mathcal{O} = \mathcal{O}' = k'_\uparrow \rho_\uparrow + k'_\downarrow \rho_\downarrow + k'_+ S_- + k'_- S_+. \tag{A.3}$$

This allows us to write $\mathcal{O}$ as a vector and $\mathcal{S}$ as a 4×4 matrix, the elements of which are superoperators that act on the nuclear spin space, and are determined by (A.2) and (A.3):

$$\vec{\mathcal{O}} = (k_\uparrow, k_\downarrow, k_+, k_-)^T \tag{A.4}$$

$$\vec{\mathcal{O}}' = \left(k'_\uparrow, k'_\downarrow, k'_+, k'_-\right)^T, \tag{A.5}$$

$\vec{\mathcal{O}}' = [\mathcal{S}]\,\vec{\mathcal{O}}$ and $k'_\alpha = \sum_\beta \mathcal{S}_{\alpha\beta} k_\beta$, where $\alpha, \beta = \uparrow, \downarrow, +, -$.

Laplace transforming the reduced self-energy given in (3.26) yields

$$\Sigma_S(s) = -i\mathrm{Tr}_I L \frac{1}{s + iQL} L_V \rho_I(0), \tag{A.6}$$

which is expanded in powers of L_V

$$\frac{1}{s+iQL}=\sum_{k=0}^{\infty}\frac{1}{s+iQL_0}\left(-iQL_V\frac{1}{s+iQL_0}\right)^k. \tag{A.7}$$

To obtain these higher order terms in the self-energy, we form products of the free propagator $\frac{1}{s+iQL_0}$ and the perturbation QL_V. The free propagator is diagonal in the basis of $\left\{\rho_{\uparrow/\downarrow},\, S_\pm\right\}$, and is given in terms of 2×2 blocks by

$$\left[\frac{1}{s+iQL_0}\right] = \left(\begin{array}{cc} G_I^0(s) & 0 \\ 0 & G_I^{0\prime}(s)\end{array}\right), \tag{A.8}$$

where

$$\begin{aligned} G_I^0(s) &= \left(\begin{array}{cc} G_\uparrow^0(s) & 0 \\ 0 & G_\downarrow^0(s)\end{array}\right), & \text{(A.9)}\\ G_I^{0\prime}(s) &= \left(\begin{array}{cc} G_+^0(s) & 0 \\ 0 & G_-^0(s)\end{array}\right). & \text{(A.10)}\end{aligned}$$

In the above,

$$\begin{aligned} G_{\uparrow/\downarrow}^0(s) &= \frac{1}{s\pm i\frac{Q}{2}L_\omega^-}, & \text{(A.11)}\\ G_\pm^0(s) &= \frac{1}{s\mp i\frac{Q}{2}L_\omega^+}, & \text{(A.12)}\end{aligned}$$

where we define the new (nuclear spin) Liouvillians by their action on an arbitrary operator $\mathcal{O}$: $L_\omega^\pm\mathcal{O}=[\omega,\mathcal{O}]_\pm$, $\omega=b'+h_z$. The perturbation term contains only off-diagonal elements when written in terms of 2×2 blocks:

$$[QL_V] = \left(\begin{array}{cc} 0 & V_I \\ V_I' & 0\end{array}\right), \tag{A.13}$$

where we find

$$V_I=\frac{Q}{2}\left(\begin{array}{cc} h_-^L & -h_+^R \\ -h_-^R & h_+^L\end{array}\right),\quad V_I'=\frac{Q}{2}\left(\begin{array}{cc} h_+^L & -h_+^R \\ -h_-^R & h_-^L\end{array}\right). \tag{A.14}$$

In the above expression, we have introduced superoperators for right and left multiplication:

$$\begin{aligned} \mathcal{O}^R\mathcal{A} &= \mathcal{A}\mathcal{O} & \text{(A.15)}\\ \mathcal{O}^L\mathcal{A} &= \mathcal{O}\mathcal{A}. & \text{(A.16)}\end{aligned}$$

Only even powers of L_V can contribute to the final trace over the nuclear system, so we consider a general term in the expansion of the self-energy

$$\left([QL_V]\left[\frac{1}{s+iQL_0}\right]\right)^{2k} = \left(\begin{array}{cc} \Sigma_k & 0 \\ 0 & \Sigma_k'\end{array}\right), \tag{A.17}$$

$$\Sigma_k=\left(V_IG_I^{0\prime}V_I'G_I^0\right)^k,\quad \Sigma_k'=\left(V_I'G_I^0V_IG_I^{0\prime}\right)^k. \tag{A.18}$$

By inspection of the form of V_I, V_I', we find that the 2×2 matrix $\mathrm{Tr}_I\Sigma_k'\rho_I(0)$ is diagonal when $\rho_I(0) = |n\rangle\langle n|$, and $|n\rangle$ is an eigenstate of h_z (as in Eq. (3.20)), since the off-diagonal components always contain terms proportional to h_+^2 or h_-^2. Thus, to all orders in the perturbation L_V, the reduced self-energy takes the form

$$\Sigma_S(s) = \begin{pmatrix} \Sigma_{\uparrow\uparrow}(s) & \Sigma_{\uparrow\downarrow}(s) & 0 & 0 \\ \Sigma_{\downarrow\uparrow}(s) & \Sigma_{\downarrow\downarrow}(s) & 0 & 0 \\ 0 & 0 & \Sigma_{++}(s) & 0 \\ 0 & 0 & 0 & \Sigma_{--}(s) \end{pmatrix}. \tag{A.19}$$

The number of matrix elements left to calculate can be further reduced with the relationships $\Sigma_{\uparrow\uparrow}(s) = -\Sigma_{\downarrow\uparrow}(s)$, $\Sigma_{\uparrow\downarrow}(s) = -\Sigma_{\downarrow\downarrow}(s)$, which follow directly from the condition $\mathrm{Tr}\dot{\rho}_S = 0 \Rightarrow \dot{\rho}_\uparrow(t) = -\dot{\rho}_\downarrow(t)$ and the GME $\dot{\rho}_\alpha = -i\sum_{\beta=\uparrow,\downarrow}\int_0^t dt'\Sigma_{\alpha\beta}(t-t')\rho_\beta(t')$, $\alpha = \uparrow,\downarrow$. By direct calculation we find

$$\begin{aligned}
\Sigma_{\uparrow\uparrow}^{(2)}(s) &= -\frac{i}{4}\sum_k [h_-]_{nk}[h_+]_{kn}\left(\frac{1}{s-i\bar{\omega}_{nk}} + \frac{1}{s+i\bar{\omega}_{nk}}\right) && \text{(A.20)}\\
\Sigma_{\uparrow\downarrow}^{(2)}(s) &= \frac{i}{4}\sum_k [h_+]_{nk}[h_-]_{kn}\left(\frac{1}{s-i\bar{\omega}_{nk}} + \frac{1}{s+i\bar{\omega}_{nk}}\right) && \text{(A.21)}\\
\Sigma_{++}^{(2)}(s) &= -\frac{i}{4}\sum_k \left([h_+]_{nk}[h_-]_{kn} + [h_-]_{nk}[h_+]_{kn}\right)\frac{1}{s-i\delta\omega_{nk}}. && \text{(A.22)}
\end{aligned}$$

In the above, $\bar{\omega}_{nk} = \frac{1}{2}(\omega_n + \omega_k)$, $\delta\omega_{nk} = \frac{1}{2}(\omega_n - \omega_k)$, and $\omega_j = b' + [h_z]_{jj}$. At fourth order,

$$\begin{aligned}
&\Sigma_{\uparrow\uparrow}^{(4)}(s) = \\
&\frac{i}{16}\left\{\sum_{k_1k_2k_3}[h_-]_{nk_3}[h_+]_{k_3k_2}[h_-]_{k_2k_1}[h_+]_{k_1n}\left((1-\delta_{nk_2})\sigma_{4A}^{k_1k_2k_3}(s) + \sigma_{4B}^{k_1k_2k_3}(s)\right)\right.\\
&\qquad\left. -\frac{1}{s}\sum_{k_1k_2}[h_-]_{nk_2}[h_+]_{k_2n}[h_+]_{nk_1}[h_-]_{k_1n}\,\sigma_{4C}^{k_1k_2}(s)\right\}, \qquad \text{(A.23)}
\end{aligned}$$

$$\begin{aligned}
&\Sigma_{\uparrow\downarrow}^{(4)}(s) = \\
&-\frac{i}{16}\left\{\sum_{k_1k_2k_3}[h_+]_{nk_3}[h_-]_{k_3k_2}[h_+]_{k_2k_1}[h_-]_{k_1n}\left((1-\delta_{nk_2})\bar{\sigma}_{4A}^{k_1k_2k_3}(s) + \bar{\sigma}_{4B}^{k_1k_2k_3}(s)\right)\right.\\
&\qquad\left. -\frac{1}{s}\sum_{k_1k_2}[h_+]_{nk_2}[h_-]_{k_2n}[h_-]_{nk_1}[h_+]_{k_1n}\,\sigma_{4C}^{k_1k_2}(s)\right\}, \qquad \text{(A.24)}
\end{aligned}$$

where the overbar indicates complex conjugation for s real and

$$\begin{aligned}
\sigma_{4A}^{k_1k_2k_3}(s) = &\frac{1}{s-i\delta\omega_{nk_2}}\frac{1}{s-i\bar{\omega}_{nk_1}}\left(\frac{1}{s-i\bar{\omega}_{nk_3}} + \frac{1}{s+i\bar{\omega}_{k_2k_3}}\right)\\
&+\frac{1}{s+i\delta\omega_{nk_2}}\frac{1}{s+i\bar{\omega}_{nk_3}}\left(\frac{1}{s+i\bar{\omega}_{nk_1}} + \frac{1}{s-i\bar{\omega}_{k_1k_2}}\right), \qquad \text{(A.25)}
\end{aligned}$$

$$\sigma_{4B}^{k_1k_2k_3}(s) =$$

$$\frac{1}{s - i\delta\omega_{k_1k_3}} \left(\frac{1}{s - i\bar{\omega}_{k_1k_2}} + \frac{1}{s + i\bar{\omega}_{k_2k_3}} \right) \left(\frac{1}{s + i\bar{\omega}_{nk_3}} + \frac{1}{s - i\bar{\omega}_{k_1n}} \right), \quad \text{(A.26)}$$

$$\sigma_{4C}^{k_1k_2}(s) = \frac{4s^2}{\left(s^2 + \bar{\omega}_{nk_1}^2\right)\left(s^2 + \bar{\omega}_{nk_2}^2\right)}. \quad \text{(A.27)}$$

Every two powers of the perturbation L_V are associated with an additional sum over $\approx N$ nuclear spin sites, since every spin flip up must be paired with a flop down. Non-analyticities (poles) of the self-energy occur in two regions of the complex plane: at high frequencies, near $s \approx \pm i\omega_n$, and at low frequency, around $s \approx 0$. Expanding near either of these two points gives an extra factor $\frac{1}{\omega_n}$ for every two orders of $QL_V \frac{1}{s - iQL_0}$. The self-energy at $(2k)^{\text{th}}$ order is then suppressed at least by the factor Δ^k, where $\Delta = \frac{N}{\omega_n}$:

$$\Sigma_S^{(2k)}(s) \quad \propto \quad \Delta^k, \quad \text{(A.28)}$$

$$\Sigma_S^{(2k)}(s - i\omega_n) \quad \propto \quad \Delta^k. \quad \text{(A.29)}$$

Thus, in general, for the perturbation series to be well-controlled, we require $|\Delta| \ll 1$.

Appendix B

Coefficients $c_{\pm}$

We are interested in evaluating the expressions given in Eqs. (A.20), (A.21), and (A.22). To do this, we investigate objects of the form

$$\sum_{k} [h_{\pm}]_{nk} \, [h_{\mp}]_{kn} \, f_{\mp}(k), \tag{B.1}$$

where $f_{\mp}(k)$ is a function of the state index k. Inserting $|n\rangle$, as given in Eq. (3.20), into (B.1), we find

$$\sum_{k} [h_{\pm}]_{nk} \, [h_{\mp}]_{kn} \, f_{\mp}(k) = \sum_{k} A_k^2 c_{\mp}^k f_{\mp}(k), \tag{B.2}$$

where the state index k now labels sites at which a nuclear spin has been raised or lowered, and with the help of the matrix elements: $\langle I, m \pm 1| \, I^{\pm} \, |I, m\rangle = \sqrt{(I \mp m)(I \pm m + 1)}$, we have

$$c_{\pm}^k = \sum_{j=1}^{g_n} |\alpha_j|^2 \left[I(I+1) - m_k^j (m_k^j \pm 1) \right]. \tag{B.3}$$

We assume the initial nuclear system is uniform, so that $c_{\pm}^k$ is independent of the site index k, and for a large number of degenerate states $g_n \gg 1$ that contribute to $|n\rangle$, we replace the sum over weighting factors $|\alpha_j|^2$ by an appropriate probability distribution. This gives $c_{\pm}^k = c_{\pm}$ with $c_{\pm}$ defined in Eq. (3.38) of the main text.

Appendix C

Continuum limit

Here, we find a rigorous bound on corrections to the memory kernels, after we have changed sums to integrals. We consider the real-time version of the functions $I_{\pm}(s)$, given in (3.37), with coupling constants for a Gaussian wave function in two dimensions ($m = d = 2$ in Eq. (3.9)):

$$I_{\pm}(t) = \frac{1}{4N} \sum_k A_k^2 e^{\pm i A_k t/2},\ A_k = 2e^{-k/N}. \tag{C.1}$$

The Euler-MacLauren formula gives an upper bound to the corrections involved in the transformation of sums to integrals for a summand that is a smooth monotonic function of its argument. For times $t \gg 1$, the summand of $I_{\pm}(t)$ is not monotonic on the interval $k = 1, \ldots, N$, where it has appreciable weight. We divide the sum into t subintervals of width $\Delta k \approx \frac{N}{t}$. The summand is then monotonic over each of the t subintervals, and the Euler-MacLauren formula gives a remainder $R \leq \frac{2}{N}$ when the sum over each subinterval is changed to an integral. Adding the errors incurred for each subinterval, we find (for $t \gg 1$):

$$I_{\pm}(t) = \left[\left(e^{\pm it} - 1 \right) \frac{1}{t^2} \mp \frac{i e^{\pm it}}{t} \right] + R(t). \tag{C.2}$$

The remainder term $|R(t)| \leq \frac{2t}{N}$, so the corrections can become comparable to the amplitude of the integral itself when $t \approx \sqrt{N/2}$. This represents a strict lower bound to the time scale where the continuum limit is valid for $m = d = 2$.

Appendix D

Perturbation theory

In this Appendix we apply standard perturbation theory to the problem of finding the electron spin dynamics. We do this to illustrate the connection between our perturbative expansion of the self-energy and the standard one, and to demonstrate the need for a non-perturbative approach.

We choose the initial state

$$\left|i\right\rangle = \left(\sqrt{\rho_\uparrow(0)}\left|\uparrow\right\rangle + e^{i\phi}\sqrt{1-\rho_\uparrow(0)}\left|\downarrow\right\rangle\right) \otimes \left|n\right\rangle, \tag{D.1}$$

where $\left|n\right\rangle$ is an eigenstate of h_z and

$$\begin{aligned} \left\langle S_z\right\rangle_0 &= \frac{1}{2}\left(\rho_\uparrow(0) - \rho_\downarrow(0)\right), & \text{(D.2)} \\ \left\langle S_+\right\rangle_0 &= \sqrt{\rho_\uparrow(0)\left(1-\rho_\downarrow(0)\right)}e^{i\phi}. & \text{(D.3)} \end{aligned}$$

We then apply standard interaction picture perturbation theory to evaluate $\left\langle S_X\right\rangle_t$, $X = +, z$. To lowest nontrivial (second) order in the perturbation $\mathcal{H}_V$, we find

$$\begin{aligned} \left\langle S_+\right\rangle_t = e^{i\omega_n t}\left\langle S_+\right\rangle_0 & \\ - \frac{\left\langle S_+\right\rangle_0}{4}\sum_k &\left(\left[h_-\right]_{nk}\left[h_+\right]_{kn} g_k^-(t) + \left[h_+\right]_{nk}\left[h_-\right]_{kn} g_k^+(t)\right) \end{aligned} \tag{D.4}$$

$$g_k^\pm = \frac{te^{i\omega_n t}}{i\bar{\omega}_{nk}} - \frac{1}{\bar{\omega}_{nk}^2}\left(e^{\pm i\frac{A_k}{2}t} - e^{i\omega_n t}\right) \tag{D.5}$$

$$\begin{aligned} \left\langle S_z\right\rangle_t = \left\langle S_z\right\rangle_0 + \frac{1}{2}\sum_k &\left[\left(1-\rho_\uparrow(0)\right)\left[h_+\right]_{nk}\left[h_-\right]_{kn}\right. \\ &\left. - \rho_\uparrow(0)\left[h_-\right]_{nk}\left[h_+\right]_{kn}\right]\frac{\left[1-\cos\left(\bar{\omega}_{nk}t\right)\right]}{\bar{\omega}_{nk}^2}. \end{aligned} \tag{D.6}$$

The expression for $\left\langle S_z\right\rangle_t$ has been given previously, [15,17] where it was noted that the perturbative expression for the transverse components $\left\langle S_+\right\rangle_t$ contains a term that grows unbounded in time (as above). Inserting an initial nuclear state $|n\rangle$ with uniform polarization, performing the continuum limit, and expanding to leading order in $\frac{1}{\omega_n}$ gives the final result, presented in Eqs. (3.44) and (3.45).

Appendix E

Branch cut asymptotics

E.1 Long times

Here we give explicit expressions for the leading-order terms in asymptotic expansions of the branch cut integrals for long times

$$K_0^z(t\to\infty) = -i\frac{\pi}{(c_+ + c_-)N}\left[2\left\langle S_z\right\rangle_0 - \Delta(c_+ + c_-)\right]\frac{1}{\ln t} + O\left(\frac{1}{\ln^2 t}\right),\ b' = 0, \quad \text{(E.1)}$$

$$K_0^z(t\to\infty) = \frac{i\pi}{b'}\left[\frac{N}{b'}(c_+ + c_-)\left[2\left\langle S_z\right\rangle_0 - \Delta\right] - 2pI\Delta\right]\frac{1}{t^2} + O\left(\frac{1}{t^3}\right),\ b' \neq 0, \quad \text{(E.2)}$$

$$K_\pm^z(t\to\infty) = \mp\frac{\pi e^{\pm it}}{Nc_\mp}\left[2\left\langle S_z\right\rangle_0 \mp \Delta\left(\frac{b'}{N} \pm (c_+ + c_-) \mp c_\pm 2\ln 2\right)\right]\frac{1}{t\ln^2 t} + O\left(\frac{1}{t\ln^3 t}\right), \quad \text{(E.3)}$$

$$\begin{aligned}
K_0^+(t\to\infty) &= -i\frac{2\pi}{(c_+ + c_-)N}\left\langle S_+\right\rangle_0\frac{1}{\ln t} + O\left(\frac{1}{\ln^2 t}\right),\ b' = 0, && \text{(E.4)}\\
K_0^+(t\to\infty) &= i2\pi(c_+ + c_-)\frac{N}{(b')^2}\left\langle S_+\right\rangle_0\frac{1}{t^2} + O\left(\frac{1}{t^3}\right),\ b' \neq 0, && \text{(E.5)}\\
K_\pm^+(t\to\infty) &= \mp\frac{2\pi e^{\pm it}}{Nc_\mp}\left\langle S_+\right\rangle_0\frac{1}{t\ln^2 t} + O\left(\frac{1}{t\ln^3 t}\right). && \text{(E.6)}
\end{aligned}$$

E.2 High fields

For asymptotically large magnetic fields, the x-dependence of the denominator term $D(-x+\gamma_\alpha \pm i\eta)$ that appears in the branch cut integrals (Eq. (3.75)) is dominated by the constant contribution $\sim -i\omega_n$, except at very large values of x, where it may be that $D(-x+\gamma_\alpha \pm i\eta) \approx 0$. We expand the numerator $N_z(s_\alpha^X(x) \pm i\eta)$ and denominator in $\frac{1}{x}$, retaining terms up to $\mathcal{O}(1)$ in the numerator and $\mathcal{O}\left(\frac{1}{x}\right)$ in the denominator. Expanding to leading order in $\frac{1}{x_0} \propto \frac{1}{\omega_n}$, except where there is the possibility of a near-singular contribution ($D \simeq 0$), and assuming $b' > 0$, we find the branch cut integrals

$$
\begin{aligned}
K_+^X(t) &\simeq 2\pi i\delta C_-^X x_0 \int_{-i}^{-i+\infty} dz \frac{ze^{-zt}}{z-z_0} && \text{(E.7)}\\
K_0^X(t) &\simeq -2\pi i\delta \left(C_+^X + C_-^X\right) x_0 \int_0^\infty dz \frac{ze^{-zt}}{z-z_0} && \text{(E.8)}\\
K_-^X(t) &\simeq -2\pi i\delta C_+^X \int_i^{i+\infty} dz z e^{-zt} && \text{(E.9)}
\end{aligned}
$$

where z_0 and x_0 are defined in Eqs. (3.81) and (3.82). The coefficients $C_\pm^X$ are given by Eq. (3.51). The sum over all three branch cut integrals can now be written in terms of two contour integrals

$$
\sum_{\alpha=(0,+,-)} K_\alpha^X(t) = -2\pi i\delta C_-^X x_0 \int_{C''} dz \frac{ze^{-zt}}{z-z_0} - 2\pi i\delta C_+^X \int_{C'} dz z e^{-zt}. \qquad \text{(E.10)}
$$

C'' runs clockwise from the origin to $z = \infty$ along the real axis, then returns to $z = -i$, enclosing the pole at $z = z_0$. C' runs from $z = i$ to $z = i + \infty$, then returns along the real axis to $z = 0$. These integrals can be evaluated immediately by closing the contours along the imaginary axis. The sum of the contributions along the imaginary axis and from the residue of the pole at $z = z_0$ gives the result in Eq. (3.80).

Appendix F

Estimating the Overhauser field

In this appendix we estimate the size of the Overhauser field inhomogeneity for a typical double quantum dot, and show that this quantity depends, in a sensitive way, on the form of the orbital wavefunctions.

As in the main text, we take the average Overhauser field and the Overhauser field inhomogeneity to be $\mathbf{h} = \frac{1}{2}\left(\mathbf{h}_1 + \mathbf{h}_2\right)$ and $\delta\mathbf{h} = \frac{1}{2}\left(\mathbf{h}_1 - \mathbf{h}_2\right)$ respectively, where $\mathbf{h}_l = Av\sum_k \left|\psi_0^l(\mathbf{r}_k)\right|^2 \mathbf{I}_k$, and $\psi_0^l(\mathbf{r})$ is orbital eigenstate l in the double quantum dot. In the presence of tunneling, the eigenstates of a symmetric double quantum dot will be well-described [14, 39] by the symmetric and antisymmetric linear combination of dot-localized states $\phi_l(\mathbf{r})$, $l = 1, 2$: $\psi_0^{1,2}(\mathrm{r}) = \frac{1}{\sqrt{2}}\left(\phi_1(\mathrm{r}) \pm \phi_2(\mathrm{r})\right)$. In this case, we find

$$\langle\delta\mathbf{h}\rangle_{\mathrm{rms}} = Av\left\langle\sum_k \mathrm{Re}\left[\phi_1^*(\mathbf{r}_k)\phi_2(\mathbf{r}_k)\right]\mathbf{I}_k\right\rangle_{\mathrm{rms}}. \tag{F.1}$$

We take $\left\langle\frac{1}{N}\sum_k \mathbf{I}_k\right\rangle_{\mathrm{rms}} \approx \sqrt{I(I+1)/N}$ to be the r.m.s. value for a system of N nuclear spins with uniform polarization $p \ll 1$. Changing the sum to an integral according to $v\sum_k \to \int d^3r$ then gives

$$\langle\delta\mathbf{h}\rangle_{\mathrm{rms}} \approx \gamma\sqrt{\frac{I(I+1)}{N}}A = \gamma\alpha, \tag{F.2}$$

where $\gamma = \int d^3r\,\mathrm{Re}\left[\phi_1^*(\mathbf{r})\phi_2(\mathbf{r})\right]$ is the overlap of the localized orbital dot states and we have introduced the energy scale $\alpha = \sqrt{I(I+1)}A/\sqrt{N}$. The result in Eq. (F.2) suggests that the Overhauser field inhomogeneity can be drastically reduced in a symmetric double quantum dot simply by separating the two dots, reducing the wavefunction overlap. If, however, the double dot is sufficiently asymmetric, the correct orbital eigenstates will be well-described by localized states $\psi_0^l(\mathrm{r}) = \phi_l(\mathrm{r}),\ l = 1, 2$, (with overlap $\gamma \ll 1$), in which case we find

$$\langle\delta\mathbf{h}\rangle_{\mathrm{rms}} \approx \sqrt{\frac{I(I+1)}{N}}A = \alpha. \tag{F.3}$$

Thus, great care should be taken in determining $\langle \delta\mathbf{h} \rangle_{\mathrm{rms}}$ based on microscopic parameters. In particular, for a symmetric double quantum dot, the overlap γ must also be known to determine $\langle \delta\mathbf{h} \rangle_{\mathrm{rms}}$ based on N.

In contrast, for the total Overhauser operator $\mathbf{h}$, in both of the above cases ($\psi_0^{1,2}(\mathrm{r}) = \frac{1}{\sqrt{2}}\left(\phi_1(\mathrm{r}) \pm \phi_2(\mathrm{r})\right)$ or $\psi_0^l(\mathrm{r}) = \phi_l(\mathrm{r}),\ l = 1, 2$), we find

$$\langle \mathbf{h} \rangle_{\mathrm{rms}} \approx \sqrt{\frac{I(I+1)}{N}} A = \alpha. \tag{F.4}$$

Appendix G

Effective Hamiltonians for two-electron states in a double quantum dot

In this appendix we derive effective Hamiltonians for a two-electron system interacting with nuclear spins in a double quantum dot via the contact hyperfine interaction.

We begin from the two-electron Hamiltonian in second-quantized form,

$$H = H_{SP} + H_C + H_T + H_Z + H_{\mathrm{hf}}, \tag{G.1}$$

where H_{SP} describes the single-particle charging energy, H_C models the Coulomb interaction between electrons in the double dot, H_T describes tunneling between dot orbital states, H_Z gives the electron Zeeman energy (we neglect the nuclear Zeeman energy, which is smaller by the ratio of nuclear to Bohr magneton: $\mu_N/\mu_B \sim 10^{-3}$) and H_{hf} describes the Fermi contact hyperfine interaction between electrons on the double dot and nuclei in the surrounding lattice. Explicitly, these terms are given by

$$\begin{aligned}
H_{SP} &= \sum_{l\sigma} V_{gl} n_{l\sigma}; \quad n_{l\sigma} = d_{l\sigma}^{\dagger} d_{l\sigma}, && \text{(G.2)}\\
H_C &= U \sum_l n_{l\uparrow} n_{l\downarrow} + U'(n_{1\uparrow} + n_{1\downarrow})(n_{2\uparrow} + n_{2\downarrow}), && \text{(G.3)}\\
H_T &= t_{12} \sum_{\sigma} \left(d_{1\sigma}^{\dagger} d_{2\sigma} + d_{2\sigma}^{\dagger} d_{1\sigma} \right), && \text{(G.4)}\\
H_Z &= \frac{\epsilon_z}{2} \sum_l (n_{l\uparrow} - n_{l\downarrow}), && \text{(G.5)}\\
H_{\mathrm{hf}} &= \sum_l \mathbf{S}_l \cdot \mathbf{h}_l; \quad \mathbf{S}_l = \frac{1}{2} \sum_{\sigma\sigma'} d_{l\sigma}^{\dagger} \boldsymbol{\sigma}_{\sigma\sigma'} d_{l\sigma'}. && \text{(G.6)}
\end{aligned}$$

Here, $d_{l\sigma}^{\dagger}$ creates an electron with spin σ in orbital state l ($l = 1, 2$), V_{gl} is the single-particle charging energy for orbital state l, U is the two-particle charging energy for two electrons in the same orbital state, and U' is the two-particle charging energy when there is one electron in each orbital. When the orbital eigenstates are localized states in quantum dot $l = 1, 2$, V_{gl} is supplied by the back-gate voltage on dot l and U (U') is the on-site (nearest-neighbor) charging energy. t_{12} is the hopping matrix element between the two orbital states, ϵ_z is the electron Zeeman splitting, $\mathbf{h}_l$ is the nuclear field (Overhauser operator) for an electron in orbital l, and $\boldsymbol{\sigma}_{\sigma\sigma'}$ gives the matrix elements of the vector of Pauli matrices $\boldsymbol{\sigma} = (\sigma_x, \sigma_y, \sigma_z)$. In the subspace of two electrons occupying two orbital states, the spectrum of $H_{SP} + H_C$ consists of four degenerate "delocalized" states with one electron in each orbital, all with unperturbed energy $E_{(1,1)}$ (a singlet $|S(1,1)\rangle$ and three triplets: $|T_j(1,1)\rangle$; $j = \pm, 0$), and two non-degenerate "localized" singlet states $|S(2,0)\rangle$ and $|S(0,2)\rangle$, with two electrons in orbital $l = 1$ or $l = 2$, having energy $E_{(2,0)}$ and $E_{(0,2)}$, respectively.

To derive an effective Hamiltonian H_{eff} from a given Hamiltonian H, which has a set of nearly degenerate levels $\{|i\rangle\}$, we use the standard procedure [172],

$$H_{\text{eff}} = PHP + PHQ\frac{1}{E - QHQ}QHP, \tag{G.7}$$

where $P = \sum_i |i\rangle\langle i|$ is a projection operator onto the relevant subspace and $Q = 1 - P$ is its complement.

We choose the arbitrary zero of energy such that $E_{(1,1)} = V_{g1} + V_{g2} + U' = 0$ and introduce the detuning parameters

$$\delta_1 = E_{(1,1)} - E_{(2,0)} = -2V_{g1} - U = -\delta - U - U', \tag{G.8}$$

$$\delta_2 = E_{(1,1)} - E_{(0,2)} = -2V_{g2} - U = \delta. \tag{G.9}$$

We then project onto the four-dimensional subspace formed by the delocalized singlet $|S(1,1)\rangle$ and three delocalized triplet states $|T_j(1,1)\rangle$, $j = \pm, 0$. That is, we choose $Q = |S(0,2)\rangle\langle S(0,2)| + |S(2,0)\rangle\langle S(2,0)|$, $P = 1 - Q$. When $\delta_1, \delta_2 \gg t_{12}$, we have $E \approx E_{(1,1)} = 0$ in the denominator of Eq. (G.7). This gives an effective spin Hamiltonian in the subspace of one electron in each orbital state:

$$H_{\text{eff}} = \epsilon_z \sum_l S_l^z + \sum_l \mathbf{h}_l \cdot \mathbf{S}_l - J\left(\frac{1}{4} - \mathbf{S}_1 \cdot \mathbf{S}_2\right), \tag{G.10}$$

$$J \approx -2t_{12}^2\left(\frac{1}{\delta} - \frac{1}{\delta + U + U'}\right). \tag{G.11}$$

This Hamiltonian is more conveniently rewritten in terms of the sum and difference vectors of the electron spin and Overhauser operators $\mathbf{S} = \mathbf{S}_1 + \mathbf{S}_2$, $\delta\mathbf{S} = \mathbf{S}_1 - \mathbf{S}_2$ and $\mathbf{h} = \frac{1}{2}(\mathbf{h}_1 + \mathbf{h}_2)$, $\delta\mathbf{h} = \frac{1}{2}(\mathbf{h}_1 - \mathbf{h}_2)$:

$$H_{\text{eff}} = \epsilon_z S^z + \mathbf{h} \cdot \mathbf{S} + \delta\mathbf{h} \cdot \delta\mathbf{S} + \frac{J}{2}\mathbf{S} \cdot \mathbf{S} - J. \tag{G.12}$$

Neglecting the constant term, in the basis of singlet and three triplet states, $\{|S(1,1)\rangle = |S\rangle, |T_j(1,1)\rangle = |T_j\rangle, j = \pm, 0\}$, the Hamiltonian matrix for H_{eff} takes the form

$$\begin{pmatrix} 0 & -\delta h^+/\sqrt{2} & \delta h^z & \delta h^-/\sqrt{2} \\ -\delta h^-/\sqrt{2} & J + \epsilon_z + h^z & h^-/\sqrt{2} & 0 \\ \delta h^z & h^+/\sqrt{2} & J & h^-/\sqrt{2} \\ \delta h^+/\sqrt{2} & 0 & h^+/\sqrt{2} & J - \epsilon_z - h^z \end{pmatrix}, \tag{G.13}$$

where $\delta h^\pm = \delta h^x \pm i\delta h^y$ and $h^\pm = h^x \pm ih^y$. We are interested in this Hamiltonian in two limiting cases, where it becomes block-diagonal in a two-dimensional subspace.

G.1 Effective Hamiltonian in the $|S\rangle - |T_0\rangle$ subspace

Projecting H onto the two-dimensional subspace spanned by $|T_0\rangle \rightarrow |\tau^z = +1\rangle$ and $|S\rangle \rightarrow |\tau^z = -1\rangle$, we find

$$H_0 = N_0 + \frac{1}{2}\mathbf{v}_0 \cdot \boldsymbol{\tau}, \tag{G.14}$$

where $\boldsymbol{\tau} = (\tau^x, \tau^y, \tau^z)$ is a vector of Pauli matrices. The leading and first subleading corrections to H_0 in powers of $1/\epsilon_z$ are ($H_0 = H_0^{(0)} + H_0^{(1)} + \cdots$, $H_0^{(i)} = N_0^{(i)} + \mathbf{v}_0^{(i)}$):

$$\begin{aligned}
N_0^{(0)} &= \frac{J}{2}, && \text{(G.15)}\\
v_0^{z(0)} &= J, && \text{(G.16)}\\
v_0^{+(0)} &= 2\delta h^z, && \text{(G.17)}\\
N_0^{(1)} &= \frac{1}{4\epsilon_z}\left(\left[h^-, h^+\right] + \left[\delta h^-, \delta h^+\right]\right), && \text{(G.18)}\\
v_0^{z(1)} &= \frac{1}{2\epsilon_z}\left(\left[h^-, h^+\right] - \left[\delta h^-, \delta h^+\right]\right), && \text{(G.19)}\\
v_0^{+(1)} &= \frac{1}{\epsilon_z}\left(\delta h^+ h^- + \delta h^- h^+\right). && \text{(G.20)}
\end{aligned}$$

Here, $\mathbf{N}_X = (N_X^x, N_X^y, N_X^z)$, $\mathbf{v}_X = (v_X^x, v_X^y, v_X^z)$, $N_X^\pm = N_X^x \pm iN_X^y$, and $v_X^\pm = v_X^x \pm iv_X^y$. For a typical unpolarized system, we estimate the size of all subleading corrections from their r.m.s. expectation values, taken with respect to an unpolarized nuclear state. This gives

$$\left\langle H_0^{(1)} \right\rangle_{\text{rms}} = O\left(\frac{\alpha^2}{\epsilon_z}\right), \tag{G.21}$$

where α is given by $\alpha = \sqrt{I(I+1)}A/\sqrt{N}$ (for a GaAs quantum dot containing $N \approx 10^5$ nuclear spins, $1/\alpha \approx 5\,\text{ns}$). We therefore expect dynamics calculated under $H_0^{(0)}$ to be valid up to timescales on the order of $\epsilon_z/\alpha^2 \gg 1/\alpha$, when $\epsilon_z \gg \alpha$.

G.2 Effective Hamiltonian in the $|S\rangle - |T_+\rangle$ subspace

When the Zeeman energy of the $|T_+\rangle$ triplet state approximately compensates the exchange, $\max\left(\langle \mathbf{h} \rangle_{\text{rms}}, \langle \delta\mathbf{h} \rangle_{\text{rms}}, |\Delta|\right) \ll J$ (where $\Delta = \epsilon_z + J$), we find an effective Hamiltonian in the subspace $|T_+\rangle \rightarrow |\tau^z = +1\rangle$, $|S\rangle \rightarrow |\tau^z = -1\rangle$:

$$H_+ = N_+ + \frac{1}{2}\mathbf{v}_+ \cdot \boldsymbol{\tau}, \tag{G.22}$$

where the leading and subleading corrections in powers of $1/J$ are

$$\begin{aligned}
N_+^{(0)} &= \frac{1}{2}\left(\Delta + h^z\right), && \text{(G.23)}\\
v_+^{z(0)} &= \Delta + h^z, && \text{(G.24)}\\
v_+^{+(0)} &= -\sqrt{2}\delta h^+, && \text{(G.25)}\\
N_+^{(1)} &= -\frac{1}{2J}\left(\left(\delta h^z\right)^2 + \frac{1}{4}\delta h^- \delta h^+ + \frac{1}{2} h^- h^+\right), && \text{(G.26)}\\
v_+^{z(1)} &= \frac{1}{J}\left(\left(\delta h^z\right)^2 + \frac{1}{4}\delta h^- \delta h^+ - \frac{1}{2} h^- h^+\right), && \text{(G.27)}\\
v_+^{+(1)} &= -\sqrt{2}\frac{\delta h^z h^+}{J}. && \text{(G.28)}
\end{aligned}$$

Once again, we estimate the influence of the subleading corrections from their r.m.s. value with respect to a nuclear spin state of polarization $p \ll 1$, giving

$$\left\langle H_+^{(1)} \right\rangle_{\mathrm{rms}} = O\left(\frac{\alpha^2}{J}\right). \tag{G.29}$$

We therefore expect the dynamics under $H_+^{(0)}$ to be valid up to time scales on the order of $t \sim J/\alpha^2 \gg 1/\alpha$ for $J \gg \alpha$.

Appendix H

Asymptotics

H.1 $C_{T_0}(\infty)$ for $J \gg 2\sigma_0$, $J \ll 2\sigma_0$

In the limit of $J \to 0$, we perform an asymptotic expansion of the integral in Eq. (4.14) by separating the prefactor into a constant piece and an unnormalized Lorentzian of width $J/2$:

$$C(x) = \frac{1}{2}\left(1 - \frac{(J/2)^2}{(J/2)^2 + x^2}\right). \tag{H.1}$$

The Gaussian average over the constant term gives 1/2 and when $J/2 \ll \sigma_0$, the typical x contributing to the Lorentzian part of Eq. (4.14) is $x \lesssim J/2 \ll \sigma_0$, so we approximate $\exp(-\frac{1}{2}x^2/\sigma_0^2) \approx 1$ in the integrand of this term. Integrating the Lorentzian then gives the result in Eq. (4.15) for $J \ll 2\sigma_0$. In the opposite limit of $J \gg 2\sigma_0$, the Lorentzian is slowly-varying with respect to the Gaussian, and the prefactor can be expanded within the integrand $C(x) \approx 2x^2/J^2$. Performing the remaining Gaussian integral gives the result in Eq. (4.15) for $J \gg 2\sigma_0$.

H.2 $C^{\mathrm{int}}_{T_0}(t)$ for $t \to \infty$

To evaluate the integral in Eq. (4.13) at long times when $J \neq 0$, we make the change of variables $u = \sqrt{\lambda^2 + (x/\sigma_0)^2} - \lambda$, $\lambda = J/2\sigma_0$, $\tilde{t} = 2\sigma_0 t$, which gives

$$\tilde{C}^{\mathrm{int}}_{T_0}(\tilde{t}/2\sigma_0) = -\frac{1}{\sqrt{2\pi}}\int_0^\infty du \frac{\sqrt{u(u+2\lambda)}}{u+\lambda}\exp\left\{-\frac{1}{2}\left(u^2 + 2u\lambda\right) + i(u+\lambda)\tilde{t}\right\}, \tag{H.2}$$

$$\lambda = J/2\sigma_0, \quad \tilde{t} = 2\sigma_0 t. \tag{H.3}$$

At long times, the major contributions to this integral come from a region near the lower limit, where $u \lesssim 1/\tilde{t}$. For $\tilde{t} \gg \max(1/\lambda, 1)$ (i.e. $t \gg \max(1/J, 1/2\sigma_0)$), we approximate the integrand by its form for $u \ll \max(\lambda, 1)$, retaining the exponential term as a cutoff. This gives

$$\tilde{C}^{\mathrm{int}}_{T_0}(\tilde{t}/2\sigma_0) \sim -\frac{e^{i\lambda\tilde{t}}}{\sqrt{\pi\lambda}}\int_0^\infty du\sqrt{u}e^{-(\lambda - i\tilde{t})u} = -\frac{e^{i\lambda\tilde{t}}}{2\sqrt{\lambda}\left(\lambda - i\tilde{t}\right)^{3/2}}. \tag{H.4}$$

When $\tilde{t} \gg \lambda$ (i.e. $t \gg J/4\sigma_0^2$), we expand the denominator of the above expression, which gives the result in Eq. (4.17).

Appendix I

Drift in δh^z

In addition to spin diffusion, driven by the nuclear dipole-dipole interaction, there may also be a change in δh^z due to corrections to the projected effective Hamiltonian considered here (see Ref. [50], Appendix B for details). After tracing out the electron pseudo–spin in state ρ_S, these correction terms give rise to an electron-mediated nuclear spin-spin interaction which, in general, takes the form of an anisotropic (XYZ) Heisenberg interaction

$$H_{nn} = \mathrm{Tr}_S\{\rho_S H\} = \sum_{i,j,\alpha=\{x,y,z\}} J_{ij}^\alpha I_i^\alpha I_j^\alpha. \tag{I.1}$$

Here, the indices i and j run over all nuclear spin sites.

We use the corrections to leading order in the inverse Zeeman splitting $1/\epsilon_z$ ($\epsilon_z = g\mu_B B$) given in Ref. [50]. This gives the typical value of the exchange constants $\left|J_{ij}^\alpha\right| \sim A^2/N^2\epsilon_z$. Assuming an unpolarized nuclear spin state, each nuclear spin will therefore precess in an effective mean field generated by all other spins in the dot of typical magnitude

$$h_{\mathrm{eff}} \sim \sqrt{N}\left|J_{ij}^\alpha\right| \sim A^2/N^{\frac{3}{2}}\epsilon_z. \tag{I.2}$$

This effective field will result in precession of the nuclear spins about an arbitrary angle (and hence, may change the value of δh^z) on a time scale

$$\tau_p \sim N^{\frac{3}{2}}\epsilon_z/A^2 \sim 10^{-2}\,\mathrm{s}, \tag{I.3}$$

where we have assumed $N = 10^6$ nuclear spins within the quantum dot, and $\epsilon_z/g\mu_B = A/g\mu_B \simeq 3.5\,\mathrm{T}$ for the time estimate. This is only a worst–case estimate, which neglects the effects, e.g., of a Knight-shift gradient (due to strong confinement of the electron), which may further weaken the dynamical effect discussed here. We expect the dipolar nuclear spin diffusion time to be the limiting time scale for nuclear spin dynamics, in light of experiments on diffusion near donor impurities in GaAs. [139] If the effect giving rise to τ_p in Eq. (I.3) were significant, it could be further suppressed by choosing a larger quantum dot size or stronger magnetic field, thus allowing many electron spin measurements on the time scale of variation of δh^z.

Appendix J

Nuclear spin state measurement

In this appendix we describe how a single measurement of the two–electron system affects the nuclear spin state. We give the analytical expression for the diagonal elements of the nuclear spin density operator after a measurement.

At t=0 the system is described by the following density operator

$$\rho(0) = \rho_e(0) \otimes \rho_I(0) = |+\rangle \langle +| \otimes \sum_i p_i \left|\psi_I^i\right\rangle \left\langle\psi_I^i\right|, \tag{J.1}$$

with nuclear spin state $\left|\psi_I^i\right\rangle = \sum_n a_n^i |n\rangle$. The Hamiltonian H_0 of Eq.(5.1) acts on the the nuclear–spin system as $H_0 |n\rangle = H_n |n\rangle$, where in H_n the operator δh^z has been replaced by δh_n^z (because $\delta h^z |n\rangle = \delta h_n^z |n\rangle$). Since $[H_0, \delta h^z] = 0$, only the diagonal elements of the nuclear density operator ρ_I (in the basis of δh^z) enter in matrix elements for operators acting only on the two–electron system. As described in Section 5.2.1, these diagonal elements $\rho_I(n) = \rho_I(n,0) = \langle n| Tr_e\{\rho(0)\} |n\rangle$ describe a continuous Gaussian distribution in the continuum limit. The trace over the electron system is defined as $Tr_e\rho(t) = \langle +| \rho(t) |+\rangle + \langle -| \rho(t) |-\rangle$ and for $\rho_I(n,0)$ we have

$$\rho_I(n,0) = \sum_i p_i |a_n^i|^2. \tag{J.2}$$

The time evolution operators $U(t)$ and $U_n(t)$ are defined through $i\dot{U}(t) = H_0(t)U(t)$ and $i\dot{U}_n(t) = H_n(t)U_n(t)$ and thus the density operator $\rho(0)$ evolves under the Hamiltonian H_0 as

$$\begin{aligned}
\rho(t) &= U(t)\rho(0)U^\dagger(t) \\
&= U(t) \left(\rho_e(0) \otimes \sum_i \sum_{n,l} p_i a_n^i a_l^{i*} |n\rangle \langle l| \right) U^\dagger(t) \\
&= \sum_{n,l} \left(U_n(t)\rho_e(0)U_l^\dagger(t) \otimes \sum_i p_i a_n^i a_l^{i*} |n\rangle \langle l| \right).
\end{aligned} \tag{J.3}$$

At time t_m a measurement in the basis of $|+\rangle$ and $|-\rangle$ is performed on one single two-electron system coupled to nuclear spins. Since the outcome of this measurement is known, the state of the system after the measurement is[1] (the result depends on whether $|+\rangle$ or $|-\rangle$ was measured)

$$\begin{aligned}\rho^{(1,\pm)}(t_m) &= \frac{|\pm\rangle\langle\pm|\,\rho(t_m)\,|\pm\rangle\langle\pm|}{P^{\pm}(t_m)} \\ &= \sum_{n,l}\Big(|\pm\rangle\langle\pm|\,U_n(t_m)\rho_e(0)U_l^{\dagger}(t_m)\,|\pm\rangle\langle\pm| \\ &\qquad\otimes\sum_i p_i a_n^i a_l^{i*}\,|n\rangle\langle l|\Big)\frac{1}{P^{\pm}(t_m)}, \qquad (J.4)\end{aligned}$$

with

$$\begin{aligned}P^{\pm}(t_m) &= Tr_I Tr_e\{|\pm\rangle\langle\pm|\,\rho(t_m)\} \qquad (J.5)\\ &= \sum_i\sum_n\frac{1}{2}\left(1\pm\langle\tau^z(t_m)\rangle_n\right)p_i|a_n^i|^2, \qquad (J.6)\end{aligned}$$

where $Tr_I A = \sum_n \langle n|\,A\,|n\rangle$ and $\langle\tau^z(t)\rangle_n$ is given in Eq.(5.4). Here, $P^{\pm}(t_m)$ is the probability to measure $|\pm\rangle$ at time t_m. We are mainly interested in the diagonal elements of the nuclear density operator ρ_I after the measurement.

$$\begin{aligned}\rho_I^{(1,\pm)}(n,t_m) &= \langle n|\,Tr_e\rho^{(1,\pm)}(t_m)\,|n\rangle \qquad (J.7)\\ &= \frac{\rho_I(n,0)}{P^{\pm}(t_m)}\langle\pm|\,U_n(t_m)\rho_e(0)U_n^{\dagger}(t_m)\,|\pm\rangle \qquad (J.8)\\ &= \frac{\rho_I(n,0)}{P^{\pm}(t_m)}\frac{1}{2}\left(1\pm\langle\tau^z(t_m)\rangle_n\right). \qquad (J.9)\end{aligned}$$

Using Eq.(5.4) we find

$$\rho_I^{(1,+)}(n,t_m) = \frac{\rho_I(n,0)}{P^{+}(t_m)}\frac{1}{2}\left(\frac{2(\Omega_n-\omega)^2}{(\Omega_n-\omega)^2+(j/2)^2}+\frac{(j/2)^2(1+\cos(\omega' t_m))}{(\Omega_n-\omega)^2+(j/2)^2}\right) \qquad (J.10)$$

and

$$\rho_I^{(1,-)}(n,t_m) = \frac{\rho_I(n,0)}{P^{-}(t_m)}\frac{1}{2}\frac{(j/2)^2(1-\cos(\omega' t_m))}{(\Omega_n-\omega)^2+(j/2)^2}, \qquad (J.11)$$

where ω' is given in Eq.(5.5) and depends on the eigenvalue δh_n^z of the nuclear spin eigenstate through Ω_n.

Parenthetically, we note that in the case (not described in this article) where the measurement is performed on an ensemble of many different double quantum dots, the state of the ensemble after the measurement is [173]

$$\begin{aligned}\rho_{ens}^{(1)}(t_m) &= \sum_{n,l}\Big(|+\rangle\langle+|\,U_n(t_m)\rho_e(0)U_l^{\dagger}(t_m)\,|+\rangle\langle+| \\ &\quad + |-\rangle\langle-|\,U_n(t_m)\rho_e(0)U_l^{\dagger}(t_m)\,|+\rangle\langle+|\Big) \\ &\quad\otimes\sum_i p_i a_n^i a_l^{i*}\,|n\rangle\langle l|, \qquad (J.12)\end{aligned}$$

---

[1] The measurement performed at t_m is not sufficient to distinguish the different states $|\psi_I^i\rangle$. This is because it is a measurement in the two–electron system and it only has an effect on the nuclear spin system in a way that some eigenstates $|n\rangle$ gain weight and some loose. This happens for all states $|\psi_I^i\rangle$ in the same way and thus from such a measurement we cannot tell into which of the states $|\psi_I^i\rangle$ the system has collapsed.

and the nuclear–spin distribution has not changed. If a complete measurement of the Rabi–resonance lineshape would be performed on an ensemble of double dots, the result would be the Voigt profile described in Sec. 5.2.1.

Bibliography

[1] D. Loss and D. P. DiVincenzo, Phys. Rev. A**57**, 120 (1998).

[2] C. Fasth, A. Fuhrer, M. Bjork, and L. Samuelson, Nano Letters **5**, 1487 (2005).

[3] N. Mason, M. J. Biercuk, and C. M. Marcus, Science **303**, 655 (2004).

[4] M. Biercuk, S. Garaj, N. Mason, J. Chow, and C. Marcus, Nano Letters **5**, 1267 (2005).

[5] M. R. Gräber, W. A. Coish, C. Hoffmann, M. Weiss, J. Furer, S. Oberholzer, D. Loss, and C. Schönenberger, Phys. Rev. B**74**, 075427 (2006).

[6] S. Sapmaz, C. Meyer, P. Beliczynski, P. Jarillo-Herrero, and L. P. Kouwenhoven, Nano Lett. **6**, 1350 (2006).

[7] H. I. Jorgensen, K. Grove-Rasmussen, J. R. Hauptmann, and P. E. Lindelof, arXiv.org:cond-mat/0606374 (2006).

[8] L.-A. Wu, D. A. Lidar, and M. Friesen, Phys. Rev. Lett.**93**, 030501 (2004).

[9] E. Medeiros-Ribeiro, E. Ribeiro, and H. Westfahl, Appl. Phys. A **77**, 725 (2003).

[10] J. Kyriakidis and S. J. Penney, arXiv.org:cond-mat/0407139 (2004).

[11] J. Schliemann, D. Loss, and A. H. MacDonald, Phys. Rev. B**63**, 085311 (2001).

[12] J. Schliemann and D. Loss, in *Proc. Int. School of Physics "E. Fermi": Quantum Phenomena in Mesoscopic systems* (IOS Press, Amsterdam, 2003), p. 135.

[13] R. Requist, J. Schliemann, A. G. Abanov, and D. Loss, Phys. Rev. B**71**, 115315 (2005).

[14] G. Burkard, D. Loss, and D. DiVincenzo, Phys. Rev. B**59**, 2070 (1999).

[15] A. V. Khaetskii, D. Loss, and L. Glazman, Phys. Rev. Lett.**88**, 186802 (2002).

[16] I. A. Merkulov, A. L. Efros, and M. Rosen, Phys. Rev. B**65**, 205309 (2002).

[17] A. Khaetskii, D. Loss, and L. Glazman, Phys. Rev. B**67**, 195329 (2002).

[18] J. Schliemann, A. V. Khaetskii, and D. Loss, Phys. Rev. B**66**, 245303 (2002).

[19] Y. B. Lyanda-Geller, I. L. Aleiner, and B. L. Altshuler, Phys. Rev. Lett.**89**, 107602 (2002).

[20] K. Ono and S. Tarucha, Phys. Rev. Lett.**92**, 256803 (2004).

[21] J. R. Petta, A. C. Johnson, J. M. Taylor, E. A. Laird, A. Yacoby, M. D. Lukin, C. M. Marcus, M. P. Hanson, and A. C. Gossard, Science **309**, 2180 (2005).

[22] F. H. L. Koppens, J. A. Folk, J. M. Elzerman, R. Hanson, L. H. W. van Beveren, I. T. Vink, H. P. Tranitz, W. Wegscheider, L. P. Kouwenhoven, and L. M. K. Vandersypen, Science **309**, 1346 (2005).

[23] E. A. Laird, J. R. Petta, A. C. Johnson, C. M. Marcus, A. Yacoby, M. P. Hanson, and A. C. Gossard, Phys. Rev. Lett.**97**, 056801 (2006).

[24] F. H. L. Koppens *et al.*, Unpublished (2006), (to appear in Nature).

[25] A. M. Stoneham, in *Theory of Defects in Solids* (Clarendon, ADDRESS, 1975), pp. 455–466.

[26] G. Breit and F. W. Doermann, Phys. Rev. **36**, 1732 (1930).

[27] D. Paget, G. Lampel, B. Sapoval, and V. I. Safarov, Phys. Rev. B**15**, 5780 (1977).

[28] V. Cerletti, W. A. Coish, O. Gywat, and D. Loss, Nanotechnology **16**, R27 (2005).

[29] L. P. Kouwenhoven, D. G. Austing, and S. Tarucha, Reports on Progress in Physics **64**, 701 (2001).

[30] W. G. van der Wiel, S. de Franceschi, J. M. Elzerman, T. Fujisawa, S. Tarucha, and L. P. Kouwenhoven, Rev. Mod. Phys.**75**, 1 (2003).

[31] G. Klimeck, G. Chen, and S. Datta, Phys. Rev. B**50**, 2316 (1994).

[32] P. Pals and A. MacKinnon, Journal of the Physics of Condensed Matter **8**, 5401 (1996).

[33] J. M. Golden and B. I. Halperin, Phys. Rev. B**53**, 3893 (1996).

[34] R. Ziegler, C. Bruder, and H. Schoeller, Phys. Rev. B**62**, 1961 (2000).

[35] T. Fujisawa, D. G. Austing, Y. Tokura, Y. Hirayama, and S. Tarucha, Nature **419**, 278 (2002).

[36] D. M. Zumbühl, C. M. Marcus, M. P. Hanson, and A. C. Gossard, Phys. Rev. Lett.**93**, 256801 (2004).

[37] D. R. Stewart, D. Sprinzak, C. M. Marcus, C. I. Duruoz, and J. Harris, J. S., Science **278**, 1784 (1997).

[38] T. Fujisawa, Y. Tokura, and Y. Hirayama, Phys. Rev. B**63**, 081304 (2001).

[39] V. N. Golovach and D. Loss, Phys. Rev. B**69**, 245327 (2004).

[40] T. Schmidt, R. J. Haug, K. V. Klitzing, A. Förster, and H. Lüth, Phys. Rev. Lett.**78**, 1544 (1997).

[41] G. Schedelbeck, W. Wegscheider, M. Bichler, and G. Abstreiter, Science **278**, 1793 (1997).

[42] R. Blick, D. Pfannkuche, R. Haug, K. Klitzing, and K. Eberl, Phys. Rev. Lett.**80**, 4032 (1998).

[43] M. Brodsky, N. Zhitenev, R. Ashoori, L. Pfeiffer, and K. West, Physical Review Letters **85**, 2356 (2000).

[44] M. Bayer, P. Hawrylak, K. Hinzer, S. Fafard, M. Korkusinski, Z. Wasilewski, O. Stern, and A. Forchel, Science **291**, 451 (2001).

[45] T. Ota, M. Rontani, S. Tarucha, Y. Nakata, H. Z. Song, T. Miyazawa, T. Usuki, M. Takatsu, and N. Yokoyama, Phys. Rev. Lett.**95**, 236801 (2005).

[46] A. K. Hüttel, S. Ludwig, H. Lorenz, K. Eberl, and J. P. Kotthaus, Phys. Rev. B**72**, 081310 (2005).

[47] T. Hatano, M. Stopa, and S. Tarucha, Science **309**, 268 (2005).

[48] C. Beenakker, Phys. Rev. B**44**, 1646 (1991).

[49] J. R. Petta, A. C. Johnson, A. Yacoby, C. M. Marcus, M. P. Hanson, and A. C. Gossard, Phys. Rev. B**72**, 161301 (2005).

[50] W. Coish and D. Loss, Phys. Rev. B**72**, 125337 (2005).

[51] J. M. Taylor, J. R. Petta, A. C. Johnson, A. Yacoby, C. M. Marcus, and M. D. Lukin, http://arXiv.org/cond-mat/0602470 (2006).

[52] M. Stopa and C. M. Marcus, http://arxiv.org/cond-mat/0604008 (2006).

[53] S. Tarucha, D. G. Austing, T. Honda, R. J. van der Hage, and L. P. Kouwenhoven, Phys. Rev. Lett.**77**, 3613 (1996).

[54] M. Ciorga, A. Sachrajda, P. Hawrylak, C. Gould, P. Zawadzki, S. Jullian, Y. Feng, and Z. Wasilewski, Phys. Rev. B**61**, 16315 (2000).

[55] J. Elzerman, R. Hanson, J. Greidanus, L. Willems van Beveren, S. de Franceschi, L. Vandersypen, S. Tarucha, and L. Kouwenhoven, Phys. Rev. B**67**, 161308 (2003).

[56] J. R. Petta, A. C. Johnson, C. M. Marcus, M. P. Hanson, and A. C. Gossard, Phys. Rev. Lett.**93**, 186802 (2004).

[57] K. Ono, D. G. Austing, Y. Tokura, and S. Tarucha, Science **297**, 1313 (2002).

[58] A. K. Hüttel, J. Weber, A. W. Holleitner, D. Weinmann, K. Eberl, and R. H. Blick, Phys. Rev. B**69**, 073302 (2004).

[59] A. M. Steane, Phys. Rev. A**68**, 042322 (2003).

[60] A. V. Khaetskii and Y. V. Nazarov, Phys. Rev. B**61**, 12639 (2000).

[61] A. V. Khaetskii and Y. V. Nazarov, Phys. Rev. B**64**, 125316 (2001).

[62] V. N. Golovach, A. Khaetskii, and D. Loss, Phys. Rev. Lett.**93**, 016601 (2004).

[63] D. Bulaev and D. Loss, Phys. Rev. B**71**, 205324 (2005).

[64] M. Borhani, V. Golovach, and D. Loss, Phys. Rev. B**73**, 155311 (2005).

[65] S. I. Erlingsson, Y. V. Nazarov, and V. I. Fal'ko, Phys. Rev. B**64**, 195306 (2001).

[66] S. I. Erlingsson and Y. V. Nazarov, Phys. Rev. B**66**, 155327 (2002).

[67] J. Schliemann, A. Khaetskii, and D. Loss, J. Phys.: Condens. Matter **15**, R1809 (2003).

[68] R. de Sousa and S. Das Sarma, Phys. Rev. B**68**, 115322 (2003).

[69] R. de Sousa and S. Das Sarma, Phys. Rev. B**67**, 033301 (2003).

[70] W. Coish and D. Loss, Phys. Rev. B**70**, 195340 (2004).

[71] V. Abalmassov and F. Marquardt, Phys. Rev. B**70**, 075313 (2004).

[72] S. I. Erlingsson and Y. V. Nazarov, Phys. Rev. B**70**, 205327 (2004).

[73] R. de Sousa, N. Shenvi, and K. Whaley, Phys. Rev. B**72**, 045330 (2005).

[74] N. Shenvi, R. de Sousa, and K. B. Whaley, Phys. Rev. B**71**, 224411 (2005).

[75] N. Shenvi, R. de Sousa, and K. B. Whaley, Phys. Rev. B**71**, 144419 (2005).

[76] J. M. Taylor and M. D. Lukin, arXiv:quant-ph/0512059 (2005).

[77] W. Yao, R.-B. Liu, and L. J. Sham, arXiv.org:cond-mat/0508441 (2005).

[78] W. M. Witzel, R. de Sousa, and S. Das Sarma, Phys. Rev. B**72**, 161306 (2005).

[79] D. Klauser, W. A. Coish, and D. Loss, Phys. Rev. B**73**, 205302 (2005).

[80] W. Yao, R.-B. Liu, and L. J. Sham, http://arXiv.org/cond-mat/0604634 (2006).

[81] A. Bracker, E. Stinaff, D. Gammon, M. Ware, J. Tischler, A. Shabaev, A. Efros, D. Park, D. Gershoni, V. Korenev, and I. Merkulov, Phys. Rev. Lett.**94**, 047402 (2005).

[82] M. Gurudev Dutt, J. Cheng, B. Li, X. Xu, X. Li, P. Berman, D. Steel, A. Bracker, D. Gammon, S. Economou, R.-B. Liu, and L. Sham, Phys. Rev. Lett.**94**, 227403 (2005).

[83] A. C. Johnson, J. R. Petta, J. M. Taylor, A. Yacoby, M. D. Lukin, C. M. Marcus, M. P. Hanson, and A. C. Gossard, Nature **435**, 925 (2005).

[84] A. C. Johnson, J. R. Petta, C. M. Marcus, M. P. Hanson, and A. C. Gossard, Phys. Rev. B**72**, 165308 (2005).

[85] D. Bulaev and D. Loss, Phys. Rev. Lett.**95**, 076805 (2005).

[86] M. Friesen, P. Rugheimer, D. E. Savage, M. G. Lagally, D. W. van der Weide, R. Joynt, and M. A. Eriksson, Phys. Rev. B**67**, 121301 (2003).

[87] C. P. Slichter, *Principles of Magnetic Resonance* (Springer-Verlag, Berlin, 1980).

[88] J. M. Elzerman, R. Hanson, L. H. Willems van Beveren, B. Witkamp, L. M. K. Vandersypen, and L. P. Kouwenhoven, Nature**430**, 431 (2004).

[89] S. Amasha, K. MacLean, I. Radu, D. Zumbuhl, M. Kastner, M. Hanson, and A. Gossard, arXiv.org:cond-mat/0607110 (2006).

[90] P. San-Jose, G. Zarand, A. Shnirman, and G. Schon, Phys. Rev. Lett.**97**, 076803 (2006).

[91] W. Coish, V. Golovach, J. Egues, and D. Loss, arXiv.org:cond-mat/0606782 (2006).

[92] M. Gaudin, Jour. de Phys. **37**, 1087 (1976).

[93] K. Schulten and P. G. Wolynes, Jour. Chem. Phys. **68**, 3292 (1978).

[94] Y. G. Semenov and K. W. Kim, Phys. Rev. B**67**, 073301 (2003).

[95] S. I. Erlingsson, O. N. Jouravlev, and Y. V. Nazarov, Phys. Rev. B**72**, 033301 (2005).

[96] P.-F. Braun, X. Marie, L. Lombez, B. Urbaszek, B. Amand, P. Renucci, V. Kalevich, K. Kavokin, O. Krebs, P. Voisin, and Y. Masumoto, Phys. Rev. Lett.**94**, 116601 (2005).

[97] E. A. Yuzbashyan, B. L. Altshuler, V. B. Kuznetsov, and V. Z. Enolskii, J. Phys. A **38**, 7831 (2004).

[98] J. M. Taylor, W. Dür, P. Zoller, A. Yacoby, C. M. Marcus, and M. D. Lukin, Phys. Rev. Lett.**94**, 236803 (2005).

[99] J. M. Taylor, H. A. Engel, W. Dur, A. Yacoby, C. M. Marcus, P. Zoller, and M. D. Lukin, Nat Phys **1**, 177 (2005).

[100] Jouravlev, Phys. Rev. Lett.**96**, 176804 (2006).

[101] J. M. Geremia, J. K. Stockton, and H. Mabuchi, Science **304**, 270 (2004).

[102] F. M. Cucchietti, J. P. Paz, and W. H. Zurek, Phys. Rev. A**72**, 052113 (2005).

[103] K. Al-Hassanieh, V. Dobrovitski, E. Dagotto, and B. Harmon, Phys. Rev. Lett.**97**, 037204 (2006).

[104] M. Eto, T. Ashiwa, and M. Murata, Physica E Low-Dimensional Systems and Nanostructures **22**, 426 (2004).

[105] J. J. Sakurai, *Modern Quantum Mechanics* (Addison Wesley, Redwood City, California, 1985), Chap. 3, p. 192.

[106] S. A. Wolf, D. D. Awschalom, R. A. Buhrman, J. M. Daughton, S. von Molnár, M. L. Roukes, A. Y. Chtchelkanova, and D. M. Treger, Science **294**, 1488 (2001).

[107] D. D. Awschalom, D. Loss, and N. Samarth, *Semiconductor Spintronics and Quantum Computing* (Springer-Verlag, Berlin, 2002).

[108] J. Preskill, Proc. R. Soc. London, Ser. A **454**, 385 (1998).

[109] J. M. Kikkawa and D. D. Awschalom, Phys. Rev. Lett.**80**, 4313 (1998).

[110] V. N. Golovach and D. Loss, Europhys. Lett. **62**, 83 (2003).

[111] J. M. Taylor, C. M. Marcus, and M. D. Lukin, Phys. Rev. Lett.**90**, 206803 (2003).

[112] J. M. Taylor, A. Imamoglu, and M. D. Lukin, Phys. Rev. Lett.**91**, 246802 (2003).

[113] A. Imamoğlu, E. Knill, L. Tian, and P. Zoller, Phys. Rev. Lett.**91**, 017402 (2003).

[114] Y. G. Semenov and K. W. Kim, Phys. Rev. Lett.**92**, 026601 (2004).

[115] S. Saykin, D. Mozyrsky, and V. Privman, Nano Letters **2**, 651 (2002).

[116] M. Dobers, K. von Klitzing, J. Schneider, G. Weimann, and K. Ploog, Phys. Rev. Lett.**61**, 1650 (1988).

[117] K. R. Wald, L. P. Kouwenhoven, P. L. McEuen, N. C. van der Vaart, and C. T. Foxon, Phys. Rev. Lett.**73**, 1011 (1994).

[118] J. H. Smet, R. A. Deutschmann, F. Ertl, W. Wegscheider, G. Abstreiter, and K. von Klitzing, Nature **415**, 281 (2002).

[119] G. Salis, D. T. Fuchs, J. M. Kikkawa, D. D. Awschalom, Y. Ohno, and H. Ohno, Phys. Rev. Lett.**86**, 2677 (2001).

[120] R. J. Epstein, J. Stephens, M. Hanson, Y. Chye, A. C. Gossard, P. M. Petroff, and D. D. Awschalom, Phys. Rev. B**68**, 041305 (2003).

[121] A. M. Tyryshkin, S. A. Lyon, A. V. Astashkin, and A. M. Raitsimring, Phys. Rev. B**68**, 193207 (2003).

[122] V. Dobrovitski, H. de Raedt, M. Katsnelson, and B. Harmon, Phys. Rev. Lett.**90**, 210401 (2003).

[123] W. H. Zurek, F. M. Cucchietti, and J. P. Paz, arXiv:quant-ph/0312207 (2003).

[124] J. R. Klauder and P. W. Anderson, Physical Review **125**, 912 (1962).

[125] D. Loss and D. P. DiVincenzo, (2003).

[126] E. Fick and G. Sauermann, *The Quantum Statistics of Dynamic Processes* (Springer-Verlag, Berlin, 1990).

[127] H.-A. Engel and D. Loss, Phys. Rev. Lett.**86**, 4648 (2001).

[128] H.-A. Engel and D. Loss, Phys. Rev. B**65**, 195321 (2002).

[129] E. Abe, K. Itoh, J. Isoya, and S. Yamasaki, Phys. Rev. B**70**, 033204 (2004).

[130] M. Fanciulli, P. Höfer, and A. Ponti, Physica B **340**, 895 (2003).

[131] M. Kroutvar, Y. Ducommun, D. Heiss, M. Bichler, D. Schuh, G. Abstreiter, and J. J. Finley, Nature **432**, 81 (2004).

[132] D. Bulaev and D. Loss, cond-mat/0503181 (unpublished).

[133] A. Greilich, R. Oulton, S. Y. Verbin, D. R. Yakovlev, M. Bayer, V. Starvarache, D. Reuter, and A. Wieck, cond-mat/0505446 (unpublished).

[134] R. Hanson, L. H. W. van Beveren, I. T. Vink, J. M. Elzerman, W. J. M. Naber, F. H. L. Koppens, L. P. Kouwenhoven, and L. M. K. Vandersypen, Phys. Rev. Lett.**94**, 196802 (2005).

[135] F. Meier, J. Levy, and D. Loss, Phys. Rev. Lett.**90**, 047901 (2003).

[136] F. Meier, J. Levy, and D. Loss, Phys. Rev. B**68**, 134417 (2003).

[137] F. Troiani, A. Ghirri, M. Affronte, S. Carretta, P. Santini, G. Amoretti, S. Piligkos, G. Timco, and R. E. P. Winpenny, Phys. Rev. Lett.**94**, 207208 (2005).

[138] H.-J. Werner, Z. Schulten, and K. Schulten, J. Chem. Phys. **67**, 646 (1977).

[139] D. Paget, Phys. Rev. B**25**, 4444 (1982).

[140] M. Seck, M. Potemski, and P. Wyder, Phys. Rev. B**56**, 7422 (1997).

[141] H.-A. Engel, V. N. Golovach, D. Loss, L. M. K. Vandersypen, J. M. Elzermann, R. Hanson, and L. P. Kouwenhoven, Phys. Rev. Lett.**93**, 106804 (2004).

[142] K. Blum, in *Density Matrix Theory and Applications* (Plenum, New York, 1981), Chap. 8, pp. 277–308.

[143] T. Hayashi, T. Fujisawa, H. D. Cheong, Y. H. Jeong, and Y. Hirayama, Phys. Rev. Lett.**91**, 226804 (2003).

[144] H.-A. Engel and D. Loss, Science **309**, 586 (2005).

[145] Y. Kato, R. Myers, D. Driscoll, J. Gossard, A.C.and Levy, and D. Awschalom, Science **299**, 1201 (2003).

[146] G. Giedke, J. M. Taylor, D. D'Alessandro, M. D. Lukin, and A. Imamoğlu, Phys. Rev. A**74**, 032316 (2006).

[147] D. Stepanenko, G. Burkard, G. Giedke, and A. Imamoglu, Phys. Rev. Lett.**96**, 136401 (2005).

[148] J. Levy, Phys. Rev. Lett.**89**, 147902 (2002).

[149] B. Armstrong, J. Quant. Spectrosc. Radiat. Transfer **7**, 61 (1967).

[150] A. Stoneham, Journal of Physics D Applied Physics **5**, 670 (1972).

[151] P. Minguzzi and A. di Lieto, Journal of Molecular Spectroscopy **109**, 388 (1985).

[152] A. Barenco, C. Bennett, R. Cleve, D. DiVincenzo, N. Margolus, P. Shor, T. Sleator, J. Smolin, and H. Weinfurter, Phys. Rev. A**52**, 3457 (1995).

[153] C. Livermore, C. Crouch, R. Westervelt, K. Campman, and A. Gossard, Science **274**, 1332 (1996).

[154] A. Holleitner, R. Blick, A. Huttel, K. Eberl, and J. Kotthaus, Science **297**, 70 (2002).

[155] S. Sahoo, T. Kontos, J. Furer, C. Hoffmann, M. Gräber, A. Cottet, and C. Schönenberger, Nature Physics **1**, 99 (2005).

[156] M. Buitelaar, T. Nussbaumer, and C. Schönenberger, Physical Review Letters **89**, 256801 (2002).

[157] Y. Doh, J. van Dam, A. Roest, E. Bakkers, L. Kouwenhoven, and S. De Franceschi, Science **309**, 272 (2005).

[158] M.-S. Choi, C. Bruder, and D. Loss, Phys. Rev. B**62**, 13569 (2000).

[159] J. Furer, Ph.D. thesis, University of Basel, 2005.

[160] E. Knill, Nature **434**, 39 (2005).

[161] R. Hanson and G. Burkard, arXiv:cond-mat/0605576 (2006).

[162] J. Kyriakidis and G. Burkard, arXiv:cond-mat/0606627 (2006).

[163] E. I. Rashba and A. L. Efros, Phys. Rev. Lett.**91**, 126405 (2003).

[164] D. Stepanenko and N. E. Bonesteel, Phys. Rev. Lett.**93**, 140501 (2004).

[165] C. Flindt, A. S. Sørensen, and K. Flensberg, arXiv:cond-mat/0603559 (2006).

[166] V. N. Golovach, M. Borhani, and D. Loss, http://arXiv.org/cond-mat/0601674 (2006).

[167] Y. Tokura, W. G. van der Wiel, T. Obata, and S. Tarucha, Phys. Rev. Lett.**96**, 047202 (2006).

[168] X. Hu and S. Das Sarma, Phys. Rev. Lett.**96**, 100501 (2006).

[169] W. A. Coish and D. Loss, arXiv:cond-mat/0606550 (2006).

[170] M. A. Nielsen and I. L. Chuang, *Quantum Computation and Quantum Information* (Cambridge, ADDRESS, 2001).

[171] C. Zener, Proceedings of the Royal Society of London **137**, 696 (1932).

[172] A. M. Stoneham, in *Theory of Defects in Solids* (Clarendon, ADDRESS, 1975), pp. 887–888.

[173] A. Peres, *Quantum Theory: Concepts and Methods* (Kluwer Academic Publishers, ADDRESS, 1993).

Lebenslauf

von William Anthony Coish
Geboren am 12. Mai 1978 in Winnipeg, Kanada
Staatsangehörigkeit: kanadisch

Ausbildung

1983-1985	Carpathia Elementary School, Winnipeg, Manitoba, Kanada
1985-1986	Inuglak School, Whale Cove, Nunavut, Kanada
1986-1988	Atausiunasuarniq School, Coral Harbour, Nunavut, Kanada
1988	Westgrove Elementary School, Winnipeg, Manitoba, Kanada
1988-1990	Grosvenor Elementary School, Winnipeg, Manitoba, Kanada
1990-1993	École River Heights School, Winnipeg, Manitoba, Kanada
1993-1996	Kelvin High School, Winnipeg, Manitoba, Kanada
1996-2000	Studium der Physik an der University of Manitoba und der University of Winnipeg, Winnipeg, Manitoba, Kanada
Mai 2000	B.Sc. (honours) in Physik
2000-2002	Studium der Physik an der McMaster University, Hamilton, Ontario, Kanada
Sept. 2002	M.Sc. in Physik Masterarbeit “Lattice Landau theory for two-dimensional superconductors” in theoretischer Festkörperphysik unter der Anleitung von Prof. Dr. A. J. Berlinsky und Prof. Dr. C. Kallin
2002-2006	Promotionsstudium in Theoretscher Physik an der Universität Basel Dissertation “Spins in quantum dots: Hyperfine interaction, transport, and coherent control” unter der Anleitung von Prof. Dr. D. Loss

Publications

[1] W. A. Coish and Daniel Loss
Exchange-controlled single-spin rotations in quantum dots
cond-mat/0610443; Submitted to Phys. Rev. Lett.

[2] W. A. Coish, E. A. Yuzbashyan, B. L. Altshuler, and Daniel Loss
Quantum vs. classical hyperfine-induced dynamics in a quantum dot
cond-mat/0610633; To appear in Jour. Appl. Phys. (conference proceedings for ICPS06).

[3] W. A. Coish, Vitaly N. Golovach, J. Carlos Egues, and Daniel Loss
Measurement, control, and decay of quantum-dot spins
cond-mat/0606782; Invited feature article accepted for publication in a special issue of Phys. Stat. Solidi.

[4] W. A. Coish and Daniel Loss
Quantum computing with spins in solids
cond-mat/0606550; Review to appear in the Handbook of Magnetism and Advanced Magnetic Materials, vol. 5, Wiley.

[5] D. Klauser, W. A. Coish, and Daniel Loss
Quantum-dot spin qubit and hyperfine interaction
cond-mat/0604252; (to appear in proceedings of the DPG meeting (2006), Adv. Sol. State Phys. vol. **46**, (2006)).

[6] M. R. Graeber, W. A. Coish, C. Hoffmann, M. Weiss, J. Furer, S. Oberholzer, D. Loss, and C. Schoenenberger
Molecular states in carbon nanotube double quantum dots
Phys. Rev. B **74**, 075427 (2006).

[7] D. Klauser, W. A. Coish, and Daniel Loss
Nuclear spin state narrowing via gate–controlled Rabi oscillations in a double quantum dot
Phys. Rev. B **73**, 205302 (2006).

[8] W. A. Coish and Daniel Loss
Singlet-triplet decoherence due to nuclear spins in a double quantum dot
Phys. Rev. B **72**, 125337 (2005).

[9] Veronica Cerletti, W. A. Coish, Oliver Gywat, and Daniel Loss
Recipes for spin-based quantum computing
Nanotechnology **16**, R27 (2005).

[10] W. A. Coish and Daniel Loss
Non-Markovian dynamics of a localized electron spin due to the hyperfine interaction
Hyperfine Interactions **158**, 235 (2005) (Proceedings of HFI2004, Bonn, Germany).

[11] W. A. Coish and Daniel Loss
Hyperfine interaction in a quantum dot: Non-Markovian electron spin dynamics
Phys. Rev. B **70**, 195340 (2004).

[12] J. M. Vail, W. A. Coish, H. He, and A. Yang
F center in BaF_2: Diffuse excited state
Phys. Rev. B **66**, 014109 (2002).